UNIVERSIDAD COMPLUTENSE DE MADRID

FACULTAD DE FARMACIA


# TESIS DOCTORAL

Bases reactivas de la toxicidad de nanomateriales

Reactive bases of nanomaterial toxicity

MEMORIA PARA OPTAR AL GRADO DE DOCTOR

PRESENTADA POR

Víctor Alcolea Rodríguez

DIRECTORES

Dr. Miguel Ángel Bañares González
Dra. Raquel Portela Rodríguez

# UNIVERSIDAD COMPLUTENSE DE MADRID

## FACULTAD DE FARMACIA

PROGRAMA DE DOCTORADO: QUÍMICA MÉDICA

# TESIS DOCTORAL

BASES REACTIVAS DE LA TOXICIDAD DE NANOMATERIALES//

REACTIVE BASES OF NANOMATERIAL TOXICITY

MEMORIA PARA OPTAR AL GRADO DE DOCTOR PRESENTADA POR

Víctor Alcolea Rodríguez

DIRECTORES

Prof. Dr. Miguel Ángel Bañares González

Dra. Raquel Portela Rodríguez

CENTRO DE REALIZACIÓN DE LA TESIS

Instituto de Catálisis y Petroleoquímica (ICP-CSIC) & Federal Institute for Risk Assessment (BfR)

# Agradecimientos. Acknowledgements

Hace algo más de 4 años me mudé a Madrid para empezar esta tesis doctoral. Fue una decisión difícil por comprometerme a estar unos años más fuera de mi casa, y por irme a una ciudad en la que no conocía a nadie. Qué suerte tuve de encontrar la propuesta de Raquel y Miguel Ángel e incorporarme al ICP. Desde entonces, tengo mucha gente a la que agradecer el haber llegado hasta aquí.

Me gustaría empezar agradeciendo a todos aquellos amigos que me reciben tan bien siempre que vuelvo a casa. Por todos esos viajes y buenos momentos… y los que nos quedan. Gracias a los äms (¡y amëras!), brownie, casanovas, strawers y a muchos más que saben que también están incluidos en ese grupo de personas a las que yo considero fundamentales y tan necesarias para recargar pilas cada vez que aterrizo en casa. Entre tantos mallorquines, por supuesto, también están mis compañeros de piso. Qué mérito aguantar mis rarezas en el día a día. Gracias de corazón.

Hablando de amigos, hay 3 que también se han ganado una mención especial: Álex, Marcos y Rubén, gracias por demostrarme que la distancia nunca será un obstáculo para apoyarnos. Nos queda mucho por vivir juntos.

Madrid (y la tesis) me ha permitido conocer a personas increíbles. Gracias Pedro, Albertico y en general a toda la gente con la que he disfrutado de esta ciudad, como Marta, Fran, Oscar y un largo etcétera. Especialmente, muchas de estas personas forman parte de un club de baloncesto que ya considero como mío. Gracias a toda la gente del Estudiantes por acogerme y hacerme sentir uno más desde el primer día, en especial a Carlos, Guille, Juan D., Manu, Jose, Juanje, Rula, Gabi… Lo que empezó un miércoles en el Manolo ha acabado como "los bestias". Injusto sería no mencionar a Pablo Borrás. Ojalá volver pronto a los banquillos con vosotros al lado.

Y como no todo ha sido Madrid, quiero agradecer a Gon, junto con Lena, Alex y Gabi, por esos 7 meses en Berlín. Me queda un gran recuerdo de la ciudad y de los momentos compartidos. Berlín siempre será una visita obligatoria para ir a veros. En cuanto al BfR, creo que nada de lo que conseguimos habría sido posible sin Verónica ni Rico. Verónica, tu apoyo fue fundamental para afrontar el reto de trabajar en otro país. Nadie mejor que tú para guiarme, ¡gracias por todo!

Respecto al ICP y a la UCM, agradecer a tod@s los trabajadores que día a día me han recibido con una sonrisa, desde el personal de limpieza hasta mantenimiento, informática y conserjería. Sois imprescindibles para que todo funcione. Gracias Toñi por tu amabilidad y por tu buen trato como tutora de esta tesis, te agradezco la oportunidad de haber podido participar en la docencia de una universidad como la UCM.

En cuanto a mi grupo, SpeiCat, solo puedo tener palabras positivas para tod@s. Una suerte la mía por haber compartido estos años con vosotr@s. Mención especial para Ana, por su apoyo y cariño incondicional, Flavio, por esta gran amistad que hemos forjado, y Nico, con quien creo haber congeniado desde el primer minuto (una pena no haber trabajado más tiempo juntos). Creo que hemos sido un buen equipo. También agradecer a todos los estudiantes de prácticas, TFG y TFM por haberme ayudado a completar las innumerables horas de laboratorio, y a los visitantes que han pasado por el grupo, entre ellos a Carlinhos, a quien espero visitar pronto en Brasil. Por último, Miguel Ángel y Raquel, Raquel y Miguel Ángel… los directores y "culpables" de esta tesis doctoral. Creo que tan solo la gente que acaba una tesis puede entender la relación doctorando-director/a. Gracias por la oportunidad que me disteis en octubre 2019 para empezar esta aventura, y por la comprensión y aprendizaje durante los buenos y malos momentos que hay a lo largo de toda una tesis. Empezamos juntos y acabamos más unidos que nunca. Por no ponerme límite a las ideas, la imaginación y las ganas… ¡MUCHAS GRACIAS!

Creo que lo justo es acabar los agradecimientos con las personas más cercanas a mi, entre las que hay una última incorporación que ha revolucionado mi día a día. Laura, el apoyo de este último año de tesis ha sido imprescindible para mí, gracias por aguantar mis días malos y por ser parte tan importante de los días buenos. Empieza una nueva etapa que seguro que nos trae aventuras de esas que tanto nos gustan, entre viajes, experiencias y un montón de planes que vamos a cumplir, ya lo sabes. Turno para mis herman@s y sobrin@s ("los cabritos"): Jorge, Noelia, Raquel, Philippe, Sergi, Carlota, Martina y Daniela... Estos 4 años no os he visto todo lo que me gustaría, la distancia no es fácil. Que sepáis que me siento un afortunado por ser parte de vuestra familia, y no hay día que no valore el apoyo incondicional que tengo de todos vosotros. Muchas gracias por estar siempre disponibles para un abrazo, un consejo, una charla o lo que haya necesitado. Estos 4 años he necesitado muchas de esas cosas. Os quiero mucho.

Acabamos con papá y mamá, mamá y papá… La fuerza que me hacéis sentir cada mañana sabiendo que estáis orgullosos de mí, es inagotable, por eso os dedico este trabajo que he hecho con todo mi esfuerzo. Aquí está… ¡Lo conseguimos!

Gracias a tod@s, también a los que ya no están,

Víctor Alcolea Rodríguez

Este trabajo va dedicado a toda mi familia,

Víctor.

# Agradecimiento a sponsors

Este trabajo fue apoyado por los proyectos EU H2020 HARMLESS (acuerdo de subvención, GA, número 953183), BIORIMA (GA 760928), NanoInformaTIX (GA 814426), PlasticFate (GA 965367) y CHARISMA (GA 952921)

# Acknowledgements to sponsors

This work was supported by the EU H2020 projects HARMLESS (grant agreement, GA, No 953183), BIORIMA (GA 760928), NanoInformaTIX (GA 814426), PlasticFate (GA 965367) and CHARISMA (GA 952921)

# CONTENTS

# Abstract

The extensive production of engineered nanomaterials (ENMs) has resulted in increased human and environmental exposure, sparking significant safety concerns and underscoring the need for exhaustive risk assessments. Traditional *in vivo* hazard assessments face limitations, prompting the need for alternative methods. This study presents i*n chemico* reactivity measurements and *in vitro* assays to uncover the reactive mechanisms responsible for nanomaterial toxicity, with the potential contribute to the development of Adverse Outcome Pathways (AOPs) and New Approach Methodologies (NAMs). This methodology accentuates the significance of intrinsic nanomaterial reactivity, recognizing it as a pivotal aspect in the categorization of ENMs. In this context, characterizing nanomaterial surface reactivity with probe molecules and linking them with *in vitro* toxicity data emerges as a promising screening tool for detecting potentially hazardous nanomaterials. These *in chemico* and *in vitro* alternatives to *in vivo* share a common goal: minimizing the experimental use of animals while reducing the cost and time associated with current risk assessment methods.

Determining dose-metrics associated with toxic effects is essential to understand the relevance of surface reactivity in nanotoxicity. Exploring approaches beyond traditional normalization methods based on mass or surface area is crucial, as these parameters may not accurately correlate with the actual exposure to reactive sites. One proposed general method for ascertaining the number and nature of reactive surface sites on nanomaterials involves gas-phase methanol chemisorption followed by temperature-programmed surface reaction (TPSR). Specifically, the oxidizing capacity may be quantified through liquid-phase probe reactions, with thiol consumption and ROS formation measured to categorize nanomaterial reactivity. Regarding toxicity, cell viability (WST-1 assay), LDH release, autophagosome formation, as well as protein dysregulation via proteomics are proposed for the A549 and PMA-treated THP-1 lung cell lines. The methodology has been validated using ten benchmark ENMs, among which

are eight reference nanomaterials from the Joint Research Centre (JRC) and two commercially used models commonly referenced in the literature.

The implementation of these strategies identifies CuO, along with ZnO (NM-110 and NM-111), as the most oxidizing materials, as well as the ones having the greatest impact on cell viability in A549 and PMA-treated THP-1 cell lines, leading to a disruption of homeostasis due to their high toxic nature. In contrast, $SiO_2$ (NM-200 and NM-201) exhibits low adsorption capacity and reactivity, which is linked to the absence of adverse effects in the evaluated cell lines. Nanomaterials with moderate oxidative reactivity, such as $CeO_2$ (NM-211 and NM-212), as well as acidic ENMs as $TiO_2$ (NM-101 and NM-105), induce the formation of autophagosomes in both lung cell lines. Therefore, autophagy is found to be as a cytoprotective mechanism to prevent the loss of homeostasis.

The scope of the study progresses towards the examination of other advanced nanomaterials, including nanobiomaterials, engineered multicomponent nanomaterials, and other emerging materials such as micro and nanoplastics. These nanomaterials display unique physicochemical characteristics, presenting challenges for uniform assessment. Consequently, alternative methodologies are proposed to ascertain their reactivity and structure. Raman microscopy is proposed as a non-destructive technique for the molecular analysis. It is complemented by other analytical methods, such as methanol temperature-programmed reaction (MeOH-TPRx), which is instrumental in understanding the reactivity of less reactive nanomaterials Additionally, Scanning Electron Microscopy (SEM) is employed to assess the morphology of these emerging nanomaterials in both their pristine state and after undergoing various processes, including dispersion or simulated transit through the human gastrointestinal system. This expansion of focus allows the study to encompass a wider array of nanomaterials, thereby enriching our comprehension of their interactions and effects within biological environments.

# Resumen

La extensa producción de nanomateriales de ingeniería (ENMs) ha resultado en un incremento de la exposición humana y ambiental, generando significativas preocupaciones de seguridad y subrayando la necesidad de evaluaciones exhaustivas de riesgos. Las evaluaciones tradicionales basadas en ensayos *in vivo* presentan limitaciones, lo que incita la necesidad de métodos alternativos. Este estudio presenta medidas de reactividad *in chemico* y ensayos *in vitro* para determinar los mecanismos reactivos responsables de la toxicidad de los nanomateriales, con el potencial de contribuir al desarrollo de Vías de Resultados Adversos (AOPs) y Nuevas Metodologías de Enfoque (NAMs). Esta metodología resalta la importancia de la reactividad intrínseca de los nanomateriales, reconociéndola como un aspecto crucial en la categorización de los ENMs. En este contexto, caracterizar las reactividades superficiales de los nanomateriales con moléculas sonda y vincularlas con efectos adversos observados *in vitro* se propone como una herramienta de cribado prometedora para detectar nanomateriales potencialmente peligrosos. Estas alternativas innovadoras comparten un objetivo común: minimizar el uso experimental de animales mientras se reducen los costos y el tiempo asociados con los métodos actuales de evaluación de riesgos.

La determinación de las métricas de dosis asociadas con efectos tóxicos es esencial. Explorar enfoques más allá de los métodos tradicionales de normalización basados en masa o área superficial es crucial, ya que estos parámetros pueden no correlacionarse con precisión con la exposición real a centros reactivos. Un método general propuesto para determinar el número y la naturaleza de los centros reactivos superficiales en los nanomateriales implica la quimisorción de metanol en fase gaseosa seguida de una reacción superficial a temperatura programada (TPSR). Específicamente, la capacidad oxidante puede cuantificarse a través de reacciones con sondas en fase líquida, con la evaluación del consumo de tioles y la formación de especies reactivas de oxígeno (ROS) para categorizar la reactividad de los nanomateriales. En cuanto a la toxicidad, se evalúan la viabilidad celular (ensayo WST-1), la liberación de LDH, la formación de

autofagosomas, así como la disfunción proteica a través de la proteómica para las líneas celulares pulmonares A549 y THP-1 tratadas con PMA. La metodología presentada ha sido validada a través de la evaluación de 10 nanomateriales de referencia, incluyendo 8 nanomateriales procedentes del Centro Común de Investigación (Joint Research Centre, JRC) y 2 óxidos comerciales frecuentemente citados en la literatura científica.

La implementación de estas estrategias identifica a CuO, junto con ZnO (NM-110 y NM-111), como los materiales más oxidantes, así como los que tienen el mayor impacto en la viabilidad celular en las líneas celulares A549 y THP-1 tratadas con PMA, lo que lleva a una alteración de la homeostasis debido a su alta toxicidad. En cambio, $SiO_2$ (NM-200 y NM-201) exhibe baja capacidad de adsorción y reactividad, lo que se vincula con la ausencia de efectos adversos en las líneas celulares evaluadas. Los nanomateriales con reactividad oxidante moderada, como $CeO_2$ (NM-211 y NM-212), así como los ENMs ácidos como $TiO_2$ (NM-101 y NM-105), inducen la formación de autofagosomas en ambas líneas celulares pulmonares. Por lo tanto, la autofagia se describe como un mecanismo citoprotector para prevenir la pérdida de homeostasis.

El alcance del estudio avanza hacia la evaluación de otros nanomateriales avanzados, incluidos nanobiomateriales, nanomateriales multicomponentes y otros materiales emergentes como micro y nanoplasticos. Estos nanomateriales muestran características fisicoquímicas únicas, presentando desafíos para una evaluación uniforme. En consecuencia, se proponen metodologías alternativas para determinar su reactividad y estructura. Se propone la microscopía Raman como una técnica no destructiva para el análisis molecular. Se complementa con otros métodos analíticos, como la reacción programada por temperatura con metanol (MeOH-TPRx), que es fundamental para comprender la reactividad de los nanomateriales menos reactivos. Además, se emplea la Microscopía Electrónica de Barrido (SEM) para evaluar la morfología de estos nanomateriales emergentes tanto en su estado original como después de someterse a varios procesos, incluida la dispersión o el tránsito simulado a través del tracto gastrointestinal humano. Esta ampliación del enfoque permite que el estudio abarque una gama más amplia de nanomateriales, enriqueciendo así nuestra comprensión de sus interacciones y efectos en entornos biológicos

# List of abbreviations

AFM: Atomic Force Microscopy

AOP: Adverse Outcome Pathways

BALF: Bronchoalveolar lavage fluid

CPH: 1-hydroxy-3-carboxy-2,2,5,5-tetramethylpyrrolidine

DLS: Dynamic Light Scattering

DMPO: 5,5-dimethyl-1-pyrroline-N-oxide

DTT: Dithiothreitol

ECHA: European Chemicals Agency

ENM: Engineered nanomaterial

HMDM: Human Monocyte-Derived Macrophages

IATA: Integrated approach to testing and assessment

IT: intratracheal instillationKE: Key Event

LDH: Lactate dehydrogenase

MIE: Molecular Initiating Event

MoA: Mode of Action

MWCNT: Multi-wall carbon nanotubes

NAM: New Approach Methodology

NF: Nanoform

OCDE: Organisation for Economic Co-operation and Development

ROS: Reactive oxygen species

SbD: Safe-by-design

SEM: Scanning electron microscopy

STIS: short-term inhalation study

TEM: Transmission electron microscopy

TGA: Thermogravimetric analysis

TPRx: Temperature-programmed reaction

TPSR: Temperature-programmed surface reaction

WST-1: Water Soluble Tetrazolium

XPS: X-ray photoelectron spectroscopy

# Chapter I. Introduction

## 1.1 Nanomaterials

### 1.1.1 Definition

The European Chemicals Agency (ECHA) defines nanomaterials as chemical substances or materials whose particles exhibit dimensions falling within the range of 1 to 100 nm in at least one of their three principal dimensions.[1] At the nanoscale, these materials demonstrate distinct properties when compared to their larger counterparts of the same composition, with a noteworthy emphasis on the increase in specific surface area per unit volume, a key factor influencing reactivity. [2]Engineered nanomaterials (ENMs), which are characterized as nanomaterials intentionally designed, conceived, and produced by human intervention, can be categorized as organic, inorganic, organometallic or combinations thereof (nanocomposites). The most prevalent types of engineered nanomaterials, ordered in decreasing abundance, include $TiO_2$, $SiO_2$, Fe, ZnO, $Al_2O_3$, $CeO_2$, Cu, Ag, carbon nanotubes, graphene, and nano-clays.[3] They exhibit specific physicochemical and electrical properties that are inherently dependent on their morphology and size. The utility of each nanomaterial is contingent upon various factors, ranging from surface reactivity to its state of aggregation in different media. Consequently, this leads to a significant disparity in the number of surface atoms compared to those within the bulk of the material, with the former being notably elevated.

### 1.1.2 Surface properties

Metal oxides possess a lattice which unit cell repeats *ad infinitum*. However, materials are finite, and interact with the surrounding environment through their surface, the end of the lattice periodic structure, which is characterized by descriptors such as specific surface area (BET area), pore size, or zeta potential (ζ).[4] Surface chemistry defines materials' reactivity (type and strength), in metal oxides often associated with surface oxygen species, such as bridging oxygen, oxide, superoxide, peroxide, or hydroxyl sites (Figure 1), which properties are determined by underlying cations, defects, and the bulk

structure. In fact, surface vacancies and defects are stabilized to keep material's neutrality, typically by interaction with environmental water, generating surface hydroxyl groups. Surface relevance is maximized in non-soluble nanomaterials, which high surface-to-volume ratio confers them with distinctive properties. For example, in the field of ecotoxicology, 40 mg/L of nano-sized CuO particles completely inhibit the growth of *S. cerevisiae,* while 4000 mg/L of CuO bulk material are needed to afford the same effect. [5]

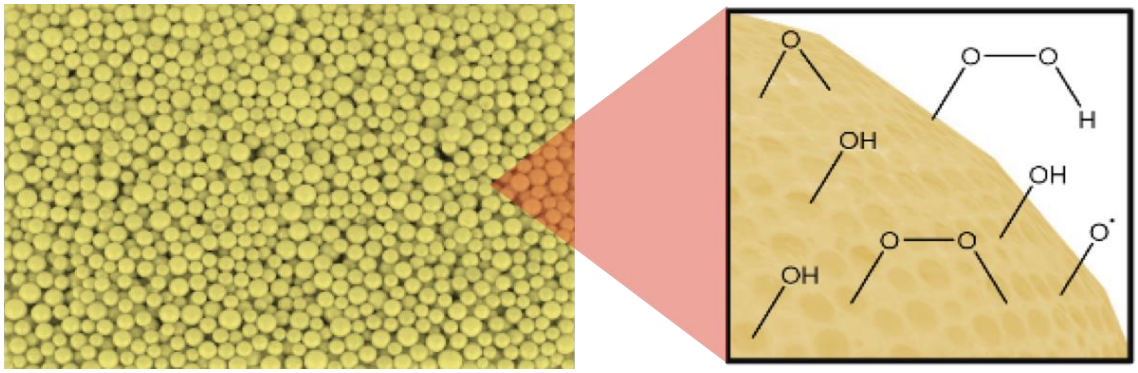


***Figure 1***. *Active sites on ENMs' surface*

### 1.1.3 Environmental and public health concerns

Nanotechnology has a significant economic impact, discernible through the increased research activities in regions such as Germany, the United Kingdom, and, notably, the United States (Figure 2). This upsurge in research is primarily driven by the keen interest of policymakers and governments in the novel properties exhibited by advanced nanomaterials, particularly in domains associated with healthcare. These properties are instrumental in an increasing number of applications that have a direct impact on the societal challenges and the economy, which has led to a boom of nanoscience and nanotechnology in Asia-Pacific, America and Europe.[6,7,8,3] In particular, engineering of new or improved transition metal oxide ENMs such as $TiO_2$, $Co_3O_4$, $Fe_2O_3$, $SiO_2$, ZnO or CuO is under permanent study for current and future applications as pigments, catalysts, sensors, cosmetics, contrast agents, controlled drug delivery or textile fibers, among many others.[9,10]

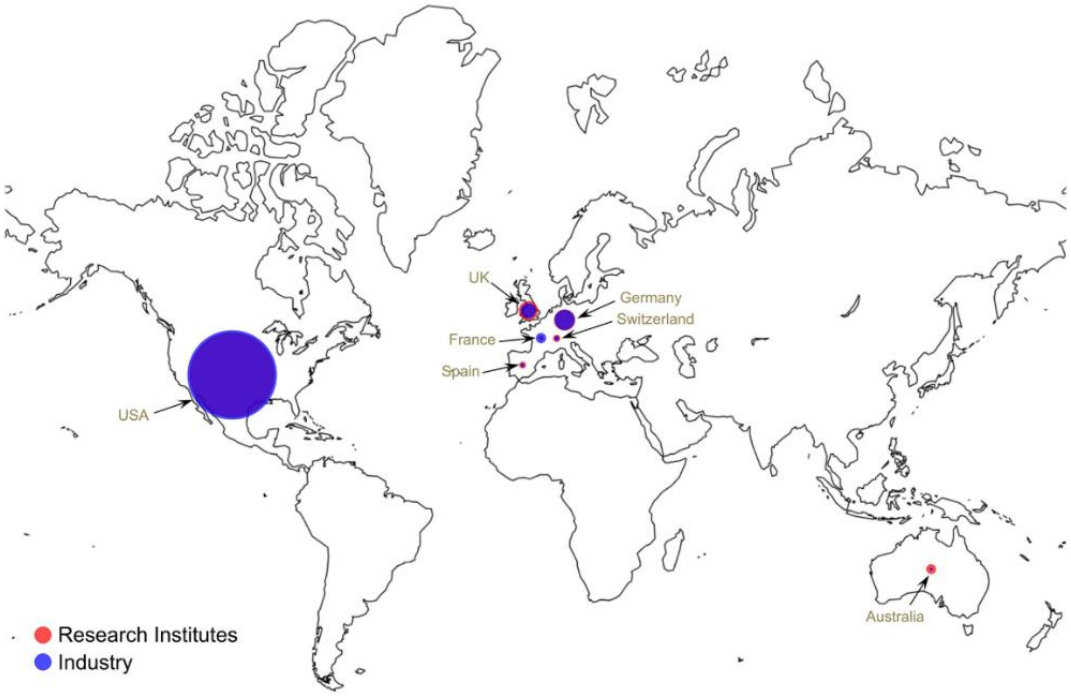


***Figure 2.*** *World map illustrating the distribution of industrialization and research within the realm of nanotechnology. Notably, the study considered only five countries from South America, Africa, and Oceania. Source: J. Talebian, 2021.*[8]

In addition to the industrial utilization of ENMs, recent studies have underscored the emission of nanoparticles stemming from natural, accidental, or industrial sources, which give rise to significant public health concerns. It is estimated that over a 60-year period (1980-2040), the annual emission of nanoparticles is set to double. Consequently, there will be a progressively heightened risk of inhalation or ingestion, thereby amplifying the significance of risk assessments aimed at averting unexpected adverse reactions. This situation parallels the initial challenges encountered with the use of asbestos.[3,11] Nanosafety initiatives have catalyzed the inception of numerous European research projects, including BioRiMa, NanoInformaTIX, NanoSolveIT, Harmless, and GRACIOUS, among others. This has prompted numerous characterization, exposure and hazard studies[12,13,14] (Figure 3) to understand and prevent possible adverse effects as, for example, asbestosis, which triggered the beginning of nanosafety, or pathologies derived from reactive oxygen species (ROS) release,[11,15,16,17] and to adopt a knowledge-based safe-by-design (SbD) approach[18,19], essential to ensure safe ENMs applications as well as faster, economic and more effective production routes.[20,21] Integrated information related to hazard (*in vitro* and *in vivo* testing) and physicochemical properties underpins

nanotoxicity prediction,[19,22,23,24,25,26] with machine learning serving as the primary tool for toxicity prediction.[27]

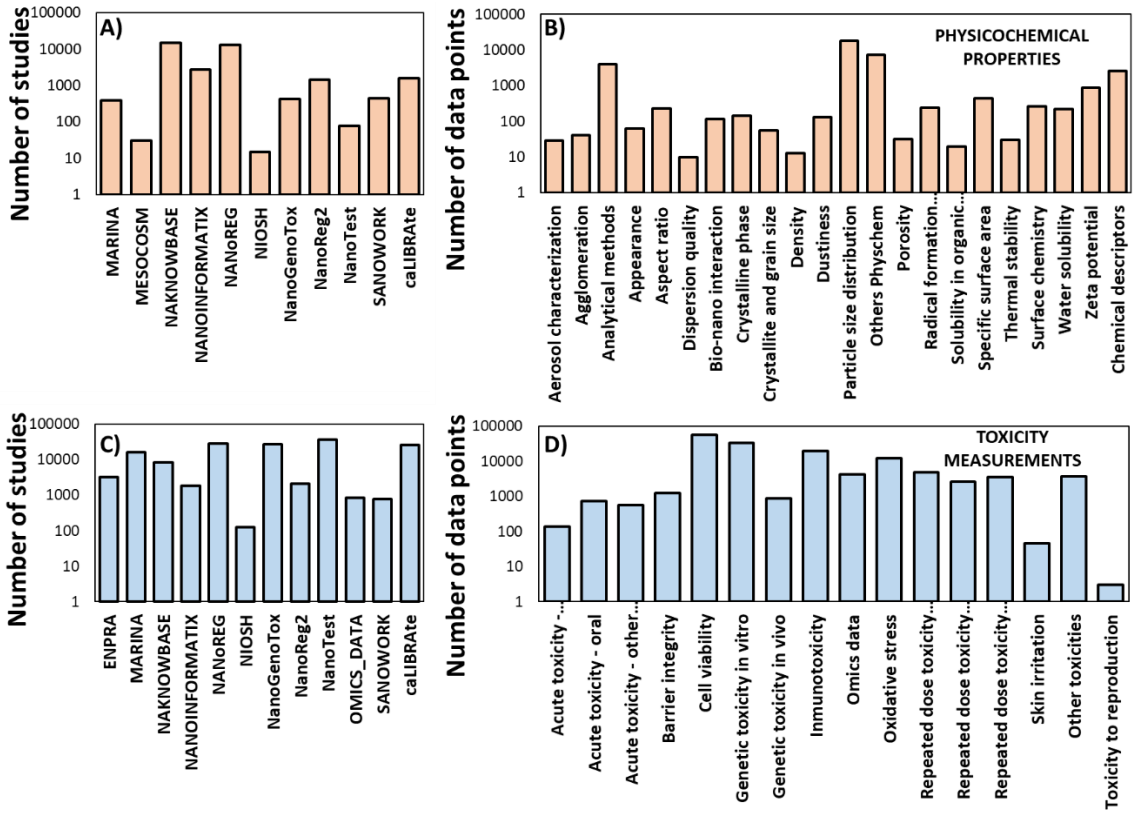


***Figure 3.*** *Number of studies (left) and data points (right) to describe physicochemical properties (A-B) and toxicological effects (C-D) in nanosafety-based finished European projects. Data extracted from eNanoMapper database (***https://search.data.enanomapper.net/***)*

## 1.2 Nanotoxicity

### 1.2.1 Basic concepts and terminology

Nanotoxicology studies the effects of nanomaterials on health and the environment, providing key information for regulatory agencies. It uses specific terms to ensure clear and consistent communication in this field. Table 1 summarizes the definitions for some prevalent terms in the scientific literature within this field.

***Table 1.*** *Terms used in the toxicology field, extracted from Jeong et al. 2017[28], Murphy et al. 2022[24], Jeliazkova et al. 2022[19] and Gerloff et al. 2017[29]*

| Concept | Definition |
|---|---|
| **Nanoform (NF)** | Nanoform refers to a form of a natural or manufactured substance. This substance contains particles that are either unbound, aggregated, or agglomerated. A key characteristic of these particles is that in their number size distribution, at least 50% of them have one or more external dimensions within the size range of 1 nm to 100 nm. This definition is inclusive and also considers materials such as fullerenes, graphene flakes, and single-wall carbon nanotubes, even when one or more of their external dimensions are below 1 nm. |
| **Grouping** | Grouping is defined by the OECD (2014) as concurrently evaluating multiple chemicals, grouping bases its rationale on various factors such as shared functional groups, similar constituents or chemical classes, comparable carbon range numbers, a common mechanism of action, or adverse outcome pathway. These may also include likelihood of similar precursors or breakdown products, or a steady change across the category. The structural similarity is crucial for any grouping or read-across method, though this alone is insufficient for grouping different nanoforms of the same ENM. |
| **Read-across** | The OECD describes read-across as a methodological approach designed to bridge data gaps. In this approach test information pertaining to a specific endpoint for one chemical, known as the source chemical, is utilized to forecast the test information for the same endpoint for another chemical. This other chemical is identified as the target chemical. The cornerstone of this approach is the principle of similarity between the source and target chemicals, which must be substantiated through a scientific rationale. |
| **Endpoint** | Hazard or toxicological endpoints are derived from toxicity tests, representing specific measurements taken during or at the end of a test, like acute toxicity (LD50, LC50) or repeated dose toxicity (LOAEL). |
| **Descriptor** | This is a single value, often with units (e.g., nm), summarizing a data distribution for a specific purpose, like D50 for particle size or LOAEL for inhalation toxicity dose-response curves. |
| **Integrated Approach to Testing and Assessment (IATA)** | IATA, as defined by the OECD (2017), comprises a set of standards that are rooted in the integration of various information related to hazard identification and characterization, as well as the assessment of the safety of chemical substances. This approach values non-animal testing, contributing to reduce animal testing. The ultimate goal of IATA is to guide regulatory bodies in accepting or rejecting a grouping or extrapolation hypothesis. [19, 22, 23, 24] |
| **Safe-by-Design (SbD)** | Initially developed in NANoREG[30] and further elaborated by OECD (2020), SbD aims to minimize human and environmental risks and uncertainties, including the safety concept at the earliest possible stage of product and process development. It encompasses safety considerations throughout a material/product's lifecycle, including R&D, production, use, recycling, and disposal. |
| **Adverse Outcome Pathway (AOP)** | An AOP is a conceptual framework that delineates the existing knowledge concerning the connection between a molecular initiating event and an adverse outcome. This pathway illustrates a sequence of causally linked events across different levels of biological organization. AOPs serve as mechanistic blueprints, providing valuable insights into the processes leading from a specific molecular interaction triggered by a chemical (the MIE) to the final adverse outcome observed at the organism or population level. This framework is widely promoted by the OECD because it will be essential for toxicity assessment strategies involving alternatives to animal testing. |
| **Key Event (KE)** | KEs are critical biological occurrences, such as gene activation, changes in cell chemistry, and tissue development. These events transpire at various biological levels (cellular, tissue, and organ) in response to a molecular initiating event. KEs lead to a specific adverse outcome, which can be profound, ranging from death and reproductive disorders to cancer or even species extinction. |

| | |
|---|---|
| **Molecular Initiating Event (MIE)** | A MIE is a specialized type of Key Event signifying the interaction between a chemical and its biological target(s) at the molecular level. It constitutes the initial biological event that triggers a toxicity pathway. Examples of such events include DNA recombination, protein oxidation, or receptor-ligand interactions. MIEs are critical in understanding the mechanism of action of a chemical substance, as they mark the onset of a cascade of biological events leading to an adverse outcome. By identifying and studying MIEs, researchers can better comprehend how chemicals induce toxic effects, which is essential for effective risk assessment and regulatory decision-making |

The extended surface area and surface structure of nanomaterials are key properties that facilitate enhanced interactions with the biological microenvironment,[31] and therefore linking physicochemical properties and specific reactivity to a key event will provide information to unravel the mode of action.[32,29,33] In particular, the generation of reactive oxygen species (ROS) or redox reactions caused by the intrinsic reactivity of a nanomaterial are postulated to potentially trigger key events that can be part of the mechanism leading to various pathologies, as confirmed *e.g.* for PM, CuO, or photo-activated $TiO_2$. For instance, oxidative stress, caused, among others, by the reactivity of ENMs, is one of the main key events in diverse pathways towards adverse outcomes of nanomaterials.[34,35,36] Consistent with these assertions, surface reactivity and characteristics (coating, zeta potential, surface area, number of active sites) have recently been defined as specified grouping descriptors, central parameters for assessing nanotoxicity in the regulatory field. [3737,38,39,40] Grouping based on similarities as functional group, breakdown products, mode of action, or adverse outcome pathway to read-across ENM's properties is a convenient approach to reduce the need for individually testing each ENM that can help regulatory agencies, researchers, and industries manage resources more efficiently while ensuring that safety and risk assessments are still thorough and reliable, and in line with OCDE guidelines that promote risk assessment based on mechanistic reasoning to minimize experiments with animals.[41,42]

### 1.2.2 Physicochemical properties of ENMs relevant to toxicity

Physicochemical properties are crucial in understanding the toxic potential of a nanomaterial and, consequently, its capacity to induce pathology, as observed in the case of asbestos: due to its considerable length, asbestos cannot be phagocytosed and expelled, leading to bioaccumulation in the pulmonary system,[15] which can eventually result in pathologies such as lung cancer, as indicated by AOP 173.[32] Moreover,

porosities, the number of active sites, different crystal structures, or metals on the surface are directly linked to the reactivity of nanomaterials, which is pivotal in the formation of reactive oxygen species (ROS) or redox reactions that disrupt the balance of oxidant-antioxidant substances necessary for vital metabolic functions in living organisms.[43,44,45] The following subsections comment the most relevant analytical techniques used to gather physicochemical information relevant to toxicity, which are summarized in Table 2. The use of probe molecules and reactions to gather information about the reactivity of ENMs will be further discussed in section 1.3.1.

***Table 2.*** *Analytical techniques used for the physicochemical characterization of nanomaterials in abiotic test.*

| Sample status | Analytic technique | Descriptor | Interest in the field of nanotoxicity |
|---|---|---|---|
| powder | $N_2$ isotherm | Specific surface area and pore size distribution | Exposed surface for dosimetry in *in vitro* tests |
| powder | XPS | Surface species | Redox reactivity |
| powder | Raman spectroscopy | Structure and chemisorption of molecules | Structure-reactivity relationship and radical chemisorption capacity |
| powder | AFM | Topology | Effect of topology on cell viability after exposure |
| powder | SEM-TEM | Morphology | Effect of morphology on cell viability after exposure |
| powder/dispersion | probe molecule/reaction | surface reactivity/sites | Interactions and reactivity |
| Dispersion | Electrophoretic techniques | z potential – isoelectric point | Surface charge and agglomeration |
| Dispersion | DLS | Particle size | Internalization capacity and agglomeration |
| Dispersion | ICP-MS | Solubility | Release of ions that can interact with cells |

#### 1.2.2.1 Characterization of powdered ENMs

The most common physicochemical characterization techniques for dry nanomaterials include $N_2$ adsorption isotherms, X-ray photoelectron spectroscopy (XPS), X-ray diffraction (XRD), Raman spectroscopy, atomic force microscopy (AFM), and electron microscopy techniques to examine the morphology of nanomaterials (SEM or TEM).[46]

X-ray photoelectron spectroscopy is used to identify surface species, particularly metals, which is essential for predicting redox reactivity, primarily in nanomaterials such as cerium oxide, where the Ce(III)/Ce(IV) ratio is critical.[47] Exciting the sample with X-ray

incision induces the emission of photoelectrons, which, when detected, enable the identification and quantification of metals on the nanomaterial's surface.[46]

X-ray diffraction and Raman spectroscopy provide structural information. XRD is based on X-ray irradiation of the material, where the rays scatter at a specific angle, allowing the determination of interplanar distance and the crystal structure of a nanomaterial. In contrast, Raman spectroscopy collects inelastic scattering of an incident beam in the detector to identify molecular vibrations (related to the bonds in the studied molecule) and chemical structure. Furthermore, Raman spectroscopy enables the assessment of the surface state of samples that have been coated, such as ZnO NM-111, or the possible formation of reactive oxygen species through the chemisorption of compounds on the surface, using *in situ* and *operando* techniques.[48,49,50]

Atomic force microscopy is a significant technique for studying surface topography. It allows the visualization of the nanomaterial's surface relief at the nanoscale by direct contact between an extremely fine tip (one atom thick) and the nanomaterial's surface. The tip-surface interaction results in a topographic map, which has implications for the biocompatibility of cells deposited on different nanobiomaterials. [51]

Electron microscopy techniques for imaging, such as transmission electron microscopy (TEM) and scanning electron microscopy (SEM), are used to determine the morphology and dry particle size. Transmission electron microscopy irradiates the sample with a high-energy electron beam, which passes through the sample and is collected in the detector to form an image. In contrast, scanning electron microscopy scans the sample's surface with the incident electron beam, causing the re-emission of photons and electrons from the nanomaterial, which allows for the acquisition of a typically sharp image.[46] Microscopy is not limited to abiotic systems; *in vitro* assays frequently employ this analytical technique to investigate the internalization/uptake of nanomaterials within cells, as well as their accumulation in various organelles.[52]

In addition, adsorption/desorption of probe molecules and probe reactions also provide information about the physicochemical characteristics of these nanosolids. Adsorption/desorption isotherms are employed to determine the pore volume and size distribution as well as the specific surface area, often expressed in $m^2/g$. Nitrogen, due

to its size and physisorption capacity, is the most commonly used adsorbent. Quantifying the amount of adsorbed gas at various pressures allows for the determination of the nitrogen adsorption isotherm, which follows the Brunnauer-Emmett-Teller (BET) model, a measure related to the number of active sites available for adsorption.[46] Furthermore, probe molecules chemisorption is used to quantify active sites in heterogeneous catalysis, being the most typical carbon monoxide, for metal NPs,[53] and small alcohols like methanol, for metal oxides. The latter is considered a "smart" probe molecule that can not only quantify the number of surface sites by chemisorption, but also report on their reactive profile by temperature-programmed surface reaction (TPSR). Chemisorption can be quantified through thermogravimetry (TGA), quantification of desorption products through TPSR, or gas flow composition analysis, for instance via mass spectrometry. [54,55,56]

#### 1.2.2.2 Characterization of ENMs in aqueous and culture medium

The behavior of nanomaterials varies when they are dispersed in a liquid medium. Factors such as the presence of surfactants, salts, pH-altering components, or microorganisms can modify their surface properties, thereby influencing their agglomeration state, ion release, and redox potential, and eventually disrupt the stability of the dispersion. This is evident in the reported phenomenon of protein corona, which has had a significant impact in the field of Nanotoxicology.[57,58] Hence, analytical techniques to characterize nanomaterials in solution (Table 2) are required for predicting their behavior in a specific medium.

The isoelectric point of a nanomaterial in a solution can be defined as the pH at which the sum of charges equals zero. According to ISO 13099, this parameter is determined through electrokinetic analytical techniques that measure the electrophoretic mobility of particles. This parameter is closely linked to the zeta potential (ζ), which is representative of the surface charge of a nanomaterial at a specific pH. At the isoelectric point, ζ is equal to 0.[59] Determining the zeta potential of a nanomaterial in a dispersion is an initial step in assessing whether its state will be more agglomerated (close to the point of zero charge, i.e., the isoelectric point) or less agglomerated (further away).

The size of individual particles or agglomerates in dispersions (called hydrodynamic diameter) is often performed by Dynamic Light Scattering (DLS). This analytical technique is fundamental for cytotoxicity studies to assess the potential phagocytosis and internalization of nanomaterials by exposed cells,[60] and therefore one of the most commonly used according to the eNanoMapper database, as shown in Figure 3, B. The DLS technique is based on the Brownian motion of nanomaterials in dispersion. A beam of light is scattered by the nanomaterial depending on its size, which is derived from the Stokes-Einstein relationship. Notwithstanding, DLS technique provides an indirect estimation of the hydrodynamic particles size, which may differ from others obtained by microscopy techniques, often yielding larger values, as the presence of aggregates is favored in a liquid medium.[61]

Another relevant parameter for understanding the state and toxicity of a nanomaterial in dispersion is its solubility, which can be quantified by measuring ion release into the medium, frequently by Inductively Coupled Plasma Mass Spectrometry (ICP-MS). This analytical technique is based on the ionization of samples using plasma and subsequent quantification of components by mass spectrometry. [62]

### 1.2.3 Reactivity of ENMs

Reactivity is an extrinsic property considered a key parameter to describe the interaction of ENMs with their surroundings.[19,22] The redox, acidic, or basic reactivity of a nanomaterial is critical in determining its role in cellular metabolic pathways. For instance, substances with stronger acidic or basic characteristics can interfere with intracellular pH, enzyme and protein activity, damage molecular components, or trigger cellular stress responses.[63] Conversely, the redox reactivity of a nanomaterial could interfere with cellular homeostasis and metabolic pathways by inducing oxidative stress through the formation of reactive oxygen species, disrupting mitochondrial function via interaction with the respiratory chain and ATP production, altering enzymes and their activity due to oxidation, or eliciting an inflammatory response and the chronic release of proinflammatory cytokines.[64] Therefore, the development of abiotic *in chemico* assays, as those described in section 1.3.1, to evaluate surface reactivity and link it with molecular

initiating and key events in reactive-based nanotoxicity would help to fundamentally understand the modes of action[32,29,33] and better group ENMs while minimizing *in vivo* testing.[65] This complements the well-known physicochemical information of nanomaterials (section 1.2.2), also relevant in the nanotoxicity field[22] to investigate toxic ion release, lung fibrosis, inflammasome activation, interference with embryonic hatching or membrane lysis, among others. Moreover, we hypothesize that it may also provide new dosimetry metrics for *in vitro* tests.

### 1.2.4 Dose metrics

Assays with different cell lines are typically normalized by mass or BET area to quantify dose-dependent cellular/biological effects. These dose metrics may sometimes not be useful to compare exposure to ENMs, because mass or exposed physical area do not necessarily correlate for different ENMs with the number of reactive sites that trigger chemical processes such as ROS formation. Research in heterogeneous catalysis has traditionally faced the same challenge when comparing the activity of catalytic materials, and has reached a consensus that the most relevant metric is the turnover frequency (TOF). TOF is the number of times that the overall catalytic reaction takes place (*i.e.*, molecules that react) per active site and unit time.[66,67,68,69,70] Formally equivalent problems have formally equivalent solutions: as phenomena that trigger molecular initiating events in reactive-based toxicity and catalytic reactions occur at the surface, more specifically, at the active sites, we propose the use of catalytic methods based on adsorption and reaction of probe molecules to quantify the surface active sites of ENMs and to characterize their reactive nature, thus delivering descriptors relevant for ENMs classification.[67,71]

## 1.3 New Approach Methodologies (NAMs)

This immense variability of new ENMs presents a formidable challenge to the conventional paradigm of hazard and risk assessment.[72] The main aspect of this challenge lies in the traditional reliance on animal experimentation as a primary method for evaluating material safety, as such experiments are extremely expensive and time-consuming. [73] Furthermore, the extensive variety of ENMs, each with its particular

properties, needs to be tested according to the current regulation. Conducting comprehensive animal studies for every new material becomes impractical and resource-intensive. Additionally, the European Union has been actively working to reduce and replace animal experimentation in various sectors, including regulatory testing, committing to the 3R principles of animal testing (Replacement, Reduction, and Refinement). As a result, the need to incorporate more efficient and cost-effective, non-animal approaches for safety assessment of these materials has never been more pressing. This imperative drives development in new approach methodologies (NAMs),[74] based on *in chemico, in vitro* and/or *in silico* studies (predictive modelling) while minimizing *in vivo* testing, as well as risk assessment frameworks to address the complexities inherent in this rapidly evolving field.

Our first hypothesis is that with the appropriate use of probe molecules we will be able to, firstly, quantify the reactive sites at ENMs' surface; secondly, identify their reactive nature and estimate their reactivity; and thirdly, calculate the TOF of relevant reactions. Our second hypothesis is that this provides relevant reactive-based dose metrics to study ENMs toxicity *in vitro*.

### 1.3.1 *In chemico* studies

*In chemico* assays to assess intrinsic reactivity or the ability to generate ROS are strategies that help distinguish less reactive and hypothetically safe nanomaterials, such as certain silicon oxides, from highly reactive and potentially hazardous nanomaterials like CuO or carbon black, which require *in vitro* and *in vivo* assays to understand their toxic effects on various organ systems. In all these cases, analytical methodologies are needed to quantify detectable products, allowing for a direct or indirect association with the reactivity of the nanomaterial under investigation.

The probe molecules CPH (1-hydroxy-3-carboxy-2,2,5,5-tetramethylpyrrolidine) and DMPO (5,5-dimethyl-1-pyrroline-N-oxide) are sensitive to reactive oxygen species, producing free radicals that are stable adducts detectable through Electron Spin Resonance (EPR). CPH is more sensitive to singlet oxygen, superoxide radicals, and peroxynitrites, while DMPO's sensitivity is based on hydroxyl and superoxide

radicals.[75,76,77] The formation of adducts between CPH or DMPO and the ROS induced by the nanomaterial results in the appearance of identifiable and quantifiable lines in the EPR spectrum, allowing direct and real-time detection of ROS, which is related to the nanomaterials' capacity to induce oxidative stress.[75,76,77] These probe molecules were well-correlated to protein carbonylation test and cell viability, so acellular experiments are expected to predict cell based interactions with ENMs.[78]

Another probe molecule of great interest is DTT (DL-dithiothreitol), a potent reducing reagent used in organic synthesis that can be employed to determine the intrinsic oxidizing capacity of a nanomaterial in suspension. Moreover, the reaction can be conducted in readily available media, like phosphate-buffered saline (PBS), at biologically relevant temperatures (37°C). The DTT molecule, which contains two thiol groups, forms a disulfide bridge when oxidized. The consumption of DTT is quantified indirectly by adding the Ellman's reagent (DTNB, 5,5'-dithiobis(2-nitrobenzoic acid)), which binds to thiol (-SH) groups that have not been affected by the redox reactivity of the nanomaterial under evaluation, forming a colored compound that can be quantified by UV-Vis spectrophotometry through absorption at 412 nm.[79,80]

Similarly, ascorbic acid (AA), also known as vitamin C, is a natural antioxidant that readily undergoes oxidation in the presence of oxidizing agents and/or reactive oxygen species. The consumption of AA after incubation with nanomaterials can also be quantified using UV-Vis spectrophotometry or chromatography. One drawback of this reagent and of DTT is that they are not selective regarding the source of oxidation.[81,82]

Another assay, the Ferric Reducing Ability of Serum (FRAS), measures the induction of ROS in human blood serum (HBS) by quantifying the total depletion of antioxidants. FRAS methodology relies on the principle that antioxidants in the serum catalyze the reduction of a colorless $Fe^{3+}$-TPTZ (2,4,6-tripyridyl-s-triazine) complex to a blue $Fe^{2+}$-TPTZ form in acid environment (pH 3.6). This reduction process, indicative of the total antioxidant capacity, is quantitatively assessed by measuring the absorbance at 593 nm via colorimetric analysis.[83] So far, it has been the primary assay for classifying nanoparticles based on their oxidative potential. However, FRAS provides a comprehensive measure of the oxidative potential of nanoparticles and cannot differentiate individual mechanisms.

[84] This limitation is not present in the assay using the lipophilic non-fluorescent molecule DCFH2-DA (Dichloro-dihydro-fluorescein diacetate) to probe ROS. The reactive mechanism is based on a two-step process involving the removal of diacetate by alkaline hydrolysis and a second reaction between ROS species generated by nanomaterials and DCFH2, producing $DCF^-$ as a molecule measurable by fluorescence. However, this highly sensitive oxidative probe is not specific to any particular reactive oxygen species, as DTT and AA, it can detect a wide variety of free radicals. [85]

An alternative to the typical probe reactions used in the field of nanotoxicity is the use of pH indicator agents, such as Acid Orange 8 (AO8) and Methylene Blue (MB). The structural change due to the reaction with ROS induced by a nanomaterial causes a color change and, consequently, a variation in absorbance at a specific wavelength that allows for quantification of the conversion percentage using UV-Vis spectrophotometry as a measure of the reactivity of a nanomaterial. AO8 is a quantifiable at 489 nm and MB at 663 nm. Both reactions can be assessed at different time intervals and temperatures, ranging from 15 to 120 min and between room temperature and 90°C (by sealing the reaction tube to prevent solvent evaporation, typically water). [86]

Finally, to identify and quantify the surface reactivity of a nanomaterial, TPSR can be performed after saturation with methanol. When the surface becomes populated with chemisorbed molecules (in the form of methoxy, $-OCH_3$), a linear increase in temperature leads to the gradual desorption of different species that can be identified by analysis of the gas phase and correlated to the various reactivities of the surface sites on which methanol was chemisorbed. The active sites produce formaldehyde, dimethyl ether, or carbon dioxide as main reaction products, depending on their reactivity, acid, redox or basic, respectively.[71,54,55]

The methodology developed in this work is based in linking the oxidative capacity of ENMs with the number and nature of surface sites. This approach is directed towards establishing surface descriptors that are indicative of nanotoxicity (Figure 4).

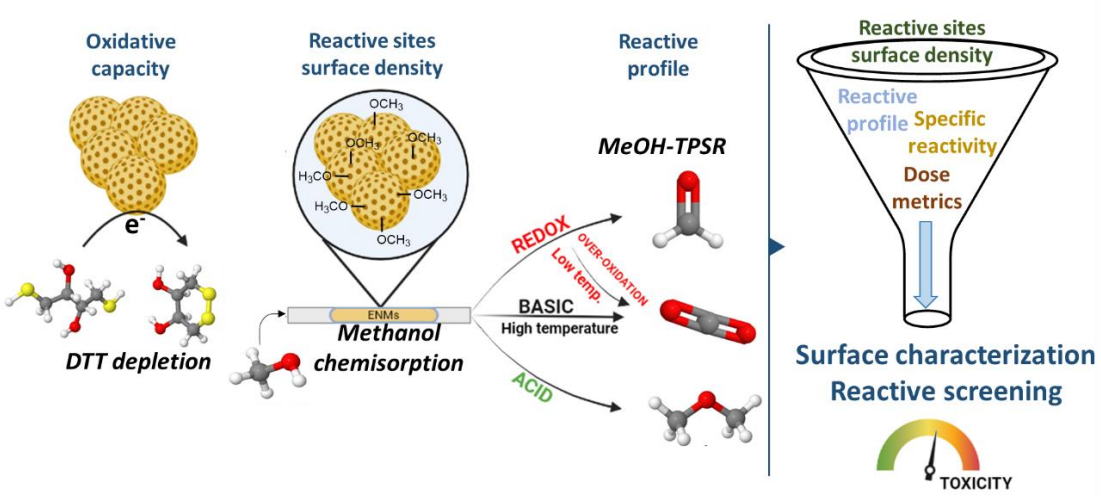


***Figure 4.*** *In chemico NAM to measure the number and nature of nanomaterial surface sites, and their relation with nanotoxicity.*

### 1.3.2 *In vitro* studies

#### 1.3.2.1 Cell lines for *in vitro* toxicity studies

Toxicity studies of nanomaterials use a wide range of cell lines, mostly originating from the lungs or directly related to the respiratory system, the main exposure route (Figure 5). The selection of the cell line is a critical step for the accurate interpretation of cytotoxic effects and their possible extrapolation to *in vivo* scenarios that should not be underestimated. It is essential that the chosen cell line accurately represents the biological characteristics of the target organ intended for study. Furthermore, the selection of an appropriate cell line can significantly influence the reliability and reproducibility of the results, thereby affecting the overall conclusions drawn about the safety and biocompatibility of the ENM.

Epithelial cell lines are the most common, as they exhibit similar behavior toward nanomaterials, unlike other cell types such as macrophages, which tend to internalize nanomaterials as a protective mechanism. Some of the most relevant epithelial cell lines include A549, 16HBE, BEAS-2B, Caco-2, H4IIE, and HeLa S3. The A549 cell line is derived from human epithelial lung carcinoma and 16HBE is a human bronchial epithelial cell line used to study the inflammatory response of bronchial epithelium. For a similar purpose, BEAS-2B is an immortalized cell line derived from human bronchial epithelial cells. These cell lines are commonly used in studies related to inhalation toxicity or pulmonary-origin

pathologies. Presently, advanced *in vitro* methodologies employing rat precision-cut lung slices (PCLuS) are being developed to assess the toxicity of inhaled engineered nanomaterials. The PCLuS method is utilized to detect early events of NM toxicity, such as changes in total protein levels and cellular responses, including cytotoxicity, apoptosis, oxidative stress, and inflammation. This approach offers a refined *in vitro* model for understanding ENM interactions with lung tissue, presenting a valuable tool for toxicological assessment.[87]

The plethora of existing epithelial cell lines provides, however, opportunities to represent a variety of biological systems, including the gastrointestinal system, another possible route of exposure to ENMs. For example, the Caco-2 cell line is of human colorectal epithelial origin, and it serves as a model for intestinal barrier studies regarding the permeability and absorption of xenobiotics. Other cell lines, such as H4IIE, are derived from rat hepatocytes and are used for studies related to hepatic toxicity, biotransformation of compounds for elimination, and the liver's response to unknown substances (contaminants, drugs, etc.). Finally, HeLa S3 cells are derived from human cervical carcinoma and are widely used in toxicology and biomedicine studies due to their rapid growth and widespread availability.

Recent studies on nanomaterial toxicity also incorporate cell lines that are non-epithelial, such as macrophages, endothelial cells, or animal cells. Some of the common ones include dTHP-1, NR8383, Raw 264.7, TM3, TM4, HUVEC, HepG2, C3A, TK6, and RTG-2. dTHP-1 is a human monocyte cell line differentiated into macrophages through treatment with PMA.[89] It is used to understand the response of monocytes and macrophages to potentially inflammatory substances. NR8383 cell line consists of rat alveolar macrophages and is related to the toxicity of lung function and its immune response. The Raw 264.7 cell line is derived from murine macrophages and is used for studies of the inflammatory response to xenobiotics.

Toxicity evaluation on testicular function and hormone secretion is performed on TM3 and TM4 mouse cell lines. TM3 cells are Leydig cells used to study testicular function and hormone secretion, while TM4 cells are Sertoli cells, utilized for assessing the toxicity of xenobiotics on spermatogenesis and the blood-testis barrier. Biocompatibility studies

involving the vascular system are usually performed with HUVEC (Human Umbilical Vein Endothelial Cells), which consists of endothelial cells isolated from the human umbilical vein. They are associated with the vascular system's response to toxic compounds. HepG2 cells are derived from human hepatocytes and are used to understand how exposure to nanomaterials affects liver function.

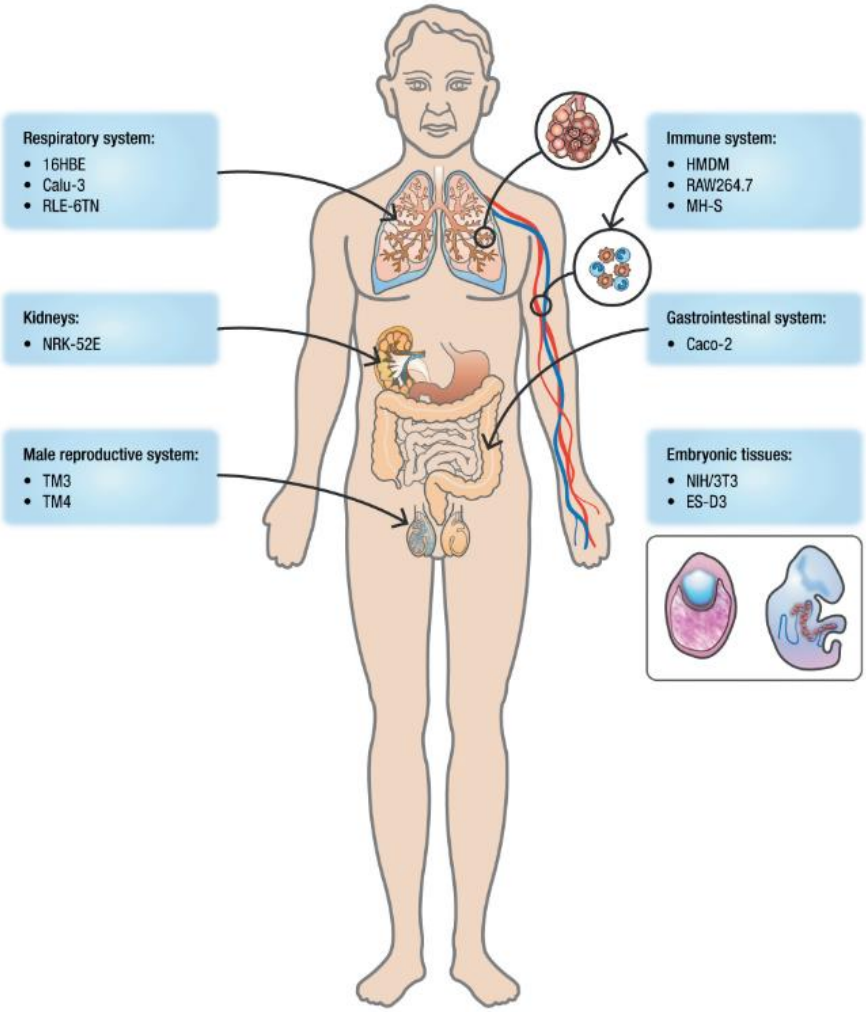


***Figure 5***. *Some common cell lines employed to investigate the toxicity of nanomaterials across various systems, as represented by cellular models. Image sourced from Farcal, 2015.*[88]

An alternative for assessing liver function damage would be the C3A cell line (derived from hepatocellular carcinoma cells). In terms of genetic damage, the TK6 cell line is commonly used. This human lymphoblast cell line, precursor to B lymphocytes, is widely employed in the fields of genotoxicity and mutagenicity. Finally, the RTG-2 cell line is

used for ecotoxicity studies. These cells originate from animal kidneys (trout) and are used in research related to the impact of nanomaterials on aquatic organisms.

#### 1.3.2.2 Cytotoxicity assays

Cell viability studies primarily assess the enzymatic activity of cells, both intracellular and secreted proteins, to determine their health status. Various techniques and commercially available kits based on the formation of colored compounds linked to the activity of specific enzymes are employed. Consequently, UV-Vis spectrophotometry plays a pivotal role in cytotoxicity testing.

The MTT (3-[4,5-dimethylthiazol-2-yl]-2,5-diphenyltetrazolium) assay is a colorimetric test used to ascertain the cell viability of a culture after exposure to a specific dose of nanomaterial. It relies on the capability of healthy, metabolically active cells to convert MTT into formazan, a reddish, insoluble product that can be readily detected using UV-Vis spectrophotometry. This assay is often conducted in parallel with the assessment of LDH enzyme secretion. LDH, or lactate dehydrogenase, is a protein present in all cells of the body that is released into the medium when there is a loss of cellular permeability, signifying cellular damage or death. Once released, LDH catalyzes the conversion of lactate to pyruvate, producing a detectable color using UV-Vis spectrophotometry.[90] Several alternatives to the MTT assay exist. The WST-1 and WST-8 tests rely on the reduction of a water-soluble tetrazolium compound by living cells, forming a measurable color compound that indicates cell viability. In contrast, the NRU (Neutral Red Uptake) test is based on the cells' ability to internalize a dye called neutral red. The amount of internalized dye is quantifiable and directly proportional to the cells' lysosomal capacity and viability. Furthermore, the MTS assay utilizes (3-(4,5-dimethylthiazol-2-yl)-5-(3-carboxymethoxyphenyl)-2-(4-sulfophenyl)-2H-tetrazolium), which is reduced to its formazan form in the presence of living and metabolizing cells, inducing a color change that can be measured spectrophotometrically and correlated with cell viability.[90,91]

The cell viability can be also evaluated with fluorescence spectroscopy through the AlamarBlue® assay, which incorporates resazurin. Resazurin is a colored indicator that is reduced to resorufin, a fluorescent compound that can be quantified in the presence of metabolically active cells. The fluorescence measurement is correlated with cell

viability.[90,92,91] In addition to UV-Vis spectroscopy, microscopy images are also a valuable tool for assessing the state of a cell culture. The Trypan Blue reagent, a dye that penetrates dead cells, giving them a characteristic blue color, allows to count the number of dead cells to determine cell viability.[93]

#### 1.3.2.3 Detection of proinflammatory proteins

Proinflammatory proteins are detected in *in vitro* assays to assess the status of cells after exposure to nanomaterials. The release of proteins or changes in their expression serve as markers of cellular response and biological effects caused by their interaction with nanomaterials. These methods involve analytical techniques such as gel electrophoresis, colorimetry, chemiluminescence, flow cytometry, or HPLC-MS (high-performance liquid chromatography coupled with mass spectrometry). The most common protein detection assays include:

- Western blot: This method allows researchers to isolate and identify specific proteins from a complex array of proteins extracted from cells. The technique is structured around three fundamental steps: (1) separation of proteins by size, achieved through gel electrophoresis; (2) transfer of these separated proteins to a solid support, typically a membrane like nitrocellulose or PVDF; and (3) detection of the target protein using appropriate primary and secondary antibodies. The primary antibody binds specifically to the target protein, while the secondary antibody, which is linked to a detection system, binds to the primary antibody. This process culminates in the visualization of the target protein, usually by colorimetry, facilitating its identification and analysis.[94]
- ELISA: An immunoassay called Enzyme-Linked Immunosorbent Assay, based on the direct or indirect capture of a protein of interest using a specific antibody, quantifiable through an enzymatic reaction that generates a detectable signal, such as fluorescence or a color change.[95]
- Proteomics: A technique for the high-throughput detection of proteins, commonly detected through HPLC-MS. It is a powerful analysis tool because it allows the identification of all proteins expressed in a cell culture, tissue, or organism. Initially, the sample is digested, and the resulting peptides are isolated and detected in the HPLC-MS system. Subsequently, through bioinformatics

analysis tools, the mass spectra generated are compared with databases that enable the recognition of protein sequences. Furthermore, the signal intensity is related to their concentration, making it possible to understand how proteins are regulated: they can be up-regulated or down-regulated, providing information about the cellular response following interaction with the nanomaterial.[96,97]

The most commonly studied proteins are TNF-alpha (tumor necrosis factor-alpha), IL-8 (interleukin-8), and IL-6 (interleukin-6) because they are key cytokines in the body's inflammatory response. Overexpression of these proteins would indicate cellular distress in the form of inflammation. In ELISA assays for the detection of such proinflammatory proteins, it is common to use LPS (lipopolysaccharide derived from gram-negative bacteria) as a positive control, as it induces the production of large amounts of these proteins.[98]

#### 1.3.2.4 Genotoxicity assays

Genotoxicity assays evaluate the effect of a nanomaterial on the cell's genetics, commonly based on DNA damage in the form of mutations or chain breaks. Similarly to other *in vitro* studies, genetic damage can be quantified using common analytical tools, such as electrophoresis or microscopy techniques. The most common genotoxicity assays include:

- Comet assay: An electrophoretic technique for detecting DNA chain breaks. Cells, after exposure to nanomaterials, are dispersed in agarose, induced for lysis, and DNA fragments are separated by electrophoresis. Damaged fragments can be visualized through microscopy, as they migrate further from the nucleus.[99]
- Micronucleus assay: A technique based on the detection of micronuclei (nuclear structures containing fragments of broken chromosomes) through staining. The presence of a higher number of micronuclei indicates greater genetic damage.[99,100]
- Chromosome aberration assay: This assay evaluates structural changes in chromosomes induced by the interaction with nanomaterials. During metaphase, agents that inhibit cell division are introduced, making it possible to visualize the

chromosomes and chromosome aberrations (breaks, fusions, or chromosome losses, indicating genetic damage).[101]

- Mutation assay in specific genes (Ames test): A technique based on the use of living organisms (cellular systems or bacteria) containing specific genes, which are subsequently analyzed through DNA sequencing to detect mutations or sequence changes caused by the toxicity of nanomaterials.[102]

The underlying mechanisms of ENM-induced genotoxicity remain elusive, and it is often ambiguous whether the impact on DNA is specific to ENMs. Genotoxic effects may arise from a direct interaction between ENMs and genetic material, or, alternatively, from indirect damage due to ROS generated by ENMs or to the release of toxic ions from soluble nanoparticles.[103,104] Additionally, secondary genotoxicity may occur as a consequence of oxidative attacks on DNA by ROS, which are mediated through activated phagocytes such as neutrophils and macrophages, during inflammation provoked by NPs.[105,106] The uptake mechanism of ENMs, including their ability to penetrate the nucleus, is crucial in determining the type of genotoxicity. Smaller ENMs can enter the nucleus through pores, while larger ones may use other pathways. Once inside, ENMs can interfere with various cellular processes, including DNA replication, transcription, and mitosis.[107]

# Chapter II. Objectives

The primary aim of this study is to develop NAMs based on *in vitro* and *in chemico* experiments to understand what reactive features trigger events leading to AOPs, and thus identify the reactive basis of engineered nanomaterials toxicity. To achieve the primary objective, a series of specific objectives must be defined. These objectives entail understanding the state of the art (Chapter IV), evaluating new approaches based on quantifying the number and nature (primary reactivity) of reference ENMs' reactive surface sites (Chapter V), analyzing the oxidative capacity of the ENMs in cell-free reactions (Chapter VI and VII), and conducting *in vitro* tests (Chapter VIII) to establish the link between the surface sites reactivity and potential adverse effects. This constitutes a screening approach that aims to forecast toxicity by assessing the nanomaterials' reactivity using *in chemico* and *in vitro* methods (Chapter IX). Therefore, the specific objectives of this research are the following:

- To review the existing knowledge about reactivity and toxicity of common reference nanomaterials (Chapter IV).
- To determine the reactive sites surface density of ENMs as well as their reactivity (acidic, basic, or redox) (Chapter V).
- To establish the oxidation rate per site, referred to as the Oxidative Turnover Frequency (OxTOF) (Chapter VI).
- To categorize ENMs based on their oxidative capacity in a cell-free environment through the evaluation of thiol consumption (DTT, GSH, and CyS) as well as consumption of RNO and $DCFH_2$ by reactive oxygen species (Chapter VII).
- To ascertain the cytotoxicity of ENMs in relevant lung cell lines, evaluating their proteomes and the formation of autophagosomes after exposure (Chapter VIII).
- To correlate *in chemico* and *in vitro* data to elucidate the relationship between ENMs reactivity and toxicity (Chapter IX).

A secondary objective of this work is to contribute to the evaluation of new emerging nanomaterials by existing and alternative methodologies, in particular:

- To evaluate the impact of dispersion methods on the reactive (*in chemico*) and toxicological (*in vitro*) assessment of fibrous nanomaterials (Chapter X).
- To implement Raman spectroscopy as a tool for molecular characterization of emerging materials such as multicomponent engineered nanomaterials and micro/nanoplastics (Chapter X).

# Chapter III. Experimental procedures and methods

## 3.1 Rationale for methodology selection

The reactivity of ENMs has been reported to play a pivotal role in the production of reactive oxygen species, which are implicated in the mode of action of various pathologies,[81,108,16] with inhalation being the primary route of administration (Figure 6).[109] The first approach to understand the reactive bases of toxicity is to decipher the oxidative capacity with *in chemico* methodologies. Then, use *in vitro* methods to understand their toxicity, and link it to the oxidative potential previously measured in the *in chemico* methodology. In this context, owing to the significance of inhalation toxicity of ENMs, this study conducts *in vitro* analyses to ascertain the effects of ENMs on A549 and dTHP-1 cell lines. Benchmark ENMs from JRC and common commercial ENMs are used to validate the methodology.

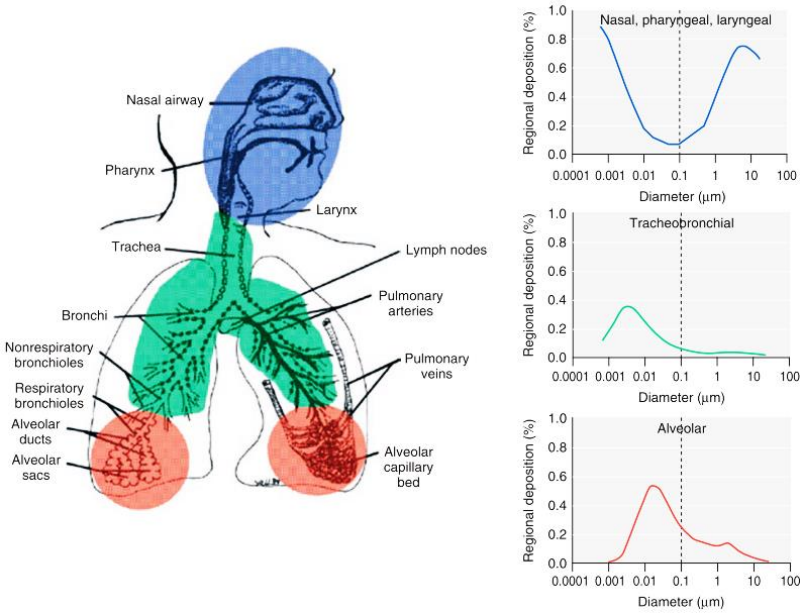


***Figure 6.*** *Prediction of particle deposition following nasal inhalation in different regions: nasopharyngeal, tracheobronchial, and alveolar. Source: Landsiedel R, 2012.*[109]

The study of inhalation toxicity of ENMs is crucial because: 1) Nanoscaled materials can be more toxic than their microscaled counterparts, 2) ENMs have varying toxic effects based on their surface structure and reactivity, 3) Similarities in size and shape to asbestos fibers suggest that certain ENMs might have comparable health risks, and 4) The systemic effects of inhaled ENMs are underexplored, particularly in relation to chronic diseases linked to air pollution, such as respiratory, cardiovascular, neurological, and reproductive disorders. Understanding these effects is vital,[110] given the increasing of health impacts from ambient air pollution, including ultrafine particles.[109,111]

Finally, due to the relevance of new emerging materials as multicomponent (composite) engineered nanomaterials, hydroxyapatite nanobiomaterials or micro and nanoplastics, the surface evaluation with alternative methodologies, involving methanol-TPRx and Raman spectroscopy, is proposed.

## 3.2 Research plan

The research plan is summarized in Figure 7, including the experiments developed by the PhD candidate (yellow boxes) and complementary experiments performed by national and international collaborations (blue boxes).

The experiments conducted in terms of reactivity include methanol-TPSR, DTT consumption assay, and DCFH-DA assay. *In vitro* assays for discerning toxicity mechanisms encompass LDH and WST-1 for cell viability, quantification of autophagosomes to identify autophagy, and protein dysregulation via proteomics. The physicochemical properties of the nanomaterials have been characterized using SEM, Raman spectroscopy, methanol chemisorption, and $N_2$ adsorption isotherms. Lastly, collaborative groups have contributed through the employment of additional probe reactions for antioxidant consumption (cysteine and glutathione depletion), ROS production (RNO depletion), morphology (SEM), and *in vitro* studies to investigate genotoxic effects and the impact on the digestive system (Simgi®).

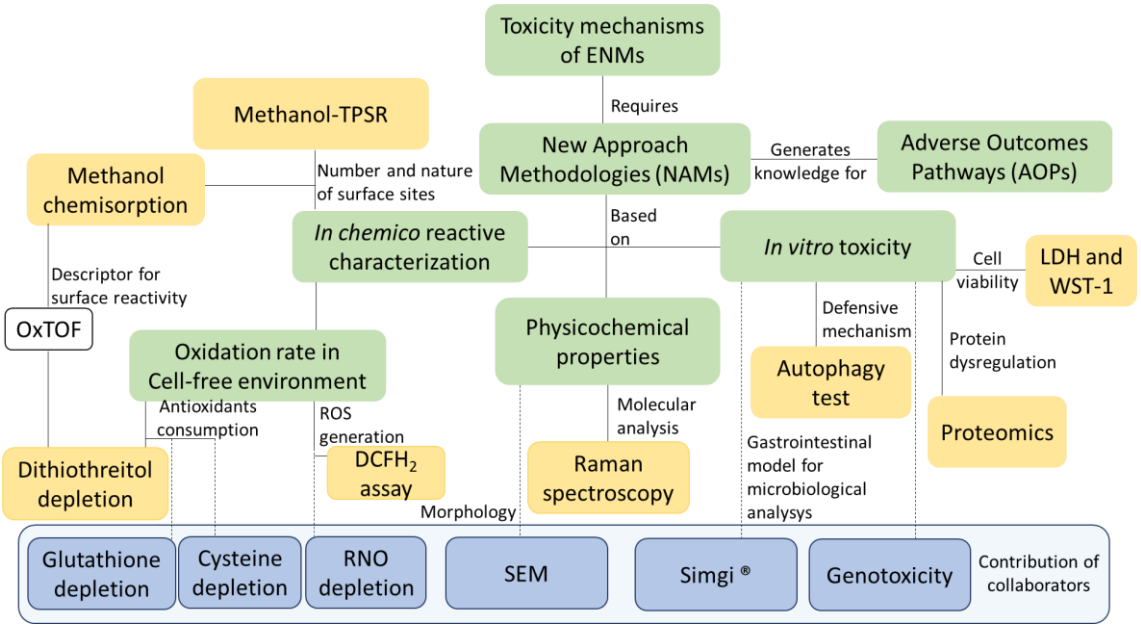


***Figure 7.*** *Research plan applied to understand the toxicity mechanism of ENMs. Green boxes are concepts, yellow boxes are techniques or assays performed by the PhD candidate, and blue boxes are complementary experiments, models or assays performed by collaborators.*

## 3.3 Engineered nanomaterials

The Organization for Economic Cooperation and Development (OECD) has dedicated one of its divisions to the study of the safety of new advanced nanomaterials. According to the latest report, to manage the risks associated with manufactured nanomaterials, it is imperative to apply existing international and national regulatory frameworks or other management systems, taking into consideration the specific properties of these nanomaterials.[112] For the research, standardization, and validation of safety assessment protocols for new nanomaterials, the European Joint Research Center (JRC) has synthesized nanomaterials to be employed as reference. As a result, and due to their widespread use, 10 JRC reference nanomaterials (5 pairs of compounds) were selected to be used in the experimental comparative studies of this thesis (chapters V to IX) and for the literature review (Chapter IV) performed to explore the state of the art concerning their physicochemical properties and toxicological assessment: $TiO_2$ NM-101 (JRCNM01001a), $TiO_2$ NM-105 (JRCNM01005a), $CeO_2$ NM-211 (JRCNM02101a), $CeO_2$ NM-212 (JRCNM02102a), ZnO NM-110 (JRCNM62101a), ZnO NM-111 (JRCNM01101a), $SiO_2$ NM-200 (JRCNM02000a), $SiO_2$ NM-201 (JRCNM02001a), MWCNT NM-400 and

MWCNT NM-401.[113] $TiO_2$ NM-105, a typical reference material for photocatalysis, is frequently described in the literature as $TiO_2$ P25 Degussa powder, which comprises 73–85% anatase, 14–17% rutile, and 0–13% amorphous.[114,115]

Additionally, four commercial ENMs, including anatase DT51 (CristalACTiV™), CuO (ref. number: 544868), carbon black (PRINTEX® 90), and $Fe_2O_3$ (ref. number: 544884), were obtained from Sigma-Aldrich (SA). $Mn_2O_3$ nanoparticles were synthesized at lab-scale and supplied by collaborators (Dr. Felice Simeone, CNR). The basic physicochemical properties of these 15 ENMs are summarized in Table 3. Chapter 10 evaluates the MWCNTs and emerging materials such as different hydroxyapatite nanobiomaterials, multicomponent nanomaterials and micro and nano plastic particles that are specifically described in the chapter.

The powdered nanomaterials were compared without any pretreatment unless specified. The selection of nanomaterials for each test is guided by the specific needs of the nanosafety projects, including BIORIMA, PlasticFate, NanoInformatix, SUNSHINE, and Harmless, in which our research group participates.

***Table 3.*** *Physicochemical properties reported in the literature for the studied nanomaterials.*

| NM | Supplier code | Particle size (nm) | Particle size distribution (nm) | Specific surface area ($m^2/g$) | Other information | Ref. |
|---|---|---|---|---|---|---|
| $TiO_2$ DT-51 | CristalACTiV™ DT-51 | NA | NA | 90 | Anatase, $SO_3$: 1.25 wt% pH = 3 | 116 |
| $TiO_2$ NM-101 | JRCNM01001a | 5-9 | <100 → 95%<br><50 → 77 %<br><10 → 11 % | 170/316 | Anatase<br>Thermal synthesis<br>photocatalytic activity | 113,117, 118,87 |
| | | | 4-8 to 50-100 | 322 | | |
| | | | NA | 320 | | |
| $TiO_2$ NM-105 | JRCNM01005a | 15-24 | NA | 52.81-55.49<br>46 | 83% anatase-17% rutile | 117,113 |
| $CeO_2$ NM-211 | JRCNM02101a | <10 to 20 | In water:<br>$D_{10}$ 810 ± 160<br>$D_{50}$ 202 ± 17<br>$D_{90}$ 130 ± 60 | 65 | Precipitated | 113,119, 87 |
| | | 10.3 | NA | 66 ± 2 | Ce:O = 1:2 (XPS) | |
| $CeO_2$ NM-212 | JRCNM02102a | 28.4 ± 10.4 | NA | 27.2 ± 0.9 | Cubic cerionite | 119 |
| ZnO NM-110 | JRCNM62101a | 70-90 | NA | 12.4 | Zincite<br>ζ: -19.1 ± 0.5 mV<br>Zincite structure | 113,120<br>121,122 |
| | | 202.6 ± 12.8 | DI water (nm)<br>D10 286±2<br>D50 82.8±1.9<br>D90 107.3±1.7 | 14 | | |
| ZnO NM-111 | JRCNM01101a | 140.8 ± 65.8<br>76 | NA | 15.1 ± 0.6 | Coated with triethoxycapryl silane | 113, 120 |
| $SiO_2$ NM-200 | JRCNM02000a | 14-23 | <100 → 89%<br><50 → 70 %<br><10 → 2 % | 189 | Amorphous<br>Precipitated | 113 |
| $SiO_2$ NM-201 | JRCNM02001a | 17-20 | <100 nm - 81.5%,<br><50 nm – 55.3%<br><10 nm – 1.1% | 140 | ζ (pH 6.9, milliQ water): -51.7 mV<br>Na-4400 ppm, Al- 7400 ppm, S- 4600 ppm, Si - 45.27 wt %, O- 53.08 wt% | 123 |

| | | | | | | |
|---|---|---|---|---|---|---|
| $Fe_2O_3$ | 544884 (Sigma-Aldrich) | 35 ± 14 | NA | 39 | Impurities <0.5% | 124 |
| CuO | 544868 (Sigma-Aldrich) | <50 | NA | NA | Tenorite<br>77-82.6 % Cu<br>Crystallite size: 17 nm<br>IEP: 8.3, ζ: 15.1 ± 9.4 mV | 125,126, 45,127, 128 |
| | | NA | NA | 11 | | |
| | | 37 | NA | 11 | | |
| | | 33.3 ± 10.7 | 10-100 nm | NA | | |
| $Mn_2O_3$ | Produced at lab-scale | 36 | NA | 17-20 | Z at pH 7: -5 mV | 37 |
| Carbon black | Printex90 | 14 | NA | 317 | Polycyclic aromatic hydrocarbons: 0.0742 mg/g<br>Endotoxin level: 0.142 EU/mg<br>Composition: 99% C, 0.8% N and 0.01% $H_2$ | 129, 130 |
| MWCNTs NM-400 | JRCNM04000a | L: 846 nm<br>D: 11 nm | NA | 254 | Composition: 89,81% C, 4.15% O<br>Impurities (ppm by weight): 46100 Al, 400 Si, 7600 Fe, 2500 Co, 2000 Cu and 1900 Zn. | 113 |
| MWCNTs NM-401 | JRCNM04001a | L: 4048 nm<br>D: 67 nm | NA | 140 | Composition: 99,19% C, 0.6% O<br>Impurities (ppm by weight): 500 Si, 2300 Cu and 2200 Zn. | 113 |

## 3.4 *In chemico* methodologies

### 3.4.1 $N_2$ adsorption isotherm

Specific surface area was calculated by BET equation with data obtained in a Micromeritics ASAP 2020 adsorption isotherm equipment. All ENMs were pretreated by degassing under vacuum for 16 h at 120 ºC prior to nitrogen adsorption at liquid nitrogen temperature.

### 3.4.2 Methanol chemisorption and TPSR

Methanol chemisorption/TPSR procedure is made on a clean dehydrated sample. 100-250 mg of nanomaterial (aggregates size between 25 and 100 μm) diluted with 500 mg of inert SiC (black 180, Navarro SiC S.A.) to ensure isothermal conditions is placed in a fixed-bed reactor (0.4 cm internal diameter). The sample is first pretreated by heating to 450 $^0$C at 10 $^0$C/min in a synthetic air flow of 150 mL/min and kept at this temperature for 35 min to remove moisture and burn away impurities from its surface. After pretreatment, the sample is cooled to 100 ºC in synthetic air, so that the surface is hydroxylated, but not hydrated, and the flow feed is switched to argon (100 mL/min) purge. After purge, still at 100ºC, 100 mL/min of 2000 ppm methanol in argon with 5% helium is fed until saturation, as determined by online mass spectrometry residual gas analysis. Helium is used as an internal concentration standard for online mass spectrometry. Methanol molecules do not physisorb at this temperature but chemisorb titrating surface hydroxyls (or dissociating bridging surface oxygens), forming methoxy species (-$OCH_3$) and releasing $H_2O$. At this moment, the feed is switched to 100 mL/min Ar to first purge residual methanol vapor, and then run the TPSR of the chemisorbed methoxy species by linearly heating the sample from 100 to 450 $^0$C at 10 $^0$C/min. Blank tests were performed with 500 mg of inert SiC (Figure 8).

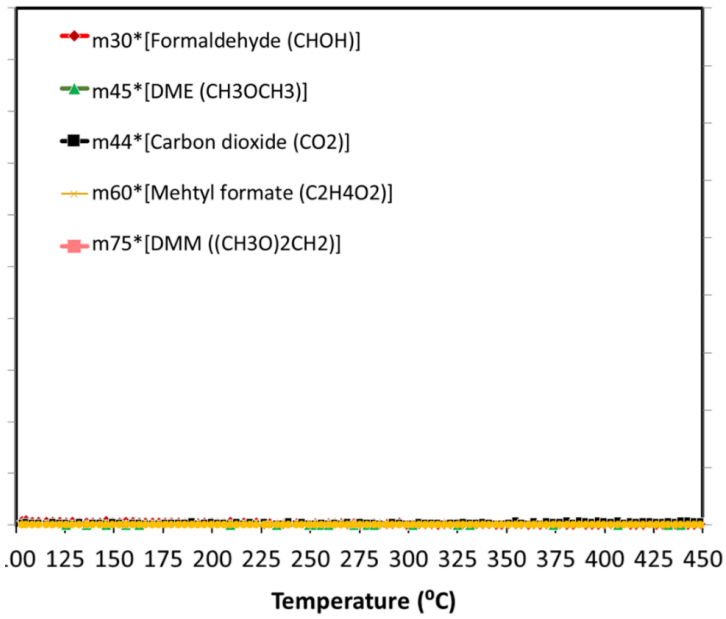


***Figure 8**. Methanol temperature-programmed surface reaction (TPSR) for SiC (blank).*

The reactor outlet was analyzed online by a quadrupole residual gas analyzer Pfeiffer OmniStar mass spectrometer, setup described in Figure 9. The m/z values followed were: $CH_3OH$ (methanol) = 31, HCHO (formaldehyde) = 30, $CH_3OCH_3$ (dimethyl ether, DME) = 45, $CH_3OOCH$ (methyl formate) = 60, $(CH_3O)_2CH_2$ (dimethoxy methane) = 75, $H_2O$ (water) = 18, and $CO_2$ (carbon dioxide) = 44. Methyl formate, dimethyl ether and formaldehyde signals were corrected for the contributions of methanol and carbon monoxide to the selected m/z values. For active sites calculation, the m/z = 31 signal is integrated during the chemisorption step to quantify the moles or molecules of methanol retained by the material on the surface ($MeOH_s$), and during the TPSR step to calculate the fraction of methanol that is released unreacted ($MeOH_u$). The reacted methanol ($MeOH_r$) is obtained by subtracting both values and is equal to the number of surface sites. The specific number of active sites is calculated by dividing this number by the mass of ENM used for the experiment. Dividing the specific number of surface sites by the ENM BET area delivers the active sites surface density.

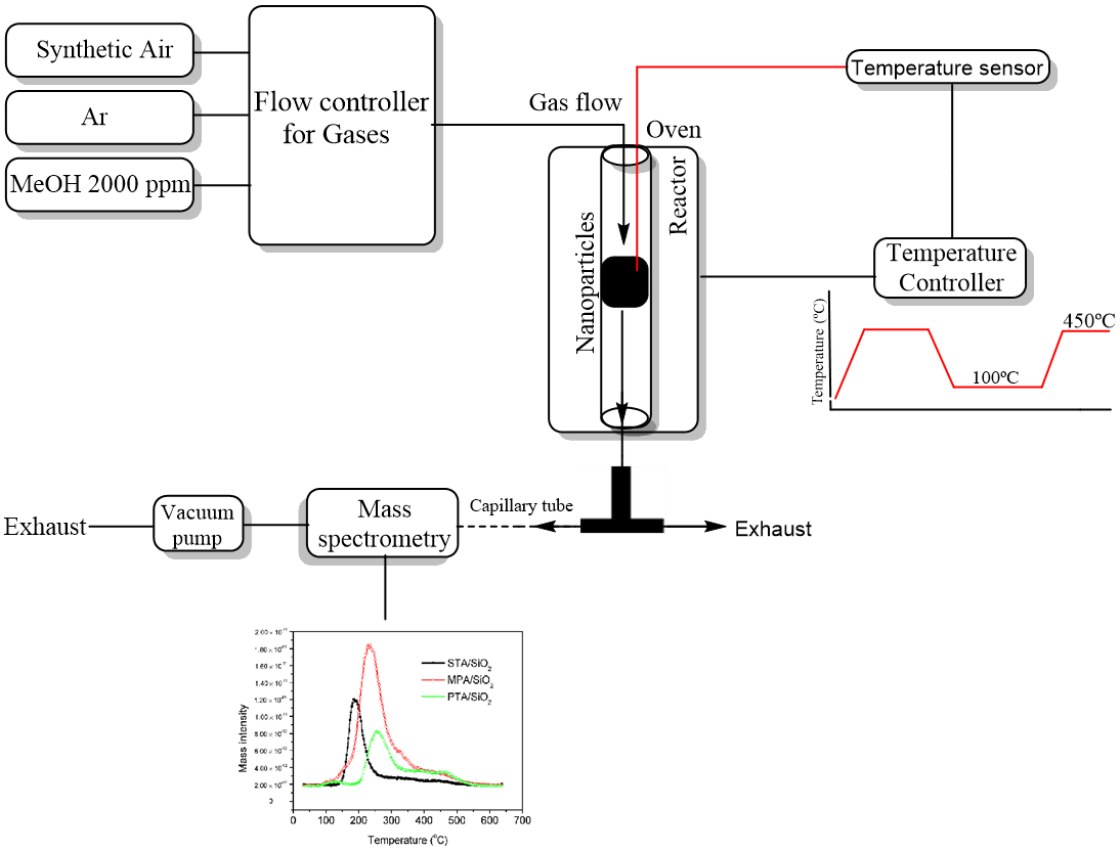


***Figure 9**. Experimental setup for methanol chemisorption and temperature-programmed surface reaction (TPSR).*

### 3.4.3 Methanol-TPRx

TPRx is performed when TPSR cannot be performed due to the low methanol chemisorption of the sample (section 10.3.1). The experimental procedure encompassed four phases: pretreatment, initial purge, methanol chemisorption, and TPRx. Pretreatment involved heating the sample from 100 to 450 °C at a rate of 10 °C·min$^{-1}$ with the introduction of 150 mL·min$^{-1}$ of synthetic air to eliminate surface moisture and impurities. Following pretreatment, an initial purge with inert gas (150 mL·min$^{-1}$ of Ar) at 100 °C was conducted until impurities were no longer detected in the mass spectrometer spectra. Subsequently, methanol chemisorption was carried out with a methanol/argon mixture at a constant temperature of 100 °C, concluding when a stable methanol signal was observed in the mass spectrometer (m/z = 31). The final phase, TPRx, involved maintaining the methanol/argon flow while increasing the temperature from 100 to 450 °C at a rate of 10 °C·min$^{-1}$. The experiment utilized a sample of 0.1 g (mesh size: 25-100

μm) diluted with 0.5 g of SiC (black 180, Navarro SiC S.A.) to ensure uniform temperature distribution.

Finally, the methodology to perform Raman maps for micro and nanoplastics is described in chapter X, due to the different nature of the samples.

### 3.4.4 Consumption of thiol-based antioxidants

Three antioxidants were used for cell-free estimation of oxidative potential: i) dithiothreitol, ii) cysteine (Cys) and iii) glutathione (GSH). DTT is a disulfide used as unspecific reducing agent.[131,132] Glutathione is a natural antioxidant characterized by the lowest redox potential that can be found in a cell.[133] This low redox potential (i.e., high thermodynamic tendency to reduce oxidants) enables the direct oxidation of the terminal -S by reduction of species other than ROS, which have a very high redox potential. Cysteine is an aminoacid, and the oxidation of its –SH group is relevant for the oxidative damage to proteins.

#### 3.4.4.1 DTT

DTT oxidation was performed in a batch reactor for 1h. First, a 200 μg/mL suspension of NM in 1 mM phosphate buffer is obtained by sonication, following NanoGenoTox SOP (16 min at 400 W and 10% amplitude).[134] 3 mL of the NM suspension is incubated for 1 h at 37 °C and 500 rpm with 3 mL of 100 μM DTT, obtaining a 6 mL reaction mixture with 100 μg/mL of NM and 50 μM DTT. Then, the nanoparticles are removed by filtration, and the filtrate, with the unreacted DTT and the reaction products, is mixed with an equal volume of 1 mM Ellman's reagent (5,5'-dithiobis-(2-nitrobenzoic acid), DTNB) to quantify the non-oxidized DTT. Ellman's reagent reacts with the thiol groups (-SH) of the free DTT molecules, forming 5-mercapto-2-nitrobenzoic acid, a colorful complex that is measured at 412 nm by UV-Vis spectrophotometry (Shimadzu, UV-2100). In parallel, as negative control, DTT in phosphate buffer without NM is incubated under the same conditions and mixed with the Ellman's reagent to evaluate DTT consumption by direct reaction without catalyst. Hydrogen peroxide 30 % (w/w) in $H_2O$ is used as a positive control, as

it provides similar DTT conversion as 1,4-naphthoquinone,[135] being safer and not requiring filtration. All reactions were performed in triplicate. Linearity in measurements at 412 nm of DTT-DTNB nm complex was calibrated (Figure 10).

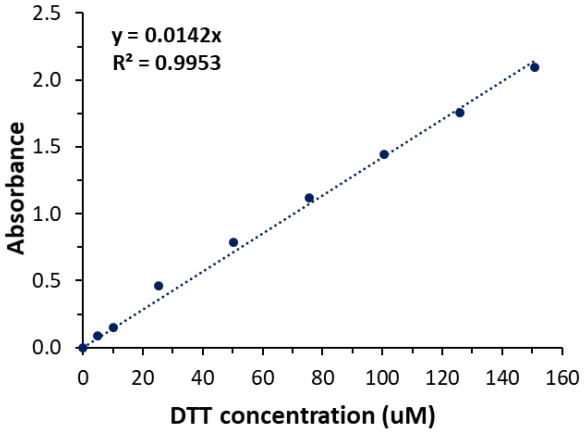


***Figure 10**. Calibration for DTNB-DTT complex measured to 412 nm.*

ENM's oxidative potential is expressed as DTT conversion (Eq. 1, as normalized index of oxidant generation using hydrogen peroxide as a positive control (Eq. 2), or as DTT reaction rate, normalized *vs*. mass (Eq. 3), *vs.* surface area (Eq. 4), or *vs.* number of active sites (Eq. 5), i.e, oxidative turnover frequency (OxTOF).

$$\text{DTT depleted (mol \%)} = 100 - \frac{Reaction\ absorbance}{Blank\ absorbance} \cdot 100 \quad \text{(Eq. 1)}$$

$$\text{NIOG (0-1)} = \frac{DTT\ depleted\ by\ nanomaterial}{DTT\ depleted\ by\ positive\ control} \quad \text{(Eq. 2)}$$

$$OP_{mass}\ (mol \cdot s^{-1} \cdot g^{-1}) = \frac{depleted\ DTT\ moles}{time \cdot mass\ of\ NM} \quad \text{(Eq. 3)}$$

$$OP_{area}\ (\mu mol \cdot s^{-1} \cdot m^{-2}) = \frac{depleted\ DTT\ moles}{time \cdot surface\ area\ of\ NM} \quad \text{(Eq. 4)}$$

$$OxTOF\ (s^{-1}) = \frac{depleted\ DTT\ molecules}{time \cdot active\ sites\ of\ NM} \quad \text{(Eq. 5)}$$

#### 3.4.4.2 Glutathione and cysteine

*Tests performed by international collaborators (Lara Faccani and Dr. Felice Simeone at National Research Council of Italy, CNR, Institute of Science and Technology for Ceramics, ISTEC)*

A 1 mM suspension of ENM in 2 mM solution of GSH and Cys in PBS (0.01 M; pH=7.4) was prepared in a 12 mL test tube. After incubation for 24 h, the suspension was filtered to eliminate the nanoparticles. Non-oxidized thiols groups were quantified by adding the Ellman's reagent up to a final concentration of 3 mM. Absorbance at 410 nm was measured to calculate the amount of unreacted -SH groups from a calibration curve. For each nanoparticle, -SH consumption was measured in triplicate.

### 3.4.5 Generation of reactive oxygen species

Quantification of ROS generation by acellular assays is proposed to understand the intrinsic capacity of ENMs to produce radical species in liquid media by two probe molecules: N, N-Dimethyl-4-nitrosoaniline (RNO), which is specific for reaction with hydroxyl radicals, and 2',7'-dichlorodihydrofluorescein diacetate ($DCFH_2$-DA), a highly sensitive oxidative probe molecule that is not specific to any reactive oxygen species, and therefore can detect a great range of free radicals.[136]

#### 3.4.5.1 Hydroxyl radicals trapping with RNO

*Tests performed by international collaborators (Lara Faccani and Dr. Felice Simeone at National Research Council of Italy, CNR, Institute of Science and Technology for Ceramics, ISTEC)*

A 2mM NM solution in PBS was mixed in a test tube with 3 mM RNO. After 24 h incubation, nanoparticles were filtered out and the absorbance of the solution at 430 nm was measured to calculate RNO depletion from a linear calibration curve, and thus quantify the production of OH* radicals. The assay was repeated in triplicate for each nanoparticle.

#### 3.4.5.2 $DCFH_2$ assay

$DCFH_2$-DA is a lipophilic non-fluorescent probe molecule commonly used in a well-known methodology for ENMs screening in previous literature[137,138,132,139,140] to unravel ROS induction in both a cell-free environment and *in vitro* assays. The reactive

mechanism is based on a first step of diacetate removal by alkaline hydrolysis, followed by the reaction between different kinds of generated ROS species and $DCFH_2$ to produce $DCF^-$, which is quantified by fluorescence at 485/520 nm (excitation/emission).

$DCFH_2$-DA was hydrolyzed to $DCFH_2$ by incubation of 0.01M NaOH with 200 µM $DCFH_2$-DA at room temperature for 30 min in a covered vessel protected from light. Then, 0.1 M PBS was introduced to finish deacetylation, until a concentration of 50 µM $DCFH_2$. A second dilution was performed with 0.01M PBS to obtain a 10 µM solution that was kept on ice until use. Test ENM stock suspensions were prepared by sonication following NanoGenoTox SOP at a concentration of 2.56 mg/mL. Then, dilutions to 15, 31, 63, 125, 250, 500 and 1000 µg/mL were prepared with phenol red-free medium (MEM). Finally, using a multi-channel pipette, in each of the wells of a clear-flat-bottom 96-well plate 225 µL $DCFH_2$ solution was added to 25 µL NM suspension. Final test NM concentration in reaction mixtures was: 1.5, 3.1, 6.3, 12.5, 25.0, 50.0 and 100.0 µg/mL. Fluorescence at ex/em 485/520 was measured immediately after reaction sample preparation as well as after 30, 60 and 90 min incubation performed at 37ºC protected from light. The assay was done in triplicate (n=3). In order to assess the interference of nanomaterials, interference tests were conducted, employing positive controls and a calibration curve to ensure the proper execution of the assay.

***Calibration***. Fluorescein solutions were used as standard to obtain a calibration curve for quantification. Fluorescein diacetate (F-DA) 200 µM was incubated with 0.01M NaOH at room temperature, protected from light, for 5 min. The reaction finished when 0.1M PBS was added, generating fluorescein 50 µM. 0.01M PBS was used to prepare serial dilutions at the following concentrations: 0.001, 0.004, 0.012, 0.037, 0.111, 0.333, 1.000 µM.

***Positive controls***. Printex® 90 carbon black and 3-Morpholinosydnonimine hydrochloride (SIN-1) were used as nanomaterial and chemical positive controls, respectively, suspensions were prepared following the same procedure as with the test ENMs for final concentrations of 1.6, 3.1, 6.3 and 12.5 µg/mL. SIN-1 100 µM solutions were prepared in MEM and diluted to 13, 25 and 50 µM to provide a final assay concentration after mixture with $DCFH_2$ of 1.3, 2.5, 5.0 and 10.0 µM.

***Nanomaterial interference evaluation.*** Fluorescence quenching and auto-fluorescence of ENMs was assessed at all experimental doses (from 1.6 to 100 µg/mL) in a black clear-bottom 96-well plate. 225 µL of F-DA or PBS were added to 25 µL of test NM dispersion to evaluate fluorescence or auto-fluorescence quenching, respectively. All wells were immediately measured at ex/em 485/520.

### 3.4.6 Statistical analysis

DTT $OP_{mas}$, $OP_{area}$ and OxTOF are expressed as average ± sd (standard deviation). The statistical analysis was performed with SPSS 20 (IBM, Armonk, USA) using logarithmic scale to display values in a compact way. One-way ANOVA (Analysis of Variance) was performed to determine statistically significant differences. Subsequently, a Tukey test was performed to assess pairwise differences with a significance level of $p < 0.05$ and classify ENMs according to the oxidative potential.

Clustering methods such as K-means unsupervised learning algorithms are used to unravel similarity-based descriptors and patterns of the reactivity data,[141,19,142] with the mail goal to group the ENMs by distance-based metrics or similarity according to their oxidative potential.

Nanomaterials reactivity based on mass, surface and active sites exposed to the probe molecule are compared in a pairplot, where rows and columns represent the x and y axis, respectively. The diagonal subplots provide the probability density function (PDF) for the respective normalization variable and probe molecule. The outcomes of various probe reactions were assessed through the Pearson correlation coefficient, as a linear correlation is anticipated in the reactivity context.

## 3.5 *In vitro* methodologies

### 3.5.1 Cell cultures

The human lung epithelial cell line A549 was obtained from the American Type Culture Collection, Manassas, USA (ATCC, CRM-CCL-185 LOT: 83114291). Cells were cultured at

37°C in a humidified 5% $CO_2$ atmosphere in in MEM GlutaMAX (Gibco, Cat. No. 41090-028) supplemented with 10% heat inactivated fetal calf serum (FCS) GOOD, (PAN Biotech, Cat. No. P40-37500) and 1% penicillin-streptomycin, (PAN Biotech, Cat. No. P06-07100) were incubated at 37°C, 5% $CO_2$.

The human monocytic cell line THP-1 was obtained from the Leibniz Institute DSMZ-German Collection of Microorganisms and Cell Cultures GmbH (Braunschweig, DE). Cells were cultured at 37ºC in a humidified 5% $CO_2$ atmosphere in RPMI 1640 (PAN Biotech, P04-17500) supplemented with 10 % heat inactivated fetal calf serum (FCS) GOOD, (PAN Biotech, Cat. No. P40-37500) 1% penicillin-streptomycin, (PAN Biotech, Cat. No. P06-07100), 1% L-Glutamine (PAN Biotech, order no. P04-80100). THP-1 monocytes were induced to polarise into non-activated M0 macrophages by adding 61.68 ng/mL phorbol-12-myristate 13-acetate (PMA) (P1585, Sigma Aldridge, 2407201).

### 3.5.2 Cell viability tests

LDH assay (11644793001, Roche, Mannheim, Germany) was utilized to estimate cell viability by measuring cell permeability. The enzyme involved in the conversion of lactate to pyruvate is a biomarker for cell damage, as dying cells release LDH into the extracellular space and assay measures the conversion of NADH to NAD+ catalyse by LDH followed by absorbance. The assay was performed following the instructions provided by the supplier.

The WST-1 (*water soluble tetrazolium*) (11644807001, Roche, Mannheim, Germany) kit was used to determine cell viability. WST-1 is a water-soluble tetrazolium dye that can penetrate cells. When cleaved by mitochondrial dehydrogenases in viable cells, formazan is produced and its quantity can be determined by measuring the absorbance at 450 nm, as indicative of cell viability.

For both assays, tests were performed in quadruplicates for each sample and concentration, obtaining a total of three biological replicates.

### 3.5.3 Proteomics

***Cell pellet preparation.*** A549 and THP-1 were seeded in 6-well plate with a cell density of $3 \cdot 10^5$ and $10^6$ cells/well, respectively. Cells were exposed to the highest concentration

at which cell viability was not significantly affected, and incubated for 24 h at 37ºC with 5% $CO_2$.

***Sample preparation and Liquid Chromatography–Electrospray Ionization–Tandem Mass Spectrometry (LC–ESI–MS/MS) measurements***. Cell pellets were prepared for proteomics measurements using the PreOmics iST kit to obtaine a tryptic digest. Desalted peptides were reconstituted in 0.1% (v/v) TFA, 5% (v/v) acetonitrile to obtain a final concentration of 50 ng total protein and 5 µL were analyzed by a reversed-phase capillary nano liquid chromatography system (Ultimate 3000, Thermo Scientific) connected to an Orbitrap QExactive+ mass spectrometer (Thermo Scientific). The LC system was coupled to the mass spectrometer via a nanospray flex ion source equipped with a stainless-steel emitter (Thermo Scientific). Samples were injected and concentrated on a trap column (PepMap100C18, 3 µm, 100 Å, 75 µmi.d. × 2 cm, Thermo Scientific) equilibrated with 0.05% TFA, 2% acetonitrile in water. After switching the trap column inline, LC separations were performed on a capillary column (Acclaim PepMap100C18, 2 µm, 100 Å, 75 µmi.d. × 25 cm, Thermo Scientific) at an eluent flow rate of 300 nL/min using a linear gradient of 3–80% B in 120 min. Mobile phase A contained 0.1% formic acid in water, and mobile phase B contained 0.1% formic acid in acetonitrile. Mass spectra were acquired in a data-dependent mode utilizing a single MS survey scan with a resolution of 70,000 in the Orbitrap, and MS/MS scans of the 10 most intense precursor ions in the linear trap quadrupole. The MS survey range was m/z 300-2000. The dynamic exclusion time (for precursor ions) was set to 60 s, automatic gain control was set to $1 \times 10^6$ and 5.000 for Orbitrap-MS, and LTQ-MS/MS scans, respectively.

***Protein Identification and data analysis for proteomics.*** MS and MS/MS data from each LC/MS run were analyzed using the MaxQuant software (Version 1.6.14). Identification of proteins was performed using the MaxQuant-implemented Andromeda peptide search engine against a reference proteome database of Homo sapiens. Initial maximum precursor and fragment mass deviations were set to 7 ppm and 0.5 Da, respectively. Variable modification (methionine oxidation and N-terminal acetylation) and fixed modification (cysteine carbamidomethylation) were set for the search and trypsin with a maximum of three missed cleavages was chosen for searching. The

minimum peptide length was set to 7 amino acids and the false discovery rate (FDR) for peptide and protein identification was set to 0.01.

### 3.5.4 Autophagosome detection

Autophagy Assay Kit provided by Sigma-Aldrich (references: MAK138) measures autophagy in cells using a fluorescent autophagosome marker. A549 and THP-1 were seeded in 96-well plate with a cell density of $2 \cdot 10^4$ and $5 \cdot 10^4$ cells/well, respectively. Cells were exposed to the two highest concentrations at which cell viability was not significantly affected, and incubated for 24 h at 37ºC with 5% $CO_2$. Then, following provider instructions, a working solution of the autophagosome detection reagent was performed by adding 20 µL of the 500x solution to 10 mL of the stain buffer to analysis one 96 well-plate. Then, after incubation period, the medium was removed and 100 µL of the autophagosome detection reagent working solution were added to each well, and the incubation was carried out during 1 h at 37ºC with 5% $CO_2$. After incubation, the supernatant was removed to wash cells with 100 µL of wash buffer 3 times. Finally, fluorescence intensity was measured at $\lambda_{ex}$ = 360 / $\lambda_{em}$ = 520 nm. Four wells were filled with cell control media to serve as negative control. Experiments were performed by triplicate and all biological replicates consist of 4 technical replicates.

This analysis highlighted the pronounced impact of certain concentrations of ENMs relative to the control group, which was only exposed to cell culture media. The study specifically examined $TiO_2$ NM-101, $TiO_2$ NM-105, $CeO_2$ NM-211, $CeO_2$ NM-212, $SiO_2$ NM-200, $SiO_2$ NM-201, and $Fe_2O_3$ at concentrations of 25 and 50 µg/mL. This concentration range was chosen because no harmful effects were detected in both cell lines when assessed with LDH and WST-1 assays. For CuO, ZnO NM-110, and ZnO NM-111, dosages were adjusted in line with cytotoxicity data to discern a dose-dependent response while ensuring cell viability remained intact.

### 3.5.5 Statistical analysis

LDH release, WST-1 test and fluorescence autophagosome detection were performed by quadrupled for each sample and concentration, obtaining a total of three biological replicates. Data was analyzed for statistical significance using one-way analysis of variance (ANOVA) followed by Bonferroni's post hoc test ($p<0.05$).

# Chapter IV. Review of ENM's reactivity and toxicity

## 4.1 Introduction

The surge in scientific publications concerning the toxicity of Engineered Nanomaterials (ENMs) has been prominent in the past decade. The initial phase of the present study is grounded in a comprehensive literature review of the studies on reactivity, characterization, and toxicity of the nanomaterials that will be assessed in the subsequent chapters, specifically those presented in Section 3.3. Conducting a bibliographic search serves as an invaluable tool for grasping the current state-of-art, which is essential for planning and discussing the experimental results in the forthcoming chapters.

## 4.2 *In chemico* reactivity data

Table 4 summarizes the chemical information reported in the literature to describe the reactivity of the tested engineered nanomaterials under study. Surface reactive characterization for several of these ENMs is missing in the literature. This data gap needs to be filled to understand the reactive bases of nanomaterials' toxicity. To the best of our knowledge, 4 ENMs has not been reactively evaluated previously by any abiotic methodology: Sigma Aldrich $Fe_2O_3$, $Mn_2O_3$, $SiO_2$ NM-200 and $SiO_2$ NM-201.

DMPO reaction showed the photoactivity of $TiO_2$ NM-101; however, ROS generation in the absence of radiation was also detected, contrary to results of terephthalic acid assay.[143] $TiO_2$ NM-105 (P25) depleted a similar amount of CPH and DMPO probe molecules than the negative control, but was highly reactive in the FRAS assay.[37] Driessen et al[78] obtained three times more oxidation for $TiO_2$ NM-105 in DMPO than the blank.

Cerium oxides NM-211 and NM-212 exhibit high reactivity in the surface-based values obtained from CPH. DMPO reaction probe was not relevant due to the low reactivity of this ENM. FRAS methodology presented high values of AUC (Area Under Curve) for both cerium oxides.[37] $CeO_2$ NM-212 was tested elsewhere, showing a concentration dependent responses to FRAS but non-reactive behavior in front $DCFH_2$, DMPO and CPH.[140]

ZnO NM-110 is the most evaluated nanomaterial in the series. Reported data confirms no ROS production in $DCFH_2$ assay.[140,136] CPH and DMPO were more depleted for NM-110 than blank, and the surface-based values evidenced the oxidative capacity for EPR experiments.[37,78] FRAS assay showed the highest sensitivity to ZnO NM-110 reactivity.[37,140] ZnO NM-111 tested positive in FRAS experiments, being one of the highest oxidant in the series.[37] CPH and DMPO were depleted during NM-111 exposure, testing positive for both molecules (2.8 and 3.5 in the ratio sample/blank, respectively).[78]

Carbon based nanomaterials showed different reactivities. While carbon black printex 90 is used as a positive control in $DCFH_2$ assay due to the high dose-dependent ROS production and high DTT depletion, MWCNT NM-401 tested negative for $DCFH_2$.[85,144,136,132] Contrary to CB results for DTT and $DCFH_2$, the spin probe molecules CPH and DMPO are not affected after CB exposure. However, this ENM is highly reactive in FRAS measurements.[37] In addition, MWCNT NM-400 induces significant increase of ROS levels for Cytochrome C assay.[145]

**Table 4.** *In chemico* reactivity data reported in the literature for the ENMs of the study. TA = terephthalic acid, PBS = Phosphate Buffered Saline, DMPO = 5,5-dimethylpyrroline N-oxide, CPH = 1-hydroxy-3-carboxy-pyrrolidine, MeOH-TPSR = methanol temperature-programmed surface reaction, Human Blood Serum = HBS, Ethylenediaminetetraacetic acid =EDTA, 9H-1,8-Diazafluoren-9-one = DFO, Minimum Essential Medium = MEM, Fetal calf serum = FCS, Area under curve = AUC.

| Powder NM reference | Probe molecule /Technique | Reaction time | Medium | NM concentration | Quantification parameter | Final report | Ref. |
|---|---|---|---|---|---|---|---|
| $TiO_2$ NM-101 | TA | 15 min | Irradiation: full spectrum lamp | 1 mg/mL | Concentration of generated ·OH radicals | 10-15 µM ·OH radical | 143 |
| | TA | 15 min | No irradiation | 1 mg/mL | Concentration of generated ·OH radicals | Non reactivity | |
| | DMPO | 5 min | Irradiation: full spectrum lamp | 1 mg/mL | p<0.05 | Photoactivity ROS generation | |
| | DMPO | 5 min | No irradiation | 1 mg/mL | p<0.05 | ROS generation | |
| $TiO_2$ NM-105 | CPH | 15 min | PBS + DFO 0.1 mM | 0.5 mg/mL | Ratio sample/blank | 0.69 | 37 |
| | | | | 1 $m^2$/mL | Ratio sample/blank | 1.09 | |
| | DMPO | 15 min | PBS + $H_2O_2$ | 0.25 mg/mL | Ratio sample/blank | 1.01 | |
| | | | | 1 $m^2$/mL | Ratio sample/blank | 1.66 | |
| | FRAS | 90 min | HBS | 0.75, 2, 5.5,15 and 40 mg/ml | AUC | 677,867 | |
| | | | | 1 $m^2$/mL | AUC | 18.64 | |
| | CPH | - | $H_2O$ | 0.5 mg/mL | Ratio sample/blank | 0.82 (positive) | 78 |
| | DMPO | - | $H_2O$ | 0.25 mg/mL | Ratio sample/blank | 3 (positive) | 78 |
| $CeO_2$ NM-211 | CPH | 15 min | PBS + DFO 0.1 mM | 0.5 mg/mL | Ratio sample/blank | 1.80 | 37 |
| | | | | 1 $m^2$/mL | | 268.60 | |
| | DMPO | 15 min | PBS + $H_2O_2$ | 0.25 mg/mL | | 1.28 | |
| | | | | 1 $m^2$/mL | | 1.37 | |
| | FRAS | 90 min | HBS | 0.75, 2, 5.5,15 and 40 mg/ml | AUC | 837,353 | |
| | | | | 1 $m^2$/mL | | 14.16 | |
| $CeO_2$ NM-212 | CPH | 15 min | PBS + DFO 0.1 mM | 0.5 mg/mL | Ratio sample/blank | 1.42 | 37 |
| | | | | 1 $m^2$/mL | | 189.41 | |
| | | 15 min | PBS + $H_2O_2$ | 0.25 mg/mL | | 2.07 | |

| | | | | | | |
|---|---|---|---|---|---|---|
| | DMPO | | | 1 $m^2$/mL | | 2.32 | |
| | FRAS | 90 min | HBS | 0.75, 2, 5.5,15 and 40 mg/mL | AUC | 570,057 | |
| | | | | 1 $m^2$/mL | | 12.90 | |
| | FRAS | 180 min | HBS | 0.02 to 40 mg/mL | Oxidative damage/molt TEU/L | Positive slope. Concentration dependent responses | 140 |
| | DMPO | 60 min | 0.01 M EDTA and PBS | 0.002 and 4 mg/mL | EPR intensity | Non reactive | 140 |
| | CPH | 60 min | 0.01 M EDTA and PBS | 0.002 and 4 mg/mL | EPR intensity | Non reactive | 140 |
| | $DCFH_2$ | 90 min | PBS and phenol red-free MEM with 2% FCS | 0.5, 1, 2 and 4 mg/ mL | Fluorescence intensity | Non reactive | 140 |
| ZnO NM-110 | CPH | 15 min | PBS + DFO 0.1 mM | 0.5 mg/mL | Ratio sample/blank | 1.51 | 37 |
| | | | | 1 $m^2$/mL | | 63.38 | |
| | DMPO | 15 min | PBS + $H_2O_2$ | 0.25 mg/mL | | 2.20 | |
| | | | | 1 $m^2$/mL | | 7.36 | |
| | FRAS | | HBS | 0.75, 2, 5.5,15 and 40 mg/ml | AUC | 2,898,432 | |
| | | | | 1 $m^2$/mL | | 150.99 | |
| | $DCFH_2$ | 90 min | PBS and phenol red-free MEM with 2% FCS | 0.5, 1, 2 and 4 mg/ mL | Fluorescence intensity | Non-reactive. Non concentration-response | 140 |
| | FRAS | 180 min | HBS | 0.02 to 40 mg/mL | Oxidative damage/molt TEU/L | Positive slope. Intermediate reactive | 140 |
| | DMPO | 60 min | 0.01 M EDTA and PBS | 0.002 and 4 mg/mL | EPR intensity | low reactivity. dose-dependent reactivity | 140 |
| | CPH | 60 min | 0.01 M EDTA and PBS | 0.002 and 4 mg/mL | EPR intensity | Non-reactive. Non concentration-response | 140 |
| | $DCFH_2$ | 30, 60, and 90 min | PBS and phenol red-free MEM with 2% FCS | 1.6, 3.1, 6.3, 12.5, 25, 50, 100 mg/ml | Slope: positive or negative | Negative. No ROS generation | 136 |
| ZnO NM-111 | FRAS | 90 min | HBS | 0.75, 2, 5.5,15 and 40 mg/ml | AUC | 1,069,431 | 37 |
| | | | | 1 $m^2$/mL | | 20.31 | |
| | CPH | - | $H_2O$ | 0.5 mg/mL | Ratio sample/blank | 2.8 (POSITIVE) | 78 |

| | | | | | | | |
|---|---|---|---|---|---|---|---|
| | DMPO | - | $H_2O$ | 0.25 mg/mL | Ratio sample/blank | 3.5 (POSITIVE) | 78 |
| Carbon Black Printex 90 | CPH | | PBS + DFO 0.1 mM | 0.5 mg/mL | Ratio sample/blank | 1.21 | 37 |
| | DMPO | | PBS + H2O2 | 0.25 mg/mL | | 0.98 | |
| | FRAS | | HBS | 0.75, 2, 5.5,15 and 40 mg/ml | AUC | 2,100,127 | |
| | $DCFH_2$ | 90 min | PBS and phenol red-free MEM with 2% FCS | 1.6, 3.1, 6.25, 12.5 µg/ml | Slope: positive or negative | Positive. ROS generation | 85 |
| | DTT | 30 min | Tris–HCl buffer | 1, 10 and 100 µg/ml | DTT consumption (nmol) | High and dose-dependent reactivity | 144 |
| | $DCFH_2$ | 30, 60, and 90 min | PBS and phenol red-free MEM with 2% FCS | 1.6, 3.1, 6.25, 12.5 µg/ml | Slope: positive or negative | Positive. ROS generation | 136 |
| | DTT | 15-90 min | PBS | 5–40 $mg{\cdot}mL^{-1}$ | pmol/min/µg | 67 ± 18 | 132 |
| | DTT | 15-90 min | PBS | 5–40 $mg{\cdot}mL^{-1}$ | $nmol/min/m^2$ | 263 ± 51 | 132 |
| MWCNTs NM-400 | Cytochrome C | 4 min | Tris-HCl (pH 7.5) | 10 µg/mL | DA/min (different absorbance during time) | Induction of significant increase of ROS levels | 145 |
| MWCNTs NM-401 | $DCFH_2$ | 90 min | PBS and phenol red-free MEM with 2% FCS | 1.6, 3.1, 6.25, 12.5 µg/ml | Slope: positive or negative | Negative. No ROS generation | 85 |

## 4.3 Physicochemical properties

Josje H.E. et al[39] evaluated the physicochemical properties of MWCNT NM-400, $CeO_2$ NM-211, NM-212, $TiO_2$ NM-105, ZnO NM-110, NM-111 and $SiO_2$ NM-200, concluding that their water solubility was below 20 mg/L in all cases, except for $SiO_2$ nanomaterial, which solubility was 67-115 mg/L. Regarding dissolution in biological media, ZnO nanomaterials presented significant solubility for Gamble (simulated lung fluid), ALF (artificial lysosomal fluid) and PSF (phagolysosomal simulant fluid). In addition, relevant impurities were found for MWCNT NM-400, expressed in mg/kg: 42192 for Al, 1911 for Co and 3455 for Fe. ZnO NM-111 characterization confirmed the coating information provided by the supplier, based on triethoxy-caprylylsilane. The cerium cations at ceria nanomaterials are redox-active, as confirmed by surface chemical states (XPS): 14 % cerium in ceria NM-212 is Ce(III), whereas the fraction increases to 22 % for the ceria NM-211.[47]

## 4.4 *In vitro* toxicological data

Table 5 summarizes the reported toxicological data for the nanomaterials evaluated in this work.

**$TiO_2$ NM-101** was evaluated across various cell lines, including A549, HK-2, HepG2, C3A, HUVEC, BEAS-2B and RAW 264.7 macrophages, over an exposure of 24 h, resulting in no detrimental effects up to a concentration of 100 µg/mL, with the exception of IL-8 secretion in C3A cells, genotoxic oxidative damage in BEAS-2B, and the release of IL-6/TNF-alpha in RAW 264.7 macrophages.[146,118,122,147] $TiO_2$ NM-101 uptake in bronchial epithelial cells (BEAS-B2) was observed by TEM imaging with particles >200 nm, but this uptake was not reflected in significant adverse effects.[148] **$TiO_2$ NM-105** was described as a high potency cytotoxic nanomaterial after exposure for RLE-6TN alveolar epithelial cells after 24 and 48 h (EC50 = 7 µg/cm$^2$).[149] In addition, genotoxicity of $TiO_2$ NM-105 in different cell lines was summarized in Lamon et al[150], classifying this nano-$TiO_2$ as genotoxic, contrary to $TiO_2$ NM-101. Completely different trends are obtained from other toxicity evaluations: $TiO_2$ NM-105 did not reach cytotoxic concentrations up to 100

µg/mL, as reported by Landsiedel et al[151], in A549, HepG2, THP-1, Caco-2 or HT29-MTX, assessed by MTT,[152,153,154] but high cytotoxicity was reported for NRK-52E cells exposed to $TiO_2$ NM-105.[78]

Reports on the toxicity of $CeO_2$ nanomaterials cite ROS formation as the main mechanism to produce cell damage.[155] The toxic mechanism of **$CeO_2$ NM-211** remains unclear, but protein aggregation and fibrillation are proposed hypotheses.[156,157] *In vitro*, A549 cells exposed to similar cerium oxide nanoparticles at concentrations up to 100 µg/mL showed no cytotoxicity.[158] In contrast, NR8383 alveolar macrophages exhibited cytotoxicity at 90 µg/mL along with signs of inflammation, including TNF-α release, after $CeO_2$ NM-211 exposure, but $H_2O_2$/ROS were not detected.[159] In experiments involving H4IIE and RTG-2 cell lines, two distinct trends were observed: the cellular viability of H4IIE cells was significantly compromised after 24 h exposure to a concentration of 6.25 µg/mL, whereas the RTG-2 cells exhibited no adverse effects at any concentration up to 100 µg/mL.[160] $CeO_2$ NM-211 induced moderate pro-inflammatory cytokine release in rat precision-cut lung slices at 100 µg/mL.[87] **$CeO_2$ NM-212** has been evaluated with several cell lines: A549, PMA-treated THP-1, H4IIE, and NR8383. The results indicated that A549 and dTHP-1 cells remained unaffected at concentrations up to 22 µg/cm² and 100 µg/mL, respectively.[161,162] In contrast, the H4IIE cell line exhibited sensitivity at a lower concentration of 0.78 µg/mL after 24 hours, indicating greater cytotoxicity compared to $CeO_2$ NM-211.[160] Furthermore, in the NR8383 cell line, LDH release was observed, indicating cytotoxicity at a concentration of 90 µg/mL.[159]

**ZnO NM-110**, extensively studied *in vitro*, exhibits adverse effects in multiple cell lines, with immune system alterations observed in Raw 264.7 and MH-S macrophages (EC50: 10-25 µg/mL), pulmonary cell lines displaying cytotoxic and genotoxic effects (LC50: 76 µg/mL),[163,164] and respiratory and male reproductive cell lines affected (EC50 < 20 µg/mL).[88] Hepatic damage in C3A was evidenced by WST-1 test.[118] Proteomic analysis in NRK-52E reveals pronounced effects, particularly in actin carbonylation; this NM is classified as highly cytotoxic and a protein carbonylation agent.[78] Caco-2 cell lines exhibit cytotoxicity due to dissolved $Zn^{2+}$, and HUVEC cell lines show reduced mitochondrial viability attributed to intracellular Zn ions and ROS.[165,122] Immune response after ZnO NM-110 inhalation was evaluated with PMA-differentiated THP-1 macrophages-like

exposure after 24 h. Zinc oxide produced a proinflammatory response by IL-8 and TNF-α release, and this NM was classified as cytotoxic at 50 μg/mL, concentration at which a significant decrease of cell viability was observed. Contrary to $SiO_2$ NM-200, NM-110 was not internalized, probably due to $Zn^{2+}$ release under endosomal acidic pH.[166] ZnO NM-110 (uncoated) and **NM-111** (coated) were classified as high toxic for testicular cells TM3 Leydig and TM4 Sertoli, with EC50 values around 10 μg/mL, while complete inhibition of cell viability was induced at 25 μg/mL for uncoated NM-110 and 12.5 μg/mL for coated NM-111.[88] A proteomic analysis of ZnO NM-110 and NM-111 behavior suggested protein carbonylation as main toxic mechanism for NRK-52E cells.[78] Both ZnO ENMs expressed significant ROS formation after 4 h exposure to HK-2 cells at 1.5 $\mu g/cm^2$,[121] and presented PCLuS tissue destruction at 10-1000 μg/mL after 24 h exposure. However, $TiO_2$ NM-101, $CeO_2$ NM-211, $CeO_2$ NM-212 and MWCNT NM-401 exhibited cytotoxicity in WST-1 assay at concentrations not causing tissue destruction in PCLuS.[167]

**Silica NM-200** was classified as non-embryo-toxic[168,88] and as a safe food additive for the gastrointestinal system: no toxic concentration was reached up to 1.25 mg/L for human lymphocytes and balb/3T3 mouse fibroblasts, and no DNA damage was produced, as tested by chromosome aberration assay in V79 cells. Gastrointestinal toxicity was also evaluated by Caco-2 cells exposure to 0.98-125 μg/mL for 24 h: no adverse effects were produced in terms of cell viability or IL-8 release, compared to control. Similar data was obtained from HePG2/C3A cell viability after 24 h exposure: relevant concentration for a significant cell viability decrease was not reached up to 96 μg/mL. However, at 48 μg/mL, a significant increase of IL-8 release was detected by real time PCR and ELISA after 24 h.[169] The PMA-differentiated THP-1 macrophage-like response to $SiO_2$ NM-200 is summarized in IL-8 release (marker of neutrophils activation), growth factors (VEGF and IGF-1) production, and generation of superoxide radicals in a non-dose-dependent manner. In terms of cell viability, at 50 μg/mL exposure, a significant decrease is produced after 24 h, when compared to untreated cells by MTS assay. Furthermore, internalization occurs as TEM imaging confirms, so cytotoxic effects caused by direct contact and uptake are expected.[166] In contrast, HMDM (Human Monocyte-Derived Macrophages) cell viability assessed by LDH release after 24 h unravel a significant decrease at 50 μg/mL.[88] Genotoxicity of silica NM-200 in bronchial epithelial

cell line as BEAS-2B was tested by micronucleus assay: no significant of micronucleus detected for 24 and 48 h at 1, 2.5 and 5 µg/mL.[148] Calu-3 bronchial cells were tested after 24 h exposure, and EC50 values were not reached up to 100 µg/mL.[88] *In vitro* data for **$SiO_2$ NM-201** is missed.

**$Fe_2O_3$** has been exposed to A549 and BEAS-2B cells to determine its toxicity. *In vitro* data suggested no high pulmonary toxicity for that NM: cell viability, ATP levels, mitochondrial activity and intracellular ROS generation were not relevant in terms of significance ($p<0.05$).[170] However, internalization in BEAS-2B and A549 was observed by TEM.[170]

**Carbon black** cell toxicity is difficult to evaluate by colorimetric assays due to indicators interaction with printex 90 nanoparticles. To solve this problem, clonogenic assays have been performed in A549, BEAS-2B and HaCaT, concluding that carbon black is highly effective to inhibit cell proliferation in all three cell lines after 7-10 days exposure.[171]

**CuO-SA** is highly toxic to pulmonary cells, causing cell death and impairing cell functions after 24-hour exposure.[128] The mechanism involves ion release, autophagy activation, and increased lipid peroxidation.[172,62,173] Animal models support its lung inflammatory effects but do not show teratogenic potential.[45] This ENM, the most oxidant in the series, exhibits significant effects on A549 cell viability at 5, 10 and 17.75 µg/mL.[172]

**Table 5**. *In vitro* toxicity data reported in the literature for the ENMs of the study. Results summarized as concentration at which an ENM induces effects significantly different to control, as quantified by "p" value ($p<0.05$, 0.01 or 0.001) or the half-maximal effective concentration (EC50).

| NM | Cell line | Test | Parameter | Time (h) | Report or concentration | Ref. |
|---|---|---|---|---|---|---|
| $TiO_2$ NM-101 (JRCNM1001a) | BEAS-2B | Micronucleus | $p<0.05$ | 24 | Not reached up to 25 µg/mL | [148] |
| | BEAS-2B | Micronucleus | $p<0.05$ | 48 | Not reached up to 25 µg/mL | [148] |
| | A549 | Alamar blue | $p<0.05$ | 24 | Not reached up to 100 | [163] |
| | A549 | WST-1 | $EC_{50}$ | 24 | Not reached up to 80 µg/cm$^2$ | [146] |
| | HepG2 | WST-1 | $EC_{50}$ | 24 | Not reached up to 80 µg/cm$^2$ | [146] |
| | HK-2 | WST-1 | $EC_{50}$ | 24 | Not reached up to 80 µg/cm$^2$ | [146] |
| | C3A | WST-1 | $EC_{50}$ | 24 | Not reached up to 80 µg/cm$^2$ | [118] |
| | C3A | IL-8 | $p<0.05$ | 24 | 20 µg/cm$^2$ | [118] |
| | HUVEC | IL-6 | $p<0.05$ | 24 | Not reached up to 32 µg/mL | [122] |
| | HUVEC | TNF-α | $p<0.05$ | 24 | Not reached up to 32 µg/mL | [122] |
| | HUVEC | WST-1 | $p<0.05$ | 24 | Not reached up to 32 µg/mL | [122] |
| | HUVEC | NRU | $p<0.05$ | 24 | Not reached up to 32 µg/mL | [122] |
| | BEAS-2B | Trypan blue | $p<0.05$ | 24 | Not reached up to 100 µg/mL | [147] |
| | BEAS-2B | Fpg-Comet assay | $p<0.05$ | 24 | 10 µg/mL Direct damage | [147] |
| | BEAS-2B | Fpg-Comet assay | $p<0.05$ | 24 | 100 µg/mL Oxidative damage | [147] |
| | BEAS-2B | Micronucleous assay | $p<0.001$ | 24 | Not reached up to 100 µg/mL | [147] |
| | BEAS-2B | IL-6 | $p<0.05$ | 24 | 100 µg/mL | [147] |
| | BEAS-2B | IL-8 | $p<0.05$ | 24 | Not reached up to 100 µg/mL | [147] |
| | BEAS-2B | TNF-α | $p<0.05$ | 24 | Not reached up to 100 µg/mL | [147] |
| | RAW 264.7 macrophages | MTS | $p<0.05$ | 24 | Not reached up to 100 µg/mL | [147] |
| | RAW 264.7 macrophages | IL-6 | $p<0.05$ | 18 | 10 µg/mL | [147] |
| | RAW 264.7 macrophages | TNF-α | $p<0.05$ | 18 | 100 µg/mL | [147] |

| | | | | | | |
|---|---|---|---|---|---|---|
| $TiO_2$ NM-105 (JRCNM1005) | RLE-6TN | WST-1 | EC50 | 24 | 7 µg/cm$^2$ | [149] |
| | RLE-6TN | WST-1 | EC50 | 48 | 7 µg/cm$^2$ | [149] |
| | Caco-2 | MTT | p<0.05 | 24 | Not reached up to 14.30 µg/mL | [152] |
| | HT29-MTX | MTT | p<0.05 | 24 | Not reached up to 14.30 µg/mL | [152] |
| | Caco-2 | MTT | p<0.05 | 6 | Not reached up to 200 µg/mL | [153] |
| | HT29-MTX | MTT | p<0.05 | 6 | Not reached up to 200 µg/mL | [153] |
| | Caco-2 | MTT | p<0.05 | 48 | Not reached up to 200 µg/mL | [153] |
| | HT29-MTX | MTT | p<0.05 | 48 | Not reached up to 200 µg/mL | [153] |
| | HepG2 | MTT | p<0.05 | 24 | Not reached up to 100 µg/mL | [154] |
| | HepG2 | MTT | p<0.05 | 48 | Not reached up to 100 µg/mL | [154] |
| | HepG2 | MTT | p<0.05 | 72 | Not reached up to 100 µg/mL | [154] |
| | A549 | MTT | p<0.05 | 24 | Not reached up to 100 µg/mL | [154] |
| | A549 | MTT | p<0.05 | 48 | Not reached up to 100 µg/mL | [154] |
| | A549 | MTT | p<0.05 | 72 | Not reached up to 100 µg/mL | [154] |
| | THP-1 | MTT | p<0.05 | 24 | Not reached up to 100 µg/mL | [154] |
| | THP-1 | MTT | p<0.05 | 48 | Not reached up to 100 µg/mL | [154] |
| | THP-1 | MTT | p<0.05 | 72 | Not reached up to 100 µg/mL | [154] |
| | NR8383 | LDH | p < 0.05 | 24 | 90 µg/mL | [159] |
| | NR8383 | GLU | p < 0.05 | 24 | 90 µg/mL | [159] |
| | NR8383 | TNF-α | p < 0.05 | 24 | 90 µg/mL | [159] |
| | NR8383 | Intracellular ROS/H2O2 | p < 0.05 | 24 | Not reached up to 180 µg/mL | [159] |
| | A549 | LDH | p < 0.05 | 80 | Not reached up to 100 µg/mL | [162] |
| $CeO_2$ NM-211 (JRCNM02101a) | NR8383 | LDH | p<0.05 | 16 | 90 | [159] |
| | NR8383 | GLU | p<0.05 | 16 | 180 | [159] |
| | NR8383 | TNF-α | p<0.05 | 16 | 22.5 | [159] |
| | NR8383 | Extracellular $H_2O_2$/ROS | p<0.05 | 1.5 | Not reached up to 180 µg/mL | [159] |

| | | | | | | |
|---|---|---|---|---|---|---|
| | H4IIE | MTT | $p<0.05$ | 24 | 6.25 µg/mL | [160] |
| | H4IIE | MTT | $p<0.05$ | 72 | 0.098 µg/mL | [160] |
| | H4IIE | NRU | $p<0.05$ | 24 | Not reached up to 100 µg/mL | [160] |
| | H4IIE | NRU | $p<0.05$ | 72 | Not reached up to 100 µg/mL | [160] |
| | H4IIE | LDH | $p<0.05$ | 24 | Not reached up to 100 µg/mL | [160] |
| | H4IIE | LDH | $p<0.05$ | 72 | 100 | [160] |
| | RTG-2 | NRU and MTT | $p<0.05$ | 24 | Not reached up to 100 µg/mL | [160] |
| | RTG-2 | NRU and MTT | $p<0.05$ | 72 | Not reached up to 100 µg/mL | [160] |
| $CeO_2$ NM-212 (JRCNM02102a) | A549 | LDH | $p < 0.001$ | 24 | Not reached up to 22 µg/cm$^2$ | [161] |
| | A549 | Alamar blue | $p < 0.001$ | 24 | Not reached up to 22 µg/cm$^2$ | [161] |
| | PMA treated THP-1 | LDH | $p < 0.001$ | 24 | Not reached up to 22 µg/cm$^2$ | [161] |
| | PMA treated THP-1 | Alamar blue | $p < 0.001$ | 24 | Not reached up to 22 µg/cm$^2$ | [161] |
| | A549 | Cytokines release | $p < 0.001$ | 24 | Not reached up to 22 µg/cm$^2$ | [161] |
| | PMA treated THP-1 | Cytokines release | $p < 0.001$ | 24 | Not reached up to 22 µg/cm$^2$ | [161] |
| | H4IIE | MTT | $p < 0.05$ | 24 | 0.78 µg/mL | [160] |
| | H4IIE | MTT | $p < 0.05$ | 72 | 0.024 µg/mL | [160] |
| | H4IIE | NRU | $p < 0.05$ | 24 | Not reached up to 10 µg/mL | [160] |
| | H4IIE | MTT | $p < 0.05$ | 72 | 50 µg/mL | [160] |
| | NR8383 | LDH | $p < 0.05$ | 24 | 90 µg/mL | [159] |
| | NR8383 | GLU | $p < 0.05$ | 24 | 180 µg/mL | [159] |
| | NR8383 | TNF-α | $p < 0.05$ | 24 | 22.5 µg/mL | [159] |
| | NR8383 | Intracellular ROS/$H_2O_2$ | $p < 0.05$ | 24 | Not reached up to 180 µg/mL | [159] |
| | A549 | LDH | $p < 0.05$ | 80 | Not reached up to 100 µg/mL | [162] |
| ZnO NM-110 (JRCNM62101a) | PMA-treated THP-1 | MTS | $p<0.001$ | 24 | 50 µg/mL | [166] |
| | TM4 | WST-1 | $p<0.001$ | 24 | 12.5 µg/mL | [88] |
| | Calu-3 | Resazurin | $p<0.05$ | 24 | 128 µg/mL | [88] |

| | | | | | | |
|---|---|---|---|---|---|---|
| | Calu-3 | NRU | $p<0.05$ | 24 | 128 µg/mL | [88] |
| | HMDM | LDH | $p<0.001$ | 24 | 25 µg/mL | [88] |
| | TM4 | WST-1 | $p<0.001$ | 24 | 25 µg/mL | [88] |
| | TM3-TM4 | WST-1 | EC50 | 24 | 10 µg/mL | [88] |
| | RAW 264.7 | Resazurin | $EC_{50}$ | 24 - 72 | 12.16-14.72 | [88] |
| | RAW 264.7 | NRU | $EC_{50}$ | 24 - 72 | 18.40-25.48 | [88] |
| | MH-S | Resazurin | $EC_{50}$ | 24 - 72 | 22.08-17.92 | [88] |
| | MH-S | NRU | $EC_{50}$ | 24 - 72 | 19.68-23.04 | [88] |
| | TM3 | WST-1 | $EC_{50}$ | 24 | 10.06 | [88] |
| | TM4 | WST-1 | $EC_{50}$ | 24 | 11.88 | [88] |
| | 16HBE | WST-8 | $EC_{50}$ | 24 | 17.79 | [88] |
| | HUVEC | WST-1 | $p<0.001$ | 24 | 32 | [122] |
| | HUVEC | NRU | $p<0.001$ | 24 | 32 | [122] |
| | A549 | Resazurin | $EC_{50}$ | 24 | 76 | [163,164] |
| | A549 | Resazurin | $p<0.05$ | 24 | 48 | [163,164] |
| | A549 | Resazurin | $EC_{50}$ | 3 | 215 | [163,164] |
| | A549 | Resazurin | $p<0.05$ | 3 | 120 | [163,164] |
| | TK6 | Comet assay, DNA damage | Saturation, high damage | 3 | 14 | [164] |
| | TK6 | Comet assay, DNA damage | Saturation, high damage | 24 | 14 | [164] |
| | A549 | Comet assay, DNA damage | $p<0.0001$ | 3 | 14 | [164] |
| | Caco-2 | MTT | $EC_{50}$ | 24 | 25 | [165] |
| | Caco-2 | WST-1 | $EC_{50}$ | 24 | 28 | [165] |
| | PMA treated THP-1 | WST-1 | $EC_{50}$ | 24 | 8.5 | [174] |
| | PMA treated THP-1 | LDH | $EC_{50}$ | 24 | 6.4 | [174] |
| | PMA treated THP-1 | Resazurin | $EC_{50}$ | 24 | 9.5 | [174] |

| | | | | | | |
|---|---|---|---|---|---|---|
| | C3A | WST-1 | $EC_{50}$ | 24 | 5-10 µg/cm$^2$ | [118] |
| | C3A | Resazurin | $EC_{50}$ | 24 | ca.10 µg/cm$^2$ | [118] |
| | C3A | IL-8 | $p<0.05$ | 24 | 0.31 µg/cm$^2$ | [118] |
| | A549 | Alamar blue | $p < 0.05$ | 3 | 75 µg/cm$^2$ | [175] |
| | A549 | Alamar blue | $p < 0.05$ | 24 | 75 µg/cm$^2$ | [175] |
| | A549 | Alamar blue | EC50 | 3 | 166 µg/mL | [175] |
| | A549 | Alamar blue | EC50 | 24 | 53 µg/mL | [175] |
| | HK-2 | WST-1 | EC50 | 24 | 1 µg/cm$^2$ | [121] |
| | HK-2 | Oxidative stress | $p < 0.05$ | 4 | 1.5 µg/cm$^2$ | [121] |
| | NRK-52E | WST-1 | EC50 | 24 | 12.5 µg/mL | [78] |
| ZnO NM-111 | Calu-3 | Resazurin | $p<0.05$ | 24 | 32 µg/mL | [88] |
| | Calu-3 | NRU | $p<0.05$ | 24 | 128 µg/mL | [88] |
| | HMDM | LDH | $p<0.001$ | 24 | 25 µg/mL | [88] |
| | TM4 | WST-1 | $p<0.001$ | 24 | 12.5 µg/mL | [88] |
| | TM3-TM4 | WST-1 | EC50 | 24 | 10 µg/mL | [88] |
| | NR8383 | LDH | $p < 0.05$ | 24 | 5.6 µg/mL | [159] |
| | NR8383 | GLU | $p < 0.05$ | 24 | 11.3 µg/mL | [159] |
| | NR8383 | TNF-α | $p < 0.05$ | 24 | 22.5 µg/mL | [159] |
| | NR8383 | Intracellular ROS/H2O2 | $p < 0.05$ | 24 | Not reached up to 180 µg/mL | [159] |
| | A549 | Alamar blue | $p < 0.05$ | 3 | 75 µg/cm$^2$ | [175] |
| | A549 | Alamar blue | $p < 0.05$ | 24 | 30 µg/cm$^2$ | [175] |
| | A549 | Alamar blue | EC50 | 3 | 87 µg/mL | [175] |
| | A549 | Alamar blue | EC50 | 24 | 37 µg/mL | [175] |
| | HK-2 | WST-1 | EC50 | 24 | 0.9 µg/cm$^2$ | [121] |
| | HK-2 | Oxidative stress | $p < 0.05$ | 4 | 1.5 µg/cm$^2$ | [121] |
| | NRK-52E | WST-1 | EC50 | 24 | 20 µg/mL | [78] |

| | | | | | | |
|---|---|---|---|---|---|---|
| $SiO_2$ NM-200 | PMA-treated THP-1 | MTS | p<0.001 | 24 | 50 µg/mL | [166] |
| | BEAS-2B | Micronucleus | p<0.05 | 24 | Not reached up to 5 µg/mL | [148] |
| | BEAS-2B | Micronucleus | p<0.05 | 48 | Not reached up to 5 µg/mL | [148] |
| | Caco-2 | Alamar blue | p<0.05 | 24 | Not reached up to 125 µg/mL | [169] |
| | Caco-2 | IL-8 | p<0.05 | 24 | Not reached up to 48 µg/mL | [169] |
| | HepG2/C3A | Alamar blue | p<0.05 | 24 | Not reached up to 96 µg/mL | [169] |
| | HepG2/C3A | IL-8 | p<0.05 | 24 | Not reached up to 48 µg/mL | [169] |
| | HMDM | LDH | p<0.001 | 24 | 50 µg/mL | [88] |
| | TM3 | WST-1 | p<0.001 | 24 | Not reached up to 200 µg/mL | [88] |
| | TM4 | WST-1 | p<0.001 | 24 | 200 µg/mL | [88] |
| | Calu-3 | Resazurin | EC50 | 24 | Not reached up to 100 µg/mL | [88] |
| | Calu-3 | NRU | EC50 | 24 | Not reached up to 100 µg/mL | [88] |
| | NR8383 | LDH | p < 0.05 | 24 | 22.5 µg/mL | [159] |
| | NR8383 | GLU | p < 0.05 | 24 | 22.5 µg/mL | [159] |
| | NR8383 | TNF-α | p < 0.05 | 24 | 22.5 µg/mL | [159] |
| | NR8383 | Intracellular ROS/H2O2 | p < 0.05 | 24 | Not reached up to 180 µg/mL | [159] |
| $SiO_2$ NM-201 | A549 | Micronuclei | Positive/negative | - | Positive | [176] |
| | A549 | Comet assay | Positive/negative | 3 | Positive | [176] |
| | A549 | Micronuclei | Positive/negative | 4 | Positive | [176] |
| | 16HBE | Micronuclei | Positive/negative | - | Positive | [176] |
| $Fe_2O_3$ | BEAS-2B | Internalization | Positive/negative | 24 | Positive at 5 µg/mL | [170] |
| | A549 | Internalization | Positive/negative | 24 | Positive at 5 µg/mL | [170] |
| | BEAS-2B | MTT | p < 0.05 | 24 | Not reached up to 200 µg/mL | [170] |
| | A549 | MTT | p < 0.05 | 24 | Not reached up to 200 µg/mL | [170] |
| | BEAS-2B | ROS generation | p < 0.05 | 24 | Not reached up to 200 µg/mL | [170] |
| | A549 | ROS generation | p < 0.05 | 24 | Not reached up to 200 µg/mL | [170] |
| | A549 | MTT | p<0.001 | 3 | 10 | [172] |

| | | | | | | |
|---|---|---|---|---|---|---|
| CuO #544848 Sigma Aldrich | A549 | MTT | p<0.001 | 24 | 5 | [172] |
| | A549 | NRU | p<0.001 | 3 | 50 | [172] |
| | A549 | NRU | p<0.001 | 24 | 10 | [172] |
| | A549 | IL-8 release | p<0.001 | 3 | 100 | [172] |
| | A549 | IL-8 release | p<0.001 | 24 | 10 | [172] |
| | A549 | MTT | $EC_{50}$ | 24 | 17.75 | [172] |
| | A549 | CFA | p<0.001 | 24 | 10 | [62] |
| | HeLa S3 | CFA | p<0.001 | 24 | 10 | [62] |
| | A549 | MTT | p<0.05 | 6 | 100 | [45] |
| | A549 | MTT | p<0.05 | 24 | 10 | [45] |
| | A549 | MTT | p<0.05 | 1 | 25 | [128] |
| | A549 | MTT | p<0.05 | 3 | 25 | [128] |
| Carbon blak printex 90 | A549 | Clonogenic assay | p<0.05 Colony number | 240 (10 days) | 400 | [171] |
| | A549 | Clonogenic assay | p<0.05 Colony size | 240 (10 days) | 1.56 | [171] |
| | A549 | Clonogenic assay | EC50 Colony number | 240 (10 days) | Not reached up to 400 | [171] |
| | A549 | Clonogenic assay | Ec50 Colony size | 240 (10 days) | 20.63 | [171] |
| | BEAS-2B | Clonogenic assay | p<0.05 Colony number | 240 (10 days) | 1.56 | [171] |
| | BEAS-2B | Clonogenic assay | EC50 Colony number | 240 (10 days) | 14.66 | [171] |
| | HaCaT | Clonogenic assay | p<0.05 Colony number | 240 (10 days) | 25 | [171] |
| | HaCaT | Clonogenic assay | p<0.05 Colony size | 240 (10 days) | 25 | [171] |
| | HaCaT | Clonogenic assay | EC50 Colony number | 240 (10 days) | 180.90 | [171] |

| | | | | | | |
|---|---|---|---|---|---|---|
| | HaCaT | Clonogenic assay | Ec50<br>Colony size | 240<br>(10 days) | 78.78 | [171] |
| | A459 | NucleCounter | $p<0.05$ | 6 | Not reached up to 160 | [177] |
| | A459 | NucleCounter | $p<0.05$ | 24 | Not reached up to 160 | [177] |
| | PMA treated THP-1 | NucleCounter | $p<0.05$ | 6 | Not reached up to 80 | [177] |
| | PMA treated THP-1 | NucleCounter | $p<0.05$ | 24 | Not reached up to 80 | [177] |
| | A459 | IL-8 release | $p<0.05$ | 6 | Not reached up to 160 | [177] |
| | A459 | IL-8 release | $p<0.05$ | 24 | Not reached up to 160 | [177] |
| | PMA treated THP-1 | IL-8 release | $p<0.05$ | 6 | Not reached up to 80 | [177] |
| | PMA treated THP-1 | IL-8 release | $p<0.05$ | 24 | Not reached up to 80 | [177] |
| | PMA treated THP-1 | DNA tail (%) | $p<0.05$ | 24 | 80 | [177] |
| | A549 | DNA tail (%) | $p<0.05$ | 24 | Not reached up to 160 | [177] |
| | A549 | WST-8 | $p<0.05$ | 24 | Not reached up to 50 | [178] |
| | A549 | IL-8 release | $p<0.05$ | 24 | 50 | [178] |
| | A549 | ROS generation | $p<0.05$ | 24 | 50 | [178] |
| | Calu-3 | WST-8 | $p<0.05$ | 24 | Not reached up to 50 | [178] |
| | Calu-3 | IL-8 release | $p<0.05$ | 24 | Not reached up to 50 | [178] |
| | Calu-3 | IL-6 release | $p<0.05$ | 24 | Not reached up to 50 | [178] |
| MWCNT NM-400 | A549 | MTT | $p<0.05$ | 24 | 100 | [145] |
| | A549 | Trypan Blue | $p<0.05$ | 24 | 100 | [145] |
| | A549 | LDH | $p<0.05$ | 24 | 100 | [145] |
| | A549 | IL-8 release | $p<0.05$ | 24 | Not reached up to 100 | [145] |
| | A549 | Uptake (TEM) | - | 24 | Located in cytoplasm as agglomerates in vesicles | [145] |
| | A549 | $H_2$DCFDA | $p<0.05$ | 2 | 100 | [145] |
| | A459 | NucleCounter | $p<0.05$ | 6 | Not reached up to 160 | [177] |
| | A459 | NucleCounter | $p<0.05$ | 24 | Not reached up to 160 | [177] |
| | PMA treated THP-1 | NucleCounter | $p<0.05$ | 6 | Not reached up to 80 | [177] |

| | | | | | | |
|---|---|---|---|---|---|---|
| | PMA treated THP-1 | NucleCounter | p<0.05 | 24 | Not reached up to 80 | [177] |
| | A459 | IL-8 release | p<0.05 | 6 | Not reached up to 160 | [177] |
| | A459 | IL-8 release | p<0.05 | 24 | Not reached up to 160 | [177] |
| | PMA treated THP-1 | IL-8 release | p<0.05 | 6 | Not reached up to 80 | [177] |
| | PMA treated THP-1 | IL-8 release | p<0.05 | 24 | 80 | [177] |
| | PMA treated THP-1 | DNA tail (%) | p<0.05 | 24 | Not reached up to 80 | [177] |
| | A549 | DNA tail (%) | p<0.05 | 24 | 160 | [177] |
| MWCNT NM-401 | A459 | NucleCounter | p<0.05 | 6 | Not reached up to 160 | [177] |
| | A459 | NucleCounter | p<0.05 | 24 | Not reached up to 160 | [177] |
| | PMA treated THP-1 | NucleCounter | p<0.05 | 6 | Not reached up to 80 | [177] |
| | PMA treated THP-1 | NucleCounter | p<0.05 | 24 | Not reached up to 80 | [177] |
| | A459 | IL-8 release | p<0.05 | 6 | 160 | [177] |
| | A459 | IL-8 release | p<0.05 | 24 | 40 | [177] |
| | PMA treated THP-1 | IL-8 release | p<0.05 | 6 | 80 | [177] |
| | PMA treated THP-1 | IL-8 release | p<0.05 | 24 | 40 | [177] |
| | PMA treated THP-1 | DNA tail (%) | p<0.05 | 24 | 80 | [177] |
| | A549 | DNA tail (%) | p<0.05 | 24 | Not reached up to 160 | [177] |

[1] *Cell lines: A549 (adenocarcinomic human alveolar basal epithelial cells), HeLa S3 (Human cervix carcinoma cell line), Raw 264.7 (semi-adherent macrophage-like cell line derived from BALB/c mice), MH-S(murine alveolar macrophages), TM3 and TM4 (proliferating mouse Leydig cell line), 16HBE (human bronchial epithelial cell line), HUVEC (Human Umbilical Vein Endothelial Cells), TK6 (Human lymphoblastoid, In vitro mammalian cells), Caco-2 (human colorectal adenocarcinoma cells), PMA treated THP-1 (human leukemia monocytic cell line differentiated into macrophage-like), C3A (human liver adherent cells), HepG2 (human liver cancer cell line), BEAS-B2 (immortalized but non-tumorigenic epithelial cell line from human bronchial epithelium), NR8383 (alveolar macrophages), H4IIE (rat hepatoma cell line), RTG-2a (fibroblast morphology cell line from rainbow trout ovary).*

[2] *Tests: MTT = (3-(4,5-dimethylthiazol-2-yl)-2,5-diphenyltetrazolium bromide, IL-8 = Interleukin 8 release, CFA = Colony Forming Ability, NRU = neutral red uptake, LDH = Lactate Dehydrogenase, GLU = β-glucuronidase, TNF-α = Tumor Necrosis Factor.*

## 4.5 *In vivo* toxicological data

*In vivo* toxicological data were collected from Loret et al.[179] The evaluations of biological responses were performed following a 24-hour exposure to three types of $TiO_2$ nanoparticles (NM-105, NM-101, NM-100) and one type of $CeO_2$ nanoparticle (NM-212), and the focus was on pro-inflammatory effects, specifically measuring neutrophil influx and the levels of pro-inflammatory mediators including IL-1β, IL-6, KC-GRO, and TNF-α in bronchoalveolar lavage fluid (BALF) collected from rats that had been exposed to these nanoparticles via intratracheal instillation (IT). The findings indicated significant pro-inflammatory effects with $TiO_2$ NM-105 and NM-101 as well as $CeO_2$ NM-212, while no significant effects were observed with $TiO_2$ NM-100. Following exposure to $TiO_2$ NM-105 and NM-101, a noteworthy increase in neutrophil influx in BALF supernatants was observed, accompanied by elevated concentrations of TNF-α for NM-105 and NM-101, and KC-GRO for NM-105, specifically. Additionally, the reports measured significant increases in the secretion of IL-1β, IL-6, and TNF-α with NM-212, although a significant neutrophil influx was not detected in this case. It's worth noting that the lack of a significant neutrophil influx with NM-212 may be attributed to high variability in the control sample.

In other *in vivo* studies, inflammatory markers increased in BALF after 14 days of $CeO_2$ NM-211 exposure.[180] However, non-significant genotoxicity and toxicity of $SiO_2$ NM-201 were obtained in *in vivo* experiments with Male Sprague Dawley rats, for concentrations from 0 to 20 mg/kg body weight per day.[181] Regarding inhalation of $TiO_2$ NM-105, this ENM generally exhibits a high propensity to induce inflammation and tumor formation, as observed in experiments in BALF exposure and *in vivo* responses in rat lung tissues obtained from *in vivo* instillation and short-term inhalation studies (STIS).[182,183] In addition, a study of Landsiedel et al.[47] comparatively analyzed the inhalation effects of ceria NM-211 and NM-212, over five days in BALF. NM-211 showed a higher biological impact than NM-212, evidenced by increased lymphocytes and cell mediators in BALF, along with elevated lung weights. Differences in lung overload and clearance rates between the two nanomaterials were noted, though the exact mechanisms remain unclear.

Lastly, a standard short-term inhalation study (STIS) was conducted to assess the hazards of ZnO NM-111. Rats were exposed to varying concentrations of aerosolized test materials, followed by a post-exposure analysis period of up to 21 days. Investigations included bronchoalveolar lavage fluid analysis and histopathological examination of the respiratory tract. No clinical signs of toxicity were noted; however, a significant decrease in body weight gain was observed in animal groups exposed to 2.5 and 12.5 mg/m$^3$. This effect was attributed to the systemic toxicity of released $Zn^{2+}$ ions. Hematological parameters, acute phase proteins, and cytokine levels in the blood remained unchanged in rats treated with various concentrations of ZnO. However, inhalation exposure to NM-111 led to pulmonary inflammation. This was evidenced by increased counts of PMN neutrophils, lymphocytes, and total cells in bronchoalveolar lavage fluid, with dose-dependent response.[184]

# Chapter V. Number and reactive nature of ENMs' surface sites

## 5.1 Methanol chemisorption and temperature-programmed surface reaction

Methanol is considered a "smart" probe molecule that can not only quantify the number of surface sites by chemisorption, but also provide information on their reactive profile by temperature-programmed surface reaction (TPSR),[54,185] a powerful technique to identify and quantify acidic, basic, redox, and bifunctional sites[56,55] on materials that are not thermally sensitive. The *type* and *amount* of products and the *temperature* at which they are detected correlate with the *nature*, *amount* and *reactivity* of the surface sites, respectively: oxidation of methoxy species to formaldehyde (HCHO) is indicative of redox sites (Eq. 6; dehydration of two adjacent methoxy to dimethyl ether ($CH_3OCH_3$), of acidic sites (Eq. 7); and formation of carbon dioxide ($CO_2$), of basic sites, which strongly bind methanol that is typically burnt and desorbed at high temperatures (Eq. 8); highly reactive redox sites will also produce $CO_2$ due to fast formaldehyde combustion (over-oxidation reaction), but at significantly lower temperature.[55] Bifunctional sites may be present at the surface of ENMs if two kind of reactive sites are in close vicinity, generating different products: methyl formate ($HCOOCH_3$) originates from basic-redox sites (Eq. 9) and dimethoxymethane ($(CH_3O)_2CH_2$) from acid-redox sites (Eq. 10). Water and CO are secondary products formed in several reactions and may not be correlated with a specific site. On occasions, less reactive sites release unreacted methoxy species as methanol, which typically occurs at low temperatures in the TPSR profile.

- Single sites:

Redox sites: $CH_3OH + \frac{1}{2}O_2 \rightarrow HCHO + H_2O$ (Eq. 6)

Acid sites: $2CH_3OH \leftrightarrow CH_3OCH_3 + H_2O$ (Eq. 7)

Basic or redox (over-oxidation) sites: $CH_3OH + \frac{3}{2}O_2 \rightarrow CO_2 + 2H_2O$ (Eq. 8)

- Bifunctional sites:

Basic-redox sites: $2CH_3OH + O_2 \leftrightarrow HCOOCH_3 + 2H_2O$ (Eq. 9)

Acid-redox sites: $3CH_3OH + \frac{1}{2}O_2 \rightarrow CH_2(OCH_3)_2 + 2H_2O$ (Eq. 10)

## 5.2 Results

### 5.2.1 Reactive sites number and surface density

In the series, $TiO_2$ NM-101 exhibits the largest BET area, 225 $m^2/g$; the rest of ENMs have significantly lower BET values: $TiO_2$-DT51, 84 $m^2/g$; $CeO_2$ NM-211, 76 $m^2/g$; CuO-SA, 12 $m^2/g$ and ZnO NM-110, 9 $m^2/g$ (Figure 11A). These measured data are similar to the values reported in the literature and technical data sheets from the supplier.[113,117,119,120,127] Figure 11B-C compares two more surface descriptors based on the number of active sites in the NM: the specific number of sites (mmol per g), and the surface site density (molecule per $nm^2$), calculated from Figure 11A-B data. The ENMs with the smallest surface area exhibit the largest active sites surface density: 22 and 42 sites/$nm^2$ for ZnO NM-110 and CuO-SA, respectively. Nevertheless, the variability of the latter parameter in the series indicates that surface area and reactive sites number are not linearly correlated due to differences in site types and/or distribution. It is remarkable that $TiO_2$-DT51, with 2.7 times lower specific surface area than $TiO_2$ NM-101, doubles its surface density of reactive sites (14 *vs*. 7 sites/$nm^2$). Therefore, BET (physical) is not an ideal descriptor of ENMs surface chemistry. Figure 11D summarizes the trends shown in Figure 11A-C, by data normalization to the most described nanomaterial in the literature: $TiO_2$ NM-101.

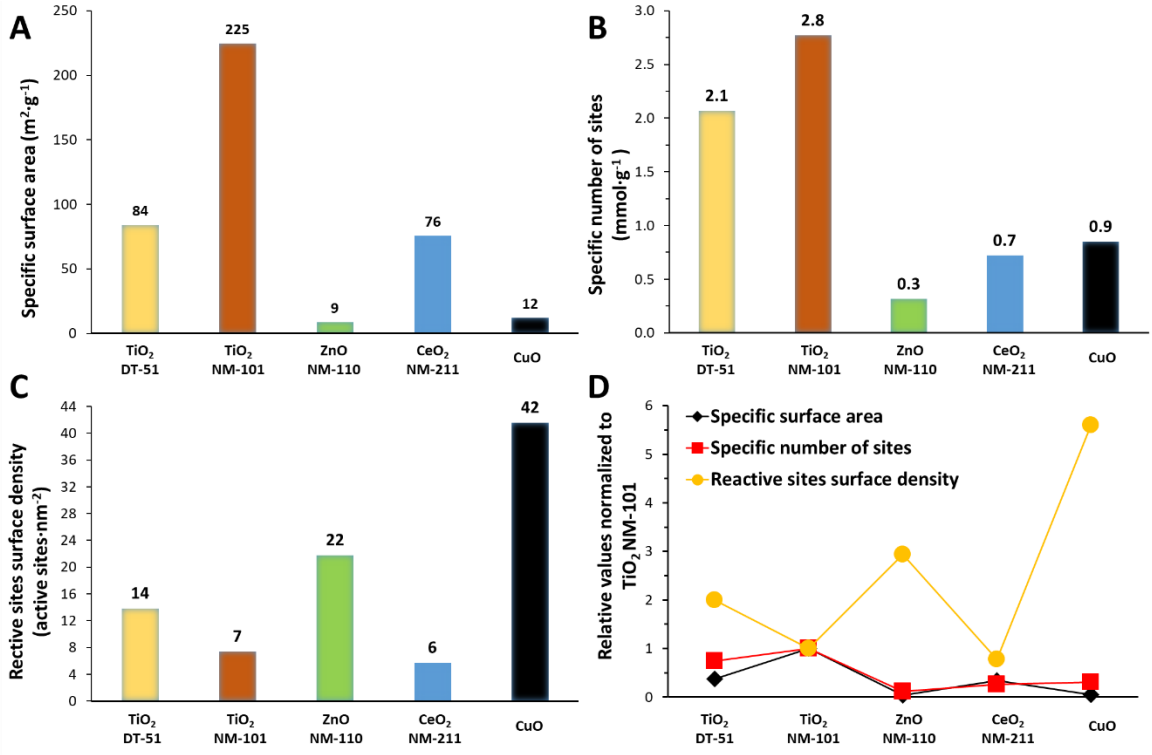


***Figure 11***. *Surface analysis: A) Specific surface area obtained by $N_2$ adsorption isotherm, B) Specific number of active sites obtained by methanol chemisorption, C) Active sites surface density obtained by combination of A and B, D) Comparison of the three surface descriptors (values normalized to $TiO_2$ NM-101).*

The surface descriptors of the evaluated ENMs are summarized in Table 6**,** showing that specific surface area does not directly correlate with the effective surface determined by methanol chemisorption capacity. The ENMs with larger specific surface area are carbon black, MWCNT NM-400 and $TiO_2$ NM-101. On the contrary, zinc oxides, manganese oxide and CuO exhibit lower values: 9 (NM-110), 15 (NM-111), 17 and 12 $m^2/g$, respectively. In terms of adsorption capacity per gram, $TiO_2$ NM-101 is the most efficient (2.8 mmol MeOH/g), followed by MWCNT NM-400, $TiO_2$ NM-105 and MWCNT NM-401, with values between 1.7-1.1 mmol/g. In contrast, zinc oxides, ceria, silica, CuO and $Mn_2O_3$ exhibit very few active sites. However, active sites surface density unravels that the NM with the most populated surface is CuO (≈ 42 sites·$nm^{-2}$), followed by ZnO NM-110, $Fe_2O_3$ and $TiO_2$ NM-105. Carbon black has the largest specific surface area of the series (317 $m^2/g$), but the number of sites could not be measured due to agglomeration leading to reactor clogging.

***Table 6.*** *Surface descriptors for the tested ENMs. Specific surface area was obtained by $N_2$ adsorption isotherms and specific number of sites by methanol chemisorption. The active sites surface density was calculated as their ratio.*

| Nanomaterial | Specific surface area ($m^2 \cdot g^{-1}$) | Specific number of sites ($mmol \cdot g^{-1}$) | Reactive sites surface density ($site \cdot nm^{-2}$) |
|---|---|---|---|
| $TiO_2$ DT-51 | 84 | 2.1 | 14.0 |
| $TiO_2$ NM-101 | 225 | 2.8 | 7.4 |
| $TiO_2$ NM-105 | 58 | 1.1 | 13.1 |
| ZnO NM-110 | 9 | 0.3 | 21.8 |
| ZnO NM-111 | 15 | 0.1 | 4.7 |
| $SiO_2$ NM-200 | 182 | 0.3 | 0.8 |
| $SiO_2$ NM-201 | 140 | 0.5 | 2.2 |
| $CeO_2$ NM-211 | 76 | 0.4 | 5.7 |
| $CeO_2$ NM-212 | 25 | 0.4 | 9.6 |
| MWCNT NM-400 | 240[a] | 1.7 | 4.1 |
| MWCNT NM-401 | 140[a] | 1.1 | 4.5 |
| CuO | 12 | 0.8 | 41.6 |
| Carbon black | 317 | NA | NA |
| $Fe_2O_3$ | 41 | 1.0 | 15.5 |
| $Mn_2O_3$ | 17 | 0.3 | 11.0 |

[a] Data obtained from supplier

### 5.2.2 Reactive profile

The intrinsic surface reactivity of the ENMs was tested by MeOH-TPSR to identify the nature of their surface active sites, resulting in their classification in three groups (Figure 12i): $TiO_2$ nanomaterials presented a main desorption band related to dimethyl ether formation (Figure 12a-b), i.e., to acidic reactivity, in line with other titania measured in the literature.[54] In addition, low signals of formaldehyde and carbon dioxide were registered, indicating the presence of some redox and basic sites. Ceria, however, mainly exhibited redox reactivity (Figure 12c-d); NM-211 showed a maximum of methanol conversion to formaldehyde at 259 ºC, whereas NM-212 formed formaldehyde at 207 ºC and 283ºC, reporting in two types of sites, one more (207 ºC) and one less (283 ºC) reactive than those of NM-211, with intermediate carbon dioxide generation around 265 ºC. In the case of ZnO, CuO, $Mn_2O_3$ and $Fe_2O_3$, carbon dioxide is the only reaction product, formed either as a consequence of surface basic reactivity or by methanol over-oxidation (Figure 12 e-h), as suggested in the literature.[55]

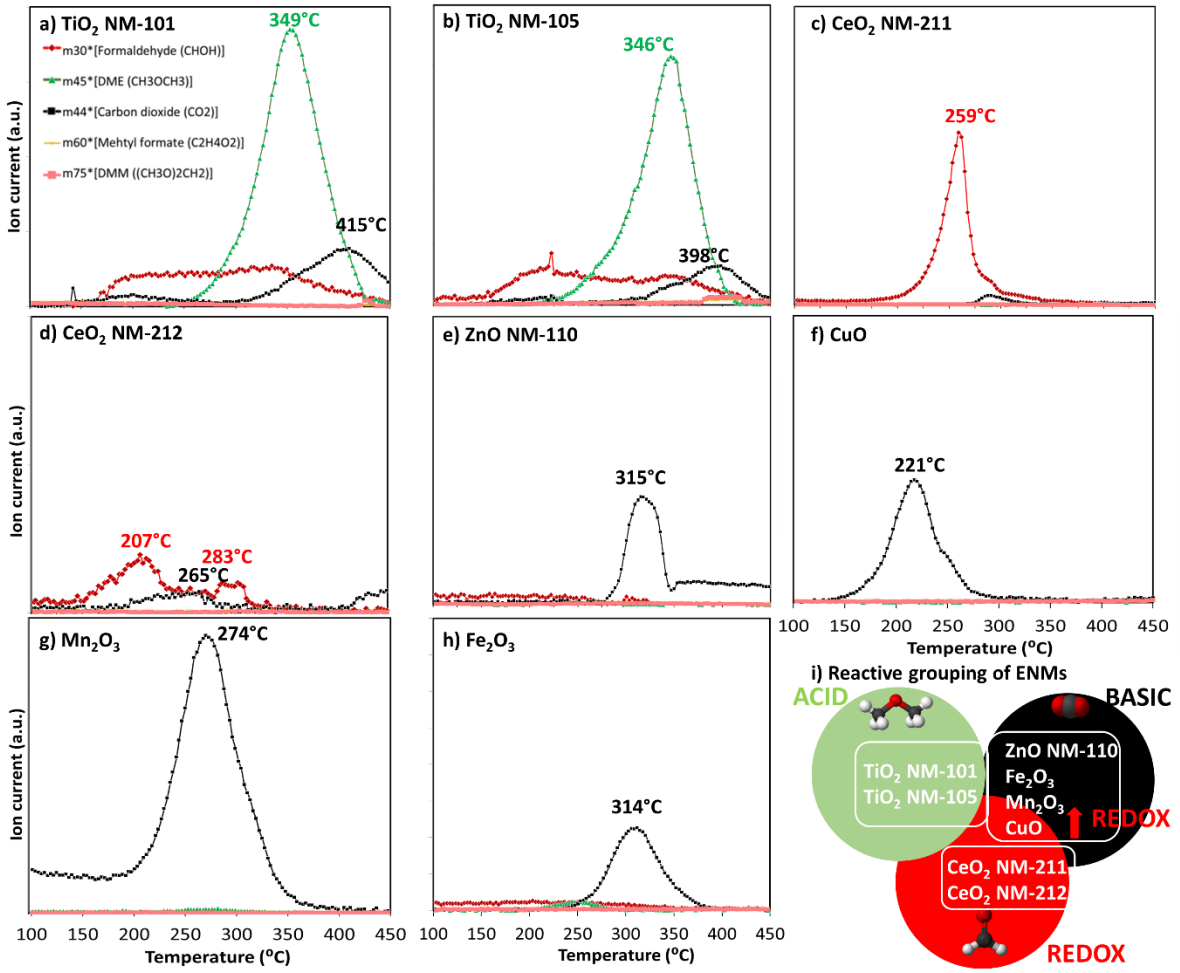


***Figure 12.*** *Temperature-programmed surface reaction products of pre-adsorbed methanol analysed by mass spectroscopy for two different $TiO_2$, NM-101 (a) and NM-105 (b), two different $CeO_2$, NM-211 (c) and NM-212 (d), ZnO NM-110 (e), $Mn_2O_3$ (f), CuO (g) and $Fe_2O_3$ (h). A summary of nanomaterials grouping by reactivity in MeOH-TPSR is shown in (i). Formaldehyde (red) is formed in redox sites, dimethyl ether (green) in acid sites, and carbon dioxide (black) in basic or highly reactive redox sites.*

The temperature of maximum product formation can be used to rank the ENMs from a reactivity point of view as follows: CuO (221 °C) > $Mn_2O_3$ (274 °C) > $Fe_2O_3$ (314 °C) > ZnO (315 °C), with lower temperatures being representative of faster methanol oxidation due to highly reactive redox sites. Methanol combustion to $CO_2$ occurs at very high temperatures, due to the strong affinity between basic sites and methoxy group.

Methanol-TPSR data for $SiO_2$ (NM-200 and NM-201) and MWCNT (NM-400 and NM-401) is summarized in Figure 13. Only $SiO_2$ NM-201 and MWCNT NM-400 showed some reactivity, with a slight band related to $CO_2$ formation that suggests a basic character of their low reactivity sites.

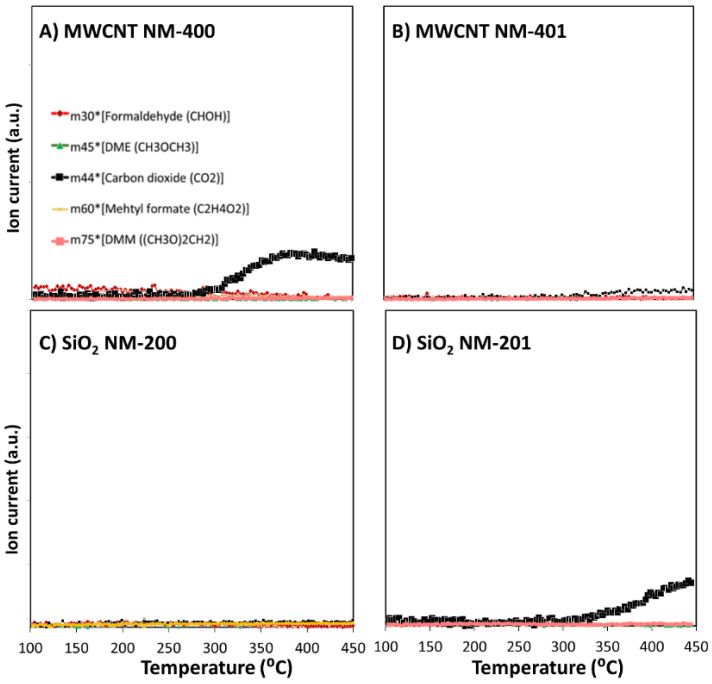


***Figure 13**. Temperature-programmed surface reaction products of pre-adsorbed methanol analysed by mass spectroscopy for two different MWCNT (NM-400 (a) and NM-401 (b)), and two different $SiO_2$ (NM-200 (c) and NM-201 (d)). Formaldehyde (red) is formed at redox sites, dimethyl ether (green) at acid sites, and carbon dioxide (black) at basic or high reactive redox sites.*

## 5.3 Discussion

The reactive sites surface density of the tested nanomaterials, between 0.8 and 41.6 sites per $nm^2$ (Table 6), is consistent with the literature.[67] Methoxy multilayers due to very reactive interactions are suggested for sites densities higher than a monolayer, as in CuO (42), ZnO NM-110 (22) and $Fe_2O_3$ (16), which is in line with desorbed $CO_2$ in MeOH-TPSR via decomposition of carbonates (high temperatures) and formates (lower temperatures).[186,187,188] However, $SiO_2$ nanomaterials NM-200 and NM-201 presented a low reactive sites surface density, so this descriptor explains the low reactivity exhibited by this material in all the reactions and the absence of MeOH-TPSR products. Their large but poorly populated surface is not sufficiently reactive to detect reaction products. The same behavior is observed for MWCNT (NM-400 and NM-401). Although both types of multi-walled carbon nanotubes have a high specific surface area, which allows a high adsorption capacity, they are, actually, two of the nanomaterials with the lowest reactive sites surface density, only above silica oxides. Therefore, due to their low site density and

the absence of products in TPSR-MeOH, it is suggested that the reactivities observed for NM-400 in the liquid-phase reactions are produced by the impurities reported for these materials.[39,189]

The adsorption capacity of ZnO NM-111 is influenced by the triethoxycapryl silane coating, so that only about 5 reactive sites per $nm^2$ are available for exposure to methanol. However, the uncoated ZnO NM-110 shows a small but highly populated surface of reactive sites. In addition, the reactive sites have been shown to be high consumers of thiols (GSH and Cys) for both nanomaterials. The site-normalized reactivity allows to reconcile the oxidative capacities of NM-110 and NM-111, which initially (mass-normalized) differed in Cys and GSH consumption, with NM-110 being high-moderate while NM-111 was poorly reactive in both reactions. As a limitation of methanol chemisorption on coated surfaces, we cannot decipher the surface structure of NM-111 after it has been chemisorbed, nor can we unmask the role of the coating in the reactivity.

## 5.4 Conclusion

The quantification of the number and nature of reactive surface sites on ENMs using methanol leads to two key conclusions: 1) ENMs active sites are quantifiable through methanol chemisorption; this value may not correlate with the specific surface area; and 2)ENMs site reactivity is measurable by methanol-TPSR, and it varies among the active sites of different ENMs and their various forms .

We have shown that MeOH chemisorption and subsequent TPSR are catalytic based new approach methodologies to quantify nanomaterials surface sites and to classify their reactivity based on acidic, basic or redox performance. Methanol probing has a three-fold benefit. On the one hand, surface sites quantification enables *site-specific dose metrics (see section 9.1)*. Normalizing to reactive site amount is particularly relevant for dose-response modelling. On the other hand, the identification of the nature of the surface reactive sites (namely, acidic, basic or redox) completes the information provided by typical probe molecules for oxidative potential evaluation. Finally, this gas-solid technique avoids usual limitations of probe reactions that require ENMs dispersion in liquid phase to understand primary reactivity: ion release, agglomeration depending on

pH, or stability limitations. However, methanol TPSR is restricted to samples with high thermal stability, such as metal oxides.

# Chapter VI. Reactivity of surface redox-active sites: OxTOF

## 6.1 Oxidative Turnover Frequency (OxTOF)

Several probe molecules may specifically determine oxidative potential,[82,190,79,191,80,192] which is particularly relevant to human health due to its involvement in cellular oxidative stress damage.[193,194,195,196,197,63] Among them, dithiothreitol has two thiol groups that are easily oxidized to a stable six-membered ring with an internal disulfide bond (Figure 14B), which has been used to quantify the oxidative capacity of particulate matter[198,135,199,200,192131,132]. We propose DTT consumption in PBS-water solutions in presence of suspended ENMs as an acellular, liquid-phase, low-temperature probe reaction to determine their oxidative potential (OP). We normalize DTT conversion rate per active site (quantified by methanol chemisorption) to obtain the DTT Oxidative Turnover Frequency (OxTOF), *i.e.*, oxidation rate per site, and evaluate it as a descriptor of the average reactivity of individual surface oxidative sites that can be used to better compare ENMs' oxidative potential.

We further propose to normalize doses to the number of active sites to evaluate possible correlations between reactive-based hazard and the number and reactivity of such sites. In this work, as a proof of all these concepts, we evaluate five representative ENMs with different modes of action: $CeO_2$, ZnO, CuO and two types of $TiO_2$.

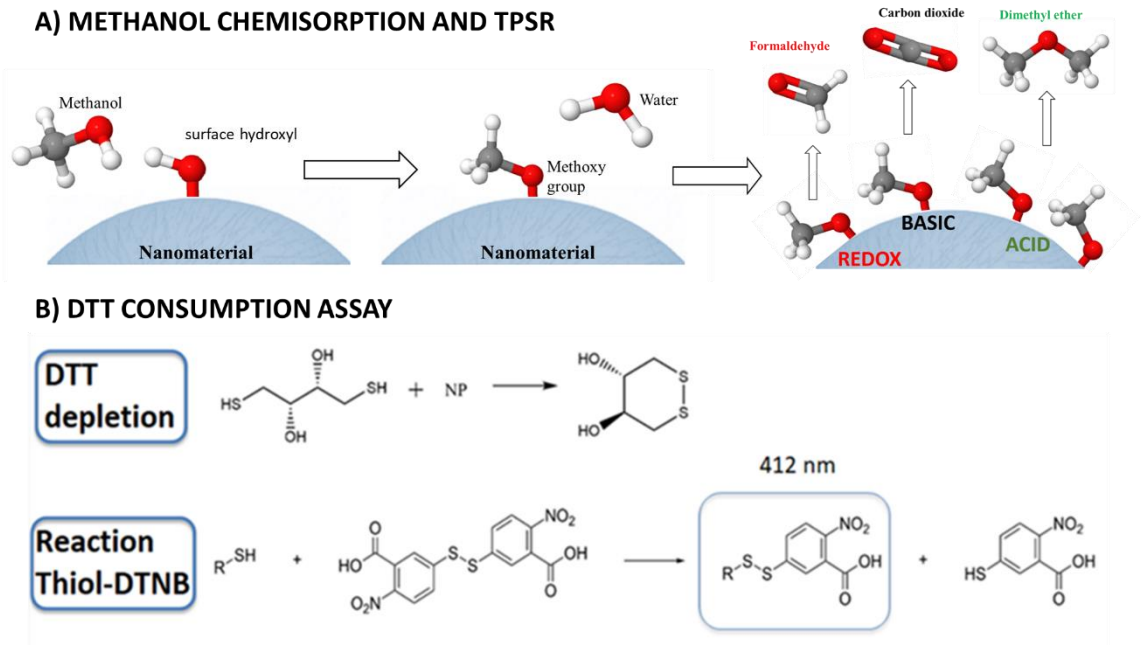


***Figure 14.*** *Probe reactions for quantitative reactive characterization of ENMs: A) Methanol chemisorption on the surface of a ENMs with formation of a methoxy group per active site, followed by surface reaction and products desorption; redox sites lead to formaldehyde formation, basic sites produce carbon dioxide, and two nearby acid sites generate dimethyl ether. B) Oxidation of dithiothreitol (DTT) catalyzed by a nanoparticle (NP) and quantification of non-oxidized DTT with Ellman's reagent (DTNB) by UV-Vis spectrophotometry detection at 412 nm of the colored product.*

## 6.2 Results

*Figure 15* illustrates with different descriptors the DTT catalytic oxidation results for 1h reaction, and Figure *16* displays the results of Tukey's test using the logarithm of $OP_{mass}$, $OP_{area}$ and OxTOF. ZnO was not included in the analysis because it dissolves in the reaction media and Zn cations get complexed by DTT,[132] so no free and uncomplexed DTT is available for interaction with the ZnO surface, and thus the results are close to the negative control. The relative oxidative potential of the other ENMs significantly depends on the descriptor, although positive control normalization, in this case, has little impact on the conversion trend (*Figure 15A and B*), that qualitatively correlates both with the reaction rate per unit mass (*Figure 15C*) and the reactive sites surface density of the ENMs (*Figure 11C*): CuO-SA >>> $TiO_2$ NM-DT-51 ≈ $TiO_2$ NM-101 ≈ $CeO_2$ NM-211; only CuO-SA has significantly higher OP (Figure *16*). The differences between these ENMs are clearly amplified when the oxidation rate is normalized to the NM surface area (Figure

15D). This underlines that CuO-SA surface, being small (Figure 11A), is significantly more reactive that other ENMs' surfaces in the series.

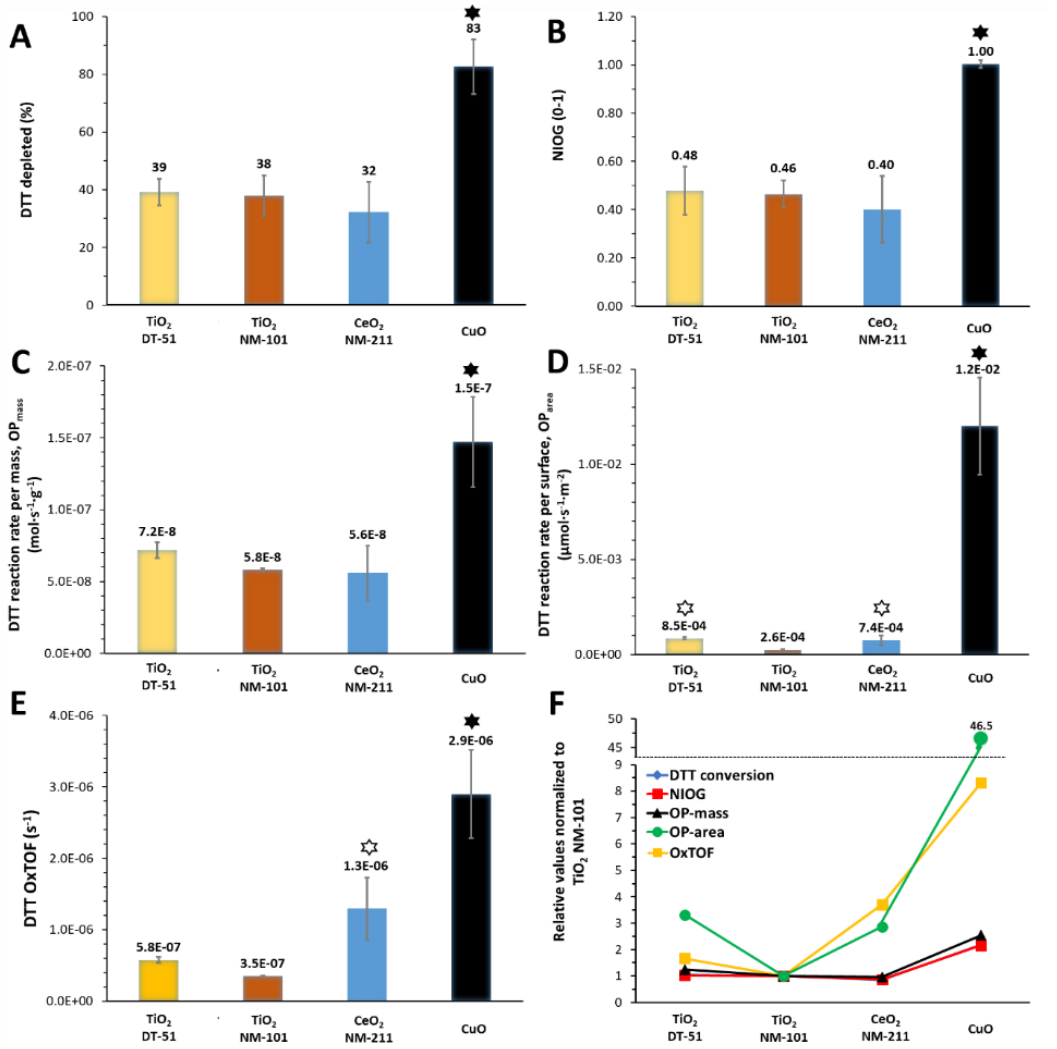


***Figure 15.*** *Oxidative potential evaluated by DTT assay expressed as conversion (A), normalised index of oxidant generation and toxicity (B), reaction rate per mass (C), reaction rate per surface (D), and oxidative turnover frequency (reaction rate per active site) (E). Averaged values (n=3) with error bars indicating the standard deviation. ENMs ranking with statistical significance ($p<0.05$) is indicated by a star, black for high reactivity and white for moderate reactivity, while materials with similar low reactivity have no star. The five oxidative potential descriptors normalized to $TiO_2$ NM-101 are compared in (F).*

Tukey's test reveals three reactivity groups of ENMs according to $OP_{area}$ descriptor: CuO-SA>> $TiO_2$ DT-51 ≈ $CeO_2$ NM-211 > $TiO_2$ NM-101. *This trend stands on assuming that all physical areas are equally populated by equally reactive sites, which is not the case. Mass or BET normalizations cannot tell how reactive each site is;* normalization per reactive site (Figure 15E) delivers the OxTOF, which shows that the activity of CuO sites is ca. twice than that of ceria sites, and both exhibit significantly higher oxidation activity than titania

sites, according to Tukey's test: CuO-SA > $CeO_2$ NM-211 > $TiO_2$ DT-51 ≈ $TiO_2$ NM-101. *Figure 15F* compares the values of the different descriptors.

CuO-SA exhibits by far the highest reactivity, with a surface area ca. 47 times more reactive than in $TiO_2$ NM-101, due to 6 times higher concentration of active sites (*Figure 11 D*) that are on average 8 times more reactive. A larger amount of less reactive sites can make up for individual site lower reactivity; both pieces of reactivity information, individual site and collective, are important to understand and classify ENMs.

Among these descriptors, only OxTOF is able to identify with statistical significance that ceria has more active redox sites than titania ENMs (Figure 16). F*rom a chemical perspective, turnover frequency values may allow a better quantitative comparison of oxidative potential and provide a more accurate insight into reactivity at a molecular scale.*

***p values of post-hoc multiple comparision testing (Tukey)***

| $TiO_2$ DT51 | $TiO_2$ NM-101 | $CeO_2$ NM-211 | CuO |
|---|---|---|---|
| 1 | 0.709 | 0.415 | 0.02 |
| | 1 | 0.979 | 0.009 |
| | | 1 | 0.003 |
| | | | 1 |

***Grouping by reactivity***

| **A) log($OP_{mass}$)** | Low | Moderate | High |
|---|---|---|---|
| $TiO_2$ DT51 | *-7.14* | | |
| $TiO_2$ NM-101 | *-7.23* | | |
| $CeO_2$ NM-211 | *-7.26* | | |
| CuO | | | *-6.83* |

| $TiO_2$ DT51 | $TiO_2$ NM-101 | $CeO_2$ NM-211 | CuO |
|---|---|---|---|
| 1 | 0.002 | 0.741 | <0.001 |
| | 1 | 0.006 | <0.001 |
| | | 1 | <0.001 |
| | | | 1 |

| **B) log($OP_{area}$)** | Low | Moderate | High |
|---|---|---|---|
| $TiO_2$ DT51 | | *-3.06* | |
| $TiO_2$ NM-101 | *-3.58* | | |
| $CeO_2$ NM-211 | | *-3.14* | |
| CuO | | | *-1.92* |

| $TiO_2$ DT51 | $TiO_2$ NM-101 | $CeO_2$ NM-211 | CuO |
|---|---|---|---|
| 1 | 0.13 | 0.013 | <0.001 |
| | 1 | 0.001 | <0.001 |
| | | 1 | 0.009 |
| | | | 1 |

| **C) log(OxTOF)** | Low | Moderate | High |
|---|---|---|---|
| $TiO_2$ DT51 | *-6.23* | | |
| $TiO_2$ NM-101 | *-6.45* | | |
| $CeO_2$ NM-211 | | *-5.9* | |
| CuO | | | *-5.54* |

***Figure 16****. Classification of the ENMs by surface reactivity based on Tukey' test comparison of different DTT oxidation descriptors: a) $OP_{mass}$, reaction rate by mass; b) $OP_{area}$, reaction rate by area, and C) OxTOF, oxidative turnover frequency. Logarithmic reactivity data for each NM (right) classified as low, medium and high according to the p values of the comparison (left). Cells are yellow for significant differences (p<0.05) and green for no significant differences.*

## 6.3 Discussion

### 6.3.1 Reactive behaviour

The ultimate understanding of catalytic performance requires identification and quantification of all reactive sites (acidic, basic, redox and combinations thereof). Similarly, reactive-based nanotoxicity is the result of processes catalyzed by ENMs at the

surface, and it may not only depend on the number and reactivity of redox (oxidative) sites, but also on the presence of basic and acidic sites, as all of them may influence the behaviour and interactions of ENMs in the environment and, eventually, in the human body. Their quantification and reactive characterization circumvent the assumption that all physical areas are equally populated by equally reactive sites, which is only true for identical nanomaterials. Therefore, specific number of sites and TOF (*e.g.,* DTT OxTOF) are key to describe the reactive (oxidative) potential of ENMs to, if possible, connect it with related adverse effects.

Active site surface density quantified by methanol chemisorption in our series is consistent with values reported in the literature for oxide ENMs, ranging between 0.4 and 60 sites/nm$^2$, but typically up to ca. 7 sites/nm$^2$, which would correspond to a monolayer.[67] The high number of active sites on CuO-SA (42) and ZnO (22) surfaces might be related to a very reactive interaction with chemisorbed methoxy groups, readily forming multilayers: carbonate multilayer formation is likely on ZnO basic sites, as suggested for $La_2O_3$, MgO or $Cr_2O_3$,[67] whereas CuO-SA is a highly oxidizing material that may form formates[186,187,188]. This is consistent with the $CO_2$ desorption in MeOH-TPSR at low temperatures for the highly reactive CuO-SA, ascribed to formates decomposition, and at high temperatures for the alkaline ZnO, related to the decomposition of carbonates.[187] Other experimental studies on the oxidative potential of these NMs reported in the literature validate our results and provide complementary insight into the oxidative potential determined by DTT oxidation. For instance, the basic character of ZnO and its high surface density of sites seem to be relevant in ferric reduction ability of serum (FRAS) assay, an indirect measurement of ROS by total antioxidant depletion, and in protein carbonylation assay.[37] In another study, electron spin resonance (EPR) spectroscopy with 3-carboxy- 2,2,5,5-tetramethylpyrrolidine 1-oxyl (CPH) and 5,5-dimethyl-1-pyrroline N-oxide (DMPO) probe molecules showed little formation of reactive oxygen species on $CeO_2$ NM-211 and ZnO NM-110 compared with copper oxide,[37] which agrees with DTT OxTOF data. CPH assay - more sensitive to singlet oxygen, superoxide radicals, and peroxynitrites- is depleted faster by ceria than by zinc oxide, whereas DMPO -more sensitive to hydroxyls and superoxide radicals- shows the opposite trend. As both probes are sensitive to superoxide species, Raman spectroscopy, highly

sensitive to peroxide-related species, can be used to further analyze these results. *In situ*[48,49] and *operando*[50] Raman spectra show that superoxide species are generated at the surface of ceria by interaction with molecular oxygen, but there are no reports of superoxide species formed at the surface of ZnO NM-110 and $TiO_2$ materials. Thus, reactive superoxide species would only account for DMPO and CPH consumption by ceria, but not for ZnO or titania; therefore, ZnO NM-110 must generate more hydroxyls than the ceria to justify DMPO results. Regarding the least-reactive materials of our study, the titania samples: these exhibit differences between themselves that underline the complexity of dose metrics and grouping strategies, since two given ENMs, even with the same composition (titania) and crystalline phase (anatase), may differ not only in BET surface area, strongly related with physisorption, but also in active sites surface density and strength, which, in turn, determine reactivity and related toxicity. $TiO_2$ NM-101, as measured by terephthalic acid assay, generates ROS upon photoirradiation, but not in the dark.[143] Conversely, DMPO probe molecule was significantly more depleted than the control by ROS generated from titania not only upon irradiation, but also in the dark, although to a lesser extent.[143] The strong influence of the titania structural variety on its surface reactivity has been described from the perspective of nanoinformatics,[201,202] which uses computational approaches to understand the surface structure and reactivity of ENMs.[141, 203]

### 6.3.2 Catalytic reactivity *vs.* bibliographic *in vitro* nanotoxicity

*In vitro* assays, as LDH, MTT, or ELISA, monitor different effects (cell viability, protein release, inflammation, etc.) in specific cell lines (A549, dTHP-1, etc.) and do not provide information about biodistribution, biopersistency or biotransformation[26] of nanomaterials; these methodologies are thus limited in predicting the overall toxicological profile, so comparisons are not straightforward and correlations with physicochemical properties of ENMs can only be done as a first approximation. In this series, CuO-SA exhibits the highest surface density of sites, but not the largest number of sites per gram; still, it is the material with the highest OxTOF (Figure 11D, Figure 15E), which would correlate with *in vitro* results highlighting it as the most toxic NM in the series, not only due to the reactivity of easily dissolved copper cations, but also to its surface sites reactivity, which is the most probable mechanism of action for CuO-SA

short-term cytotoxicity, before significant dissolution takes place.[128] The inflammatory effect induced by CuO is commonly associated with ROS generation and oxidative stress[64], correlating well with the highly redox sites of CuO-SA. This ENM and ZnO NM-110 have some similarities: ion release, methanol conversion to $CO_2$ and low BET area. However, both the higher active sites surface density and the lower temperature of maximum methanol conversion to $CO_2$ are indicative of a higher reactivity of CuO-SA that could be linked to the higher toxicity reported by cell viability assays with A549 line: $EC_{50}$ for 24 h exposure was 17.75 for CuO-SA and 76 μg/mL for ZnO NM-110.[172,163] DTT OxTOD could not be evaluated for ZnO NM-110, but the physical-chemical categorical variables reported in the literature -oxidation number, ionic potential, surface reducibility and redox reactivity- are consistent with its high toxicity.[133] Nevertheless, ZnO is a complex NM, because its surface reactivity has biocidal properties *per se*,[204] its mode of action is essentially by dissolution.[133] Compared to ZnO NM-110 and CuO-SA, both titania samples can convert methanol into carbon dioxide, but only at temperatures higher than 400 ºC and to a limited extent, as they are essentially acidic. This low redox reactivity is consistent with their low DTT OxTOF. Moreover, in line with our hypothesis, the high BET area of $TiO_2$ NM-101 is not directly related with adverse effects, because the surface density and reactivity of titania surface sites are low. Therefore, $TiO_2$ NM-101 is a relatively safe NM, with no cytotoxicity for cell viability in immune, hepatic, reproductive and pulmonary cell lines such as A549, HepG2, HK-2 or C3A. There are no toxicological data for $TiO_2$-DT51, but the lower number and reactivity of its sites predicts that DT51 is safer than NM-101. In the case of $CeO_2$, the literature has typically linked its toxicity with ROS generation and the $Ce^{3+}/Ce^{4+}$ ratio, [205] which is also key for catalytic activity. [48] The OxTOF of $CeO_2$ NM-211 is relatively high, between the OxTOF of the titania ENMs and of CuO-SA, so the same trend is expected for toxicity, despite its low BET. This is consistent with the intense formaldehyde production in MeOH-TPSR, maximum at 259 ºC, and with characterization reported in the literature: $CeO_2$ NM-211 surface contains 22% Ce (III) (XPS), indicative of redox-active sites, which induce ROS generation, as detected by EPR and *in vitro*, causing cell death by apoptosis and DNA damage in pulmonary cell lines.[47,60,37] While toxicity of $TiO_2$ NM-101 and $CeO_2$ NM-211 is not fully understood, they must behave differently in biological media, according to their different chemical reactivity profiles.

An *in chemico* classification of ENMs can thus be proposed based on methanol chemisorption capacity and conversion as well as DTT Oxidative Turnover Frequency that may correlate with *in vitro* toxicity reported in the literature:

CuO-SA > ZnO NM-110 >> $CeO_2$ NM-211 ≥ $TiO_2$ NM-110

A comparative investigation of the ENMs using the same cell lines and test conditions is required to further evaluate the relationship between surface reactivity and adverse effects, to describe the pathways affected by each group of ENMs, and to conclude about the relevance of our strategy to gain a comprehensive understanding of nanomaterial toxicity and, consequently, foster a safe-by-design approach.

## 6.4 Conclusions

*Reactive-based nanotoxicity is ultimately triggered by the surface chemistry of nanomaterials*; thus, the principles of heterogeneous catalysis science are relevant to molecularly understand related processes. CuO, ZnO, $CeO_2$ and two $TiO_2$ ENMs were ranked into three categories with statistically different reactivity based on reactive sites amount quantification and oxidative potential data obtained with methanol and DTT probe molecules. Moreover, we have demonstrated that specific surface area does not necessarily correlate with ENMs' reactivity, so BET area cannot be used as a normalization parameter for ENMs grouping and risk assessment without taking into consideration the quantity, nature and reactivity of surface sites, which can be assessed by chemisorption and reaction of probe molecules. In any case, the combination of site quantification with information provided by an oxidation reaction that occurs at physiologically relevant temperatures, such a DTT, serves to calculate the oxidative turnover frequency (OxTOF), *i.e.*, the DTT conversion rate per site, a *site-specific oxidative reactivity*.

This fundamental site-specific information may be a relevant descriptor to group ENMs and, ultimately, understand their nanotoxicity. The methodology proposed here must be tested with additional JRC reference nanomaterials and validated using a more comprehensive and comparable set of toxicity data. On a broader vista, the correlation with cellular assays will help establishing molecular insight into the reactive basis of

nanotoxicity. There are, however, significant structure, reactivity and toxicity data gaps to connect adverse effects with chemical reactivity. Filling these gaps is in the mission of UE projects about nanosafety, as NanoInformaTIX, which funded part of this research. Moreover, the behavior of a given material, *e.g.*, titania, may be significantly different depending on the specific nanoform (crystallinity, size, solubility, hydrophobicity, surface charge and shape), its reactivity and its specific environment. Therefore, understanding how the manufacturing process affects material's reactivity is a key feature to engineer ENMs with the desired functionality while being safe or as safe as possible by design.

# Chapter VII. Oxidative potential of ENMs

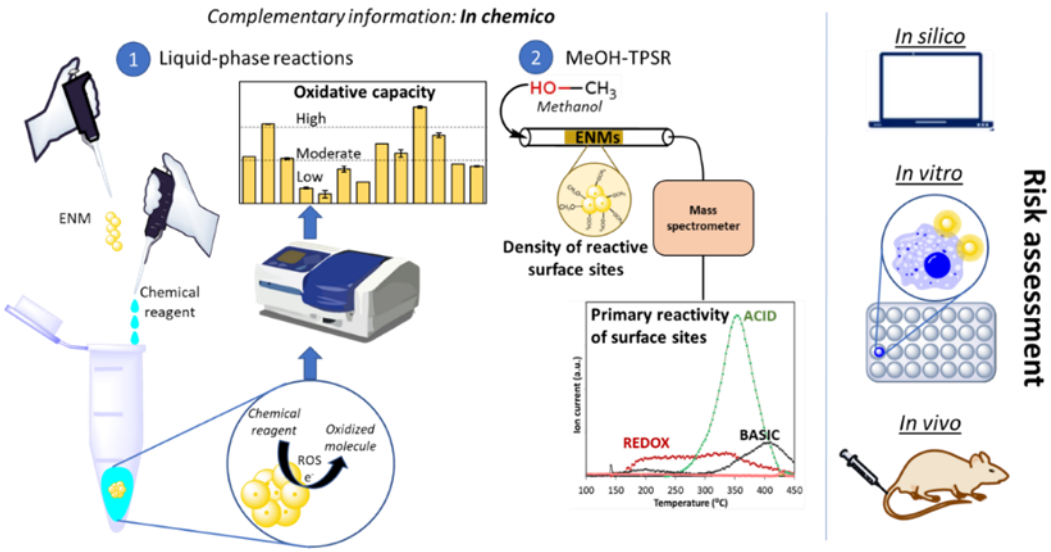


*Graphical chapter abstract*

## 7.1 Liquid-phase probe reactions

The investigation of correlations between physico-chemical characteristics and toxicological end-points has identified some drivers of ENMs' hazard.[133] In this context, the oxidative potential has been proposed as a valuable parameter for ranking the hazard of nanoparticles.[83,206,81,108,16] The goal of this chapter is to estimate the oxidative potential of nanoparticles by quantifying *in chemico* (in the absence of cells) their ability to 1) consume antioxidants, and 2) generate ROS. To get a realistic estimation of the effective dose to be considered in for biological hazard, we normalized the experimental reaction rates and amount of consumed probe molecules for the number of reactive sites at the NM surface that was determined by methanol chemisorption. With this approach, we ranked a set of 14 common ENMs, under the hypothesis that the acellular oxidative power correlates with the oxidative stress induced in a cell population.

## 7.2 Results

### 7.2.1 Antioxidant consumption

Oxidative potential results evaluated by Cys and GSH consumption after 24 h and DTT oxidation rate after 1 h are summarized in Figure 17 and classified by k-means algorithm as high, moderate or low. The most active NM according to Cys and GSH consumption is CuO for mass and surface area normalization, but the zinc oxides, NM-110 and NM-111, are more active when the normalization is sites-based. $SiO_2$ NM-200 is adamantly unreactive in all series. Carbon black consumed a quite large amount of thiols, but is in the low reactive cluster when normalizing by surface area, similarly to $TiO_2$, in particular, for NM-105 in Cys consumption.

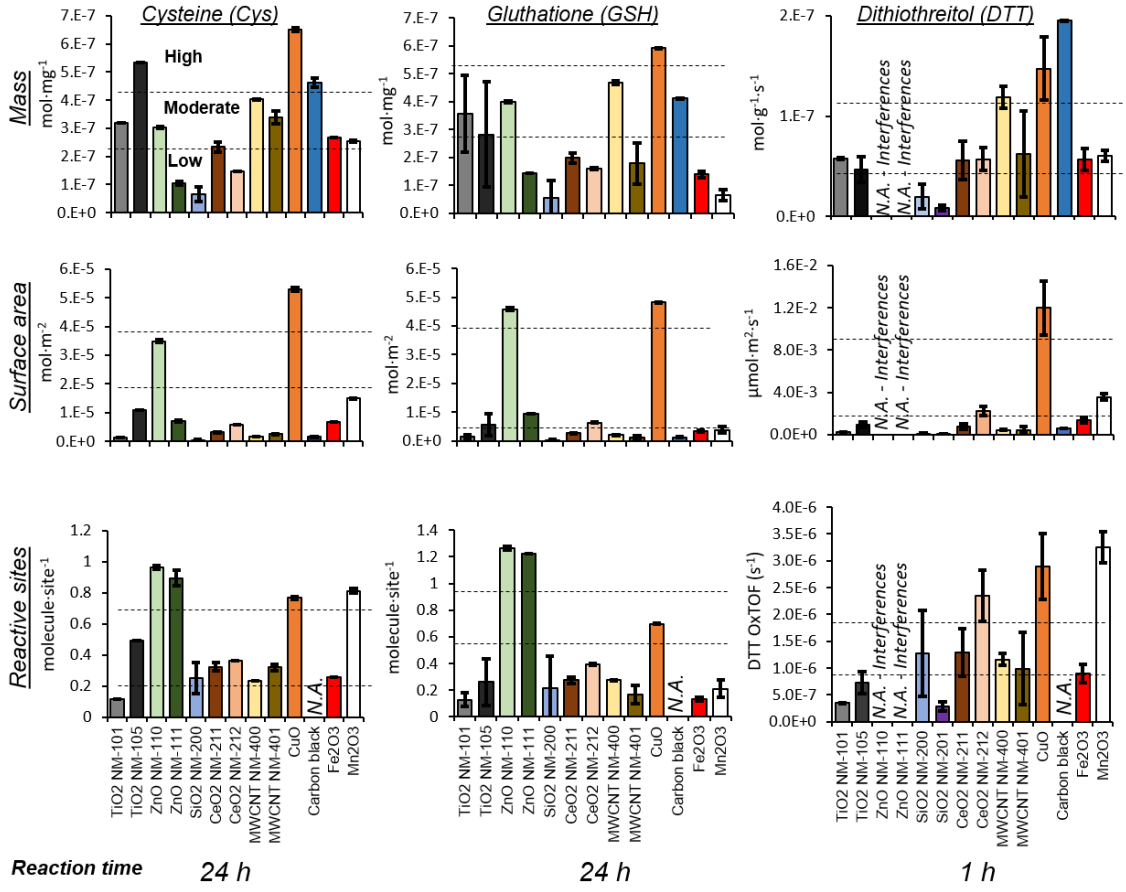


***Figure 17**. Oxidative potential of ENMs evaluated by Cys (left) and GSH (center) 24-h consumption and DTT 1-h oxidation rate (right) normalized by mass (top), surface area (middle) and reactive site (bottom) expressed as bar chart. Statistical clustering by reactivity (high-moderate-low, indicated by horizontal dashed lines) is performed by k-means algorithm. Averaged values (n=3) with error bars indicating the standard deviation.*

Both ceria exhibit low thiols consumption for GSH, but moderate Cys consumption per site. MWCNT NM-400 exhibit moderate reactivity for normalized mass data, contrary to per BET area, in which classification it remains as low reactive, together with NM-401 in both reactions. The results variability in $Fe_2O_3$ and $Mn_2O_3$ make their interpretation difficult, due to the low GSH consumption in all series. Cys and DTT consumption depend on the normalization.

Carbon black, CuO, and MWCNT NM-400 are classified as highly oxidative according to DTT mass-based oxidation rate. However, for data normalized per area and site, carbon black and MWCNT NM-400 fall to moderate and low reactivity, respectively, whereas $Mn_2O_3$, $Fe_2O_3$ and $CeO_2$ NM-212 show high reactivity according to sites normalization. $SiO_2$ NM-201 is significantly the most unreactive nanomaterial, grouped as low oxidative capacity for all normalization series. Normalization per site highlight the low reactivity of $TiO_2$ NM-101 and $TiO_2$ NM-105, initially clustered as moderate reactive due to mass normalization values (DTT conversion). $SiO_2$ NM-200 exhibited low reactivity in all parameter, except DTT OxTOF and GSH consumption per site (moderate).

### 7.2.2 ROS generation

ROS production from nanomaterials was analyzed using $DCFH_2$ depletion and *OH trapping with RNO. Results of $DCFH_2$ assay are expressed as concentration of standard-FDA to obtain normalized data (Figure 18 a-l). $DCFH_2$ depletion was observed for carbon black, MWCNT NM-400, ZnO NM-111, CeO2 NM-212, TiO2 NM-105, and $TiO_2$ NM-101, which displayed positive and linear slopes, while ROS induction occurred in a dose-dependent manner. The significantly higher slope of NM-105 compared to NM-101 is indicative of higher reactive oxygen species production by the former titania. Unlike $CeO_2$ NM-212 and ZnO NM-111, $CeO_2$ NM-211 and ZnO NM-110 show no ROS production. Four additional nanomaterials do not generate ROS: both silicon oxides (NM-200 and NM-201), CuO, and $Fe_2O_3$ (no difference compared to negative control). Carbon based ENMs and CuO were only tested between 0-12.5 µg/mL due to interference test results.

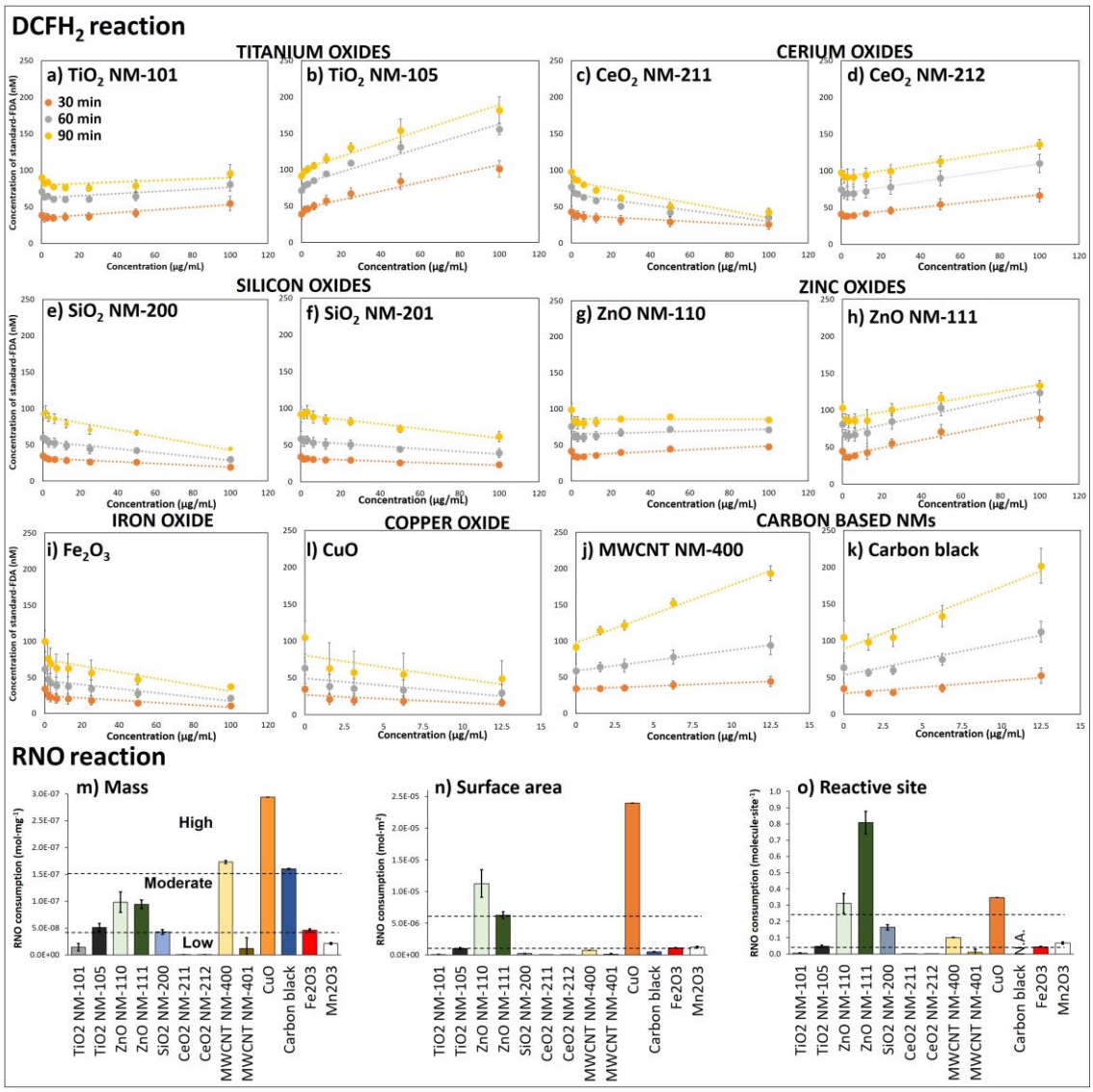


***Figure 18.*** *ROS production estimation based on $DCFH_2$ assay (a-l) and *OH trapping with RNO (m-o). Depleted $DCFH_2$ at different NM concentrations measured by standard-FDA calibration curve for $TiO_2$ NM-101 (a), $TiO_2$ NM-105 (b), $CeO_2$ NM-211 (c), $CeO_2$ NM-212 (d), $SiO_2$ NM-200 (e), $SiO_2$ NM-201 (f), ZnO NM-110 (g), ZnO NM-111 (h), $Fe_2O_3$ (i), CuO (j), MWCNT NM-400 (k) and carbon black (l). Carbon based ENMs and CuO were only tested between 0-12.5 µg/mL according to the results of the interference test. RNO depletion for the 14 ENMs is normalized per mass (m), per surface area (n) and per reactive site (o). Averaged values (n=3) with error bars indicating the standard deviation*

RNO depletion by generated *OH trapping is shown in Figure 18m-o. Five nanomaterials appeared as high or moderate oxidants due to RNO consumption per mass: ZnO NM-110, ZnO NM-111, Carbon black, CuO and MWCNT NM-400. Surface normalizations highlights the elevated oxidative capacity of zinc oxide surfaces, similar to sites-based reactivity. Low reactivity was obtained for $TiO_2$ NM-105, $Fe_2O_3$ and $Mn_2O_3$, while $TiO_2$ NM-101, both cerium oxides and MWCNT NM-401 still similar to control, so ROS

production is not exhibited. Large standard deviation for MWCNT NM-401 data caused by non-stable dispersions, probably through its high hydrophobicity.

The $DCFH_2$ oxidation rates (**Table 7**) were quantified for all nanomaterials that exhibited greater $DCFH_2$ consumption than the control group. Measurements were obtained after 90 min at the highest concentration devoid of interference, specifically at 100 µg/mL, except for carbon black (12.5 µg/mL) and MWCNT NM-400 (25 µg/mL). As indicated by the pronounced slope, MWCNT NM-400 and carbon black demonstrated the highest reactivity across all standardizations, whereas titania NM-101 was categorized as low reactive.

***Table 7.*** *$DCFH_2$ depletion rates of the active NMs normalized by mass, area and sites. NMs were clustered using k-means algorithm into three reactivity categories for ROS generation: high, moderate or low. The obtained values were after 90 min at the highest concentration without interference, 100 µg/mL, except for carbon black (12.5 µg/mL) and MWCNT NM-400 (25 µg/mL).*

| | Mass | | Area | | Site (OxTOF) | |
|---|---|---|---|---|---|---|
| Nanomaterial | Reaction rate ($nmol \cdot s^{-1} \cdot g^{-1}$) | k-means cluster | Reaction rate ($\mu mol \cdot s^{-1} \cdot m^{-2}$) | k-means cluster | Reaction rate ($s^{-1}$) | k-means cluster |
| $TiO_2$ NM-101 | 0.01 | Low | $4.81 \cdot 10^{-8}$ | Low | $3.9 \cdot 10^{-9}$ | Low |
| $TiO_2$ NM-105 | 0.33 | Moderate | $5.77 \cdot 10^{-6}$ | Moderate | $3.0 \cdot 10^{-7}$ | Low |
| ZnO NM-111 | 0.07 | Low | $4.76 \cdot 10^{-6}$ | Moderate | $7.1 \cdot 10^{-7}$ | Moderate |
| $CeO_2$ NM-212 | 0.10 | Low | $3.94 \cdot 10^{-6}$ | Moderate | $2.5 \cdot 10^{-7}$ | Low |
| MWCNT NM-400 | 2.46 | High | $1.03 \cdot 10^{-5}$ | High | $1.4 \cdot 10^{-6}$ | High |
| Carbon black | 2.77 | High | $8.73 \cdot 10^{-6}$ | High | NA | NA |

## 7.3 Discussion

### 7.3.1 Probe molecules correlation

The results of oxidative potential per reactive site obtained with the different probe molecules were compared utilizing Pearson's correlation coefficient (Figure 19). The comparison of probe molecules enables an exploration of the underlying reaction mechanisms governing their consumption. The significant Pearson correlation coefficient for reactive site-normalized data between GSH, Cys, and RNO, (0.81 and 0.84) suggests a shared oxidation mechanism. Regarding ROS generation, the correlation of $DCFH_2$ consumption with other specific probe molecules is not clear. DTT showed slight similitudes with Cys reaction (0.62).

Mass and surface area normalizations were also calculated to discern the differences between the various types of exposure dose metrics for ENMs. Surface area parameter shows a good correlation between RNO, GSH, DTT and Cys consumption, while mass normalization presented a lower prognosis.

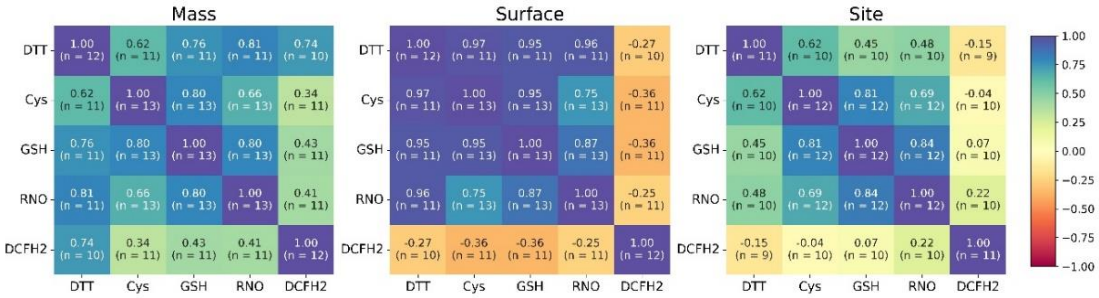


***Figure 19.*** *Heatmap of Pearson's correlation coefficients for the probe reaction results normalized by site.*

The pairplot in Figure 20 emphasizes the pairwise relationships among the normalization strategies applied to the probe reactions under study, indicating that depending on the probe molecule the data tend to cluster into three groups. The first group comprises Cys, GSH, and RNO; the second group consists of DTT, and the third group comprises $DCFH_2$.

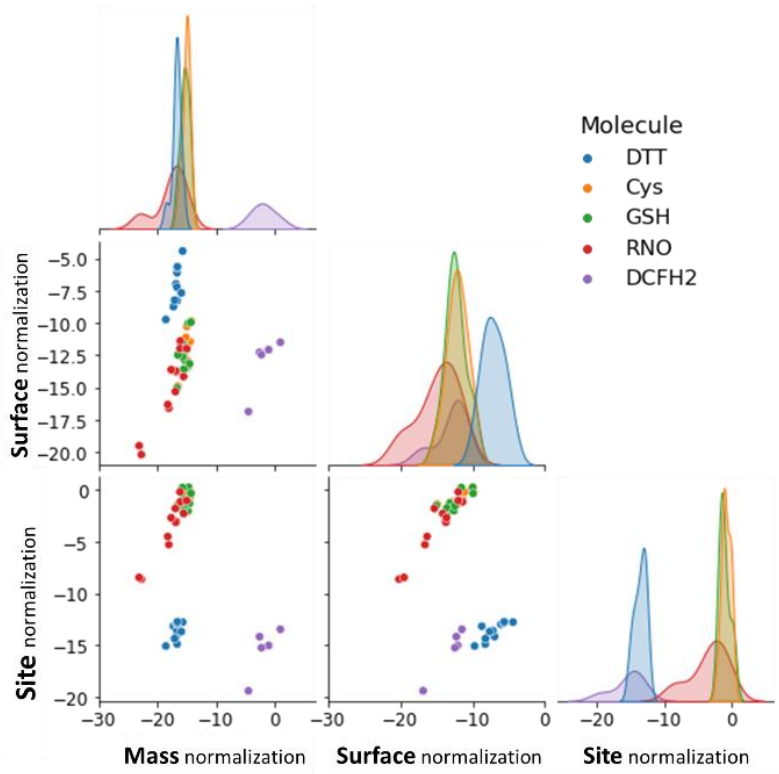


***Figure 20****. Pairplot for comparison of normalization methods in the evaluated probe reactions*

RNO and $DCFH_2$ probe reactions do not yield similar information under any normalization conditions. Consequently, in the context of DTT consumption, the formation of various reactive oxygen species, including HO·, is anticipated. In contrast, the $DCFH_2$ reaction induces specific ROS types, thereby discriminating against HO·. The $DCFH_2$-DA assay, owing to its high sensitivity to oxidants, lacks specificity for any particular ROS, and is capable of detecting a broad spectrum of reactive oxygen or nitrogen species, encompassing RO·, HOCl, and ONOO.[136]

### 7.3.2 Nanomaterials ranking

K-means ENMs reactive clustering by oxidative potential is summarized in the heat map of Figure 21.

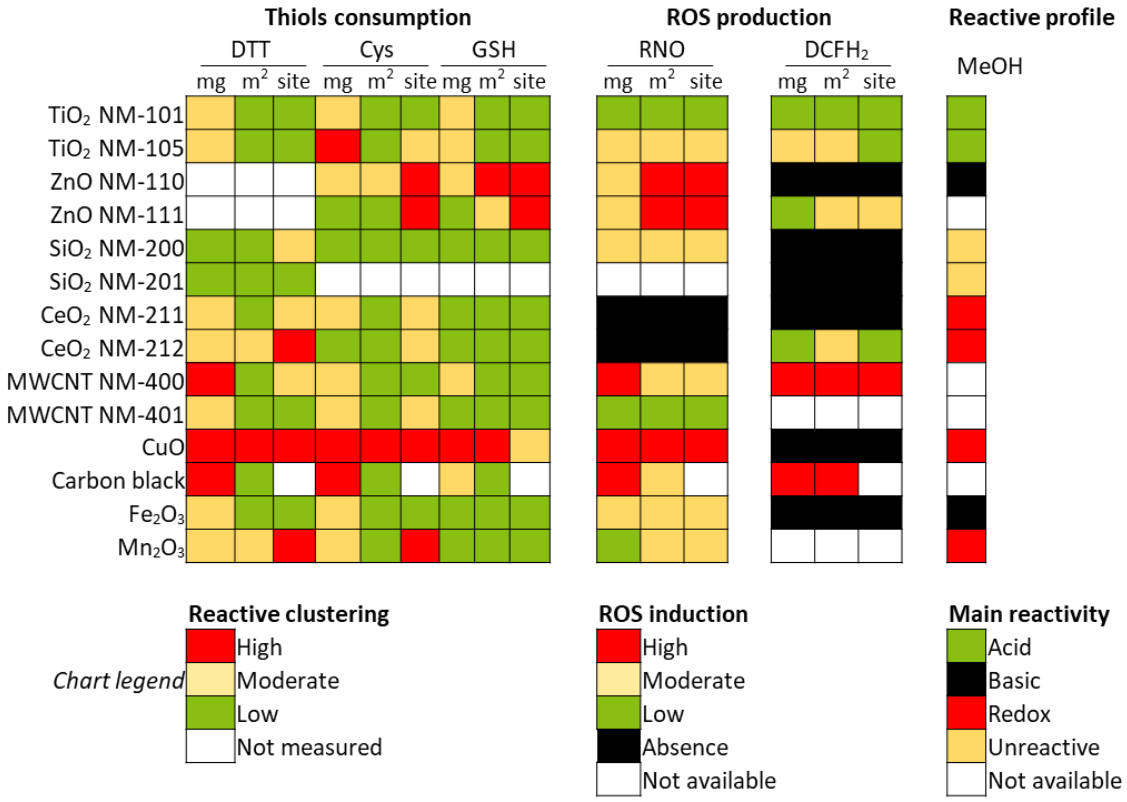


***Figure 21.*** *Heat map for the 14 ENMs evaluated by their intrinsic oxidative capacity to react with the thiol group in DTT, Cys, GSH, or their production of ROS that are trapped by RNO and DCFH2, as well as by their reactive profile obtained via methanol temperature programmed surface reaction. Clustering by reactivity is performed by k-means algorithm.*

The classification depends on the specific metric, but the effect depends also on the probe. Among the materials under evaluation, titania samples are the only ones with

acidic surface reactivity. $TiO_2$ NM-101 shows low potential for thiol group oxidation, and no ROS induction. Differently, $TiO_2$ NM-105 presents moderate/high ROS induction and moderate Cys consumption. Zinc oxide basic (measured only for NM-110) surface sites are highly reactive for thiol oxidation, both in Cys and GSH, and for hydroxyl radicals generation. However, they are clustered as medium (NM-110) and low (NM-111) oxidants with mass and area normalization, and ROS formation by ZnO NM-110 was not detected with $DCFH_2$ test. Silicon oxides are in general unreactive. Cerium oxide redox surface sites moderately oxidise DTT and GSH, but not Cys. NM-212 is slightly more reactive and induces ROS that are consumed by $DCFH_2$. MWCNT NM-401 is practically unreactive, whereas MWCNT NM-400 slightly basic abundant surface sites exhibit low reactivity, but it produces large amounts of ROS, and gravimetric thiols consumption of this sample is high for DTT and moderate for GSH-Cys. Carbon black classification is the same as MWCNT NM-401. Iron and manganese oxides have similar reactive classification, low for GSH, but high for DTT consumption by surface sites and moderate in the rest of normalizations, without correlation with the classification for CyS.

CuO stands out as the nanomaterial with the highest oxidative capacity, as it consistently exhibits a classification as highly reactive across all analyses conducted via the k-means algorithm. The exception to this trend is observed in the GSH assay when normalized by active site. However, it shows a negative slope for the probe reaction with $DCFH_2$, suggesting that no radicals are produced during oxidation, except OH·, as exhibited for RNO. Following CuO, the subsequent nanomaterials in the reactivity scale are MWCNT NM-400, ZnO NM-111, carbon black, and ZnO NM-110. These results are consistent with the literature. MWCNT NM-400 has relevant impurities, which could be decisive for its reactivity, expressed in mg/kg: 42192 for Al, 1911 for Co and 3455 for Fe.[39] ZnO NM-110 ROS production has been previously assessed using EPR and FRAS techniques. Results indicated a higher depletion of CPH and DMPO in ZnO NM-110 compared to the blank, and surface-based measurements provided further evidence of its oxidative capacity,[37,78] while the FRAS assay exhibited the highest sensitivity to ZnO NM-110, as indicated by its reactivity per site in GSH, Cys, and RNO reactions, reported data aligns with our findings, confirming the absence of ROS production in the $DCFH_2$ assay despite the high reactivity observed for ZnO NM-110.[140,136] Thus, CuO and ZnO NM-110 have great similarities: they

have high oxidizing character, form $CO_2$ in MeOH-TPSR and yet do not react against $DCFH_2$, suggesting that the reactive oxygen species formed is HO·. In a similar way, ZnO NM-111 tested positive in FRAS experiments, being one of the highest oxidant in the series,[37] and CPH and DMPO were depleted more than blank, testing positive for both molecules (2.8 and 3.5 in the ratio sample/blank, respectively).[78] The different behavior of NM-110 vs NM-111 in the $DCFH_2$ probe reaction suggests that both nanomaterials have different oxidation mechanisms, with NM-111 being a nanomaterial with higher ROS induction capacity. Lastly, carbon black is utilized as a positive control in $DCFH_2$ assay due to the high dose-dependent ROS production, high DTT depletion and high sensitivity for FRAS assay, evidencing its oxidative capacity.[144,85,136,132,37] The high reactivities of carbon black are in agreement with the results obtained by mass normalization, where a high consumption of GSH, Cys, DTT, RNO and especially a high slope in the DCFH2 reaction were obtained, suggesting its capacity to induce ROS.

All the reactions allow clustering of $CeO_2$ NM-211, $SiO_2$ NM-200, $Fe_2O_3$, $CeO_2$ NM-212, $TiO_2$ NM-101 and $TiO_2$ NM-105 in a group of lower reactivity. Among the pairs of nanomaterials by composition, it is worth noting the similarity between the two titania (as reflected by MeOH-TPSR) and the higher oxidizing capacity of NM-211 vs. NM-212, supported by results in the literature, which, by XPS, detected a higher percentage of Ce(III) on the surface of NM-211 (22%) vs. NM-212 (14%).[47] Concerning $SiO_2$ NM-200, it exhibited low reactivity in all reactions, with the exception of DTT consumption per active site. The limited number of active sites on the surface leads to high value of molecule consumption per site, even though the nanomaterial is, in fact, classified as unreactive. There is no substantial consumption of any molecule, no ROS formation, and no products observed in MeOH-TPSR.

## 7.4 Conclusion

In addition to methanol-TPSR, methods such as antioxidant consumption and as ROS generation measured by RNO and $DCFH_2$ are employed to elucidate the surface reactivity of ENMs. The *in chemico* measurements aim to establish that: 1) ENMs with identical compositions can exhibit varying oxidative capacities; 2) the number and nature of surface reactive sites significantly influence their reactivity and, consequently, their

toxicity; 3) site-based dose metrics is an effective parameter to compare the behaviour of poorly soluble ENM.

The reactivity screening conducted in this study underscores the oxidizing potential of nanomaterials such as CuO, ZnO NM-110, ZnO NM-111, and carbon black. On the other hand, nanomaterials such as MWCNT NM-400, MWCNT NM-401, $TiO_2$ NM-101, $TiO_2$ NM-105, $CeO_2$ NM-211, $CeO_2$ NM-212, $SiO_2$ NM-200, $Mn_2O_3$, and $Fe_2O_3$ are categorized into groups with moderate to low oxidative reactivity.

## 7.5 Supplementary chapter information

The data of interferences test for $DCFH_2$ assay is summarized in Table 8. MWCNT NM-400 and Carbon Black presented values up to 30% for 6.3-50 and 12.50-50 $\mu g \cdot mL^{-1}$, while CuO only for 25 and 50 $\mu g \cdot mL^{-1}$.

*Table 8. Interference test for $DCFH_2$ assay: results indicating up to 30% interference are denoted by red boxes.*

| Dose (µg/mL) | Interference (%) | | | | | | | | | | | |
|---|---|---|---|---|---|---|---|---|---|---|---|---|
| | $TiO_2$ NM-101 | $TiO_2$ NM-105 | ZnO NM-110 | ZnO NM-111 | $CeO_2$ NM-211 | $CeO_2$ NM-212 | $SiO_2$ NM-200 | $SiO_2$ NM-201 | MWCNT NM-400 | CB | $Fe_2O_3$ | CuO |
| 0 | 0 | 0 | 0 | 0 | 0 | 0 | 0 | 0 | 0 | 0 | 0 | 0 |
| 1.6 | 0 | 0 | 2 | 2 | 1 | -1 | -1 | 0 | 6 | 1 | 0 | 3 |
| 3.1 | 2 | 0 | 4 | 4 | 0 | 2 | -1 | 2 | 19 | 3 | 4 | 5 |
| 6.3 | 0 | -1 | 9 | 12 | -1 | 6 | -1 | -2 | 37 | 6 | 5 | 9 |
| 12.5 | 0 | 1 | 20 | 19 | 0 | 10 | -3 | -2 | 65 | 30 | 8 | 17 |
| 25 | 2 | 1 | 20 | 20 | 0 | 17 | -2 | -1 | 90 | 80 | 16 | 30 |
| 50 | -8 | 0 | 20 | 20 | 0 | 17 | 0 | -2 | 99 | 96 | 29 | 42 |
| 100 | 6 | 9 | 5 | 5 | 8 | 4 | 9 | 8 | 0 | 9 | 11 | 11 |

# Chapter VIII. Toxicity of ENMs in lung cell lines

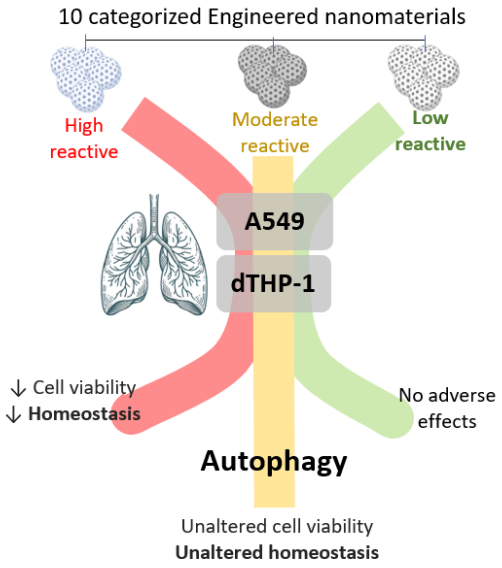


*Graphical chapter abstract*

## 8.1 *In vitro* assays

Certain ENMs that have non-redox-based reactivity, such as $TiO_2$, which also do not present cytotoxicity based on cell viability assays. Therefore, its mode of action is discussed. Contrary to $TiO_2$, $CeO_2$ presents redox reactivity, but no cytotoxicity, as reflected in cell viability and permeability. Hence, it is crucial to understand the mechanism that cells employ to protect themselves from ENM oxidative reactivity. In this section, we evaluate the role of autophagy as cytoprotective mechanisms against ENM oxidative damage.

### 8.1.1 Cell viability

We use a comprehensive approach to decipher ENM toxicity mechanisms. Cell viability is proposed as a primary descriptor of *in vitro* ENMs toxicity, measured by LDH and WST-1 assays. The LDH assay (Figure 22) operates by quantification of the level of extracellular

LDH released from damaged cells, serving as an indicator of cytotoxicity. This assay is based on the enzymatic activity of LDH in catalyzing the conversion of NADH and pyruvate to NAD+ and lactate, where NADH is transformed into beta-nicotinamide adenine dinucleotide. Given that NADH exhibits a peak absorbance at 340 nm, the assay measures the decline in NADH levels, which, in turn, is used to gauge LDH activity. However, the accuracy of this assay in measuring ENMs toxicity can be influenced by several factors. Notably, ENMs can nonspecifically inactivate LDH molecules in a solution, particularly through the generation of free radicals on their surfaces. Additionally, metal based nanoparticles pose a specific risk as they may induce metal-catalyzed oxidation (MCO) of LDH, potentially affecting the assay's reliability.[207,90,208,209]

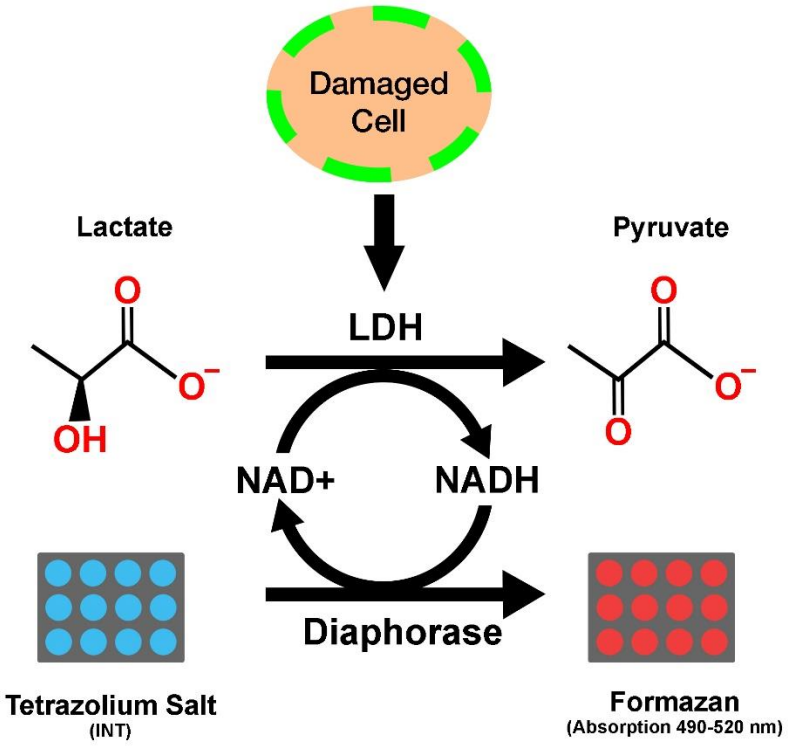


***Figure 22.*** *Schematic representation of the in vitro LDH assay for nanomaterial cytotoxicity, extracted from https://www.cephamls.com/ldh-cytotoxicity-assay-kit-colorimetric-2/ on November 15, 2023*

The WST-1 assay utilizes a tetrazolium salt that, in the presence of an intermediate electron acceptor such as 1-methoxy PMS, is converted by mitochondrial dehydrogenase enzymes into a highly water-soluble formazan. The quantity of formazan produced is directly proportional to the amount of mitochondrial dehydrogenase present in cell culture, thereby enabling the assay to measure cellular metabolic activity. WST-1

demonstrates similar sensitivity to that of XTT, but is less toxic in comparison. Moreover, WST-1 offers an operational advantage over MTT, as it does not require an additional step for dissolving formazan. This characteristic is particularly beneficial in large-scale drug screening applications, as originally noted by Ishiyama et al. in 1993.[210,211,90]

Basic cell viability tests like MTT, MTS, LDH, or WST-1, based on cellular enzymes, indicate high toxicity but are not informative of the MoA. Toxicity does not always cause cell death; understanding below cytotoxic concentrations behavior is key. Thus, these assays must be supplemented to identify specific pathways impacted by ENMs, and proteomics studies aims to better understand the cell state after ENMs exposition.

### 8.1.2 Proteomics

Proteomics has become a crucial and irreplaceable technology in the field of molecular cell biology to understand the proteome that offers extensive capabilities. It enables the identification of components in both small-scale protein complexes and large organelles. Additionally, proteomics is instrumental in determining post-translational modifications, and is increasingly used in advanced functional screening applications.[96] The common structure for peptide sequencing is shown in Figure 23.

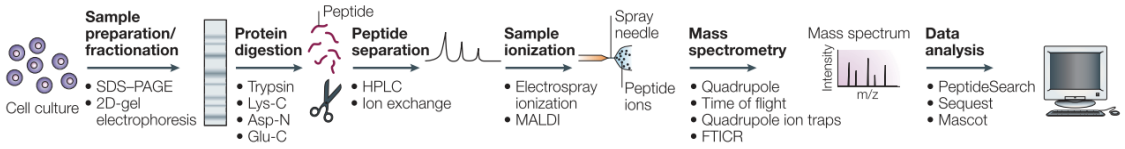


***Figure 23.*** *Structure of a peptide sequencing study for cell culture experiments, extracted from Steen et al.*[96]

Omics-based technologies have gained significant importance in toxicology due to their ability to explore toxicity mechanisms comprehensively. These technologies facilitate the generation of extensive datasets across various biological levels. Although they offer detailed insights into modes of action (MoA) at both molecular and cellular levels, omics technologies have not yet been fully integrated into routine regulatory hazard assessment procedures due to the need for standardization in the computational models used to interpret these extensive datasets.[97] In addition, not all the proteome is evaluated, so alternative techniques are required for non-cytotoxic ENMs to unravel their MoA. Autophagy kits evaluation are proposed in this section.

### 8.1.3 Autophagy

Autophagy is a non-apoptotic process, aiding in cell survival under nutrient shortage or acting as a death pathway when apoptosis is blocked, able to degrade cellular components. Triggered by external insults or defective proteins and organelles, autophagy responds to oxidative stress, inflammation, hypoxia, infections, and ER stress,[212,213,214,215] conditions that can be well triggered by ENMs.[216,108,217] This research delves into the cellular mechanisms of NM toxicity, emphasizing the role of autophagy. We evaluate 10 ENMs on A549 and dTHP-1 cells, considering the significance of inhalation as a primary entry for ENMs due to their aerosol suspension capability.[205,218,219,220]

## 8.2 Results

### 8.2.1 A549 and dTHP-1 cell viability

The viability of A549 and dTHP-1 cells was assessed through LDH release and WST-1 metabolic activity assay (Figure 24). After 24 h exposure to ENMs, concentrations up to 100 µg/mL did not induce any significant adverse effects ($p<0.05$) on both cell lines when exposed to $TiO_2$ NM-101, $TiO_2$ NM-105, $CeO_2$ NM-211, $CeO_2$ NM-212, $SiO_2$ NM-200, $SiO_2$ NM-201, and $Fe_2O_3$ ENMs.

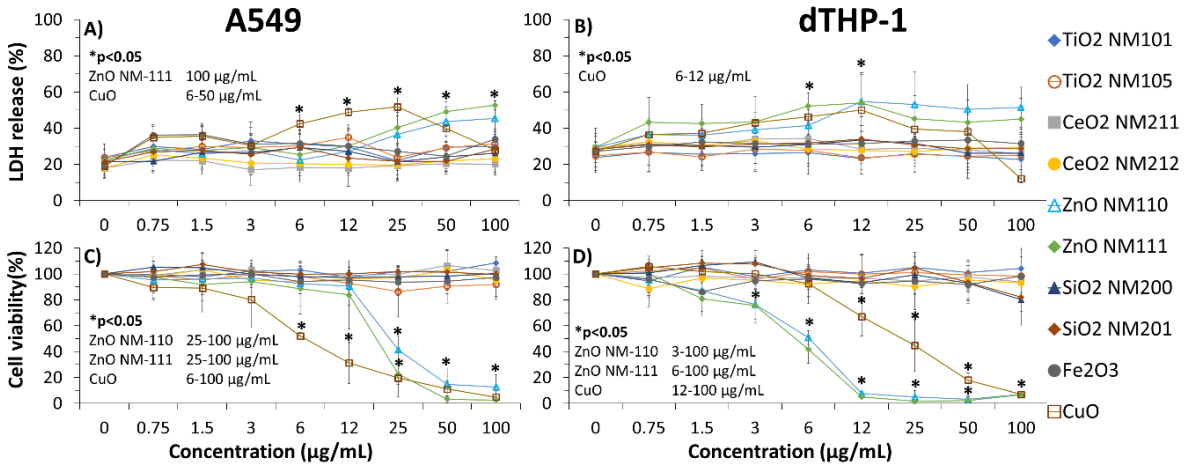


***Figure 24**. In vitro toxicity data reported for $TiO_2$ NM-101, $TiO_2$ NM-105, $CeO_2$ NM-211, $CeO_2$ NM-212, ZnO NM-110, ZnO NM-111, $SiO_2$ NM-200, $SiO_2$ NM-201, $Fe_2O_3$ and CuO in A549 and dTHP-1 cells to macrophages-like by two assays: LDH release (A-B) and cell viability via WST-1 (C-D). Results are presented as average (n=3) and the bar error is due to standard deviation. Concentration at which a ENMs induces effects significantly different to control is statistically quantified by One-way ANOVA followed of Bonferroni post-hoc test (*p<0.05). Relevant concentrations are summarized at the top of each chart.*

However, ZnO NM-110, ZnO NM-111, and CuO exhibited varying levels of cell toxicity across the two cell lines and tests. ZnO NM-110 did not alter LDH release in neither A549 nor dTHP-1 cells relative to the control. Nevertheless, it affected the metabolic activity in A549 cells at concentrations of 25-100 µg/mL and in dTHP-1 cells at 3-100 µg/mL, as indicated by the WST-1 assay results. For ZnO NM-111, a significant uptick in LDH release was noted at 100 µg/mL in A549 cells, whereas dTHP-1 cells showed no discernable change across all concentrations. The WST-1 assay revealed that NM-111 negatively impacted the cells at concentrations in the range 25-100 µg/mL for A549 and 3-100 µg/mL for dTHP-1.

CuO exposure resulted in a notable increase in LDH release at concentrations of 6-50 µg/mL for A549 and 6-12 µg/mL for dTHP-1. Interestingly, at 100 µg/mL, there was a decline in LDH release, attributable to the interference caused by Cu+ ions on the LDH enzyme, a phenomenon previously documented in the literature.[207] Regarding WST-1, cell viability decreased significantly from 6-100 µg/mL for A549 and 12-100 µg/mL for dTHP-1 cells, being the most toxic of the evaluated series.

### 8.2.2 Proteomics

Exposure to $TiO_2$ NM-101, $TiO_2$ NM-105, $CeO_2$ NM-211, and $CeO_2$ NM-212 (at a concentration of 50 µg/mL) did not result in significant alterations in any detected proteins in A549 or dTHP-1 cells. A comprehensive proteomics assessment of A549 cells treated with CuO, ZnO NM-110, and ZnO NM-111 ENMs showed limited changes to the proteome. From the 2885 proteins detected, copper oxide altered 2 proteins. ZnO NM-110 exposure disrupted the equilibrium of 6 proteins, whereas ZnO NM-111 had no effect on protein levels. In a contrasting scenario, dTHP-1 cells subjected to these engineered nanomaterials exhibited proteome alterations (Table 9).

The proteomic examination of this cell type revealed a total of 2712 proteins. ZnO NM-110 altered the level of 88 proteins, mainly focusing on exosomal proteins. On the other hand, ZnO NM-111 affected 346 proteins mostly related to cadherin binding and ribosome pathways, marking the most significant disruption in this series. CuO exposure caused a cellular stress response and affected ribosomal proteins, influencing a total of

115 protein levels. The data obtained expressed as volcano plot is summarized in **Figure 26** and **Figure 27** (supplementary chapter information section 8.5).

***Table 9.*** *Proteomic data obtained from dTHP-1 cells after 24 h exposure of seven different ENMs: $TiO_2$ NM-101, $TiO_2$ NM-105, $CeO_2$ NM-211, $CeO_2$ NM-212, ZnO NM-110, ZnO NM-111 and CuO. Each NM was exposed at highest concentration at which cell viability was not significantly affected.*

| Nanomaterial | Proteins detected | Proteins altered | Pathways affected |
|---|---|---|---|
| $TiO_2$ NM-101 | 2992 | 0 | - |
| $TiO_2$ NM-105 | 2992 | 0 | - |
| ZnO NM-110 | 2712 | 83 | Exosomal proteins |
| ZnO NM-111 | 2712 | 346 | Cadherin binding<br>Ribosomal proteins |
| $CeO_2$ NM-211 | 2992 | 0 | - |
| $CeO_2$ NM-212 | 2992 | 0 | - |
| CuO | 2712 | 115 | Stress response<br>Ribosomal proteins |

### 8.2.3 Autophagosome detection

The application of a fluorescence-based kit facilitated the identification of autophagosomes (Figure 25).

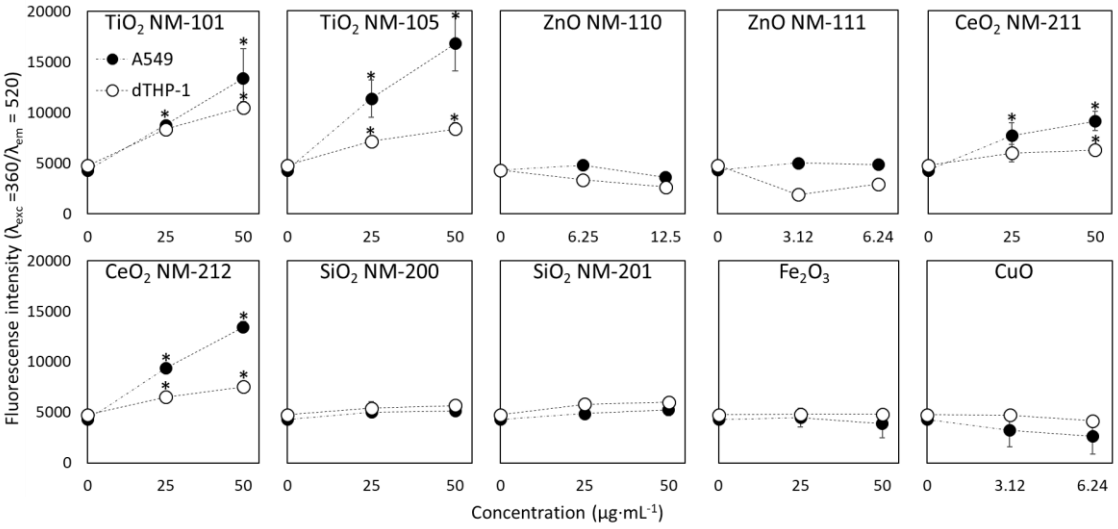


***Figure 25.*** *Autophagosome detection after 24 h exposure to TiO2 NM-101, TiO2 NM-105, CeO2 NM-211, CeO2 NM-212, ZnO NM-110, ZnO NM-111, SiO2 NM-200, SiO2 NM-201, Fe2O3 and CuO in A549 and dTHP-1 cells. Results are presented as average (n=3) and the bar error is due to standard deviation. Concentration at which a ENMs induces effects significantly different to control is statistically quantified by One-way ANOVA followed of Bonferroni post-hoc test (p<0.05).*

In the A549 cell line, fluorescence readings indicated a notable surge in autophagosome presence at 25-50 µg/mL for $TiO_2$ NM-101, $TiO_2$ NM-105, $CeO_2$ NM-211, and $CeO_2$ NM-212. The remaining nanomaterials did not demonstrate any significant divergence from the control group. On the other hand, differentiated THP-1 cells displayed evident changes in autophagosome production at 25-50 µg/mL for $TiO_2$ NM-101, $TiO_2$ NM-105, and $CeO_2$ NM-212. However, $CeO_2$ NM-211 significantly alter the cells at 50 µg/mL. The other assessed nanomaterials did not show any substantial shifts in autophagosome generation when juxtaposed with the control group.

## 8.3 Discussion

### 8.3.1 Cell viability

ENMs, while well characterized in terms of physicochemical properties, present data gaps regarding their toxicology. To our knowledge, $CeO_2$ NM-211 and $SiO_2$ NM-201 have not been tested towards A549 and dTHP-1 cells previously, and $TiO_2$ NM-101 has not been tested vs dTHP-1.

*ENMs that did not affect the cell viability.* A549 cells exposed to $TiO_2$ NM-101 showed no cytotoxic effects, in agreement with literature.[163,146] In line with our results, MTT and LDH data on dTHP-1 and A549 exposed to $TiO_2$ NM-105 for 24, 48 and 80 h also indicate no significant decrease of cell viability,[154,162] and cytotoxicity experiments (LDH, Alamar Blue and cytokines release) with $CeO_2$ NM-212 in these cell lines showed no cytokines release and absence of cytotoxic concentrations up to 22 µg/cm$^2$ and 100 µg/mL after 24 and 80 h.[161,162] Similarly, consistent with the data obtained in this work, $Fe_2O_3$ is listed in the literature among the ENMs that did not show significant effects on A549 cell viability after 24 h exposure to concentrations up to 200 µg/mL, and although internalization of $Fe_2O_3$ENMs was concluded, no adverse MTT effects or formation of reactive oxygen species were observed.[170]

Regarding $SiO_2$ NM-200, our results differ from the literature: a significant decrease in cell viability was reported for dTHP-1 after 24 h tested by MTS,[166] in contrast to our results, in which no cytotoxicity was observed up to 100 µg/mL. Cytotoxicity caused by $SiO_2$ NM-200 was not expected due to the low surface reactivity presented (chapter IV). Among the ENMs that did not show significant effects on cell viability in A549 was $Fe_2O_3$,

which was tested after 24 h exposure at concentrations up to 200 µg/mL, and internalization of the ENMs was concluded, but no adverse MTT effects or formation of reactive oxygen species were observed, consistent with the data obtained in this work.[170]

*ENMs that produced adverse effects in cell viability*. CuO, ZnO NM-110 and ZnO NM-111 altered the cell viability of A549 and dTHP-1. The literature supports our findings. CuO is described as highly cytotoxic for A549 cell viability tested by MTT decreased after 3 and 24 h exposure at concentrations of 10 and 5 µg/mL, respectively, andIL-8 was released at 10-100 µg/mL in the same time exposure.[45,172] Regarding ZnO ENMs, their rapid dissolution (half-life < 48 h) minimizes concerns regarding particle accumulation, so toxicity is primarily associated with ion release, a mechanism that leads to different biological effects compared to exposure to zinc salts.[221,222] NM-110 exhibited a decrease in cell viability in dTHP-1 cells at 50 µg/mL by MTS[166], while other markers as WST-1, LDH and resazurin unraveled adverse effects at lower concentrations: $EC_{50}$ between 6.4 and 9.5 µg/mL[174]. A549 cells suffered loss of cell viability at 48 µg/mL ($EC_{50}$ = 76) by resazurin[163,164] or 75 µg/cm$^2$ ($EC_{50}$ = 53 µg/mL) via alamar blue[175], which is consistent with our data. NM-111 has been previously tested in A549 cells, suggesting high toxicity for this NM due to the significant decrease in cell viability at 30 µg/cm$^2$, while $EC_{50}$ = 37 µg/mL.[175] The high cytotoxicity is consistent with our data, in which markers (LDH and WST-1) revealed cytotoxicity at 25-100 µg/mL.

As observed in our results for ENMs, WST-1 assay showed a higher sensitivity than LDH for cytotoxicity in A549 and dTHP-1 cells. This observation aligns with existing literature, which suggests that the results of the LDH assay may be subject to interferences arising from interactions between the LDH enzyme and metal ions released by soluble oxide.[223,207,224]

### 8.3.2 Proteomics

*Proteomics can report homeostasis alterations by ENMs*. The reactivity assessed in chapter IV ranks ZnO NM-110, ZnO NM-111, and CuO as the most reactive ENMs. Moreover, these materials exhibit some degree of solubility,[225] [226] which may lead to a higher incidence of adverse effects in *in vitro* and *in vivo* assays. In light of the observed decrease in cell viability, these ENMs were selected for proteomic evaluation. The reported results

substantiate the disruption of cellular homeostasis following exposure to these three ENMs. Previous findings on the toxicity mechanisms of these engineered nanomaterials support our hypothesis: proteomic studies on CuO, revealed alterations of proteins associated with oxidative stress.[173] Other reports on CuO have documented inflammation and oxidative stress in cell lines such as A549, BEAS-2B, and dTHP-1. [227]

### 8.3.3 Autophagy as a cytoprotection mechanism against reactive ENMs

The induction of autophagy by ENMs has been extensively documented in numerous previous articles. The connection between engineered nanomaterials and autophagy has been established in prior studies across various target organs, including the kidney.[228] Moreover, it has been identified as a mechanism of cytoprotection, based in the inhibition of autophagosome-lysosome fusion, resulting in the accumulation of autophagosomes and their associated substrates.[216] However, our hypothesis posits that autophagy acts as a defensive mechanism to compensate cytotoxic effects induced by reactive ENMs, not only in terms of oxidative capacity, but also for acidity of surface sites. This theory provides a plausible explanation for the observed accumulation of autophagosomes in both cell lines following exposure to $TiO_2$ (NM-101 and NM-105) and $CeO_2$ (NM-211 and NM-212). We would anticipate alterations to the proteome, but the proteins corresponding to autophagy pathway were not detected by our measurements. Contrary, profound proteomic shifts are observed with CuO and both ZnO ENMs. In the case of the latter, cells may not effectively counteract toxicity through mechanisms like autophagy, leading to a disruption in homeostasis. However, for moderately reactive ENMs, autophagy activation appears to protect from NM toxicity.

## 8.4 Conclusion

This work leads to the conclusion that: 1) CuO, ZnO NM-110, and ZnO NM-111 nanomaterials alter the homeostasis in A549 and dTHP-1 cell lines, in agreement with the high reactivity reported in the literature; 2) unreactive nanomaterials, specifically $SiO_2$ NM-200 and $SiO_2$ NM-201, do not produce significant effects in any of the two cell lines; and 3) exposure of A549 and dTHP-1 cell lines to $CeO_2$ NM-211, $CeO_2$ NM-212, $TiO_2$ NM-101, and $TiO_2$ NM-105 leads to a significant accumulation of autophagosomes, compared

to other treatments. This suggests that autophagy acts as a protective mechanism preventing the loss of homeostasis in response to moderately reactive nanomaterials.

The interrelationship between *in chemico* reactivity and *in vitro* toxicity in A549 and dTHP-1 illustrates several modes of action across different engineered nanomaterials. CuO, and ZnO NM-110 and NM-111, characterized by their partial solubility, display enhanced reactivity not only in liquid-phase reactions, but also in methanol-TPSR. This suggests a multifaceted interaction among solubility, surface reactivity, and cytotoxic potential. These highly reactive materials beat cellular defense mechanisms, leading to significant disruption in cell homeostasis. This is evidenced by the broad range of proteins impacted in proteomics studies in dTHP-1, with notable affected pathways including stress response (CuO), ribosomal proteins (CuO and NM-111), exosomal proteins (NM-110), and cadherin binding (NM-111). Conversely, other ENMs previously identified as moderately reactive in acellular studies using probe reactions neither exhibit significant reductions in cell viability, nor do they alter cellular homeostasis. Autophagosome quantification elucidated the cytoprotective strategies employed by cells, revealing that in response to exposure to reactive but non-cytotoxic ENMs, cells maintain homeostasis via autophagy.

## 8.5 Supplementary chapter information

The proteomic outcomes for A549 and dTHP-1 cell lines were assessed through statistical analysis using Principal Component Analysis (PCA). The results were visually represented using volcano plots, as depicted in **Figure 26** (for A549) and **Figure 27** (for dTHP-1).

### 8.5.1 Proteomics reports: A549

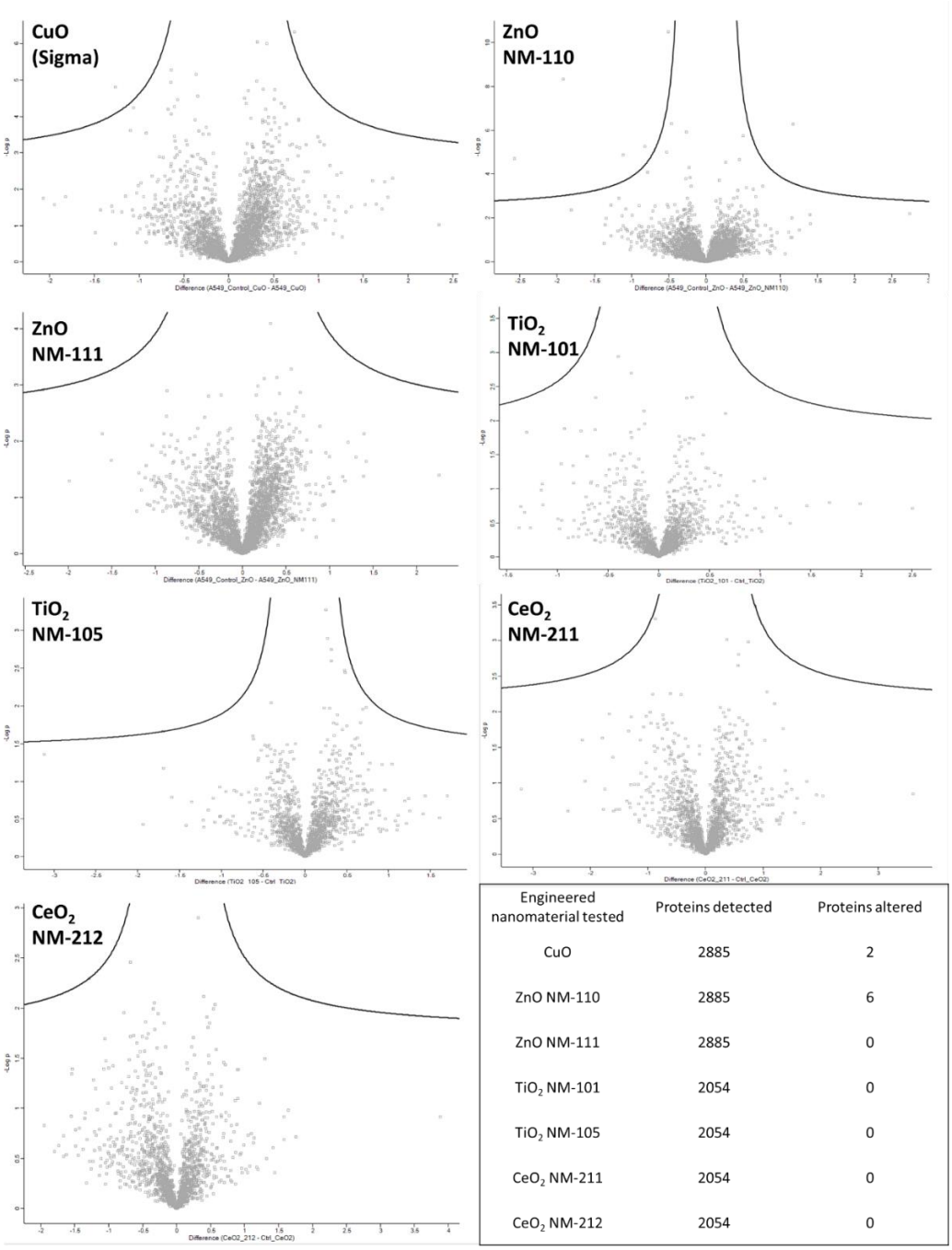


| Engineered nanomaterial tested | Proteins detected | Proteins altered |
|---|---|---|
| CuO | 2885 | 2 |
| ZnO NM-110 | 2885 | 6 |
| ZnO NM-111 | 2885 | 0 |
| $TiO_2$ NM-101 | 2054 | 0 |
| $TiO_2$ NM-105 | 2054 | 0 |
| $CeO_2$ NM-211 | 2054 | 0 |
| $CeO_2$ NM-212 | 2054 | 0 |

***Figure 26**. Proteomic reports from ENMs exposure to A549. Statistical analysis of significant altered proteins compared to control, expressed by volcano plot.*

### 8.5.2 Proteomics reports: dTHP-1

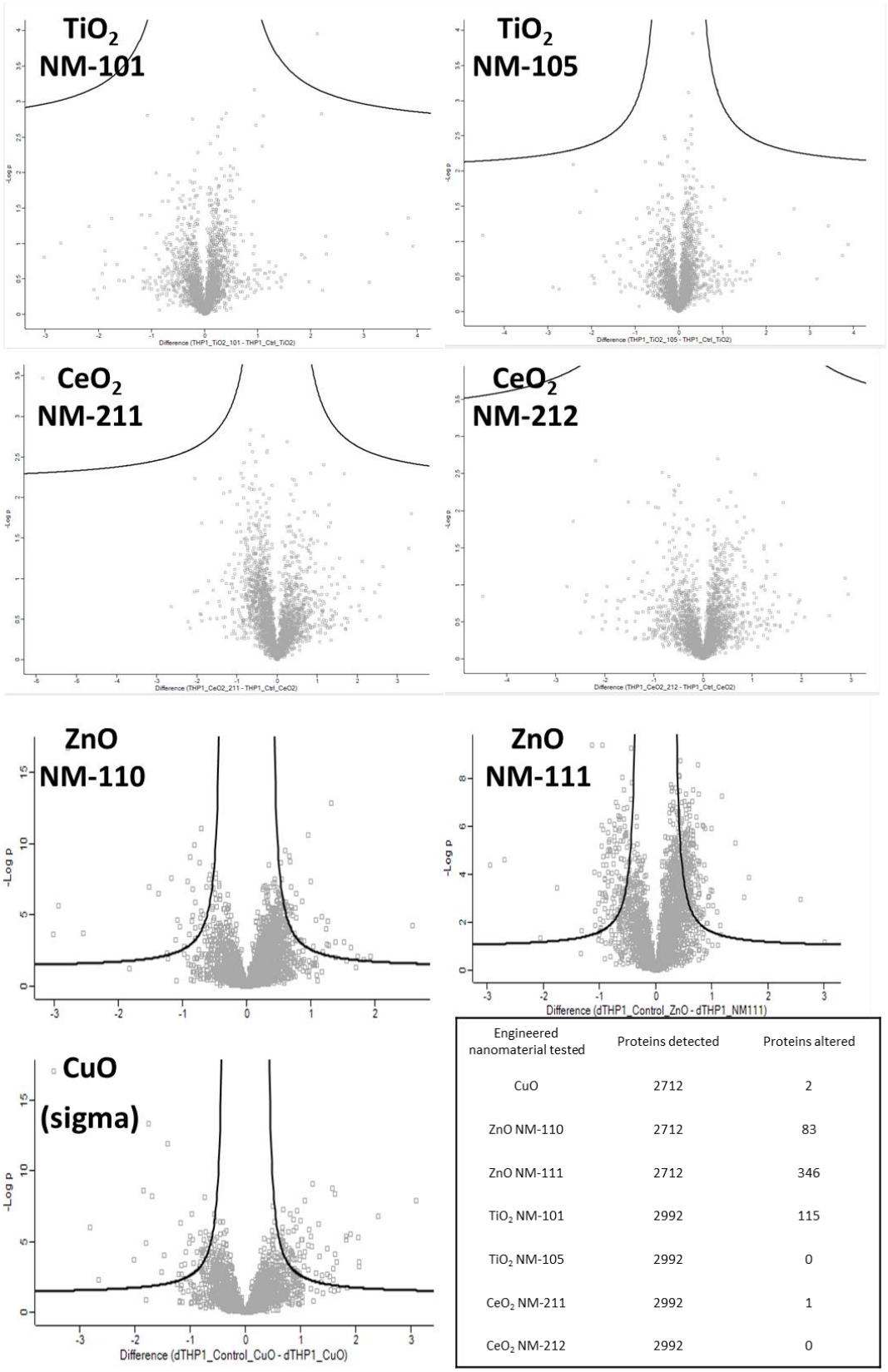


| Engineered nanomaterial tested | Proteins detected | Proteins altered |
|---|---|---|
| CuO | 2712 | 2 |
| ZnO NM-110 | 2712 | 83 |
| ZnO NM-111 | 2712 | 346 |
| $TiO_2$ NM-101 | 2992 | 115 |
| $TiO_2$ NM-105 | 2992 | 0 |
| $CeO_2$ NM-211 | 2992 | 1 |
| $CeO_2$ NM-212 | 2992 | 0 |

***Figure 27.*** *Proteomic reports from ENMs exposure to dTHP-1. Statistical analysis of significant altered proteins compared to control, expressed by volcano plot.*

# Chapter IX. *In chemico* reactivity *vs in vitro* toxicity

## 9.1 Dose-metrics for toxicological data

The development of a methodology to accurately determine the delivered dose of engineered nanomaterials to cells is a significant advancement in the field of nanotoxicology. This approach addresses a critical challenge in the development of reliable *in vitro*, *in chemico* and *in vivo* screening methods for nanomaterial toxicity. Recent works, as Cohen et al.[229], introduce an advanced methodology for *in vitro* particle dosimetry, specifically designed to account for the particokinetics within an *in vitro* environment. It outlines the use of specialized functions to calculate the delivered dose of ENMs in terms of total mass (RIDM), surface area (RIDSA), or particle number (RIDN) as a function of exposure time.[229] However, it also points out a limitation in these approaches: they do not consider the surface reactive sites of ENMs, which are crucial for understanding their reactivity and consequent toxicity. To address this, the focus shifts to a new metric: the concentration of surface reactive sites. Our hypothesis is that this novel dose-metric aims to reflect the effective dose of a engineered nanomaterial. The rationale behind this is the recognition that the reactivity of an ENM, which often drives its toxicity, primarily originates from its active surface sites. Therefore, understanding and quantifying these surface reactive sites can provide a more accurate measure of a ENM's potential toxicity, particularly for those ENMs whose MoA is based on reactivity.

This approach represents a more nuanced understanding of ENM toxicity. It moves beyond the conventional metrics of mass, surface area, and particle number to consider the specific characteristics of the ENM that contribute to their biological interactions. By focusing on the concentration of surface reactive sites, researchers can gain insights into how the unique properties of each nanomaterial influence their toxicity, leading to more

accurate NAMs and safer applications of these materials in various fields. *In this chapter, we propose the active sites concentration as a new parameter for dose-metrics.*

## 9.2 Comparing surface area and number of active sites

The dose of nanomaterial required to induce an adverse effect is a highly relevant factor in understanding its toxicity. The volumetric surface area in assays is a common dose used for *in chemico* experiments. We propose to use the concentration of active sites to have a metric for the actual surface exposure. The active sites concentration was ascertained by multiplying the conventional (gravimetric) concentration with the specific number of sites (mmol site/g). This calculation yields the number of micromoles of active sites per liter of dispersion (Eq.11).

$$\text{Active sites conc. } (\mu mol \cdot L^{-1}) = \text{ENM conc. } (\mu g \cdot mL^{-1}) \cdot \text{Spec. number of sites } (mmol \cdot g^{-1}) \quad \text{(Eq.11)}$$

Figure 28 compares the values of volumetric surface area ($cm^2/mL$) versus active sites concentration (µmol site/L) for a dose of 100 µg/mL, a common amount in *in vitro* assays.

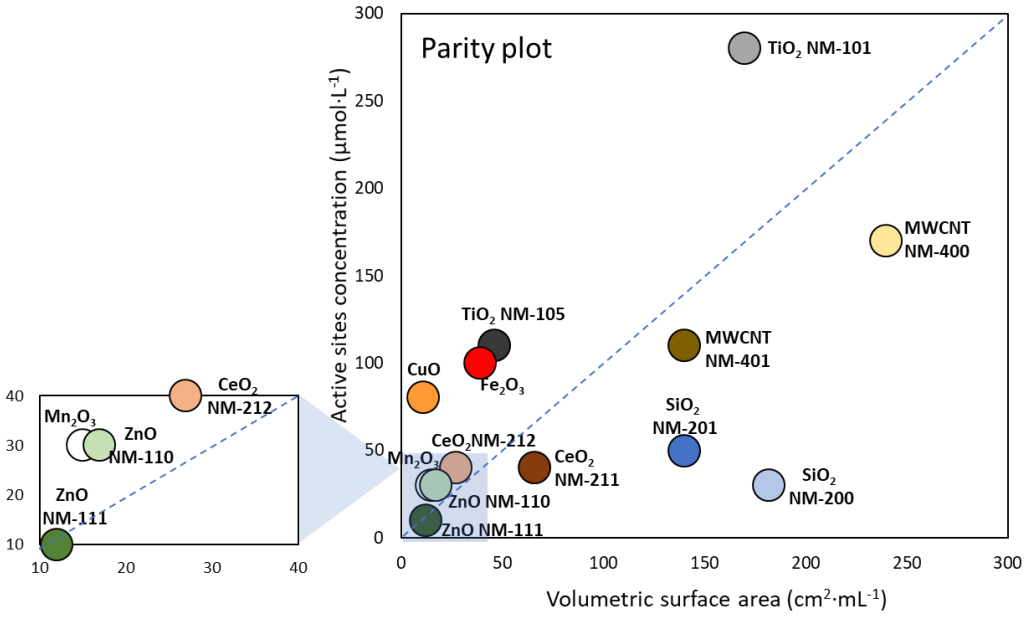


***Figure 28.*** *Metric doses based on an exposure of 100 µg/mL: a comparison between active site exposure (Y-axis) and surface area (X-axis).*

The parity line (blue) delineates the dividing zone between nanomaterials that possess a higher concentration of active sites relative to their surface area; those below the parity line expose a lower amount of active sites per BET area, while those above the line represents the ENMs that have a high exposition of active sites per $cm^2$. Titania NM-101 exposes the highest number of reactive sites (280 µmol site/L), while MWCNT NM-400 exhibits 240 $cm^2$/L, a high volumetric surface area. However, zinc oxides NM-110, NM-111 and $Mn_2O_3$ have the lowest ratio of surface area and active sites, followed by CuO and cerium oxides.

## 9.3 Experimental i*n vitro* data in active sites dose-metrics

In Chapter VIII, the *in vitro* results primarily represent the mass concentration at which an engineered nanomaterial induces an adverse effect. Nonetheless, these findings can be recalculated using the methodology described in this chapter. This recalculation yields the results presented in Table 10 (for the A549 cell line) and Table 11 (for the dTHP-1 cell line), based on the highest concentration value at which no observed adverse effect (NOAEC).

***Table 10.*** *No observed adverse effect concentration (NOAEC) of ENMs for LDH and WST-1 in vitro assays performed in A549 cell line expressed according to different dose-metrics: ENM concentration (µg·mL$^{-1}$), volumetric exposed surface area(cm$^2$·mL$^{-1}$) and reactive surface sites concentration (µmol sites · L$^{-1}$).*

| | **LDH** | | | **WST-1** | | |
|---|---|---|---|---|---|---|
| | **Mass (µg·mL$^{-1}$)** | **Surface area (cm$^2$·mL$^{-1}$)** | **Reactive site (µmol·L$^{-1}$)** | **Mass (µg·mL$^{-1}$)** | **Surface area (cm$^2$·mL$^{-1}$)** | **Reactive site (µmol·L$^{-1}$)** |
| $TiO_2$ NM-101 | 100 | 225 | 280 | 100 | 225 | 280 |
| $TiO_2$ NM-105 | 100 | 58 | 110 | 100 | 58 | 110 |
| ZnO NM-110 | 100 | 9 | 30 | 12.5 | 1.12 | 3.75 |
| ZnO NM-111 | 50 | 7.5 | 5 | 12.5 | 1.87 | 1.25 |
| $SiO_2$ NM-200 | 100 | 182 | 30 | 100 | 182 | 30 |
| $SiO_2$ NM-201 | 100 | 140 | 50 | 100 | 140 | 50 |
| $CeO_2$ NM-211 | 100 | 76 | 40 | 100 | 76 | 40 |
| $CeO_2$ NM-212 | 100 | 25 | 40 | 100 | 25 | 40 |
| CuO | 3 | 0.36 | 2.4 | 3 | 0.36 | 2.4 |
| $Fe_2O_3$ | 100 | 41 | 100 | 100 | 41 | 100 |

***Table 11***. *No observed adverse effect concentration (NOAEC) for in vitro assays performed in dTHP-1 based in different dose-metrics: NM concentration (µg·mL$^{-1}$), surface exposure per volume (cm$^2$·mL$^{-1}$) and reactive surface sites concentration (µmol sites · L$^{-1}$).*

| | LDH | | | WST-1 | | |
|---|---|---|---|---|---|---|
| | **Mass (µg·mL$^{-1}$)** | **Surface area (cm$^2$·mL$^{-1}$)** | **Reactive site (µmol·L$^{-1}$)** | **Mass (µg·mL$^{-1}$)** | **Surface area (cm$^2$·mL$^{-1}$)** | **Reactive site (µmol·L$^{-1}$)** |
| $TiO_2$ NM-101 | 100 | 225 | 280 | 100 | 225 | 280 |
| $TiO_2$ NM-105 | 100 | 58 | 110 | 100 | 58 | 110 |
| ZnO NM-110 | 100 | 9 | 30 | 1.5 | 0.13 | 0.45 |
| ZnO NM-111 | 100 | 15 | 10 | 3 | 0.45 | 0.3 |
| $SiO_2$ NM-200 | 100 | 182 | 30 | 100 | 182 | 30 |
| $SiO_2$ NM-201 | 100 | 140 | 50 | 100 | 140 | 50 |
| $CeO_2$ NM-211 | 100 | 76 | 40 | 100 | 76 | 40 |
| $CeO_2$ NM-212 | 100 | 25 | 40 | 100 | 25 | 40 |
| CuO | 3 | 0.36 | 2,4 | 6 | 0.72 | 4.8 |
| $Fe_2O_3$ | 100 | 41 | 100 | 100 | 41 | 100 |

The application of site-specific normalization concerning the concentration of nanomaterials that induce adverse effects in specific cell lines is beneficial for observing a closer alignment between the actual exposure levels of certain highly toxic nanomaterials, such as ZnO NM-110, ZnO NM-111, and CuO. However, these nanomaterials have been classified as partially soluble, making it challenging to determine their true exposure levels. This concentration model shares the same limitations as other normalizations when applied to soluble nanomaterials: ion secretion results in mass loss (leading to a reduction in nanomaterial concentration), alterations in surface area (with the exposed surface area in square meters remaining unknown), and, consequently, it is not possible to ascertain the state of active sites following such an event. Other nanomaterials not reporting solubility in the literature, such as both titanias, $Fe_2O_3$, and MWCNTs, exhibit significant disparities in their actual exposure of active sites: 100 µg/mL of $TiO_2$ NM-101 represents a high dose of sites compared to its analog NM-105 or other nanomaterials like $Fe_2O_3$. This phenomenon can lead to comparisons in terms of mass that do not equate to the true exposure of each nanomaterial.

## 9.4 Correlations between surface reactivity and *in vitro* toxicity

The Spearman correlation factor for each probe reaction values and the highest tested concentration used in *in vitro* assessment of A549 for cell viability with no observable adverse effects compared to control after 24 h is shown in Figure 29. Negative Spearman correlation coefficients are expected because higher reactivity is associated with lower tested concentrations without observable effects, making these two parameters inversely proportional.

The Spearman coefficients reveal a close relationship between the normalized RNO values by mass and the cell viability in A549 and dTHP-1. However, high correlation values are observed when normalized by surface area: GSH and cell viability correlate with values approaching -1 (-0.97 to -0.92), while the values for Cys and DTT show notable improvement. Normalization by reactive sites establishes a clear reactivity-toxicity relationship, with values exceeding -0.60 for all reactions, except for DCFH2. This latter compound demonstrates the poorest predictive capacity for effects on cell viability across any normalization method.

| | MASS | | | | | SURFACE AREA | | | | | REACTIVE SITES | | | | |
|---|---|---|---|---|---|---|---|---|---|---|---|---|---|---|---|
| | RNO | GSH | CyS | DTT | $DCFH_2$ | RNO | GSH | CyS | DTT | $DCFH_2$ | RNO | GSH | CyS | DTT | $DCFH_2$ |
| A549 LDH | -0.64 | -0.27 | -0.18 | -0.58 | -0.09 | -0.68 | -0.95 | -0.83 | -0.88 | -0.10 | -0.71 | -0.75 | -0.61 | -0.60 | 0.22 |
| A549 WST-1 | -0.84 | -0.52 | -0.28 | -0.58 | 0.09 | -0.70 | -0.97 | -0.87 | -0.88 | -0.02 | -0.73 | -0.81 | -0.68 | -0.60 | 0.11 |
| THP-1 LDH | -0.55 | -0.55 | -0.55 | -0.58 | 0.26 | -0.70 | -0.97 | -0.87 | -0.88 | -0.02 | -0.71 | -0.75 | -0.61 | -0.60 | 0.22 |
| THP-1 WST1 | -0.78 | -0.43 | -0.12 | -0.58 | 0.04 | -0.75 | -0.92 | -0.80 | -0.88 | -0.10 | -0.71 | -0.85 | -0.71 | -0.60 | 0.11 |
| n | 9 | 9 | 9 | 8 | 10 | 9 | 9 | 9 | 8 | 10 | 9 | 9 | 9 | 8 | 9 |

1.00 0.75 0.50 0.25 0.00 -0.25 -0.50 -0.75 -1.00

***Figure 29.*** *Spearman correlation values to compare the oxidative potential with the toxicological data The toxicological values (Table 10) utilized are based on the highest concentration tested in the in vitro assessment of A549 cell line for cell viability after 24 h exposure with no observable adverse effects compared to control ($p<0.05$).*

The toxicity profile of a nanomaterial cannot be predicted by a single probe reaction, as it is not possible to describe all mechanisms of action by reactivity. The comparison of reactivity with *in vitro* toxicity of nanomaterials can in turn provide insight into their modes of action, which is generally based on oxidative capacity for reaction-based

toxicity, and this complementary information may allow for a first *in chemico* screening in ENMs risk assessment.

According to the literature, among the 14 ENMs evaluated in this work, cell viability in the main lung-related cell lines is affected mainly by CuO, ZnO NM-110, ZnO NM-111 and MWCNT NM-400, with different mechanisms of action including those related to their fibrous aspect ratio (MWCNT NM-400) and ions release into the medium. [165,122] These nanomaterials are also highly reactive both in the consumption of liquid phase probe molecules or/and in gaseous methanol TPSR, which are not subjected to ion release or agglomeration effects. So, in terms of reactive-based toxicity, the reaction probe results are deeply related to the *in vitro* bibliographic data for the main cell lines: only CuO, ZnO NM-111, ZnO NM-110 and MWCNT NM-400 presented concentrations that significantly altered cell viability at a dose of up to 100 μg/ml, these nanomaterials being precisely those that were grouped, together with carbon black, as the most reactive of the series.

## 9.5 Conclusions

This chapter concludes that: 1) the normalization of concentration per active site is a valid dose-metric for assessing the dosage of a nanomaterial in a given experiment, and 2) cellular viability in A549 and dTHP-1 cell lines exhibits high prognostic levels for probe reactions such as GSH and RNO

# Chapter X. Emerging micro- and nanomaterials

Emerging micro- and nano-materials like fibers, multicomponent oxides and micro-nanoplastics (MNPs) pose challenges for risk assessment. On one hand, multicomponent engineered nanomaterials (MCENMs) are introduced to enhance the properties of pure oxides, and they must be evaluated to ascertain their composition and surface reactivity, using methodologies similar to those employed for ENMs, but also specifically relevant to the multicomponent characteristics. In particular, multicomponent nanomaterials designed for biomedical applications include hydroxyapatite nanobiomaterials, which have been doped with titanium (Ti) and iron (Fe) to investigate the variations in surface properties. Another category of materials that has recently garnered significant interest is micro and nanoplastics. The extensive human exposure to these particles, both through ingestion and inhalation, necessitates a thorough risk assessment to understand their effects. Finally, the specific properties of nanomaterials with high aspect-ratio raises a concern on the applicability of existing protocols, which must be validated.

## 10.1 Nanofibers

Carbon nanotubes (CNTs) are widely used, high-aspect-ratio engineered nanomaterials with emerging applications in the biomedical and industry/technology field, primarily due to their thermal and electrical conductivity, biocompatibility, resistance to corrosion, high surface area and capacity to be functionalized. This is most noticeable in applications as bone tissue regeneration, energy storage, water treatment and sensors.[230,231,232,233] We have selected reference MWCNTs from JRC as test nanofibers to evaluate the effect of the dispersion method in the evaluation of their toxicity.

### 10.1.1 Toxicity of nanofibers

The growing occupational and consumer exposure to fibers has raised the concern about their risk to human health, which has been extensively investigated both *in vitro* and *in vivo*. Relevant cell lines or rodent models have been exposed to physiologically relevant concentrations of single-walled or multi-walled CNTs (SWCNTs/MWCNTs), finding that deposition of these ENMs induces pulmonary toxicity.[234] Despite the great effort devoted to understanding CNT fate and mechanism of action, there are gaps in our knowledge, specifically pertaining to CNT mutagenicity in human-derived models and to promotion by CNTs of secondary mechanisms of genotoxicity *in vitro*. To fulfil these current gaps, the mutagenicity of two types of MWCNT reference materials from the JRC (NM-400 and NM-401) was assessed in human lymphoblast (TK6) cells, and their capacity to induce double-stranded DNA breaks was assessed in monocultured and co-cultured human bronchial epithelial (16HBE14o-) cells. The CNTs were dispersed using two different protocols to investigate if the dispersion method may alter the fibres and, consequently, the *in vitro* test results.

The research of this chapter was performed in national and international collaborations.

### 10.1.2 Specific methodology

#### 10.1.2.1 Dispersion protocols

*High-shear mixing was carried out in collaboration with Ceramics for Smart Systems group of CSIC-ICV (Dr. J. J. Reinosa and Prof. Dr. Jose Francisco Fernández)*

The CNTs were dispersed using either the established NanoGenoTox dispersion protocol developed by Jensen *et al* in 2011[134] or by high-shear mixing, a sonication-free alternative, high shear mixing dispersion protocol.

#### 10.1.2.2 Cell viability and mutagenicity

*Section carried out by collaborators at Swansea University (Dr. Michael Burgum)*

Cell viability and mutation frequency i*n vitro* assays following a 24h exposure to NM-400 and NM-401 were performed to investigate their genotoxic effects in human lymphoblastoid TK6.

#### 10.1.2.3 Raman spectroscopy

NM-400 and NM-401 MWCNT before and after dispersion were characterized using a Renishaw InVia Qontor micro-Raman spectrometer using a 514 nm excitation line laser and a 20x microscope objective. Some drops of the MWCNT dispersions were dropped onto a microscope glass slide, dried at room temperature and analyzed at 60 different positions, generating a representative sampling. Each spectrum consisted of 10 accumulations of 3 s with a laser power of 1.5 mW.

#### 10.1.2.4 Scanning electron microscopy

NM-400 and NM-401 MWCNT before and after dispersion were characterized by field emission scanning electron microscopy (FE-SEM) in a high-resolution FEI Nova NanoSEM 230 column microscope with Schottky filament and secondary and backscattered electron detectors. Some drops of the dispersions were dropped onto an Al support, dried at room temperature and then analyzed by FE-SEM without metallization.

### 10.1.3 Results

An extensive breakdown of the full physico-chemical characterization for both the NM-400 and NM-401 used in this study is available from the JRC. Briefly, the major differences between the two ENMs have been summarized in Table 12. NM-401 possesses a slightly higher purity and porosity compared to NM-400, and is significantly longer and wider in diameter, resulting in a very low specific surface area. In addition, XRD data indicates that graphite may be present in NM-401, and TEM reveals that NM-400 is highly bent, while NM-401 possesses a straight and thicker geometry.

The structure and morphology of the reference CNTs were evaluated by Raman spectroscopy and FE-SEM (Figure 30). Pristine NM-400 (Figure 30A) is formed by thinner and shorter CNTs than pristine NM-401 (Figure 30C), in agreement with JRC characterization data of Table 12. Both pristine materials appeared agglomerated, so no

individual fibers were appreciated, in line with the observations reported by Alig *et al.*[235] for NM-400 (called Nanocyl NC7000 CNT), who indicated that the NM-400 clusters of fibers are expected to behave as a single long and wide fiber.

***Table 12.*** *Summary of the primary physico-chemical characterisation data of the CNTs published in the JRC repository online. The elemental compositions were calculated by EDS measurements.*

| Reference material | Length (nm) | Diameter (nm) | Specific Surface Area ($m^2/g$) | Pore Volume (mL/g) | Purity (%) | Trace elements |
|---|---|---|---|---|---|---|
| NM-400 | 846 ± 446 | 11 ± 3 | 254 | 0.9613 | 89.1 | Al (46100 ppm), Si (400 ppm), Fe (7600 ppm), Co (2500 ppm), Cu (2000 ppm), Zn (1900 ppm), O (4.15 wt. %) |
| NM-401 | 4048 ± 2371 | 67 ± 24 | 140.46 | 0.0776 | 99.19 | Si (500 ppm), Cu (2300 ppm), Zn (2200 ppm), O (0.6 wt. %) |

Two typical graphite bands dominate NM-400 Raman spectra (Figure 30B), in agreement with the JRC and additional literature[236]: G band, assigned to in-plane vibration of sp2 hybridized C-C bonds, at 1575 $cm^{-1}$ with a shoulder at 1604 $cm^{-1}$, and D band at 1343 $cm^{-1}$, assigned to carbon system disorders In NM-401 spectra, the G band appeared shifted to 1567 $cm^{-1}$ and the D band at 1346 $cm^{-1}$ (Figure 30D). Moreover, due to the low intensity of the latter, the ratio $I_D/I_G$ is significantly lower for NM-401 than NM-400, which is indicative of a more graphitic structure. The NM-401 spectrum is similar to the spectra of single wall carbon nanotubes reported in the literature.[237,238]

After NanoGenoTox dispersion, NM-400 fibers were homogeneously distributed without significant fragmentation (Figure 30A, E). Similarly, after high shear mixing dispersion, a unique homogeneous cluster is shown in Figure 30I, and no significant shape changes are observed for individual but agglomerated fibers. Nevertheless, a new and intense Raman band at 1091 $cm^{-1}$ appears in all the spectra taken on NM-400 samples dispersed by both methods (Figure 30F, J), indicating that these carbon nanotubes are somehow affected by the dispersion protocols, being the ultrasonic treatment of the NanoGenoTox protocol more aggressive than the high-shear mixing, since the 1091 $cm^{-1}$ band is generally more intense.

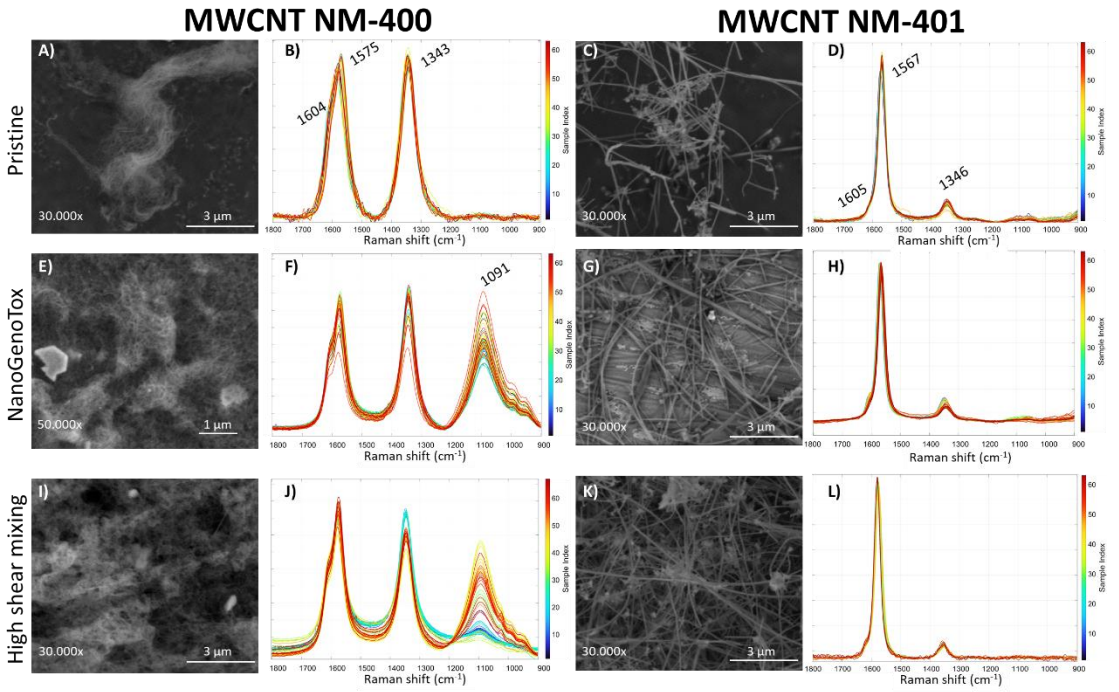


***Figure 30**. SEM images and Raman spectra of pristine MWCNT NM-400 (A-B) and MWCNT NM-401 (C-D) powder samples as well as dried samples from the corresponding dispersions obtained following the NanoGenoTox protocol (E-H) or the high-shear mixing protocol (I-L). The spectra are normalized by Standard Normal Variate (SNV) method.*

NM-401 CNTs, with physicochemical properties similar to carcinogenic Mitsui XNRi-7 fibres,[239] were also well dispersed, but the NanoGenoTox protocol resulted in some scattered fibres that were not stiff (curved morphology, Figure 30G), whereas the high-shear mixing resulted in homogeneously straight and stiff fibers (Figure 30K), similarly to NM-401 fibres in instillation medium that were long, thick and straight. No band at 1091 $cm^{-1}$ growed in the spectra of the dispersed NM-401 samples, Figure 30 D-H-L, contrary to NM-400.

The temperature-programmed surface reaction of pre-adsorbed methanol was used to quantify the surface reactive sites of NM-400 and NM-401 (Table 6, chapter V). The specific number of sites is 50% bigger in NM-400 sample, but their surface density is lower due to the bigger BET area (254 $m^2/g$ for NM-400 vs. 140 $m^2/g$ for NM-401), as reported by JRC.[240]

The oxidative capacity of the NM-400 suspensions, as analysed by DTT consumption assay, is very high, similar to the hydrogen peroxide positive control, and independent of the dispersion protocol (Figure 31). Differently, no reactivity is obtained with NM-401

when only magnetic stirring is used for dispersion, probably due to the high hydrophobicity showed during reaction (the nanotubes were floating on the surface, with no option to react with DTT). Half of the positive control oxidative reactivity is obtained for the NanoGenoTox-dispersed sample, and the NIOG increases to values close to 1 when the high-shear protocol is used to disperse the sample.

NIOG increase could be due to the modification of the nanomaterial by the NanoGenoTox and high-shear dispersion methods, but more likely it seems to indicate that the reactivity of NM-401, that is not so oxidant as NM-400, increases with a better dispersion, achieved with the high-shear mixing protocol, because the active surfaces sites are more exposed to the medium.

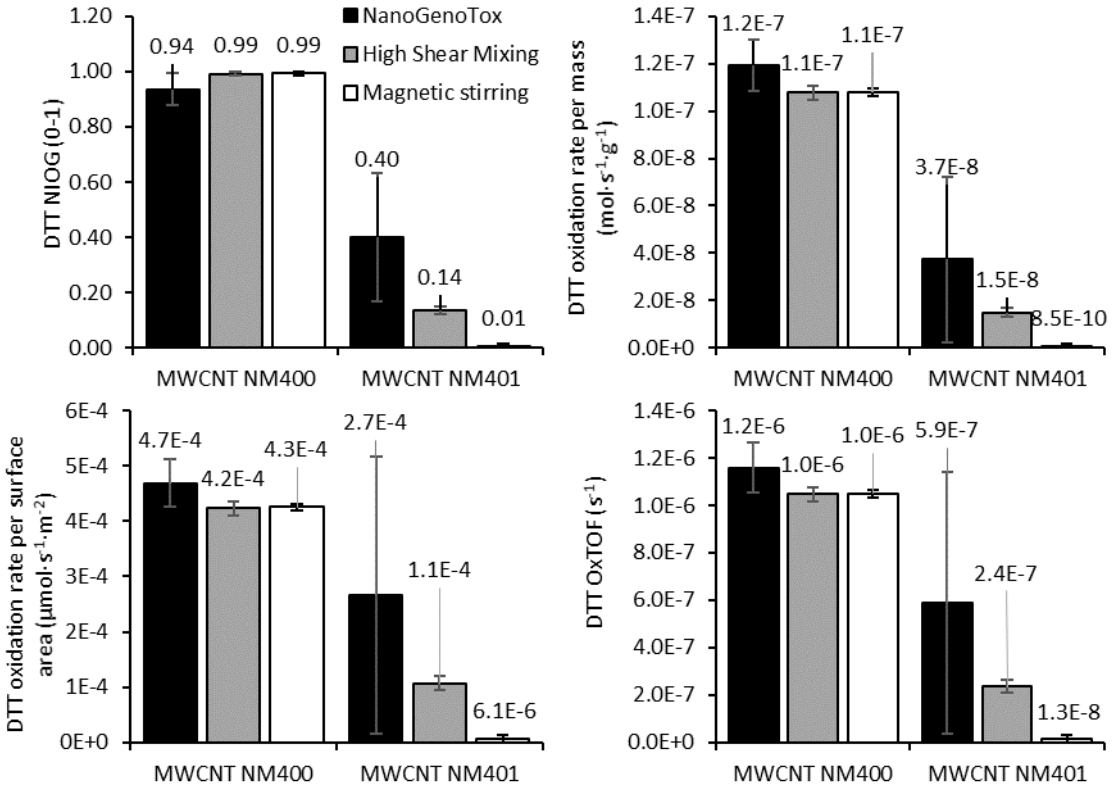


***Figure 31***. *Oxidative reactive descriptors for NM-400 and NM-401. Left, normalized index of oxidant generation (NIOG), obtained from DTT conversion. Middle, oxidative reaction rate normalized per surface. Right, oxidative reaction rate normalized per active site, OxTOF.*

The statistical analysis performed by two-way ANOVA evaluated the effect of composition and dispersion method. The results revealed significant effects of both nanomaterial composition and dispersion method on the reactivity during DTT

consumption (all $p<0.001$). The model explained a substantial portion of the variance across all metrics, with R-squared values exceeding 0.96, indicating an almost perfect fit.

Lastly, non-significant effects were obtained for cell viability and mutation frequency in TK6 cells following a 24h exposure to NM-400 and NM-401 at 20 µg/mL (Figure 32).

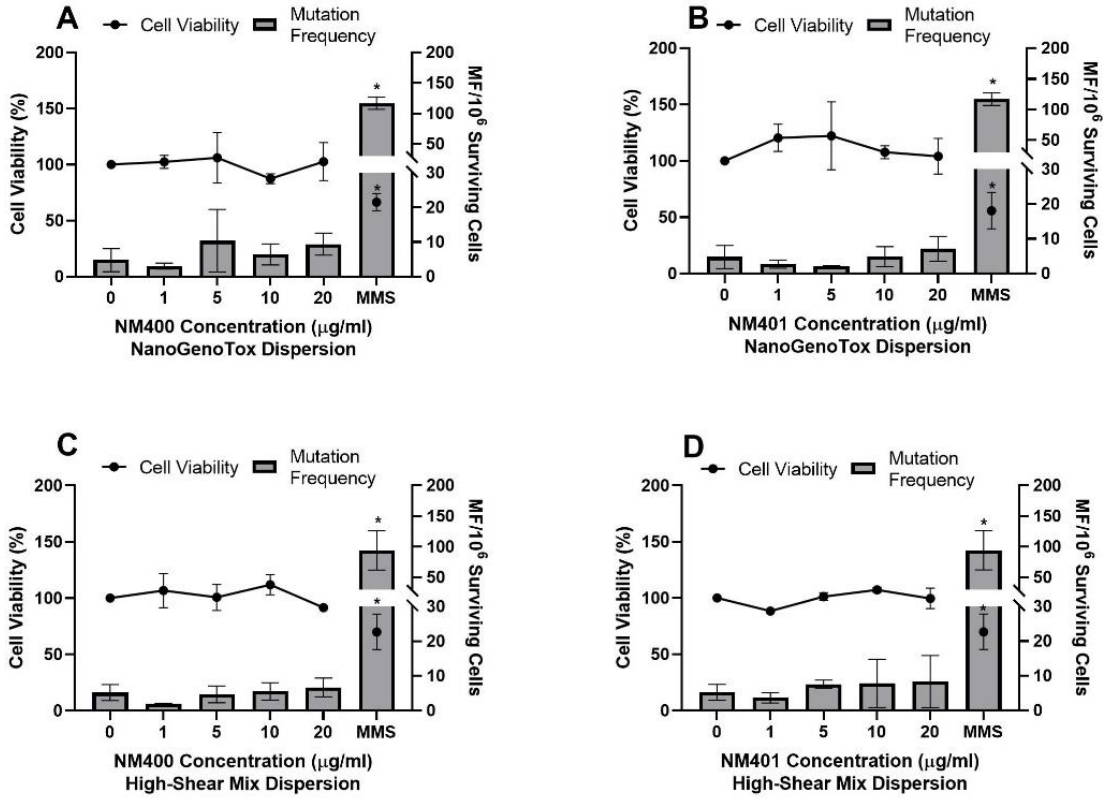


***Figure 32.*** *Cell viability and mutation frequency in TK6 cells following a 24h exposure to NM-400 and NM-401. Two dispersion approaches were utilised to generate the data, the NanoGenoTox protocol (A & B) and a high-shear mix protocol (C & D). A positive control of MMS was used throughout at a concentration of 1.5 µg/ml. The data represent the average ± the standard deviation. The data was considered statistically significant (*) when the alpha was set at $p \leq 0.05$ (n=3). Experiment performed by co-authors*

### 10.1.4 Discussion

The consistency of significant findings across different reactivity measures underscores the importance of both nanofiber type and dispersion method in catalyzing DTT oxidation. The interaction term's significance suggests that the efficacy of a dispersion method may not be generalizable across materials, necessitating tailored approaches for optimal activity. High R-squared values point to the robustness of the relationship between the factors studied and the reactivity outcomes.

As reported in chapter IV, these CNTs have been tested previously elsewhere: MWCNT NM-401 tested negative for DCFH2.[85] This low reactivity is in line with our data in chapter VII. Our measurements with different dispersion protocols demonstrate the increase of reactivity for MWCNT NM-401 when dispersed by NanoGenoTox and high-shear mixing. Moreover, MWCNT NM-400 induces significant increase of ROS levels for Cytochrome C assay,[145] which is supported by the measurements presented in this chapter and chapter VII for oxidation rates normalized to gravimetric concentration. Our hypothesis is that due to the low reactivity observed in methanol-TPSR and the low number of surface sites, the reactivity of this fiber is due to their impurities (see Table 12). Other authors detected the impurities, but they did not influence the MWCNTs toxicity.[39,189] This can explain the disparity between reactivity and toxicity, and support the literature that recognizes mode of actions based in bioaccumulation for fiber nanomaterials due to BET area and length as a main physicochemical properties to predict toxicity.[234]

## 10.2 Doped nanobiomaterials

### 10.2.1 Fe and Ti doping of hydroxyapatite

Nanobiomaterials (NBM) are natural or synthetic nanoscale materials that are highly biocompatible, i.e., nanostructured materials for biomedical applications.[241,242] The aim of this work is the surface characterization of nanobiomaterials for hazard assessment by methanol-TPSR and DTT consumption assay. We focus on the NBMs categorized as mineral nanostructures, specifically hydroxyapatites, which were selected for their diverse compositional properties relevant to applications in medical devices (MDs) and Advanced Therapy Medical Products (ATMPs). Biomineralized hydroxyapatites are particularly noteworthy for their suitability in tissue engineering, due to their ability to mimic the natural bone formation process.[243]

The hydroxyapatite nanobiomaterials tested in this study included three distinct types of laboratory synthetized hydroxyapatite, accessible through the BIORIMA project materials repository, and a commercial hydroxyapatite (referred to as HA sigma), procured from Sigma-Aldrich (Merck Life Science S.L.U., Portugal), used as reference for comparative purposes. This product, with a CAS number 12167-74-7, is a synthetic nanopowder

characterized by a particle size of less than 200 and a purity ≥97%. The three lab-synthesized materials include a calcium hydroxyapatite (referred to as CaP), distinguished by its lower crystallinity, superparamagnetic iron-doped hydroxyapatite (referred to as Fe-HA), and titanium-doped hydroxyapatite (referred to as Ti-HA). CaP, Fe-HA, and Ti-HA were prepared via an aqueous precipitation reaction, a method of high efficiency and scalability. These NBMs are designed for a range of applications including drug delivery, in vivo imaging, biosensing, therapy, tissue regeneration, and implant or wound coating. They are categorized as biomimetic/bioresorbable, eliciting specific cellular responses at the molecular level.[244,245]

### 10.2.2 Doping effect on surface reactivity

Among the two undoped and two doped hydroxyapatites, TiHA presented the highest BET surface area (95 $m^2/g$), followed by FeHA (77 $m^2/g$), CaP (58 $m^2/g$) and, finally, HA sigma with 18 $m^2/g$ (Figure 33, left) . However, the greater surface area of CaP compared to HA sigma was not reflected in a greater specific number of sites: both chemisorbed 0.15 mmol of methanol per unit mass, as shown in Figure 33 (middle). In addition, Fe and Ti doped materials exhibited higher methanol chemisorption (0.23 and 0.19 mmol of methanol per gram, respectively). The trend is reversed when active sites surfaces density is analyzed: HA sigma exhibits more active sites per surface ($nm^2$) than CaP and doped hydroxyapatites.

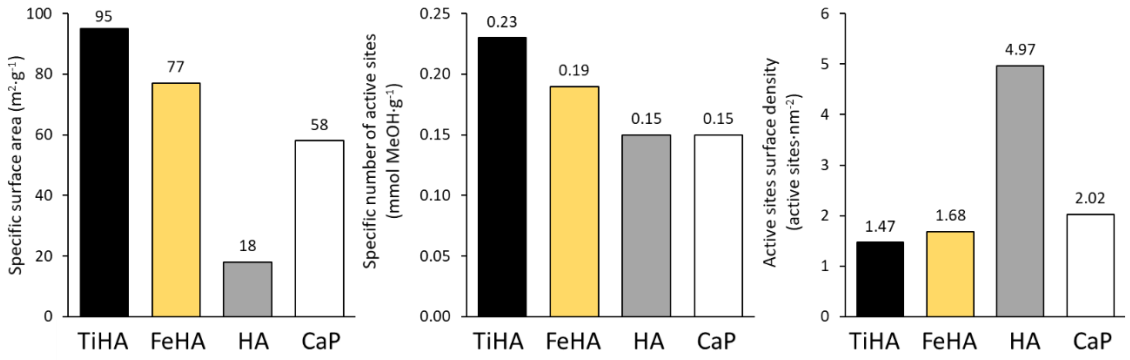


***Figure 33.*** *Left, specific surface area obtained by $N_2$ adsorption isotherm (BET). Middle, number of sites per gram. Right, active sites surface density obtained by combination of methanol chemisorption and BET data.*

According to methanol temperature-programmed surface reaction, HA sigma (Figure 34a) shows mainly redox and basic reactivity, since small amounts of carbon dioxide and formaldehyde were detected as reaction products. However, the high carbon dioxide signal obtained in the reaction with CaP (Figure 34b) indicates that it is a mainly basic nanomaterial. The trend varies for the doped NBMs: Ti doping leads to an acid reactivity not detected in HA, reflected in dimethyl ether signal (Figure 34c). In addition, a decrease in the formaldehyde signal is observed. However, Fe doped NBM (Figure 34d) shows a slight signal of dimethyl ether (acid reactivity) and a large increase in the formaldehyde and carbon dioxide signals.

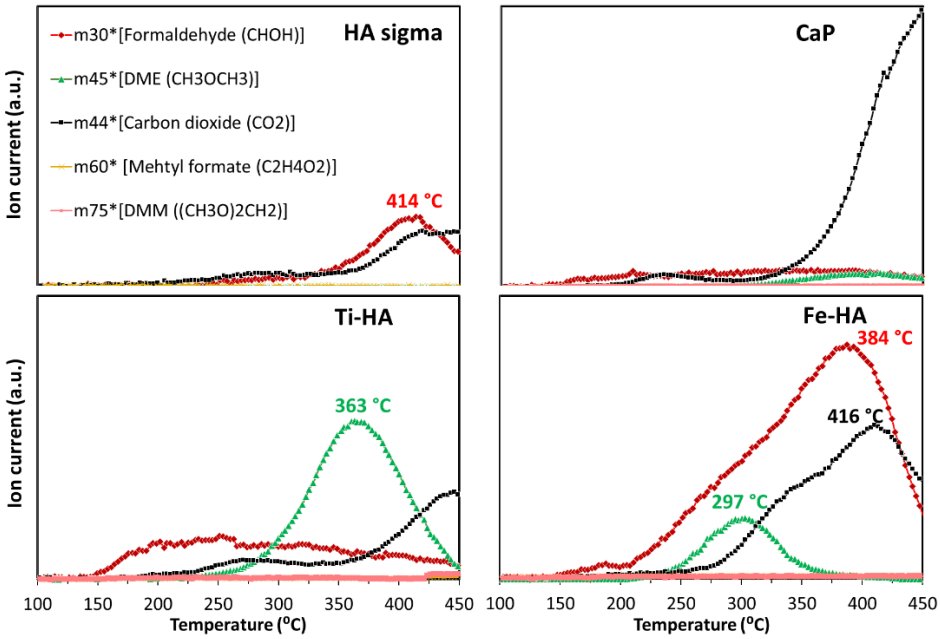


***Figure 34.*** *Temperature-programmed surface reaction products of pre-adsorbed methanol for HA sigma (a), CaP (b), Ti-HA (c) and Fe-HA (d).*

Acid, basic and redox reactivity of each nanomaterial are compared in Figure 35, based in dimethyl ether, carbon dioxide and formaldehyde signal. The biggest area for dimethyl ether signal was obtained for TiHA (Figure 35a). CaP exhibits the most basic behavior; as no $CO_2$ conversion at low temperatures (100-250ºC) was obtained, no over-oxidation occurred for any nanomaterial (Figure 35b). FeHA produced the highest methanol conversion to formaldehyde of all ENMs (Figure 35c). Ti and Fe doping produce an increase in acid reactivity in front CaP and HA, as shown in Figure 35d. In addition, adding Fe on the surface, the formaldehyde signal is increased after methanol reaction, so redox reactivity is reflected. Depleted DTT (NIOG) normalized to 0-1 values by positive control

($H_2O_2$, 30% wt.) is used as a descriptor for reactivity based on oxidative capacity. CuO from Sigma-Aldrich, evaluated in previous chapters, is used as an ENM control, to compare values between nanobiomaterials and a well-characterized ENM.

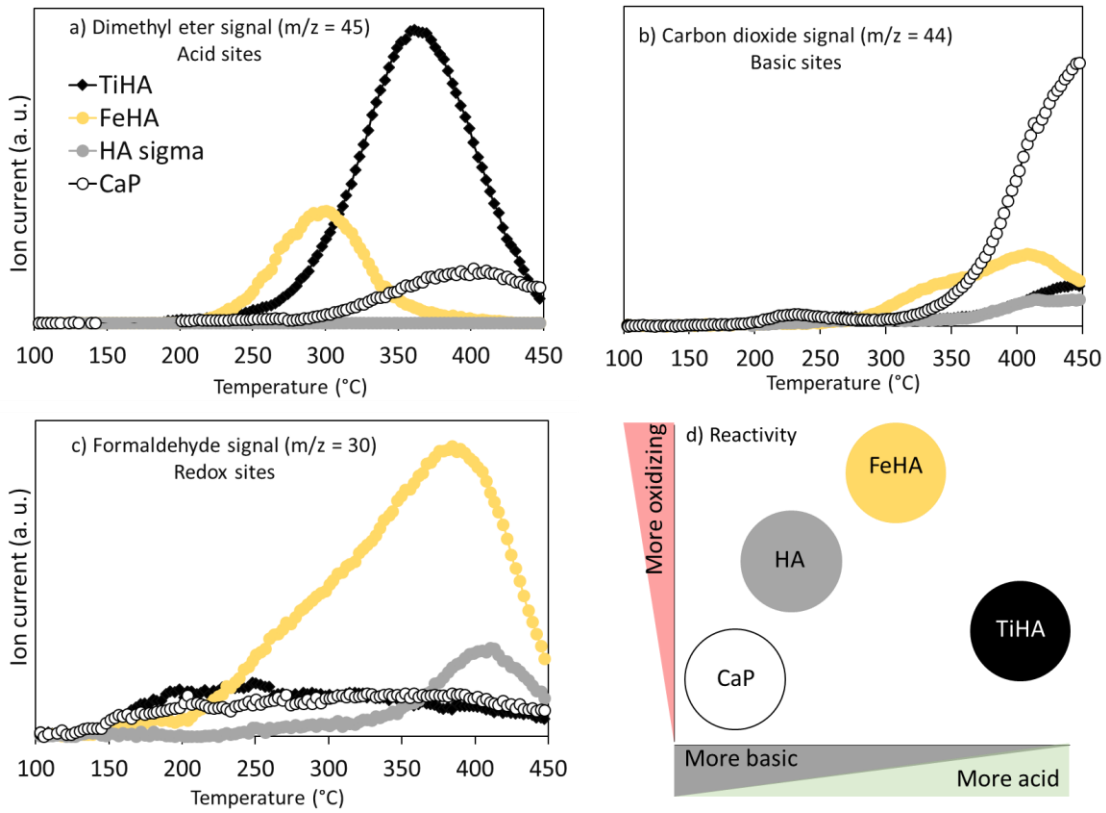


***Figure 35***. *Comparative MeOH-TPSR reactivity of HA sigma, CaP, Ti-HA and Fe-HA active sites. Acid (a), basic (b) and redox (c) sites and summarized MeOH-TPSR reactivity (d)*

Figure 36 shows a slightly higher consumption of thiol groups by FeHA (0.26). Less DTT was depleted by TiHA, HA sigma and CaP (0.20, 0.10 and 0.10 respectively). Reaction rates in DTT oxidation were evaluated and normalized by three different physical properties: mass, surfaces and active sites surfaces density (Figure 36). FeHA is the most oxidizing nanomaterial per mass and reactive sites. Reaction rate per surfaces values for HA sigma were higher than DTT reaction data normalized by mass or active sites, due to the small BET surfaces of HA. TiHA is the nanomaterial that consumed a lower amount of thiol groups for all the reaction rates. CaP and HA obtained similar results from OxTOF and DTT reaction rate per mass, contrary to normalization by surface, since CaP has three times larger BET surface area.

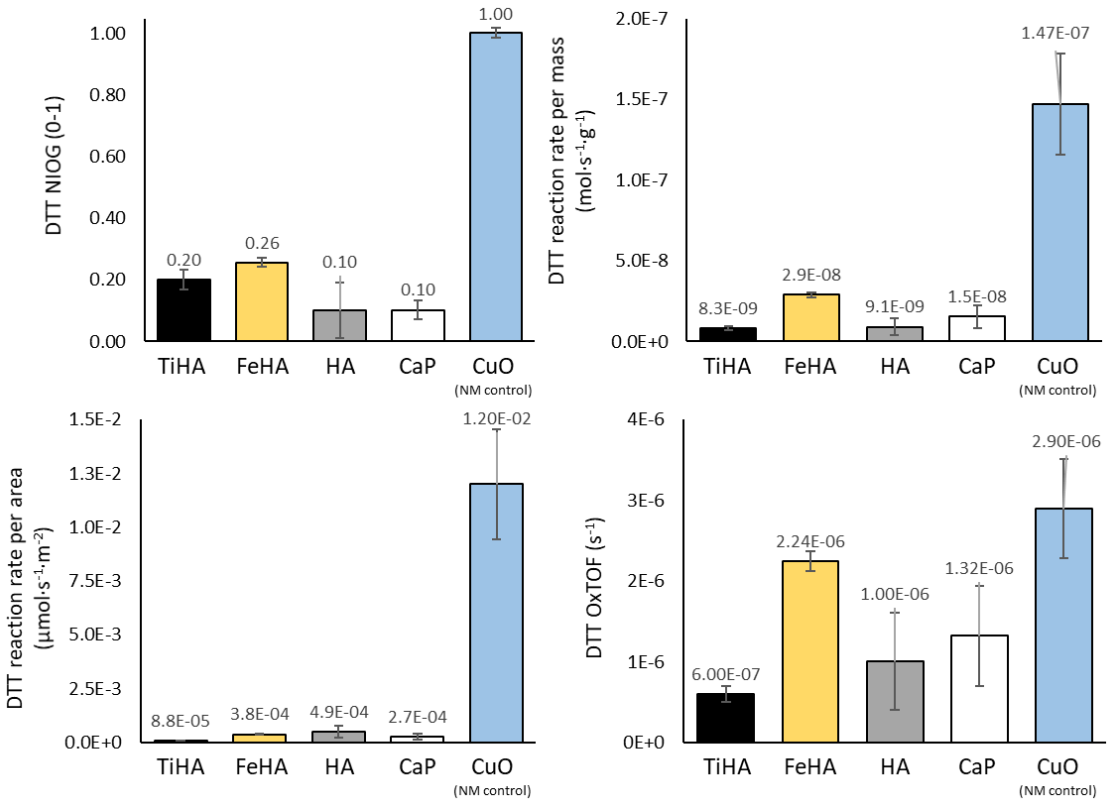


***Figure 36.*** *Oxidative capacity by DTT depletion assay. DTT depletion normalized by a positive control, NIOG (A); Oxidative reaction rates normalized per mass (B), surface (C) and reactive sites, OxTOF (D).*

## 10.3 Multicomponent nanomaterials

In recent decades, advancements in technology have spurred the proliferation of engineered nanomaterials in consumer goods. Emerging multicomponent engineered nanomaterials (MCENMs) are defined by: (i) their amalgamation of two or more nanoscale components of distinct composition, dimensions, and forms connected through robust molecular/macromolecular interactions or other physicochemical forces, or (ii) ENMs originating from a singular chemical source but modified by rigid or flexible coatings.[246] Such combinations aim to augment existing features of individual components or introduce multifunctionality. These conjugations may involve carbonaceous (e.g., fullerenes, carbon nanotubes, graphene) or metallic ENMs (e.g., gold, silver, platinum, titania, zinc oxide) paired with organic (e.g., porphyrins, phthalocyanines, enzymes) or inorganic components.[246,247] For instance, graphene's distinct attributes, such as enhanced conductivity, optical clarity, and mechanical resilience, have facilitated

its application in various devices like solar cells, fuel cells, supercapacitors, and sensors. Yet, due to its limited catalytic potential, graphene is often combined with catalytic nanoparticles or quantum dots for utilization in fuel cells or optoelectronics, generating hybrid materials that integrate the merits of both graphene and nanoparticles.[248,249] Another manifestation of this enhanced functionality is evident in the $SiO_2$·$TiO_2$ nanoparticle synergy, which amplifies the photocatalytic degradation of organic dyes introduced into aquatic ecosystems from industrial sources.[250] Similarly, $SiO_2$·$TiO_2$ core-shell nanospheres have demonstrated exceptional photocatalytic efficiency in degrading air pollutants like NOx and organic contaminants such as 4-nitrophenol.[251]

Nevertheless, alongside the manifold advantages of MCENMs, escalating apprehensions revolve around their plausible threats to human well-being and the environment. These anxieties stem from their nanometric scale and the intricacies involved in evaluating the toxicity of a complex system. Such systems may exhibit varying degradation rates and toxicities of their individual and combined components, further complicated by diverse interactions with biological and environmental matrices.

Upon exposure to environmental and biological environments, MCENMs may undergo transformations that alter their physico-chemical properties, encompassing processes like surface adsorption, ligand substitution, dissolution, re-crystallization, and reaction dynamics. Furthermore, the nature of these processes can be influenced by the properties of the surrounding medium, including factors like pH, ionic concentration, and the presence of other entities such as amino acids, natural organic substances, and solutes.[252]

### 10.3.1 Metal oxide composite nanomaterials

Both the single components and the $SiO_2$·ZnO were provided as powders by the CIAC company (Cordoba, Spain). $SiO_2$ NMs were purchased from NanoAmor (Houston, USA), while ZnO NMs were produced starting from zinc acetate dihydrate (purity 99.5% Merk, Aldrich). The selection of the three nanomaterials evaluated in this section is predetermined by the requirements of the European project SUNSHINE. The approach followed within SUNSHINE to design the $SiO_2$·ZnO has been aligned to the safety dimension of the SSbD framework.

### 10.3.2 Methanol-TPRx

The reactivity analysis of low-reactive metal oxides via MeOH-TPRx provides insight into the primary reactivity of the surface reactive sites of nanomaterials. $SiO_2$ (Figure 37, left) exhibits acidic reactivity, characterized by to the formation of dimethyl ether (DME, green trace). Additionally, a very low formation of formaldehyde (red trace) suggest the presence of redox sites, which are not typical of silica. ZnO (Figure 37, middle) displays a redox character as evidenced by the formation of formaldehyde. Lastly, the presence of ZnO on $SiO_2$ surface results in a system that has both acidic and redox properties (DME and HCHO formation, respectively). (Figure 37, right).

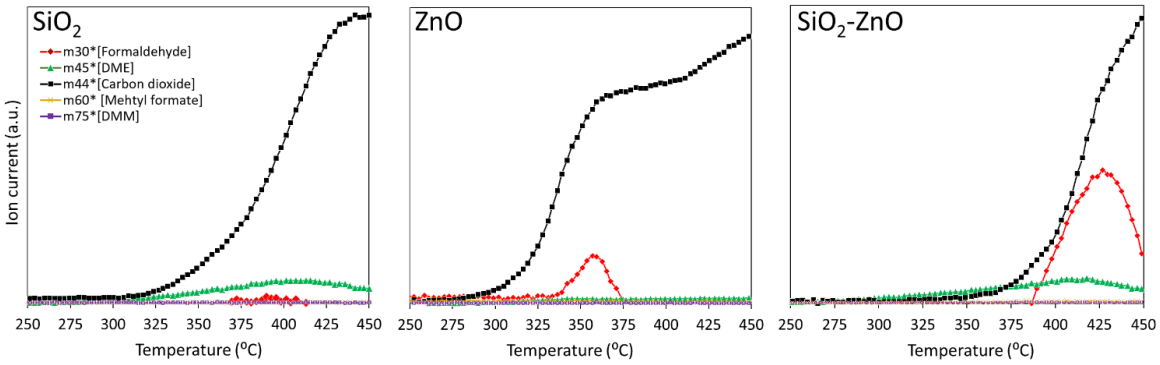


***Figure 37.*** *Temperature-programmed reaction products of pre-adsorbed methanol analyzed by mass spectroscopy for $SiO_2$ (left), ZnO (middle) and $SiO_2$·ZnO (right).*

This reactive profile indicates that silica (acidic) is not totally covered by ZnO. Therefore, $SiO_2$·ZnO exhibits reactive properties from ZnO and uncovered $SiO_2$, but no new reactive properties appear to be generated at the $SiO_2$·ZnO interface.

### 10.3.3 Raman evaluation of multi-composite nanomaterials

The Raman spectra of ZnO, $SiO_2$, and $SiO_2$·ZnO are presented in Figure 38, displaying both the mean spectrum and the standard deviation contour. $SiO_2$ exhibits a multitude of bands, some of which, such as those at 1157 and 580 $cm^{-1}$, are unusual in these samples, when compared with the literature.[253] The silica vibrations involving Si-O-Si bonds are attributed to symmetrical stretching and network bending modes, which manifest as Raman bands at 797 $cm^{-1}$ and in the range of 444-483 $cm^{-1}$, respectively, while the surface Si-OH stretching mode exhibits characteristic band at 970 $cm^{-1}$.[253]

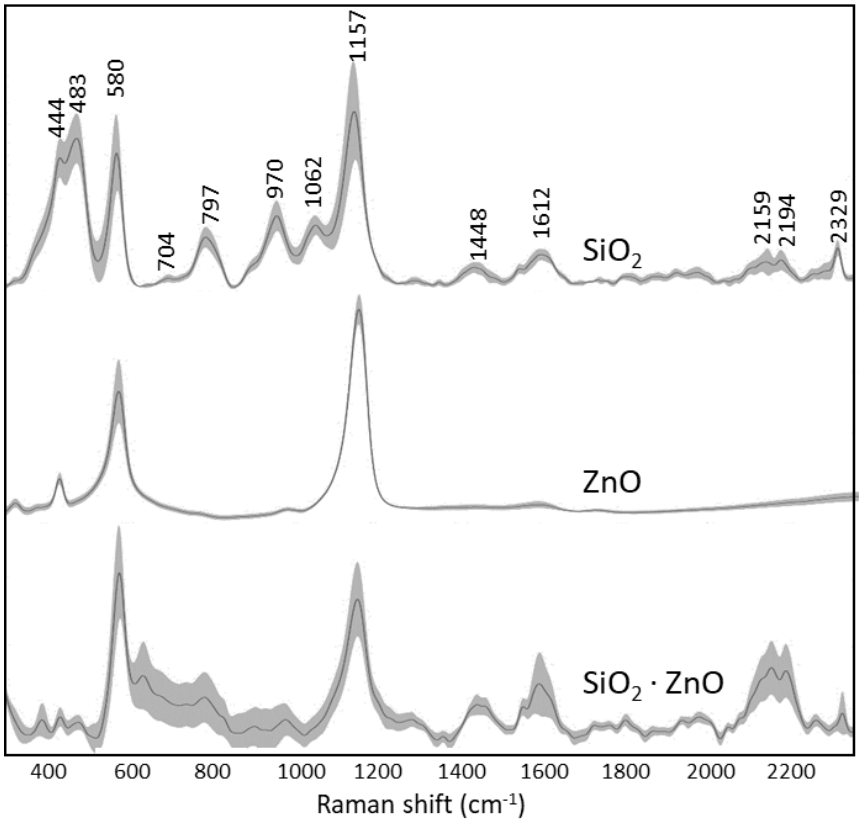


***Figure 38**. Averaged Raman spectra of $SiO_2$, ZnO and $SiO_2$·ZnO, and the standard deviation contour. Raman map contained at least 10 spectra of random points in the catalyst. The nanomaterial spectra are normalized by Standard Normal Variate (SNV) method.*

ZnO displays remarkable homogeneity in all spectra, prominently featuring two main bands at 580 and 1157 $cm^{-1}$, along with a third, less intense band at 444 $cm^{-1}$. The Raman windows between 300-600 is in line with previously reported results elsewhere for ZnO nanorods.[254] The band at 580 $cm^{-1}$ is associated to the $E_1(LO)$ mode of ZnO, while 444 $cm^{-1}$ refers to $E_2$.[254,255] The intense Raman band at 1157 $cm^{-1}$ has been assigned to wurtzite-type ZnO structures,[256] indicating its common occurrence in ZnO crystals.[257] $SiO_2$·ZnO demonstrates the presence of ZnO on the material's surface, as its two most intense bands are representative of this material. Furthermore, there are low-intensity bands at 797 $cm^{-1}$, related to Si-O-Si, and in the regions of 1400-1600 and 2000-2400 $cm^{-1}$, indicating the presence of $SiO_2$ in specific gaps on the surface of the nanomaterial. Thus, not the entire surface appears to be coated with ZnO. The high intensity of the latter's bands enables the detection of its presence on the surface and as an impurity, as seen in pure $SiO_2$, which, as commented previously, exhibits unexpected bands possibly due to contamination.

## 10.4 Micro and nano plastics

Micro and nanoplastics (MNPs) are a widely recognized global problem due to their prevalence in natural environments and the food chain.[258–261] The detection of MNPs in the food chain has sparked health concerns due to their potential ingestion.[258–261] Moreover, MNPs, either intentionally produced or from larger plastic degradation, can bind with heavy metals and other pollutants.[260] However, the impacts of MNPs on human microbiota and their possible biotransformations during the gastrointestinal tract have not been well reported.[259,262–264] Assessing their risks remains challenging for global researchers.[259,262–264]To evaluate the potential risks of micro and nanoplastics at the digestive level, completely passing a single dose of polyethylene terephthalate (PET) and Polylactic acid (PLA) through the gastrointestinal tract was simulated by combining an harmonized static model and the dynamic gastrointestinal simgi® model, which recreates the different regions of the digestive tract in physiological conditions. Lab-made test PLA and PET microplastics were obtained by cryomilling at CSIC-ICV (Dr. J.J. Reinosa). The structural changes of PLA and PET caused by the cryomilling procedure as well as by the gastrointestinal digestion and colonic fermentation were evaluated by micro-Raman using a Renishaw InVia Qontor spectrometer. Each spectrum consisted of 120 accumulations of 1 s with a laser power or 1.5 mW. First, the surface of each sample was mapped on at least 60 points with a 514 nm excitation line laser using a 50× microscope objective to generate data representative of the state of the sample. Then, in selected points of each PLA sample, where PLA surface showed spectral changes, a depth profile at 1 µm steps from over the surface towards the bulk was measured with a 405 nm excitation line laser using a 100× microscope objective in confocal configuration. Every sample was mapped on at least 20 points per depth layer to generate a representative depth profile.

### 10.4.1 MNPs: Polyethylene terephthalate

Section extracted from "PET microplastics affect human gut microbiota communities during simulated gastrointestinal digestion, first evidence of plausible polymer

biodegradation during human digestion", an article published in Scientific Reports. DOI: https://doi.org/10.1038/s41598-021-04489-w

In Europe, polyethylene terephthalate (PET) is commonly found in beverage containers.[265,266] A study revealed PET microparticles in human feces, suggesting gastrointestinal interactions.[267] Stock et al. examined MP behavior in the digestive process, but not in the colonic phase. [268] Health effects from ingested MPs might include tissue irritation or intestinal microbiome imbalance[261] with potential systemic implications. Recent studies hypothesized that chronic MNP exposure could disrupt the gut microbiome across species.[269] However, the exact effects on human gut microflora are unclear, with limited studies primarily in animal models.[270–272]

#### 10.4.1.1 Synthesis of PET nanoparticles for human fate studies

A simple approach to obtain nanoplastics consists of dissolving a macroscopic plastic in an organic solvent and then precipitating it in a controlled manner in water. We have followed this procedure to obtain PET nanospheres from additive-free PET pellets and from a PET juice bottle, being the former more difficult to dissolve in HFIP, probably due to the additives present in the juice bottle.

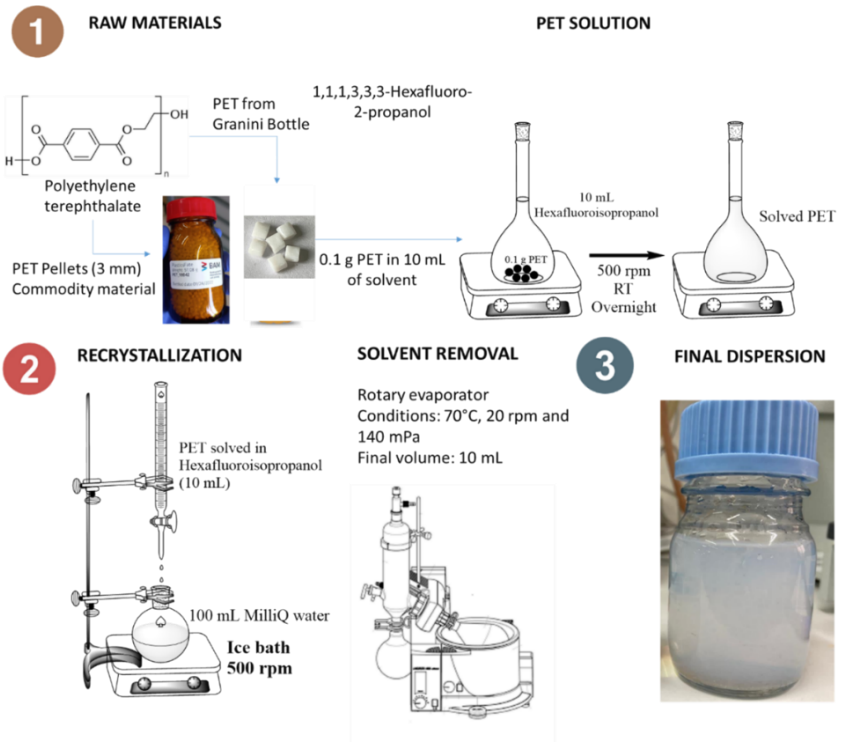


***Figure 39.*** *Synthesis protocol to obtain a reference PET at the nanoscale dispersed in MilliQ water.*

Scanning electron micrographs of the PET nanospheres show their relatively homogeneous size distribution and regular spherical shape (Figure 40, right). Their size has been measured by DLS (Figure 40, left) to be 83 nm ($D_{50}$).

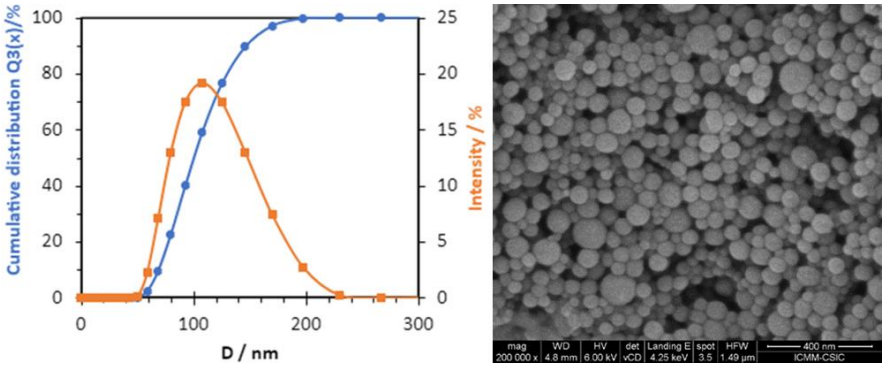


***Figure 40**. Particle size distribution (left) and FE-SEM (right) of PET nanoparticles in water suspension.*

The nano PET suspension was stable. 72 h after production the transmission between 0-39 mm height did not increase (Figure 41), indicating that the nanoparticles remained suspended without sedimentation. Some air bubbles were accumulated on the side of the vial, therefore curvatures in the transmission were obtained in those areas. The transmission increase (80%) in the height of 39-40 mm is due to the beginning of the dispersion.

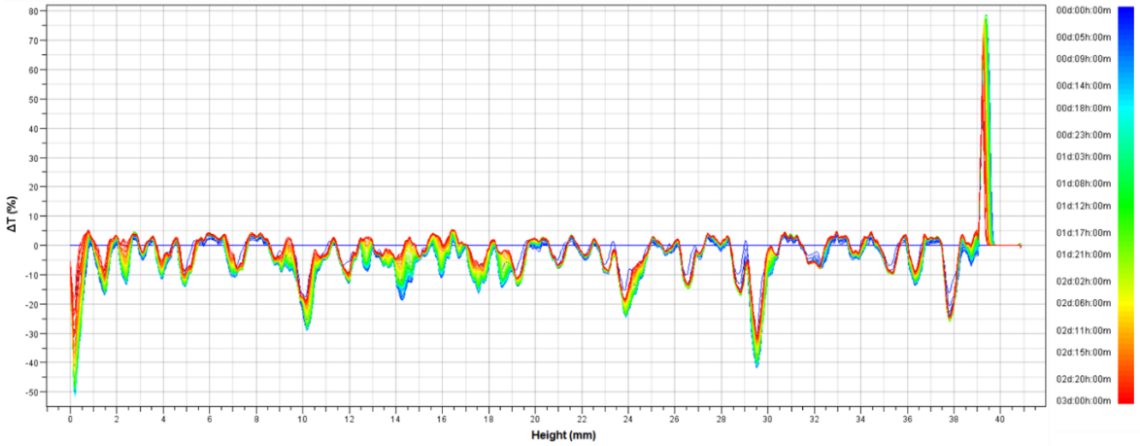


***Figure 41**. PET nano particles dispersion stability performed by Turbiscan.*

The Raman spectra of the PET raw materials (commodity and juice bottle) and the derived nanoparticles in the spectral window between 1800 and 600 $cm^{-1}$ shown in Figure 42 reflect the structural changes upon conversion of PET to nanometric size. The two most

characteristic and intense modes of polyethylene terephthalate are at 1726 (C=O stretching), associated to the conformation of the terephthalate groups, and 1614 (C=C stretching) $cm^{-1}$, assigned to the benzene ring vibration, in line with the literature.[273,274] The spectral windows at 1780-1680 and at 1220-1060 $cm^{-1}$ Raman shift have been described as indicators of crystallinity of PET.[275] Figure 42 shows a decreased intensity in mode at 1094 $cm^{-1}$, due to an amorphization of PET after treatment for conversion to nanometric size.[276] Consequently, a broadening of the Raman mode at 1726 $cm^{-1}$ is an effect of the loss of crystallinity.[277] PET bottle and commodity crystallinity is compared with 1186-1176 $cm^{-1}$ bands: Raman mode at 1186 $cm^{-1}$ is assigned to crystalline PET referred to the ring ester CCC bending, which is shifted to 1176 $cm^{-1}$ for amorphous PET. PET bottle exhibit a shifted mode to 1176, while the PET commodity presents a greater ratio 1186 vs 1176, therefore PET commodity > PET bottle in terms of crystallinity.[275] The strongest Raman mode at 1614 $cm^{-1}$ remained unaltered.

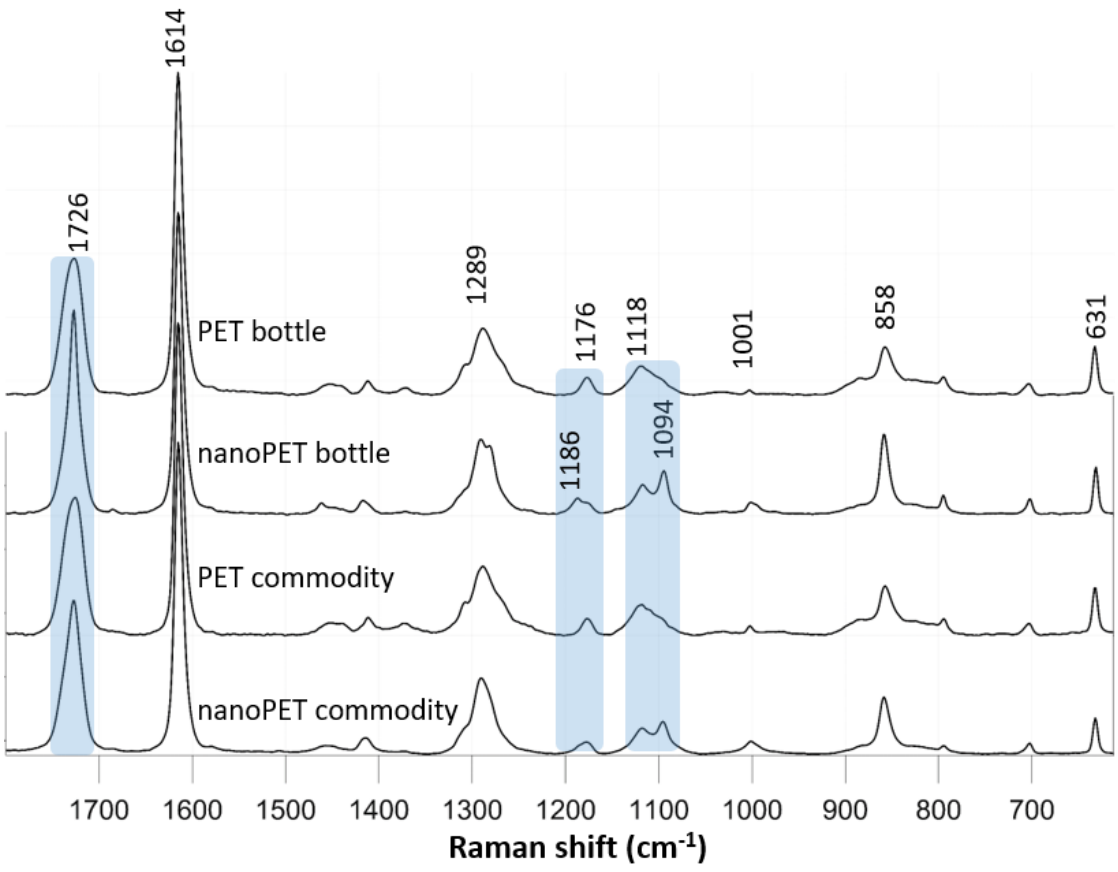


***Figure 42***. *Raman spectra of PET raw materials (bottle and commodity) and the derived nanoparticles. Laser wavelength: 514 nm.*

#### 10.4.1.2 Raman characterization of PET during human digestion

PET MPs started several biotransformations in the gastrointestinal tract and appeared to expose the colon in ways that were structurally different from the original forms. We report that the feeding with microplastics alters human microbial colonic community composition, and hypothesize that some members of the colonic microbiota could adhere to MPs surface promoting the formation of biofilms. The work presented here indicates that microplastics are indeed capable of digestive-level health effects. Considering this evidence and the increasing exposure to microplastics in consumer foods and beverages, the impact of plastics on the functionality of the gut microbiome and their potential biodegradation through digestion and intestinal bacteria merits critical investigation.

The Raman spectrum of PET presents the characteristic modes of polyethylene terephthalate, in line with known literature.[273] The spectral windows at 1780-1680 and at 1220-1060 $cm^{-1}$ Raman shift shown in Figure 43 are of particular relevance to assess the crystalline order of PET.[275,278] Figure 43A through 40 show a progressive amorphization of PET. The Raman mode at 1727 $cm^{-1}$ is associated with carbonyl stretching vibrations and is sensitive to the conformation of the terephthalate groups. In crystalline PET C=O groups are coplanar with an aromatic ring and in trans conformation with each other; these carbonyl groups arrange randomly with respect to the aromatic ring in amorphous PET[279]. A broadening of the band at 1727 $cm^{-1}$ is the consequence of a loss of crystallinity, as illustrated in the literature.[280] In addition, the Raman mode at 1186 $cm^{-1}$ associated to the ring ester CCC bending in crystalline PET shifts to 1176 $cm^{-1}$ in amorphous PET.[275] Cryomilling PET pellets to the original PET MPs results in a discrete broadening of 1727 $cm^{-1}$ Raman band of the carbonyl and shift of the 1186 $cm^{-1}$ band of the ester, which are apparent at some spectra of PET MPs.

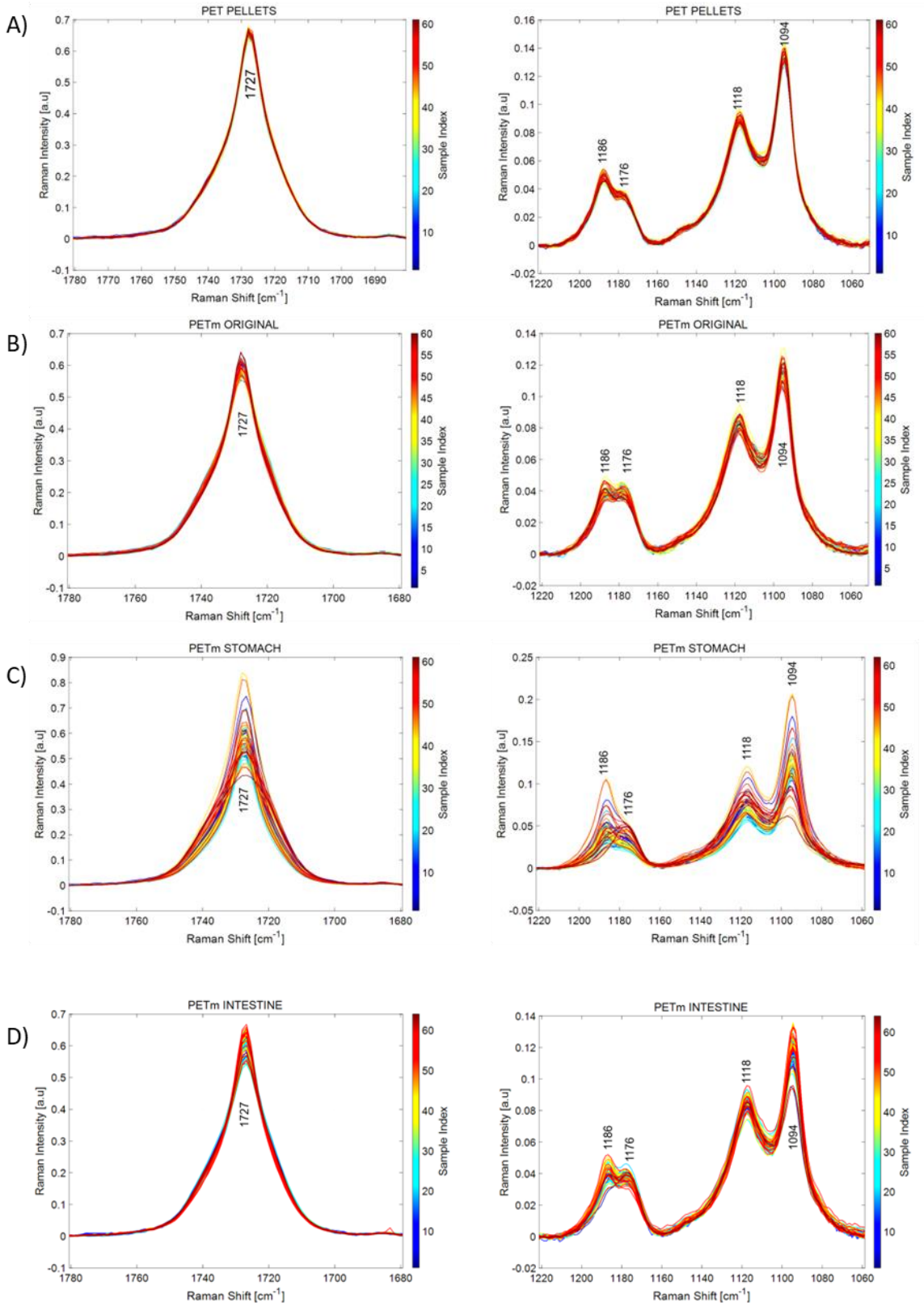
A)
PET PELLETS
Raman Intensity [a.u]
Raman Shift [cm$^{-1}$]
Sample Index
1727
PET PELLETS
1186
1176
1118
1094
B)
PETm ORIGINAL
1727
PETm ORIGINAL
1186
1176
1118
1094
C)
PETm STOMACH
1727
PETm STOMACH
1186
1176
1118
1094
D)
PETm INTESTINE
1727
PETm INTESTINE
1186
1176
1118
1094

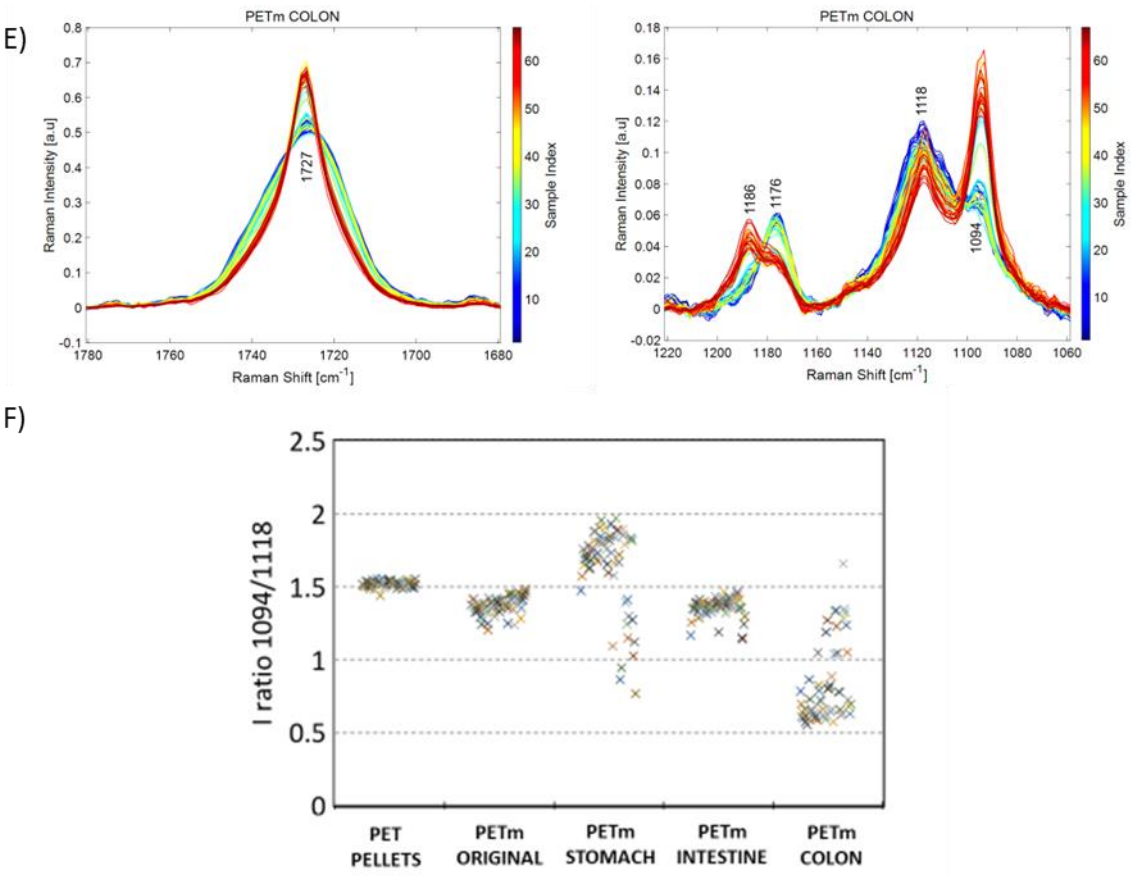


***Figure 43***. *Raman spectra at 60-70 representative points of PET pellets a); original PET microplastics (MPs) b); PET MPs after in vitro gastric digestion c); PET MPs after in vitro gastrointestinal digestion d); PET MPs after in vitro gastrointestinal digestion e); PET MPs after in vitro colonic fermentation and f) show the evolution of relative intensity of 1118 modes vs. 1094 cm$^{-1}$ during digestion simulation. Extracted from our work (Tamargo et al.)*[281]

The effect of stomach and intestine digestion is increasingly apparent on the states of PET MPs, where an increasing number of spectra show progressive amorphization. Such a trend is more evident after colonic fermentation, (Figure 43E). Further to these two Raman modes, the rise in the relative intensity of 1118 vs. 1094 cm$^{-1}$ is also associated with oxidative amorphization of PET.[278] The relative intensity of 1118 modes vs. 1094 cm$^{-1}$ is progressively higher as PET MP evolves along the different digestion stages, as observed in Figure 43F, which is consistent with the trends uncovered by the 1727 and 1186-1176 cm$^{-1}$ Raman modes. This evolution indicates a trend in the structural degradation of the PET MPs during the gastrointestinal digestion. These results were supported by FE-SEM images performed by other co-authors (Figure 44).

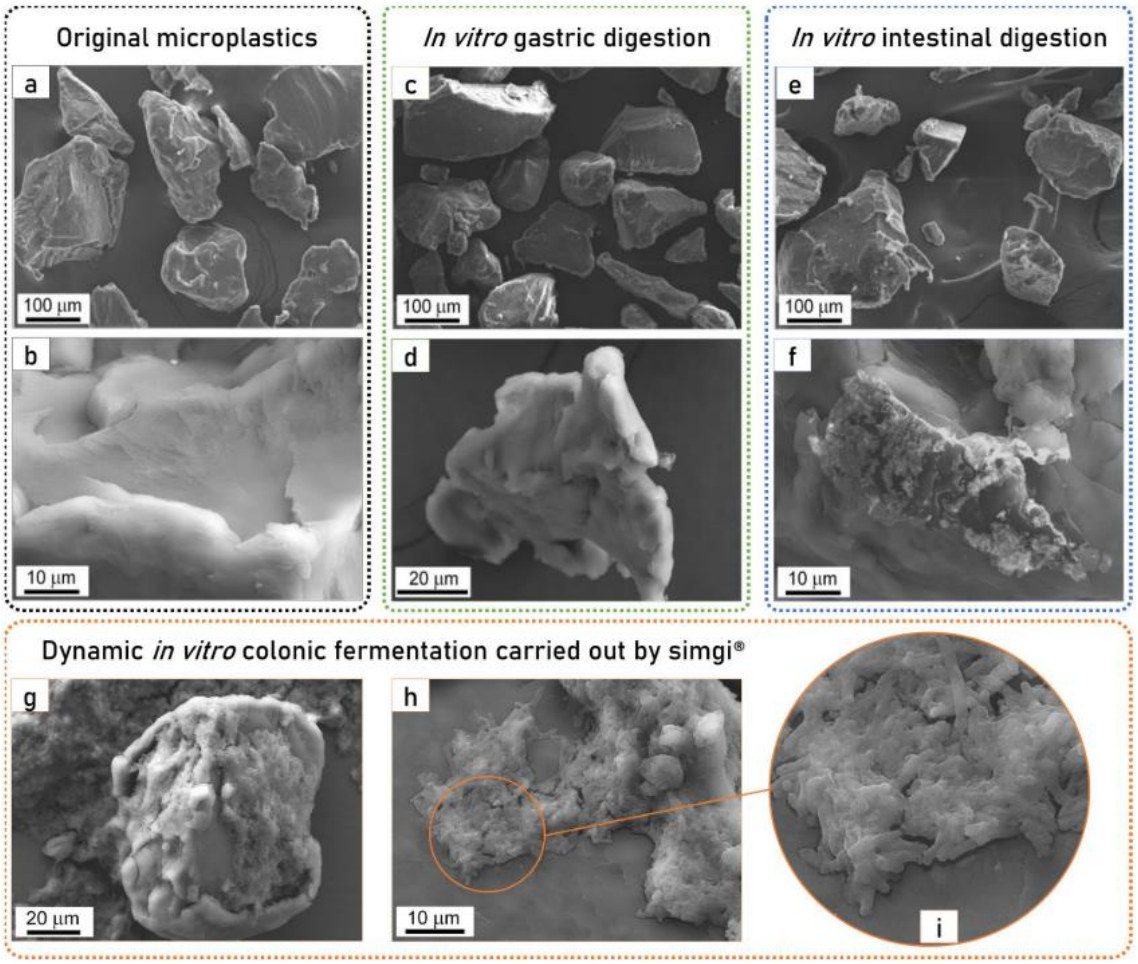


***Figure 44**. Micrographs by field emission scanning electron microscope (FESEM) of polyethylene terephthalate microplastics: (a,b) original PET microplastics (MPs), (c) and (d) PET MPs after in vitro gastric digestion, (e,f) PET MPs after in vitro gastrointestinal digestion, (g–i) PET MPs after in vitro gastrointestinal digestion and colonic fermentation. Figure and experiments performed by co-authors (Dr. J.J. Reinosa and Prof. Jose Francisco Fernandez).*

#### 10.4.1.3 Impact of PET intervention on colonic microbiota

Regarding the impact of microplastics intervention on colonic microbiota, the co-authors (Alba Tamargo, Natalia Moliero and Victoria Moreno-Arribas) performed microbiological analysis to understand the MPs-microbiota interactions. Utilizing plate counting and 16S rRNA gene sequencing, they observed that the presence of MPs affected microbial populations differently. Plate counting showed that lactic acid bacteria, *Enterococcus* spp., and *Staphylococcus* spp. largely remained stable over 72 hours of colonic fermentation in two subjects, though there was a significant reduction in *Staphylococcus spp*. in one instance following MPs exposure. A pronounced reduction was also noted in both aerobic and anaerobic bacteria, including *Bifidobacterium* spp. and *Clostridium* spp. The

Enterobacteria group exhibited a substantial decrease initially, with subsequent variable trends across subjects.

Further insights were gained through 16S rRNA sequencing, which revealed a decrease in alpha-diversity. Post-MPs exposure, significant changes in the relative abundance of several phyla were noted, which were specific to different colonic compartments. For example, increases in *Firmicutes* and *Desulfobacterota* and decreases in Bacteroidetes were observed in particular compartments. Genus-level analysis corroborated these shifts, highlighting decreases in Bacteroides and Parabacteroides, especially in certain compartments, while *Escherichia/Shigella* and *Bilophila* levels increased in others.

The exposure to PET microplastics resulted in substantial alterations in the colonic microbiota. These alterations included a decrease in microbial diversity and compartment-specific shifts in the abundance of certain microbial taxa, with these effects varying between individuals.

### 10.4.2 MNPs: Polylactic acid

Section extracted from "Simulated gastrointestinal digestion of polylactic acid (PLA) biodegradable microplastics and their interaction with gut microbiota", an article published in Science of the Total Environment (STOTEN). DOI: https://doi.org/10.1016/j.scitotenv.2023.166003 [283]

Polylactic acid (PLA), recognized as the predominant bioplastic utilized in the food and medical sectors, boasts characteristics such as biodegradability, biocompatibility, and Generally Recognized As Safe (GRAS) status.[282] Nevertheless, recent investigations using animal models have revealed that PLA MPs can disrupt intestinal microbiota. To this point, there have been no reported studies on the potential gastrointestinal and health ramifications stemming from human consumption of PLA MPs. This study aims to mimic the ingestion of a realistic daily quantity of PLA MPs and their progression through the gastrointestinal tract. It achieves this by integrating the INFOGEST method with the simgi® gastrointestinal model. Raman spectroscopy is employed to assess morphological modifications of PLA MPs post-gastric digestion phase, including

adherence of organic matter, microbial biofilm formation, and surface biodegradation during the intestinal and colonic phases. Given these findings and the burgeoning adoption of bioplastics, comprehending their effect on human health and potential biodegradation via gastrointestinal digestion and interaction with human microbiota is of paramount importance for further investigation.

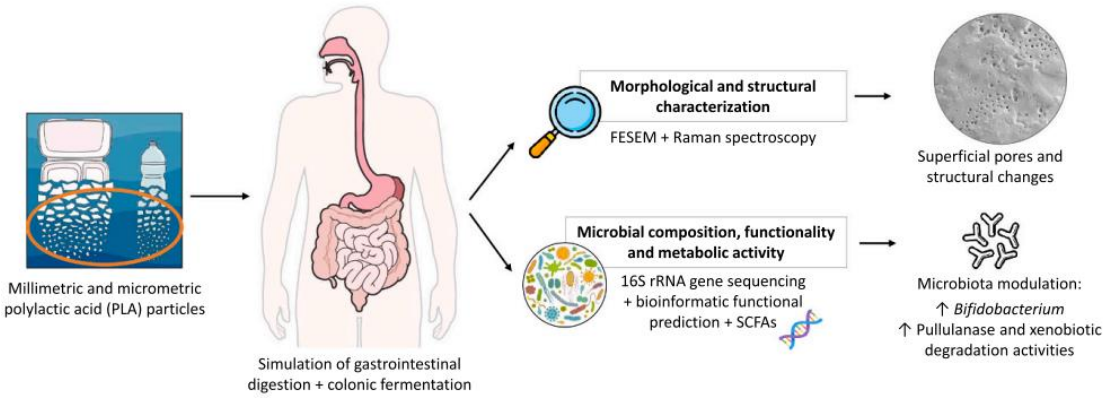


***Figure 45.*** *Methodology to unravel the mode of action of PLA MPs after exposure to gastrointestinal digestion. The protocol was divided in three different aspects: microbiological analysis to understand the impact of PLA MPs on microbiota, FE-SEM studies for deciphering the surface pores in PLA samples and microbiota deposition, and Raman spectroscopy to examine the structure of PLA in all the gastrointestinal digestion steps. Extracted from our work Jimenez-Arroyo et al.*[283]

The degradation and crystalline state of PLA was monitored by Raman spectroscopy (Figure 46). PLA Raman bands assignment can be found elsewhere. [284] The strong Raman mode at 873 $cm^{-1}$, corresponding to backbone vs C-COO in PLA has been used to normalize Raman spectra. 60 representative spectra of PLAg show no appreciable differences (Figure 46A), in line with the homogeneity observed in FESEM. In the case of the PLAm before GI stages, the slight variability between the 60 Raman spectra (Figure 46B) does indicate some structural changes in PLA as a consequence of the cryomilling process, in line with incipient modification illustrated by FESEM. The Raman spectra of PLAg and PLAm samples after the oral phase (Figure 46C and D, respectively) hardly show any difference with respect to their fresh counterparts, in line with FESEM micrographs that only show the accumulation of some salts at the particle surface, while the materials remain essentially unaltered. The Raman spectra of PLAg after the gastric and intestinal digestion and the colonic fermentation stages (Figure 46E, G, I) indicate again no clear extended alteration of PLAg, in agreement with the very localized nature of the surface

alterations observed by FESEM. Conversely, incipient inhomogeneity is apparent in PLAm after gastric stage (Figure 46F), in line with the incipient modifications uncovered by FESEM. The Raman bands at 1218, 1181 and 1091 $cm^{-1}$, associated with O-C-O ester group vibration modes, and Raman band at 514 $cm^{-1}$, associated with crystalline PLA, show some intensity variability, along with the Raman bands near 1770 and 1454 $cm^{-1}$, associated with the carbonyl group and with the methyl in-plane asymmetric wagging of the ester group.[285] These inhomogeneities are extensive after the small intestine phase (Figure 46H), particularly in the carbonyl region, near 1770 $cm^{-1}$, and the methyl modes in the 1460-1200 $cm^{-1}$ window.

Some incipient amorphous carbon deposits are already apparent (cf. broad feature in the 1250-1650 $cm^{-1}$ window, which area is presented below as $A_{1601}$); these are clear and extensively present on PLAm after colonic fermentation (Figure 46J). It is interesting to observe that the intensity of amorphous carbon deposits significantly changes from one spectrum to another, i.e., from one spot to another during mapping of these samples. This may be associated with differences in the amount of amorphous carbons residue deposited at different point. This is analyzed in detail by confocal depth Raman profile measurements (Figure 47 and Figure 48).

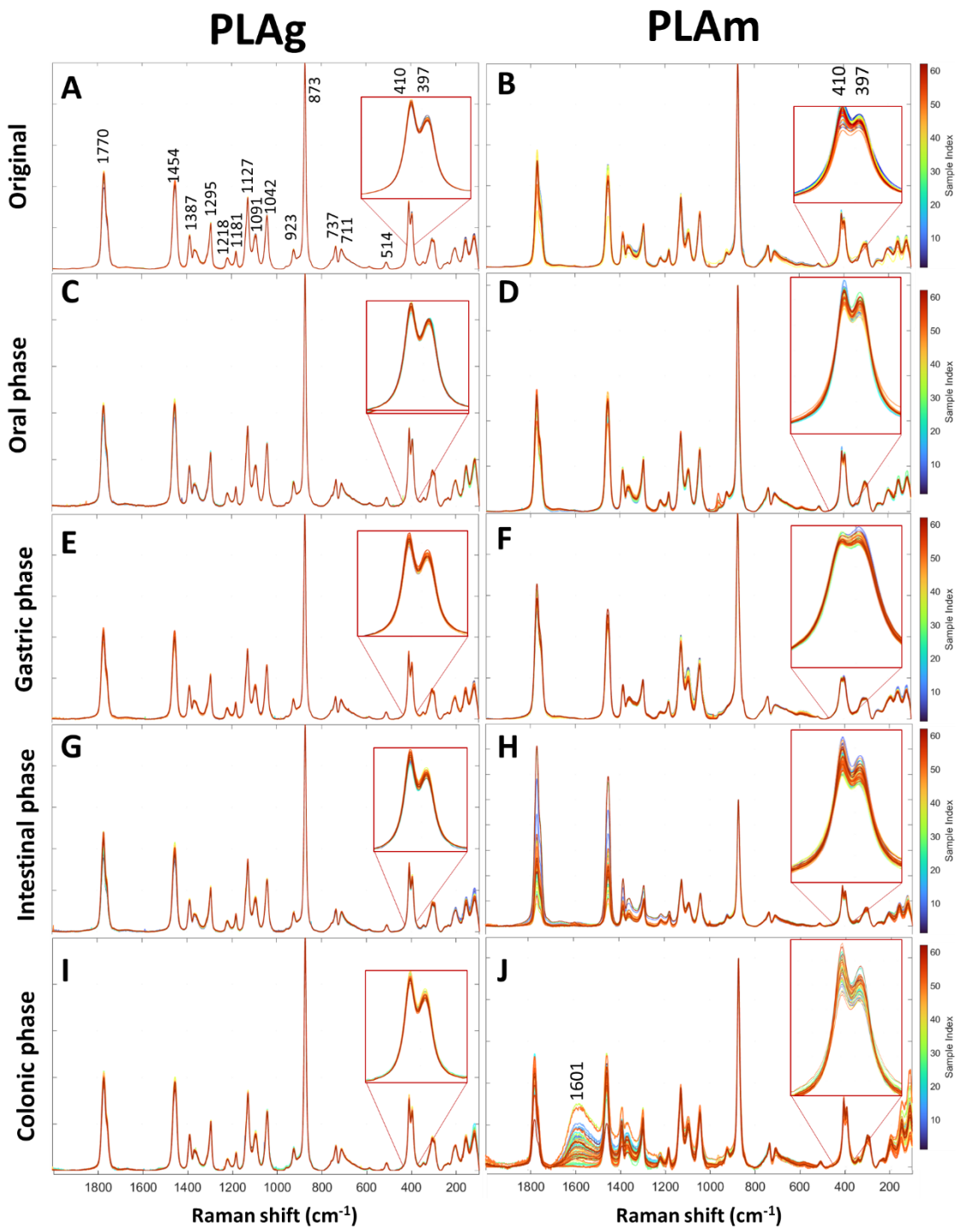


***Figure 46**. Raman spectra at 60 representative points of PLA (PLAg, millimetric, left, and PLAm, micrometric, right) in the original state (A-B), after oral (C-D), gastric (E-F), intestinal (G-H) and colonic (I-J) phases. Spectra normalized to the Raman band at 873 cm$^{-1}$.*

Several Raman modes are associated with the crystallinity degree of PLA (amorphous, semicrystalline or crystalline); their relative intensities are used as descriptors of crystallinity variations. The band at ca. 397 cm$^{-1}$ is associated with amorphous PLA

structures, while the band at ca. 409 $cm^{-1}$ is associated with crystalline.[286] Thus, the 397/410 intensity ratio in Figure 47A is related with the degree of amorphicity. This parameter indicates that PLAm series is more amorphous and with a broader crystallinity distribution than PLAg. In addition, PLAm crystallinity passes through a relative minimum in the gastric phase during the simulated human digestion. A similar result is obtained with the analysis of the Raman modes near 923 and 711 $cm^{-1}$, which are absent in amorphous samples but grow in semicrystalline.[287] The relative intensities of 923 and 711 $cm^{-1}$ Raman bands *vs*. that of 873 $cm^{-1}$ internal reference, illustrated in Figure 47B and C, respectively, show lower semicrystallinity in PLAm vs. PLAg series, and a local minimum of semicrystallinity for PLAm after the gastric phase. The Raman band near 1770 $cm^{-1}$ is a complex overlap of PLA carbonyl group signals with different degrees of crystallinity.[284] The relative area of the 1770 $cm^{-1}$ band vs. internal reference at 873 $cm^{-1}$ is not significantly different between and within PLAg and PLAm samples, but the higher dispersion of values in PLAm illustrates a broader distribution of states, in agreement with the rest of descriptors.

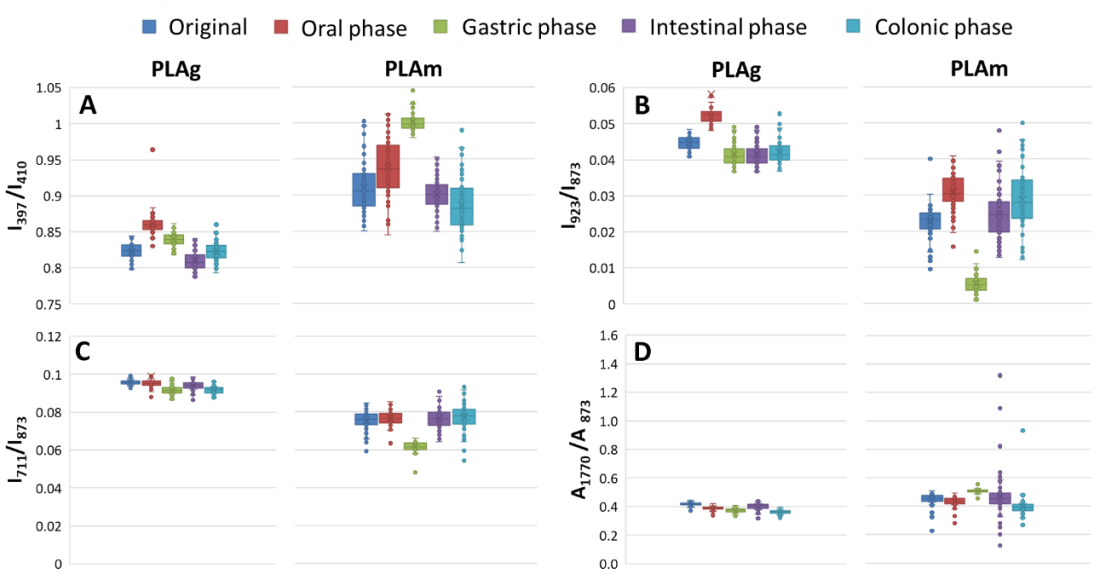


***Figure 47.*** *Raman descriptors for PLA amorphicity based on the relative intensities or areas of the Raman bands at 397 vs. 410 $cm^{-1}$ (A), at 923 va. 873 $cm^{-1}$ (B), at 711 vs. 873 $cm^{-1}$ (C), and at 1770 vas. 873 $cm^{-1}$ (D).*

The higher degradation of PLAm with respect to PLAg would be associated with its higher surface-to-volume exposure fostered by textural features generated during cryomilling. Since PLAm series were more sensitive to digestion-induced alterations than PLAg, a

confocal Raman depth profile analysis has been made on representative PLAm samples, after oral and intestine stages, to assess if the observed phenomena are essentially surface related -as expected- or may reach the bulk. It is interesting to observe, however, that while PLAg is more stable than PLAm, and the most intense variations of PLA Raman modes are associated with the presence of amorphous carbonaceous deposits on the surface (cf. Figure 46J), which would suggest that the structural modifications are at the PLA-carbon deposit interface region. For this reason, we also explored PLAg with confocal Raman microscopy in search of representative chemical modifications on the microplastic surface. Given the transparency of PLA, the ca. 1 μm confocal volume cannot prevent signal from areas outside of confocal region. Figure 48 illustrates Raman depth profiles of digested PLAm, the Raman area of the representative Raman band at 1601 $cm^{-1}$ ($A_{1601}$) and the amorphicity descriptors as a function of the distance above (positive Z values) or below (negative) the surface. Oral PLAm shows very little changes with depth scan and no presence of amorphous carbonaceous species in the range from 4 μm inside the particles (Z = -4) up to 4 μm above the surface (Z=4), except for a couple of spectra (Figure 48A, B). The semicrystallinity indicators $I_{711}/I_{873}$ and $I_{923}/I_{783}$ reveal no significant variability (Fig. 5D), and there is also no clear increase of amorphous PLA, associated with the 397/410 $cm^{-1}$ Raman bands intensity ratio (Figure 48C). The scenario is different after gastric digestion (Figure 48E), where amorphous carbon deposits are apparent; the normalized Raman area of carbonaceous species, is very low inside PLAm particles, but increasingly important above the surface (Figure 48F). The semicristallinity has hardly any fluctuation in the regions where carbon deposits are present, with few spots showing higher semicrystallinity, but without a clear trend (Figure 48H). The Raman spectra show no development of amorphous PLA, as measured by the $I_{397}/I_{410}$ ratio (Figure 48G). The small intestine stage resulted in the most apparent modifications, both in PLAm structure and in the accumulation of carbon species (Figure 48I). The area of the representative Raman band near 1601 $cm^{-1}$ ($A_{1601}$) is the highest in the samples studied and, again, much more intense above PLAm surface than inside the particle (Figure 48J). The 1601 $cm^{-1}$ band grows in parallel with several weaker bands in the 2300-2100, 2020-1950, 1850-1700, 1500-1300, 1300-1100, 1000-850, and 800-700 $cm^{-1}$ regions, associated with biofilm.[288,289,290]

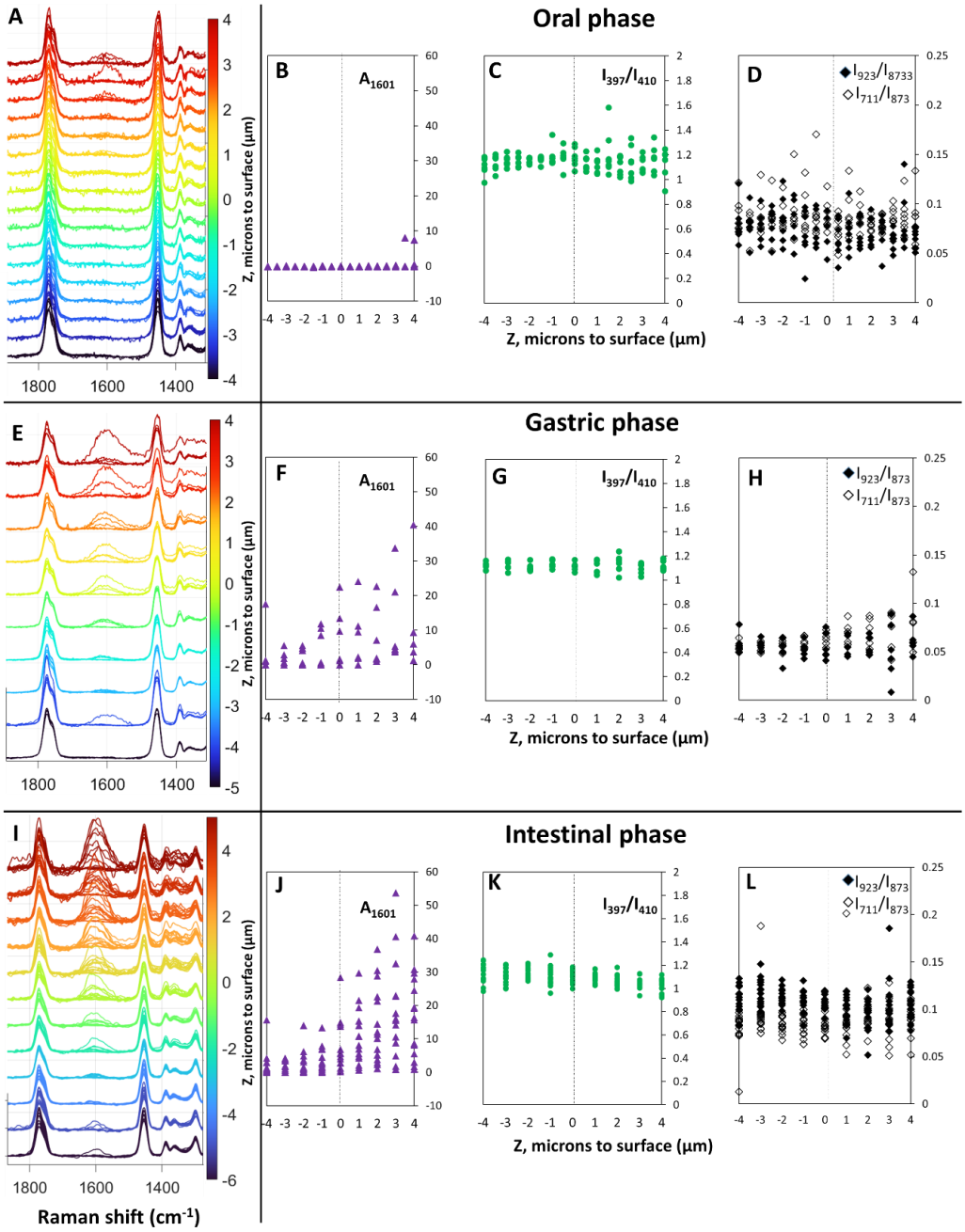


***Figure 48.*** *Depth profile Raman evaluation for PLAm after oral phase (A-D), gastric phase (E-H), and intestinal digestion (I-K). A,E,I: Raman spectra as a function of penetration depth. B, F, J: area of the 1601 $cm^{-1}$ Raman band of amorphous carbon deposits. C, G, K: relative intensity of the Raman band at 397 vs. 410 $cm^{-1}$, amorphicity indicator. D, H, L: relative intensities of the Raman bands at 923 and 711 $cm^{-1}$ with respect to the reference band at 873 $cm^{-1}$, semicrystallinity indicators. Spectra normalized to the Raman band at 873 $cm^{-1}$.*

The PLAm particles after small intestine digestion exhibit much higher semicrystallinity ($I_{873}/I_{711}$ and $I_{873}/I_{923}$ in Figure 48L) than after the gastric or oral phases, and this is concentrated near the surface, associated with the presence of carbonaceous deposits. In any case, there is no clear evolution to amorphous PLA phase ($I_{397}/I_{410}$ ratio in Figure 48K). As a whole, the carbonaceous deposits appear associated with a loss of crystallinity

at the surface towards semicrystalline PLA; there is no signal of further deconstruction towards amorphous domains in any digestion stage.

## 10.5 Conclusions

The results obtained in this research indicate multiple key conclusions. It was found that dispersion procedures may create diverse impacts on the surface of nanofibers, with NM-400 showing particularly significant changes. Furthermore, while the oxidation of these nanofibers does not show to *in vitro* toxicity, as neither NM-400 nor NM-401 caused significant adverse effects on cell viability or mutations in the TK6 cell line, it enhance the oxidative capacity for hydrophobic nanofibers like NM-401, as compared to magnetic stirring. These findings aim to conclude that the dispersion protocol is a significant factor to drive the oxidative capacity of fibers.

On the other hand, the physicochemical characterization of novel advanced nanomaterials, such as multicomponent oxides or HA nanobiomaterials doped with Ti or Fe, in particular of their surface, is crucial for understanding their behavior to avoid adverse effects after human exposure. We introduce methanol-TPRx as an *in chemico* alternative to methanol-TPSR for nanomaterials with low reactivity. Additionally, Raman spectroscopy is presented as a method to investigate the surface state after coating or doping processes.

Finally, the spectroscopic analysis of MNPs' surfaces was shown to unravel their crystallinity state evolution upon simulated human digestion at different stages, what reflects their interactions with human microbiota in a pioneering investigation. PLA experiences superficial modifications during the gastrointestinal digestion. Notably, post-colonic fermentation analysis performed by collaborators (C. Jiménez-Arroyo, A. Tamargo and M. V. Moreno-Arribas at CIAL-CSIC) revealed minor shifts in the microbial populations within the gut, particularly an observed tendency for an increase in the Bifidobacterium genus with millimetric PLA particles. The formation of microbial biofilms on the surface of PLA microplastics implies the colonization of these particles by colonic microbiota. The progressive amorphization of PET microplastics during gastrointestinal

digestion might be attributed to an oxidative effect, more pronounced following colonic fermentation. Such structural alterations in PET MPs suggesting an interaction between the colonic microbiota and PET MPs.

# Final conclusions

Nanotoxicology necessitates New Approach Methodologies to assess the hazards of advanced nanomaterials while minimizing costs, analysis time, and the use of animals. The strategy employed in this study combines *in chemico* and *in vitro* assays to understand the potential adverse effects of metallic oxides and carbonaceous materials. Methanol-TPSR stands as a pivotal tool for quantifying the number and nature (acid, basic, or redox) of nanomaterial surface sites in dry samples. This catalytic indication facilitates the determination of a nanomaterial's primary reactivity, without being contingent upon the stability of the dispersion performed, pretreatment, biotransformation, or ion release. Complementing this, the *in chemico* strategy integrates liquid-phase reactions to assess the oxidative capacity using various probe molecules and the genesis of reactive oxygen species. With the aid of statistical tools, it becomes feasible to categorize nanomaterials based on their reactivity. Thus, nanomaterials deemed unreactive can be dismissed as potential hazards in terms of reactivity-based nanotoxicity. Yet, it's imperative to recognize that additional examinations on biotransformation, bioaccumulation, protein corona formation, etc., are crucial to exclude toxicity pathways related to their size/shape or protracted ion release in relevant media. Solving these data gaps involves performing *in vitro* studies. The relevance of inhalation as the primary route of administration of the ENMs requires the evaluation of these compounds in lung cell lines as A549 and dTHP-1. Thus, cell viability, LDH release, autophagosome detection and proteomics are proposed to determine the MoA.

Building on the results derived from the reactivity assessments, nanomaterials such as $TiO_2$ NM-101, $TiO_2$ NM-105, $CeO_2$ NM-211, $CeO_2$ NM-212, $SiO_2$ NM-200, MWCNT NM-401, $Mn_2O_3$, and $Fe_2O_3$ are delineated into groups of moderate to low oxidative capacity. Hence, predicting adverse outcomes based on their reactivity remains elusive, and existing literature corroborates the lack of effects on cell viability in significant cell lines like A549 or dTHP-1 after their exposure.

Nonetheless, regarding the *in vitro* assays performed in this work, for nanomaterials such as $TiO_2$ NM-101, $TiO_2$ NM-105, $CeO_2$ NM-211, and $CeO_2$ NM-212, the homeostasis of the A549 and dTHP-1 cell lines remains intact, primarily attributed to autophagy—a cytoprotective mechanism. Contrarily, the reactivity screening undertaken emphasizes the pronounced oxidizing aptitude of nanomaterials like CuO, ZnO NM-110, ZnO NM-111, MWCNT NM-400, and carbon black. The current literature discloses the *in vitro* toxicity of these engineered nanomaterials in pulmonary cell lines, especially concerning cell viability. Hence, these nanomaterials earn their classification as potentially hazardous based on their reactivity. The *in vitro* experiments conducted confirm that, of the ten ENMs evaluated, only zinc oxide and copper oxide present a marked decline in cell viability in A549 and dTHP-1 cells. It's pivotal to consider surface reactivity in deciphering mechanisms of action, as underscored by TPSR-Methanol.

Re-evaluating dose estimation based on surface necessitates considering the quantity of reactive sites. The previously accepted notion that "the higher the surface area, the higher the dose" no longer holds. While evaluating the oxidative potential of ENMs, it's crucial to factor in their mode of action.

In the context of emerging nanomaterials, both nanobiomaterials and multicomponent engineered nanomaterials were assessed based on their reactivity using methods such as methanol-TPRx, methanol-TPSR, and dithiothreitol (DTT) consumption, unraveling the variability of surface oxidative capacity depending on composition and the effectiveness of doping. These results were supported by Raman microscopy, examining the surface state. This technique is also applicable to one of the major emerging issues related to nanoparticles, namely the presence of micro and nanoplastics in environmental and food samples. The microplastics analyzed (PLA and PET) undergo structural changes following simulated digestions, due to their interaction with intestinal microbiota. Therefore, Raman microscopy is proposed as a crucial technique for understanding the interaction of micro and nanoplastics with their environment.

In conclusion, this doctoral dissertation establishes that 1) New Approach Methodologies (NAMs) grounded *in chemico* and *in vitro* techniques are advocated for fostering the development of AOP; 2) The assessment of antioxidant consumption and ROS

generation, using probe molecules, is instrumental in classifying ENMs based on their oxidative capacities. Notably, CuO, ZnO NM-110, and ZnO NM-111 are identified as the most potent oxidizing agents; 3) The Methanol-Temperature Programmed Surface Reaction (Methanol-TPSR) method is pivotal in quantifying the quantity and character of surface sites on ENMs, thus revealing their primary reactivity, including acid, basic, and redox properties; 4) *In vitro* assays utilizing lung cell lines have elucidated diverse toxicological mechanisms corresponding to each type of reactivity. While highly reactive ENMs are associated with reduced cell viability and disrupted homeostasis, acids or moderate oxidants tend to trigger autophagy as a defense mechanism to preserve homeostasis. Conversely, inert silicon oxide does not exhibit adverse effects in the tested assays; 5) The quantification of surface sites on ENMs is proposed as a novel dosimetry approach for determining the surface exposure levels of ENMs to cell lines in *in vitro* experiments; and 6) the study underscores that advanced nanomaterials, including emergent entities like micro/nanoplastics, nanobiomaterials, or multicomponent oxides, possess distinct physicochemical characteristics. These attributes should be comprehensively analyzed using NAMs, focusing not only on reactivity but also on structural features, which can be effectively explored through Raman spectroscopy.

# Bibliography


(1) European Commission, Joint Research Centre; Rauscher, H.; Kestens, V.; Rasmussen, K.; Linsinger, T.; Stefaniak, E. Guidance on the Implementation of the Commission Recommendation 2022/C 229/01 on the Definition of Nanomaterial. *Publ. Off. Eur. Union* **2023**. https://doi.org/10.2760/237496.

(2) Joudeh, N.; Linke, D. Nanoparticle Classification, Physicochemical Properties, Characterization, and Applications: A Comprehensive Review for Biologists. *J. Nanobiotechnology* **2022**, *20* (1), 262. https://doi.org/10.1186/s12951-022-01477-8.

(3) Hochella, M. F.; Mogk, D. W.; Ranville, J.; Allen, I. C.; Luther, G. W.; Marr, L. C.; McGrail, B. P.; Murayama, M.; Qafoku, N. P.; Rosso, K. M.; Sahai, N.; Schroeder, P. A.; Vikesland, P.; Westerhoff, P.; Yang, Y. Natural, Incidental, and Engineered Nanomaterials and Their Impacts on the Earth System. *Science (80-. ).* **2019**, *363* (6434). https://doi.org/10.1126/science.aau8299.

(4) Serrano-Lotina, A.; Portela, R.; Baeza, P.; Alcolea-Rodriguez, V.; Villarroel, M.; Ávila, P. Zeta Potential as a Tool for Functional Materials Development. *Catal. Today* **2022**, No. June. https://doi.org/10.1016/j.cattod.2022.08.004.

(5) Kasemets, K.; Ivask, A.; Dubourguier, H. C.; Kahru, A. Toxicity of Nanoparticles of ZnO, CuO and TiO2 to Yeast Saccharomyces Cerevisiae. *Toxicol. Vitr.* **2009**, *23* (6), 1116–1122. https://doi.org/10.1016/j.tiv.2009.05.015.

(6) Nel, A.; Xia, T.; Mädler, L.; Li, N. Toxic Potential of Materials at the Nanolevel. *Science (80-. ).* **2006**, *311* (5761), 622–627. https://doi.org/10.1126/science.1114397.

(7) Buzea, C.; Pacheco, I. I.; Robbie, K. Nanomaterials and Nanoparticles: Sources and Toxicity. *Biointerphases* **2007**, *2* (4), MR17–MR71. https://doi.org/10.1116/1.2815690.

(8) Talebian, S.; Rodrigues, T.; Das Neves, J.; Sarmento, B.; Langer, R.; Conde, J. Facts and Figures on Materials Science and Nanotechnology Progress and Investment. *ACS Nano* **2021**, *15* (10), 15940–15952. https://doi.org/10.1021/acsnano.1c03992.

(9) Khan, I.; Saeed, K.; Khan, I. Nanoparticles: Properties, Applications and Toxicities. *Arab. J. Chem.* **2017**. https://doi.org/10.1016/j.arabjc.2017.05.011.

(10) Kinnear, C.; Moore, T. L.; Rodriguez-Lorenzo, L.; Rothen-Rutishauser, B.; Petri-Fink, A. Form Follows Function: Nanoparticle Shape and Its Implications for Nanomedicine. *Chem. Rev.* **2017**, *117* (17), 11476–11521. https://doi.org/10.1021/acs.chemrev.7b00194.

(11) LIGHT, W. G.; WEI, E. T. Surface Charge and Asbestos Toxicity. *Nature* **1977**, *265* (5594), 537–539. https://doi.org/10.1038/265537a0.

(12) Jeliazkova, N.; Apostolova, M. D.; Andreoli, C.; Barone, F.; Barrick, A.; Battistelli, C.; Bossa, C.; Botea-Petcu, A.; Châtel, A.; De Angelis, I.; Dusinska, M.; El Yamani, N.; Gheorghe, D.; Giusti, A.; Gómez-Fernández, P.; Grafström, R.; Gromelski, M.; Jacobsen, N. R.; Jeliazkov, V.; Jensen, K. A.; Kochev, N.; Kohonen, P.; Manier, N.; Mariussen, E.; Mech, A.; Navas, J. M.; Paskaleva, V.; Precupas, A.; Puzyn, T.; Rasmussen, K.; Ritchie, P.; Llopis, I. R.; Rundén-Pran, E.; Sandu, R.; Shandilya, N.; Tanasescu, S.; Haase, A.; Nymark, P. Towards FAIR Nanosafety Data. *Nat. Nanotechnol.* **2021**, *16* (6), 644–654. https://doi.org/10.1038/s41565-021-00911-6.

(13) Andrea Haase; Frederick Klaessig. *EU US Roadmap Nanoinformatics 2030*. https://doi.org/10.5281/zenodo.1486012.

(14) Singh, A. V.; Laux, P.; Luch, A.; Sudrik, C.; Wiehr, S.; Wild, A. M.; Santomauro, G.; Bill, J.; Sitti, M. Review of Emerging Concepts in Nanotoxicology: Opportunities and Challenges for Safer Nanomaterial Design. *Toxicol. Mech. Methods* **2019**, *29* (5), 378–387. https://doi.org/10.1080/15376516.2019.1566425.

(15) Kuroda, A. Recent Progress and Perspectives on the Mechanisms Underlying Asbestos Toxicity. *Genes Environ.* **2021**, *43* (1), 1–8.

https://doi.org/10.1186/s41021-021-00215-0.

(16) Manke, A.; Wang, L.; Rojanasakul, Y. Mechanisms of Nanoparticle-Induced Oxidative Stress and Toxicity. *Biomed Res. Int.* **2013**, *2013*, 1–15. https://doi.org/10.1155/2013/942916.

(17) Choi, H.; Choi, B.; Han, J.; Shin, H. E.; Park, W.; Kim, D. Reactive Oxygen Species Responsive Cleavable Hierarchical Metallic Supra-Nanostructure. *Small* **2022**, *18* (38). https://doi.org/10.1002/smll.202202694.

(18) Schwarz-Plaschg, C.; Kallhoff, A.; Eisenberger, I. Making Nanomaterials Safer by Design? *Nanoethics* **2017**, *11* (3), 277–281. https://doi.org/10.1007/s11569-017-0307-4.

(19) Jeliazkova, N.; Bleeker, E.; Cross, R.; Haase, A.; Janer, G.; Peijnenburg, W.; Pink, M.; Rauscher, H.; Svendsen, C.; Tsiliki, G.; Zabeo, A.; Hristozov, D.; Stone, V.; Wohlleben, W. How Can We Justify Grouping of Nanoforms for Hazard Assessment? Concepts and Tools to Quantify Similarity. *NanoImpact* **2022**, *25*, 100366. https://doi.org/10.1016/j.impact.2021.100366.

(20) Kraegeloh, A.; Suarez-Merino, B.; Sluijters, T.; Micheletti, C. Implementation of Safe-by-Design for Nanomaterial Development and Safe Innovation: Why We Need a Comprehensive Approach. *Nanomaterials* **2018**, *8* (4). https://doi.org/10.3390/nano8040239.

(21) Bañares, M. A.; Haase, A.; Tran, L.; Lobaskin, V.; Oberdörster, G.; Rallo, R.; Leszczynski, J.; Hoet, P.; Korenstein, R.; Hardy, B.; Puzyn, T. CompNanoTox2015: Novel Perspectives from a European Conference on Computational Nanotoxicology on Predictive Nanotoxicology. *Nanotoxicology* **2017**, *11* (7), 839–845. https://doi.org/10.1080/17435390.2017.1371351.

(22) Stone, V.; Gottardo, S.; Bleeker, E. A. J.; Braakhuis, H.; Dekkers, S.; Fernandes, T.; Haase, A.; Hunt, N.; Hristozov, D.; Jantunen, P.; Jeliazkova, N.; Johnston, H.; Lamon, L.; Murphy, F.; Rasmussen, K.; Rauscher, H.; Jiménez, A. S.; Svendsen, C.; Spurgeon, D.; Vázquez-Campos, S.; Wohlleben, W.; Oomen, A. G. A Framework for Grouping

and Read-across of Nanomaterials- Supporting Innovation and Risk Assessment. *Nano Today* **2020**, *35*, 1–15. https://doi.org/10.1016/j.nantod.2020.100941.

(23) Verdon, R.; Stone, V.; Murphy, F.; Christopher, E.; Johnston, H.; Doak, S.; Vogel, U.; Haase, A.; Kermanizadeh, A. The Application of Existing Genotoxicity Methodologies for Grouping of Nanomaterials: Towards an Integrated Approach to Testing and Assessment. *Part. Fibre Toxicol.* **2022**, *19* (1), 1–9. https://doi.org/10.1186/s12989-022-00476-9.

(24) Murphy, F. A.; Johnston, H. J.; Dekkers, S.; Bleeker, E. A. J.; Oomen, A. G.; Fernandes, T. F.; Rasmussen, K.; Jantunen, P.; Rauscher, H.; Hunt, N.; di Cristos, L.; Braakhuis, H. M.; Haase, A.; Hristozov, D.; Wohlleben, W.; Sabella, S.; Stone, V. How to Formulate Hypotheses and IATAs to Support Grouping and Read-across of Nanoforms. *ALTEX* **2023**, *40* (1), 125–140. https://doi.org/10.14573/altex.2203241.

(25) Sintes, J. R.; Blázquez, M.; Moya, S.; socorro vazquez. *Safety Issues and Regulatory Challenges of Nanomaterials A*; 2012. https://doi.org/10.2788/76363.

(26) Setyawati, M. I.; Zhao, Z.; Ng, K. W. Transformation of Nanomaterials and Its Implications in Gut Nanotoxicology. *Small* **2020**, *16* (36), 1–17. https://doi.org/10.1002/smll.202001246.

(27) Shirokii, N.; Din, Y.; Petrov, I.; Seregin, Y.; Sirotenko, S.; Razlivina, J.; Serov, N.; Vinogradov, V. Quantitative Prediction of Inorganic Nanomaterial Cellular Toxicity via Machine Learning. *Small* **2023**, *19* (19), 1–7. https://doi.org/10.1002/smll.202207106.

(28) Jeong, J.; Choi, J. Use of Adverse Outcome Pathways in Chemical Toxicity Testing: Potential Advantages and Limitations. *Environ. Health Toxicol.* **2017**, *33* (1), e2018002. https://doi.org/10.5620/eht.e2018002.

(29) Gerloff, K.; Landesmann, B.; Worth, A.; Munn, S.; Palosaari, T.; Whelan, M. The Adverse Outcome Pathway Approach in Nanotoxicology. *Comput. Toxicol.* **2017**, *1*, 3–11. https://doi.org/10.1016/j.comtox.2016.07.001.

(30) Gottardo, S.; Crutzen, H.; Jantunen, P.; Gottardo, S.; Alessandrelli, M.; Atluri, R.; Barberio, G.; Bergonzo, P.; Bleeker, E.; Andy, M.; Borges, T.; Buttol, P.; Castelli, S.; Chevillard, S.; Dekkers, S.; Delpivo, C.; Fanghella, D. P.; Dusinska, M.; Einola, J.; Ekokoski, E.; Fito, C.; Gouveia, H.; Hoehener, K.; Jantunen, P.; Laux, P.; Lehmann, H. C.; Leinonen, R.; Mech, A.; Micheletti, C.; Pesudo, L. Q.; Polci, M. L.; Walser, T.; Wijnhoven, S.; Crutzen, H. *NANoREG Framework for the Safety Assessment of Nanomaterials*; 2017. https://doi.org/10.2760/245972.

(31) AKÇAN, R.; AYDOGAN, H. C.; YILDIRIM, M. Ş.; TAŞTEKİN, B.; SAĞLAM, N. Nanotoxicity: A Challenge for Future Medicine. *TURKISH J. Med. Sci.* **2020**, *50* (4), 1180–1196. https://doi.org/10.3906/sag-1912-209.

(32) Halappanavar, S.; Van Den Brule, S.; Nymark, P.; Gaté, L.; Seidel, C.; Valentino, S.; Zhernovkov, V.; Høgh Danielsen, P.; De Vizcaya, A.; Wolff, H.; Stöger, T.; Boyadziev, A.; Poulsen, S. S.; Sørli, J. B.; Vogel, U. Adverse Outcome Pathways as a Tool for the Design of Testing Strategies to Support the Safety Assessment of Emerging Advanced Materials at the Nanoscale. *Part. Fibre Toxicol.* **2020**, *17* (1), 1–24. https://doi.org/10.1186/s12989-020-00344-4.

(33) Labib, S.; Williams, A.; Yauk, C. L.; Nikota, J. K.; Wallin, H.; Vogel, U.; Halappanavar, S. Nano-Risk Science: Application of Toxicogenomics in an Adverse Outcome Pathway Framework for Risk Assessment of Multi-Walled Carbon Nanotubes. *Part. Fibre Toxicol.* **2016**, *13* (1), 1–17. https://doi.org/10.1186/s12989-016-0125-9.

(34) Padmore, T.; Stark, C.; Turkevich, L. A.; Champion, J. A. Quantitative Analysis of the Role of Fiber Length on Phagocytosis and Inflammatory Response by Alveolar Macrophages. *Biochim. Biophys. Acta - Gen. Subj.* **2017**, *1861* (2), 58–67. https://doi.org/10.1016/j.bbagen.2016.09.031.

(35) Boyles, M. S. P.; Young, L.; Brown, D. M.; MacCalman, L.; Cowie, H.; Moisala, A.; Smail, F.; Smith, P. J. W.; Proudfoot, L.; Windle, A. H.; Stone, V. Multi-Walled Carbon Nanotube Induced Frustrated Phagocytosis, Cytotoxicity and pro-Inflammatory Conditions in Macrophages Are Length Dependent and Greater than That of Asbestos. *Toxicol. Vitr.* **2015**, *29* (7), 1513–1528.

https://doi.org/10.1016/j.tiv.2015.06.012.

(36) Nel, A.; Xia, T.; Meng, H.; Wang, X.; Lin, S.; Ji, Z.; Zhang, H. Nanomaterial Toxicity Testing in the 21st Century: Use of a Predictive Toxicological Approach and High-Throughput Screening. *Acc. Chem. Res.* **2013**, *46* (3), 607–621. https://doi.org/10.1021/ar300022h.

(37) Bahl, A.; Hellack, B.; Wiemann, M.; Giusti, A.; Werle, K.; Haase, A.; Wohlleben, W. Nanomaterial Categorization by Surface Reactivity: A Case Study Comparing 35 Materials with Four Different Test Methods. *NanoImpact* **2020**, *19* (February), 100234. https://doi.org/10.1016/j.impact.2020.100234.

(38) Arts, J. H. E.; Hadi, M.; Keene, A. M.; Kreiling, R.; Lyon, D.; Maier, M.; Michel, K.; Petry, T.; Sauer, U. G.; Warheit, D.; Wiench, K.; Landsiedel, R. A Critical Appraisal of Existing Concepts for the Grouping of Nanomaterials. *Regul. Toxicol. Pharmacol.* **2015**, *70* (2), 492–506. https://doi.org/10.1016/j.yrtph.2014.07.025.

(39) Arts, J. H. E.; Irfan, M.-A.; Keene, A. M.; Kreiling, R.; Lyon, D.; Maier, M.; Michel, K.; Neubauer, N.; Petry, T.; Sauer, U. G.; Warheit, D.; Wiench, K.; Wohlleben, W.; Landsiedel, R. Case Studies Putting the Decision-Making Framework for the Grouping and Testing of Nanomaterials (DF4nanoGrouping) into Practice. *Regul. Toxicol. Pharmacol.* **2016**, *76*, 234–261. https://doi.org/10.1016/j.yrtph.2015.11.020.

(40) Oomen, A. G.; Steinhäuser, K. G.; Bleeker, E. A. J.; van Broekhuizen, F.; Sips, A.; Dekkers, S.; Wijnhoven, S. W. P.; Sayre, P. G. Risk Assessment Frameworks for Nanomaterials: Scope, Link to Regulations, Applicability, and Outline for Future Directions in View of Needed Increase in Efficiency. *NanoImpact* **2018**, *9* (July 2017), 1–13. https://doi.org/10.1016/j.impact.2017.09.001.

(41) Godwin, H.; Nameth, C.; Avery, D.; Bergeson, L. L.; Bernard, D.; Beryt, E.; Boyes, W.; Brown, S.; Clippinger, A. J.; Cohen, Y.; Doa, M.; Hendren, C. O.; Holden, P.; Houck, K.; Kane, A. B.; Klaessig, F.; Kodas, T.; Landsiedel, R.; Lynch, I.; Malloy, T.; Miller, M. B.; Muller, J.; Oberdorster, G.; Petersen, E. J.; Pleus, R. C.; Sayre, P.; Stone, V.; Sullivan,

K. M.; Tentschert, J.; Wallis, P.; Nel, A. E. Nanomaterial Categorization for Assessing Risk Potential To Facilitate Regulatory Decision-Making. *ACS Nano* **2015**, *9* (4), 3409–3417. https://doi.org/10.1021/acsnano.5b00941.

(42) Lynch, I.; Weiss, C.; Valsami-Jones, E. A Strategy for Grouping of Nanomaterials Based on Key Physico-Chemical Descriptors as a Basis for Safer-by-Design NMs. *Nano Today* **2014**, *9* (3), 266–270. https://doi.org/10.1016/j.nantod.2014.05.001.

(43) Setyawati, M. I.; Fang, W.; Chia, S. L.; Leong, D. T. Nanotoxicology of Common Metal Oxide Based Nanomaterials: Their ROS-y and Non-ROS-y Consequences. *Asia-Pacific J. Chem. Eng.* **2013**, *8* (2), 205–217. https://doi.org/10.1002/apj.1680.

(44) Dayem, A. A.; Hossain, M. K.; Lee, S. Bin; Kim, K.; Saha, S. K.; Yang, G. M.; Choi, H. Y.; Cho, S. G. The Role of Reactive Oxygen Species (ROS) in the Biological Activities of Metallic Nanoparticles. *Int. J. Mol. Sci.* **2017**, *18* (1), 1–21. https://doi.org/10.3390/ijms18010120.

(45) Perelshtein, I.; Lipovsky, A.; Perkas, N.; Gedanken, A.; Moschini, E.; Mantecca, P. The Influence of the Crystalline Nature of Nano-Metal Oxides on Their Antibacterial and Toxicity Properties. *Nano Res.* **2015**, *8* (2), 695–707. https://doi.org/10.1007/s12274-014-0553-5.

(46) Faraldos, Marisol, and C. G. *Técnicas de Análisis y Caracterización de Materiales*; 2021.

(47) Keller, J.; Wohlleben, W.; Ma-Hock, L.; Strauss, V.; Gröters, S.; Küttler, K.; Wiench, K.; Herden, C.; Oberdörster, G.; van Ravenzwaay, B.; Landsiedel, R. Time Course of Lung Retention and Toxicity of Inhaled Particles: Short-Term Exposure to Nano-Ceria. *Arch. Toxicol.* **2014**, *88* (11), 2033–2059. https://doi.org/10.1007/s00204-014-1349-9.

(48) Wu, Z.; Li, M.; Howe, J.; Meyer, H. M.; Overbury, S. H. Probing Defect Sites on CeO2 Nanocrystals with Well-Defined Surface Planes by Raman Spectroscopy and O2 Adsorption. *Langmuir* **2010**, *26* (21), 16595–16606. https://doi.org/10.1021/la101723w.

(49) Pushkarev, V. V.; Kovalchuk, V. I.; D'Itri, J. L. Probing Defect Sites on the CeO2 Surface with Dioxygen. *J. Phys. Chem. B* **2004**, *108* (17), 5341–5348. https://doi.org/10.1021/jp0311254.

(50) Wang, Q.; Li, Y.; Serrano-Lotina, A.; Han, W.; Portela, R.; Wang, R.; Bañares, M. A.; Yeung, K. L. Operando Investigation of Toluene Oxidation over 1D Pt@CeO 2 Derived from Pt Cluster-Containing MOF. *J. Am. Chem. Soc.* **2021**, *143* (1), 196–205. https://doi.org/10.1021/jacs.0c08640.

(51) Llopis-Grimalt, M. A.; Forteza-Genestra, M. A.; Alcolea-Rodriguez, V.; Ramis, J. M.; Monjo, M. Nanostructured Titanium for Improved Endothelial Biocompatibility and Reduced Platelet Adhesion in Stent Applications. *Coatings* **2020**, *10* (9), 907. https://doi.org/10.3390/coatings10090907.

(52) Marquis, B. J.; Love, S. A.; Braun, K. L.; Haynes, C. L. Analytical Methods to Assess Nanoparticle Toxicity. *Analyst* **2009**, *134* (3), 425–439. https://doi.org/10.1039/b818082b.

(53) Gates, B. C. *Catalytic Chemistry*; 1991.

(54) Tatibouët, J. M. Methanol Oxidation as a Catalytic Surface Probe. *Appl. Catal. A Gen.* **1997**, *148* (2), 213–252. https://doi.org/10.1016/S0926-860X(96)00236-0.

(55) Jehng, J. M.; Wachs, I. E.; Patience, G. S.; Dai, Y. M. Experimental Methods in Chemical Engineering: Temperature Programmed Surface Reaction Spectroscopy—TPSR. *Can. J. Chem. Eng.* **2021**, *99* (2), 423–434. https://doi.org/10.1002/cjce.23913.

(56) Wu, Y.; Gao, F.; Wang, H.; Kovarik, L.; Sudduth, B.; Wang, Y. Probing Acid–Base Properties of Anatase TiO 2 Nanoparticles with Dominant {001} and {101} Facets Using Methanol Chemisorption and Surface Reactions. *J. Phys. Chem. C* **2021**, *125* (7), 3988–4000. https://doi.org/10.1021/acs.jpcc.0c11107.

(57) Savolainen, K.; Alenius, H.; Norppa, H.; Pylkkänen, L.; Tuomi, T.; Kasper, G. Risk Assessment of Engineered Nanomaterials and Nanotechnologies-A Review.

*Toxicology* **2010**, *269* (2–3), 92–104. https://doi.org/10.1016/j.tox.2010.01.013.

(58) Lundqvist, M.; Stigler, J.; Elia, G.; Lynch, I.; Cedervall, T.; Dawson, K. A. Nanoparticle Size and Surface Properties Determine the Protein Corona with Possible Implications for Biological Impacts. *Proc. Natl. Acad. Sci. U. S. A.* **2008**, *105* (38), 14265–14270. https://doi.org/10.1073/pnas.0805135105.

(59) Serrano-Lotina, A.; Portela, R.; Baeza, P.; Alcolea-Rodriguez, V.; Villarroel, M.; Ávila, P. Zeta Potential as a Tool for Functional Materials Development. *Catal. Today* **2022**. https://doi.org/10.1016/j.cattod.2022.08.004.

(60) Mittal, S.; Pandey, A. K. Cerium Oxide Nanoparticles Induced Toxicity in Human Lung Cells: Role of ROS Mediated DNA Damage and Apoptosis. *Biomed Res. Int.* **2014**, *2014*, 1–14. https://doi.org/10.1155/2014/891934.

(61) Dhawan, A.; Sharma, V. Toxicity Assessment of Nanomaterials: Methods and Challenges. *Anal. Bioanal. Chem.* **2010**, *398* (2), 589–605. https://doi.org/10.1007/s00216-010-3996-x.

(62) Semisch, A.; Ohle, J.; Witt, B.; Hartwig, A. Cytotoxicity and Genotoxicity of Nano - and Microparticulate Copper Oxide: Role of Solubility and Intracellular Bioavailability. *Part. Fibre Toxicol.* **2014**, *11* (1), 10. https://doi.org/10.1186/1743-8977-11-10.

(63) Mendoza, R. P.; Brown, J. M. Engineered Nanomaterials and Oxidative Stress: Current Understanding and Future Challenges. *Curr. Opin. Toxicol.* **2019**, *13*, 74–80. https://doi.org/10.1016/j.cotox.2018.09.001.

(64) Zuo, L.; Wijegunawardana, D. Redox Role of ROS and Inflammation in Pulmonary Diseases. In *Advances in Experimental Medicine and Biology*; 2021; Vol. 1304, pp 187–204. https://doi.org/10.1007/978-3-030-68748-9_11.

(65) Cronin, M. T. D.; Bajot, F.; Enoch, S. J.; Madden, J. C.; Roberts, D. W.; Schwöbel, J. The in Chemico-in Silico Interface: Challenges for Integrating Experimental and Computational Chemistry to Identify Toxicity. *ATLA Altern. to Lab. Anim.* **2009**, *37*

(5), 513–521. https://doi.org/10.1177/026119290903700508.

(66) J. M. Thomas, W. J. Thomas, N. Y. *Principles and Practice of Heterogeneous Catalysis*; VCH (1997). Page 27.

(67) Wachs, I. E. Number of Surface Sites and Turnover Frequencies for Oxide Catalysts. *J. Catal.* **2022**, *405*, 462–472. https://doi.org/10.1016/j.jcat.2021.12.032.

(68) Briand, L. E.; Hirt, A. M.; Wachs, I. E. Quantitative Determination of the Number of Surface Active Sites and the Turnover Frequencies for Methanol Oxidation over Metal Oxide Catalysts: Application to Bulk Metal Molybdates and Pure Metal Oxide Catalysts. *J. Catal.* **2001**, *202* (2), 268–278. https://doi.org/10.1006/jcat.2001.3289.

(69) Kulkarni, D.; Wachs, I. E. Isopropanol Oxidation by Pure Metal Oxide Catalysts: Number of Active Surface Sites and Turnover Frequencies. *Appl. Catal. A Gen.* **2002**, *237* (1–2), 121–137. https://doi.org/10.1016/S0926-860X(02)00325-3.

(70) Briand, L. E.; Jehng, J. M.; Cornaglia, L.; Hirt, A. M.; Wachs, I. E. Quantitative Determination of the Number of Surface Active Sites and the Turnover Frequency for Methanol Oxidation over Bulk Metal Vanadates. *Catal. Today* **2003**, *78* (1-4 SPEC.), 257–268. https://doi.org/10.1016/S0920-5861(02)00350-4.

(71) Lwin, S.; Li, Y.; Frenkel, A. I.; Wachs, I. E. Nature of WOx Sites on SiO2 and Their Molecular Structure-Reactivity/Selectivity Relationships for Propylene Metathesis. *ACS Catal.* **2016**, *6* (5), 3061–3071. https://doi.org/10.1021/acscatal.6b00389.

(72) Schmeisser, S.; Miccoli, A.; von Bergen, M.; Berggren, E.; Braeuning, A.; Busch, W.; Desaintes, C.; Gourmelon, A.; Grafström, R.; Harrill, J.; Hartung, T.; Herzler, M.; Kass, G. E. N.; Kleinstreuer, N.; Leist, M.; Luijten, M.; Marx-Stoelting, P.; Poetz, O.; van Ravenzwaay, B.; Roggeband, R.; Rogiers, V.; Roth, A.; Sanders, P.; Thomas, R. S.; Marie Vinggaard, A.; Vinken, M.; van de Water, B.; Luch, A.; Tralau, T. New Approach Methodologies in Human Regulatory Toxicology – Not If, but How and When! *Environ. Int.* **2023**, *178* (June), 108082. https://doi.org/10.1016/j.envint.2023.108082.

(73) Fischer, I.; Milton, C.; Wallace, H. Toxicity Testing Is Evolving! *Toxicol. Res. (Camb).* **2020**, *9* (2), 67–80. https://doi.org/10.1093/toxres/tfaa011.

(74) Doak, S. H.; Clift, M. J. D.; Costa, A.; Delmaar, C.; Gosens, I.; Halappanavar, S.; Kelly, S.; Pejinenburg, W. J. G. M.; Rothen-Rutishauser, B.; Schins, R. P. F.; Stone, V.; Tran, L.; Vijver, M. G.; Vogel, U.; Wohlleben, W.; Cassee, F. R. The Road to Achieving the European Commission's Chemicals Strategy for Nanomaterial Sustainability—A PATROLS Perspective on New Approach Methodologies. *Small* **2022**, *18* (17). https://doi.org/10.1002/smll.202200231.

(75) Bahl, A.; Hellack, B.; Wiemann, M.; Giusti, A.; Werle, K.; Haase, A.; Wohlleben, W. Nanomaterial Categorization by Surface Reactivity: A Case Study Comparing 35 Materials with Four Different Test Methods. *NanoImpact* **2020**, *19* (February), 100234. https://doi.org/10.1016/j.impact.2020.100234.

(76) Hellack, B.; Nickel, C.; Schins, R. P. F. Oxidative Potential of Silver Nanoparticles Measured by Electron Paramagnetic Resonance Spectroscopy. *J. Nanoparticle Res.* **2017**, *19* (12), 404. https://doi.org/10.1007/s11051-017-4084-3.

(77) Shi, T.; Schins, R. P. F.; Knaapen, A. M.; Kuhlbusch, T.; Pitz, M.; Heinrich, J.; Borm, P. J. A. Hydroxyl Radical Generation by Electron Paramagnetic Resonance as a New Method to Monitor Ambient Particulate Matter Composition. *J. Environ. Monit.* **2003**, *5* (4), 550–556. https://doi.org/10.1039/b303928p.

(78) Driessen, M. D.; Mues, S.; Vennemann, A.; Hellack, B.; Bannuscher, A.; Vimalakanthan, V.; Riebeling, C.; Ossig, R.; Wiemann, M.; Schnekenburger, J.; Kuhlbusch, T. A. J.; Renard, B.; Luch, A.; Haase, A. Proteomic Analysis of Protein Carbonylation: A Useful Tool to Unravel Nanoparticle Toxicity Mechanisms. *Part. Fibre Toxicol.* **2015**, *12* (1), 1–18. https://doi.org/10.1186/s12989-015-0108-2.

(79) Gao, D.; Ripley, S.; Weichenthal, S.; Godri Pollitt, K. J. Ambient Particulate Matter Oxidative Potential: Chemical Determinants, Associated Health Effects, and Strategies for Risk Management. *Free Radic. Biol. Med.* **2020**, *151* (May), 7–25. https://doi.org/10.1016/j.freeradbiomed.2020.04.028.

(80) Rao, L.; Zhang, L.; Wang, X.; Xie, T.; Zhou, S.; Lu, S.; Liu, X.; Lu, H.; Xiao, K.; Wang, W.; Wang, Q. Oxidative Potential Induced by Ambient Particulate Matters with Acellular Assays: A Review. *Processes* **2020**, *8* (11), 1–21. https://doi.org/10.3390/pr8111410.

(81) Delaval, M.; Wohlleben, W.; Landsiedel, R.; Baeza-Squiban, A.; Boland, S. Assessment of the Oxidative Potential of Nanoparticles by the Cytochrome c Assay: Assay Improvement and Development of a High-Throughput Method to Predict the Toxicity of Nanoparticles. *Arch. Toxicol.* **2017**, *91* (1), 163–177. https://doi.org/10.1007/s00204-016-1701-3.

(82) Daellenbach, K. R.; Uzu, G.; Jiang, J.; Cassagnes, L. E.; Leni, Z.; Vlachou, A.; Stefenelli, G.; Canonaco, F.; Weber, S.; Segers, A.; Kuenen, J. J. P.; Schaap, M.; Favez, O.; Albinet, A.; Aksoyoglu, S.; Dommen, J.; Baltensperger, U.; Geiser, M.; El Haddad, I.; Jaffrezo, J. L.; Prévôt, A. S. H. Sources of Particulate-Matter Air Pollution and Its Oxidative Potential in Europe. *Nature* **2020**, *587* (7834), 414–419. https://doi.org/10.1038/s41586-020-2902-8.

(83) Hsieh, S.; Bello, D.; Schmidt, D. F.; Pal, A. K.; Stella, A.; Isaacs, J. A.; Rogers, E. J. Mapping the Biological Oxidative Damage of Engineered Nanomaterials. *Small* **2013**, *9* (9–10), 1853–1865. https://doi.org/10.1002/smll.201201995.

(84) Bahl, A.; Hellack, B.; Wiemann, M.; Giusti, A.; Werle, K.; Haase, A.; Wohlleben, W. Nanomaterial Categorization by Surface Reactivity: A Case Study Comparing 35 Materials with Four Different Test Methods. *NanoImpact* **2020**, *19* (July), 100234. https://doi.org/10.1016/j.impact.2020.100234.

(85) Murphy, F.; Jacobsen, N. R.; Di Ianni, E.; Johnston, H.; Braakhuis, H.; Peijnenburg, W.; Oomen, A.; Fernandes, T.; Stone, V. Grouping MWCNTs Based on Their Similar Potential to Cause Pulmonary Hazard after Inhalation: A Case-Study. *Part. Fibre Toxicol.* **2022**, *19* (1), 1–23. https://doi.org/10.1186/s12989-022-00487-6.

(86) Díaz-Ufano, C.; Gallo-Cordova, A.; Santiandreu, L.; Veintemillas-Verdaguer, S.; Sáez, R.; Torralvo Fernández, M. J.; Morales, M. del P. Maximizing the Adsorption

Capacity of Iron Oxide Nanocatalysts for the Degradation of Organic Dyes. *Colloids Surfaces A Physicochem. Eng. Asp.* **2023**, *658* (November 2022), 130695. https://doi.org/10.1016/j.colsurfa.2022.130695.

(87) Sauer, U. G.; Vogel, S.; Aumann, A.; Hess, A.; Kolle, S. N.; Ma-Hock, L.; Wohlleben, W.; Dammann, M.; Strauss, V.; Treumann, S.; Gröters, S.; Wiench, K.; Van Ravenzwaay, B.; Landsiedel, R. Applicability of Rat Precision-Cut Lung Slices in Evaluating Nanomaterial Cytotoxicity, Apoptosis, Oxidative Stress, and Inflammation. *Toxicol. Appl. Pharmacol.* **2014**, *276* (1), 1–20. https://doi.org/10.1016/j.taap.2013.12.017.

(88) Farcal, L.; Andón, F. T.; Di Cristo, L.; Rotoli, B. M.; Bussolati, O.; Bergamaschi, E.; Mech, A.; Hartmann, N. B.; Rasmussen, K.; Riego-Sintes, J.; Ponti, J.; Kinsner-Ovaskainen, A.; Rossi, F.; Oomen, A.; Bos, P.; Chen, R.; Bai, R.; Chen, C.; Rocks, L.; Fulton, N.; Ross, B.; Hutchison, G.; Tran, L.; Mues, S.; Ossig, R.; Schnekenburger, J.; Campagnolo, L.; Vecchione, L.; Pietroiusti, A.; Fadeel, B. Comprehensive in Vitro Toxicity Testing of a Panel of Representative Oxide Nanomaterials: First Steps towards an Intelligent Testing Strategy. *PLoS One* **2015**, *10* (5), 1–34. https://doi.org/10.1371/journal.pone.0127174.

(89) Chanput, W.; Mes, J. J.; Wichers, H. J. THP-1 Cell Line: An in Vitro Cell Model for Immune Modulation Approach. *Int. Immunopharmacol.* **2014**, *23* (1), 37–45. https://doi.org/10.1016/j.intimp.2014.08.002.

(90) Kamiloglu, S.; Sari, G.; Ozdal, T.; Capanoglu, E. Guidelines for Cell Viability Assays. *Food Front.* **2020**, *1* (3), 332–349. https://doi.org/10.1002/fft2.44.

(91) Stoddart, M. J. Cell Viability Assays: Introduction. In *Methods in Molecular Biology*; 2011; Vol. 740, pp 1–6. https://doi.org/10.1007/978-1-61779-108-6_1.

(92) Rampersad, S. N. Multiple Applications of Alamar Blue as an Indicator of Metabolic Function and Cellular Health in Cell Viability Bioassays. *Sensors* **2012**, *12* (9), 12347–12360. https://doi.org/10.3390/s120912347.

(93) Johnson, S.; Nguyen, V.; Coder, D. Assessment of Cell Viability. *Curr. Protoc. Cytom.*

**2013**, *64* (1), 1–26. https://doi.org/10.1002/0471142956.cy0902s64.

(94) Taylor, S. C.; Posch, A. The Design of a Quantitative Western Blot Experiment. *Biomed Res. Int.* **2014**, *2014*. https://doi.org/10.1155/2014/361590.

(95) Chiswick, E. L.; Duffy, E.; Japp, B.; Remick, D. Detection and Quantification of Cytokines and Other Biomarkers. In *Methods in Molecular Biology*; 2012; Vol. 844, pp 15–30. https://doi.org/10.1007/978-1-61779-527-5_2.

(96) Steen, H.; Mann, M. The Abc's (and Xyz's) of Peptide Sequencing. *Nat. Rev. Mol. Cell Biol.* **2004**, *5* (9), 699–711. https://doi.org/10.1038/nrm1468.

(97) Bahl, A.; Ibrahim, C.; Plate, K.; Haase, A.; Dengjel, J.; Nymark, P.; Dumit, V. I. PROTEOMAS: A Workflow Enabling Harmonized Proteomic Meta-Analysis and Proteomic Signature Mapping. *J. Cheminform.* **2023**, *15* (1), 1–17. https://doi.org/10.1186/s13321-023-00710-2.

(98) Liu, X.; Yin, S.; Chen, Y.; Wu, Y.; Zheng, W.; Dong, H.; Bai, Y.; Qin, Y.; Li, J.; Feng, S.; Zhao, P. LPS-induced Proinflammatory Cytokine Expression in Human Airway Epithelial Cells and Macrophages via NF-κB, STAT3 or AP-1 Activation. *Mol. Med. Rep.* **2018**, *17* (4), 5484–5491. https://doi.org/10.3892/mmr.2018.8542.

(99) Araldi, R. P.; de Melo, T. C.; Mendes, T. B.; de Sá Júnior, P. L.; Nozima, B. H. N.; Ito, E. T.; de Carvalho, R. F.; de Souza, E. B.; de Cassia Stocco, R. Using the Comet and Micronucleus Assays for Genotoxicity Studies: A Review. *Biomed. Pharmacother.* **2015**, *72*, 74–82. https://doi.org/10.1016/j.biopha.2015.04.004.

(100) Zhang, Q. *Nanotoxicity*; Zhang, Q., Ed.; Methods in Molecular Biology; Springer New York: New York, NY, 2019; Vol. 1894. https://doi.org/10.1007/978-1-4939-8916-4.

(101) WARHEIT, D.; HOKE, R.; FINLAY, C.; DONNER, E.; REED, K.; SAYES, C. Development of a Base Set of Toxicity Tests Using Ultrafine TiO2 Particles as a Component of Nanoparticle Risk Management. *Toxicol. Lett.* **2007**, *171* (3), 99–110. https://doi.org/10.1016/j.toxlet.2007.04.008.

(102) Pan, X.; Redding, J. E.; Wiley, P. A.; Wen, L.; McConnell, J. S.; Zhang, B. Mutagenicity Evaluation of Metal Oxide Nanoparticles by the Bacterial Reverse Mutation Assay. *Chemosphere* **2010**, *79* (1), 113–116. https://doi.org/10.1016/j.chemosphere.2009.12.056.

(103) Kisin, E. R.; Murray, A. R.; Keane, M. J.; Shi, X. C.; Schwegler-Berry, D.; Gorelik, O.; Arepalli, S.; Castranova, V.; Wallace, W. E.; Kagan, V. E.; Shvedova, A. A. Single-Walled Carbon Nanotubes: Geno- and Cytotoxic Effects in Lung Fibroblast V79 Cells. *J. Toxicol. Environ. Heal. - Part A Curr. Issues* **2007**, *70* (24), 2071–2079. https://doi.org/10.1080/15287390701601251.

(104) Barnes, C. A.; Elsaesser, A.; Arkusz, J.; Smok, A.; Palus, J.; Leśniak, A.; Salvati, A.; Hanrahan, J. P.; Jong, W. H. de; Dziubałtowska, E.; Stępnik, M.; Rydzyński, K.; McKerr, G.; Lynch, I.; Dawson, K. A.; Howard, C. V. Reproducible Comet Assay of Amorphous Silica Nanoparticles Detects No Genotoxicity. *Nano Lett.* **2008**, *8* (9), 3069–3074. https://doi.org/10.1021/nl801661w.

(105) Stone, V.; Johnston, H.; Schins, R. P. F. Development of in Vitro Systems for Nanotoxicology: Methodological Considerations. *Crit. Rev. Toxicol.* **2009**, *39* (7), 613–626. https://doi.org/10.1080/10408440903120975.

(106) Magdolenova, Z.; Collins, A.; Kumar, A.; Dhawan, A.; Stone, V.; Dusinska, M. Mechanisms of Genotoxicity. A Review of in Vitro and in Vivo Studies with Engineered Nanoparticles. *Nanotoxicology* **2014**, *8* (3), 233–278. https://doi.org/10.3109/17435390.2013.773464.

(107) Kohl, Y.; Rundén-Pran, E.; Mariussen, E.; Hesler, M.; El Yamani, N.; Longhin, E. M.; Dusinska, M. Genotoxicity of Nanomaterials: Advanced In Vitro Models and High Throughput Methods for Human Hazard Assessment—A Review. *Nanomaterials* **2020**, *10* (10), 1911. https://doi.org/10.3390/nano10101911.

(108) Li, N.; Xia, T.; Nel, A. E. The Role of Oxidative Stress in Ambient Particulate Matter-Induced Lung Diseases and Its Implications in the Toxicity of Engineered Nanoparticles. *Free Radic. Biol. Med.* **2008**, *44* (9), 1689–1699.

https://doi.org/10.1016/j.freeradbiomed.2008.01.028.

(109) Landsiedel, R.; Ma-Hock, L.; Haussmann, H. J.; van Ravenzwaay, B.; Kayser, M.; Wiench, K. Inhalation Studies for the Safety Assessment of Nanomaterials: Status Quo and the Way Forward. *Wiley Interdiscip. Rev. Nanomedicine Nanobiotechnology* **2012**, *4* (4), 399–413. https://doi.org/10.1002/wnan.1173.

(110) Costa, P. M.; Fadeel, B. Emerging Systems Biology Approaches in Nanotoxicology : Towards a Mechanism-Based Understanding of Nanomaterial Hazard and Risk. **2016**, *299*, 101–111. https://doi.org/10.1016/j.taap.2015.12.014.

(111) Oberdörster, G.; Oberdörster, E.; Oberdörster, J. Nanotoxicology: An Emerging Discipline Evolving from Studies of Ultrafine Particles. *Environ. Health Perspect.* **2005**, *113* (7), 823–839. https://doi.org/10.1289/ehp.7339.

(112) Environment Directorate ORGANISATION FOR ECONOMIC COOPERATION AND DEVELOPMENT. Important Issues on Risk Assessment of Manufactured Nanomaterials Series on the Safety of Manufactured Nanomaterials No. 103 JT03489003 OFDE. **2022**, No. 103.

(113) *JRC NANOMATERIALS REPOSITORY. List of Representative Nanomaterials*; 2016.

(114) Mungsuk, C.; Yommee, S.; Supothina, S.; Chuaybamroong, P. Solar Photocatalytic Degradation of Carbendazim in Water Using TiO2 Particle- and Sol-Gel Dip-Coating Filters. *Results Eng.* **2023**, *19* (June), 101348. https://doi.org/10.1016/j.rineng.2023.101348.

(115) Ohtani, B.; Prieto-Mahaney, O. O.; Li, D.; Abe, R. What Is Degussa (Evonic) P25? Crystalline Composition Analysis, Reconstruction from Isolated Pure Particles and Photocatalytic Activity Test. *J. Photochem. Photobiol. A Chem.* **2010**, *216* (2–3), 179–182. https://doi.org/10.1016/j.jphotochem.2010.07.024.

(116) ACTIV, C. *CristalACTiV™ TiO2 DT-51 - Product Data Sheet*; 2012.

(117) Rasmussen, K.; Mast, J.; Temmerman, P. De; Verleysen, E.; Waegeneers, N.; Steen, F. Van; Pizzolon, J. C.; Temmerman, L. De; Van, E.; Jensen, K. A.; Birkedal, R.; Levin,

M.; Nielsen, S. H.; Koponen, I. K.; Axel, P.; Kofoed-sørensen, V.; Kembouche, Y.; Spalla, O.; Guiot, C.; Rousset, D.; Bau, S.; Bianchi, B.; Motzkus, C.; Shivachev, B.; Dimowa, L.; Nikolova, R.; Tarassov, M.; Petrov, O.; Gilliland, D.; Pianella, F.; Spampinato, V.; Cotogno, G.; Gibson, N. *Titanium Dioxide, NM-100, NM-101, NM-102, NM-103, NM-104, NM-105: Characterisation and Physico- Chemical Properties*; 2014. https://doi.org/10.2788/79554.

(118) Kermanizadeh, A.; Pojana, G.; Gaiser, B. K.; Birkedal, R.; Bilaničová, D.; Wallin, H.; Jensen, K. A.; Sellergren, B.; Hutchison, G. R.; Marcomini, A.; Stone, V. In Vitro Assessment of Engineered Nanomaterials Using a Hepatocyte Cell Line: Cytotoxicity, pro-Inflammatory Cytokines and Functional Markers. *Nanotoxicology* **2013**, *7* (3), 301–313. https://doi.org/10.3109/17435390.2011.653416.

(119) Singh, C.; Europäische Kommission Gemeinsame Forschungsstelle Institute for Health and Consumer Protection. *Cerium Dioxide NM-211, NM-212, NM-213, Characterisation and Test Item Preparation JRC Repository: NM-Series of Representative Manufactured Nanomaterials*; 2014. https://doi.org/10.2788/80203.

(120) Singh, C.; Friedrichs, S.; Levin, M.; Birkedal, R.; Jensen, K. A.; Pojana, G.; Wohlleben, W.; Schulte, S.; Wiench, K.; Turney, T.; Koulaeva, O.; Marshall, D.; Hund-Rinke, K.; Kördel, W.; Doren, E. Van; De Temmerman, P.-J.; Abi, M.; Francisco, D.; Mast, J.; Gibson, N.; Koeber, R.; Linsinger, T.; Klein, C. L. *Zinc Oxide NM-110, NM-111, NM-112, NM-113 Characterisation and Test Item Preparation*; 2011. https://doi.org/10.2787/55008.

(121) Kermanizadeh, A.; Vranic, S.; Boland, S.; Moreau, K.; Baeza-Squiban, A.; Gaiser, B. K.; Andrzejczuk, L. A.; Stone, V. An in Vitroassessment of Panel of Engineered Nanomaterials Using a Human Renal Cell Line: Cytotoxicity, pro-Inflammatory Response, Oxidative Stress and Genotoxicity. *BMC Nephrol.* **2013**, *14* (1), 96. https://doi.org/10.1186/1471-2369-14-96.

(122) Gu, Y.; Cheng, S.; Chen, G.; Shen, Y.; Li, X.; Jiang, Q.; Li, J.; Cao, Y. The Effects of Endoplasmic Reticulum Stress Inducer Thapsigargin on the Toxicity of ZnO or TiO2 Nanoparticles to Human Endothelial Cells. *Toxicol. Mech. Methods* **2017**, *27* (3),

191–200. https://doi.org/10.1080/15376516.2016.1273429.

(123) Rasmussen, K.; Mech, A.; Mast, J.; de Temmerman, P.-J.; Waegeneers, N.; Steen, F. Van; Pizzolon, J. C.; de Temmerman, L.; van Doren, E.; Jensen, A.; Birkedal, R.; Levin, M.; Nielsen, H.; Koponen, I. K.; Axel, P.; Kembouche, Y.; Thieriet, N.; Spalla, O.; Giuot, C.; Rousset, D.; Bau, S.; Bianchi, B.; Gilliland, D.; Pianella, F.; Ceccone, G.; Cotogno, G.; Gibson, N.; Stamm, H. *Jrc Scientific and Policy Reports*; 2013. https://doi.org/10.2788/57989.

(124) Guichard, Y.; Schmit, J.; Darne, C.; Gaté, L.; Goutet, M.; Rousset, D.; Rastoix, O.; Wrobel, R.; Witschger, O.; Martin, A.; Fierro, V.; Binet, S. Cytotoxicity and Genotoxicity of Nanosized and Microsized Titanium Dioxide and Iron Oxide Particles in Syrian Hamster Embryo Cells. *Ann. Occup. Hyg.* **2012**, *56* (5), 631–644. https://doi.org/10.1093/annhyg/mes006.

(125) Life, M. *Copper Oxide (Ref. Number: 544868) Specifications*; 2023. https://www.sigmaaldrich.com/ES/es/product/aldrich/544868.

(126) Martín-Gómez, J.; Hidalgo-Carrillo, J.; Estévez, R. C.; Urbano, F. J.; Marinas, A. Hydrogen Photoproduction on TiO2-CuO Artificial Olive Leaves. *Appl. Catal. A Gen.* **2021**, *620* (March), 118178. https://doi.org/10.1016/j.apcata.2021.118178.

(127) Martín-Gómez, J.; Hidalgo-Carrillo, J.; Montes, V.; Estévez-Toledano, R. C.; Escamilla, J. C.; Marinas, A.; Urbano, F. J. EPR and CV Studies Cast Further Light on the Origin of the Enhanced Hydrogen Production through Glycerol Photoreforming on CuO:TiO2 Physical Mixtures. *J. Environ. Chem. Eng.* **2021**, *9* (4), 105336. https://doi.org/10.1016/j.jece.2021.105336.

(128) Moschini, E.; Colombo, G.; Chirico, G.; Capitani, G.; Dalle-Donne, I.; Mantecca, P. Biological Mechanism of Cell Oxidative Stress and Death during Short-Term Exposure to Nano CuO. *Sci. Rep.* **2023**, *13* (1), 2326. https://doi.org/10.1038/s41598-023-28958-6.

(129) Jacobsen, N. R.; Saber, A. T.; White, P.; Møller, P.; Pojana, G.; Vogel, U.; Loft, S.; Gingerich, J.; Soper, L.; Douglas, G. R.; Wallin, H. Increased Mutant Frequency by

Carbon Black, but Not Quartz, in the LacZ and CII Transgenes of Muta ™ Mouse Lung Epithelial Cells. *Environ. Mol. Mutagen.* **2007**, *48* (6), 451–461. https://doi.org/10.1002/em.20300.

(130) Kyjovska, Z. O.; Jacobsen, N. R.; Saber, A. T.; Bengtson, S.; Jackson, P.; Wallin, H.; Vogel, U. DNA Damage Following Pulmonary Exposure by Instillation to Low Doses of Carbon Black (Printex 90) Nanoparticles in Mice. *Environ. Mol. Mutagen.* **2015**, *56* (1), 41–49. https://doi.org/10.1002/em.21888.

(131) Sauvain, J. J.; Deslarzes, S.; Riediker, M. Nanoparticle Reactivity toward Dithiothreitol. *Nanotoxicology* **2008**, *2* (3), 121–129. https://doi.org/10.1080/17435390802245716.

(132) Sauvain, J. J.; Rossi, M. J.; Riediker, M. Comparison of Three Acellular Tests for Assessing the Oxidation Potential of Nanomaterials. *Aerosol Sci. Technol.* **2013**, *47* (2), 218–227. https://doi.org/10.1080/02786826.2012.742951.

(133) Simeone, F. C.; Costa, A. L. Assessment of Cytotoxicity of Metal Oxide Nanoparticles on the Basis of Fundamental Physical-Chemical Parameters: A Robust Approach to Grouping. *Environ. Sci. Nano* **2019**, *6* (10), 3102–3112. https://doi.org/10.1039/c9en00785g.

(134) Jensen, K. A. *NanoGenoTox. WP4, Deliverable 3: Final Protocol for Producing Suitable MN Exposure Media. The Generic NANOGENOTOX Dispersion Protocol. Standard Operation Procedure (SOP) and Background Documentation*; 2011. https://www.safenano.re.kr/download.do?SEQ=175.

(135) Jiang, H.; Sabbir Ahmed, C. M.; Canchola, A.; Chen, J. Y.; Lin, Y. H. Use of Dithiothreitol Assay to Evaluate the Oxidative Potential of Atmospheric Aerosols. *Atmosphere (Basel).* **2019**, *10* (10), 1–21. https://doi.org/10.3390/atmos10100571.

(136) Boyles, M.; Murphy, F.; Mueller, W.; Wohlleben, W.; Jacobsen, N. R.; Braakhuis, H.; Giusti, A.; Stone, V. Development of a Standard Operating Procedure for the DCFH2-DA Acellular Assessment of Reactive Oxygen Species Produced by Nanomaterials. *Toxicol. Mech. Methods* **2022**, *32* (6), 439–452.

https://doi.org/10.1080/15376516.2022.2029656.

(137) Pal, A. K.; Bello, D.; Budhlall, B.; Rogers, E.; Milton, D. K. Screening for Oxidative Stress Elicited by Engineered Nanomaterials: Evaluation of Acellular DCFH Assay. *Dose-Response* **2012**, *10* (3), 308–330. https://doi.org/10.2203/dose-response.10-036.Pal.

(138) Foucaud, L.; Wilson, M. R.; Brown, D. M.; Stone, V. Measurement of Reactive Species Production by Nanoparticles Prepared in Biologically Relevant Media. *Toxicol. Lett.* **2007**, *174* (1–3), 1–9. https://doi.org/10.1016/j.toxlet.2007.08.001.

(139) Gliga, A. R.; Skoglund, S.; Odnevall Wallinder, I.; Fadeel, B.; Karlsson, H. L. Size-Dependent Cytotoxicity of Silver Nanoparticles in Human Lung Cells: The Role of Cellular Uptake, Agglomeration and Ag Release. *Part. Fibre Toxicol.* **2014**, *11* (1), 1–17. https://doi.org/10.1186/1743-8977-11-11.

(140) Ag Seleci, D.; Tsiliki, G.; Werle, K.; Elam, D. A.; Okpowe, O.; Seidel, K.; Bi, X.; Westerhoff, P.; Innes, E.; Boyles, M.; Miller, M.; Giusti, A.; Murphy, F.; Haase, A.; Stone, V.; Wohlleben, W. Determining Nanoform Similarity via Assessment of Surface Reactivity by Abiotic and in Vitro Assays. *NanoImpact* **2022**, *26* (September 2021), 100390. https://doi.org/10.1016/j.impact.2022.100390.

(141) Mancardi, G.; Mikolajczyk, A.; Annapoorani, V. K.; Bahl, A.; Blekos, K.; Burk, J.; Çetin, Y. A.; Chairetakis, K.; Dutta, S.; Escorihuela, L.; Jagiello, K.; Singhal, A.; van der Pol, R.; Bañares, M. A.; Buchete, N.-V.; Calatayud, M.; Dumit, V. I.; Gardini, D.; Jeliazkova, N.; Haase, A.; Marcoulaki, E.; Martorell, B.; Puzyn, T.; Agur Sevink, G. J.; Simeone, F. C.; Tämm, K.; Chiavazzo, E. A Computational View on Nanomaterial Intrinsic and Extrinsic Features for Nanosafety and Sustainability. *Mater. Today* **2023**. https://doi.org/10.1016/j.mattod.2023.05.029.

(142) Paunovska, K.; Loughrey, D.; Sago, C. D.; Langer, R.; Dahlman, J. E. Using Large Datasets to Understand Nanotechnology. *Adv. Mater.* **2019**, *31* (43), 1902798. https://doi.org/10.1002/adma.201902798.

(143) Wyrwoll, A. J.; Lautenschläger, P.; Bach, A.; Hellack, B.; Dybowska, A.; Kuhlbusch, T.

A. J.; Hollert, H.; Schäffer, A.; Maes, H. M. Size Matters - The Phototoxicity of TiO2 Nanomaterials. *Environ. Pollut.* **2016**, *208*, 859–867. https://doi.org/10.1016/j.envpol.2015.10.035.

(144) Koike, E.; Kobayashi, T. Chemical and Biological Oxidative Effects of Carbon Black Nanoparticles. *Chemosphere* **2006**, *65* (6), 946–951. https://doi.org/10.1016/j.chemosphere.2006.03.078.

(145) Bengalli, R. D.; Zerbi, G.; Lucotti, A.; Catelani, T.; Mantecca, P. Carbon Nanotubes: Structural Defects as Stressors Inducing Lung Cell Toxicity. *Chem. Biol. Interact.* **2023**, *382* (June), 110613. https://doi.org/10.1016/j.cbi.2023.110613.

(146) Thongkam, W.; Gerloff, K.; van Berlo, D.; Albrecht, C.; Schins, R. P. F. Oxidant Generation, DNA Damage and Cytotoxicity by a Panel of Engineered Nanomaterials in Three Different Human Epithelial Cell Lines. *Mutagenesis* **2017**, *32* (1), 105–115. https://doi.org/10.1093/mutage/gew056.

(147) Zijno, A.; Cavallo, D.; Di Felice, G.; Ponti, J.; Barletta, B.; Butteroni, C.; Corinti, S.; De Berardis, B.; Palamides, J.; Ursini, C. L.; Fresegna, A. M.; Ciervo, A.; Maiello, R.; Barone, F. Use of a Common European Approach for Nanomaterials' Testing to Support Regulation: A Case Study on Titanium and Silicon Dioxide Representative Nanomaterials. *J. Appl. Toxicol.* **2020**, *40* (11), 1511–1525. https://doi.org/10.1002/jat.4002.

(148) Cervena, T.; Rossnerova, A.; Zavodna, T.; Sikorova, J.; Vrbova, K.; Milcova, A.; Topinka, J.; Rossner, P. Testing Strategies of the in Vitro Micronucleus Assay for the Genotoxicity Assessment of Nanomaterials in Beas-2b Cells. *Nanomaterials* **2021**, *11* (8), 1–20. https://doi.org/10.3390/nano11081929.

(149) Karkossa, I.; Bannuscher, A.; Hellack, B.; Bahl, A.; Buhs, S.; Nollau, P.; Luch, A.; Schubert, K.; Von Bergen, M.; Haase, A. An In-Depth Multi-Omics Analysis in RLE-6TN Rat Alveolar Epithelial Cells Allows for Nanomaterial Categorization. *Part. Fibre Toxicol.* **2019**, *16* (1), 1–19. https://doi.org/10.1186/s12989-019-0321-5.

(150) Lamon, L.; Asturiol, D.; Richarz, A.; Joossens, E.; Graepel, R.; Aschberger, K.; Worth,

A. Grouping of Nanomaterials to Read-across Hazard Endpoints: From Data Collection to Assessment of the Grouping Hypothesis by Application of Chemoinformatic Techniques. *Part. Fibre Toxicol.* **2018**. https://doi.org/10.1186/s12989-018-0273-1.

(151) Landsiedel, R.; Sauer, U. G.; Ma-Hock, L.; Schnekenburger, J.; Wiemann, M. Pulmonary Toxicity of Nanomaterials: A Critical Comparison of Published in Vitro Assays and in Vivo Inhalation or Instillation Studies. *Nanomedicine* **2014**, *9* (16), 2557–2585. https://doi.org/10.2217/nnm.14.149.

(152) Bettencourt, A.; Gonçalves, L. M.; Gramacho, A. C.; Vieira, A.; Rolo, D.; Martins, C.; Assunção, R.; Alvito, P.; Silva, M. J.; Louro, H. Analysis of the Characteristics and Cytotoxicity of Titanium Dioxide Nanomaterials Following Simulated in Vitro Digestion. *Nanomaterials* **2020**, *10* (8), 1–18. https://doi.org/10.3390/nano10081516.

(153) Dorier, M.; Tisseyre, C.; Dussert, F.; Béal, D.; Arnal, M.-E.; Douki, T.; Valdiglesias, V.; Laffon, B.; Fraga, S.; Brandão, F.; Herlin-Boime, N.; Barreau, F.; Rabilloud, T.; Carriere, M. Toxicological Impact of Acute Exposure to E171 Food Additive and TiO2 Nanoparticles on a Co-Culture of Caco-2 and HT29-MTX Intestinal Cells. *Mutat. Res. Toxicol. Environ. Mutagen.* **2019**, *845* (July 2018), 402980. https://doi.org/10.1016/j.mrgentox.2018.11.004.

(154) Lankoff, A.; Sandberg, W. J.; Wegierek-Ciuk, A.; Lisowska, H.; Refsnes, M.; Sartowska, B.; Schwarze, P. E.; Meczynska-Wielgosz, S.; Wojewodzka, M.; Kruszewski, M. The Effect of Agglomeration State of Silver and Titanium Dioxide Nanoparticles on Cellular Response of HepG2, A549 and THP-1 Cells. *Toxicol. Lett.* **2012**, *208* (3), 197–213. https://doi.org/10.1016/j.toxlet.2011.11.006.

(155) Park, E. J.; Choi, J.; Park, Y. K.; Park, K. Oxidative Stress Induced by Cerium Oxide Nanoparticles in Cultured BEAS-2B Cells. *Toxicology* **2008**, *245* (1–2), 90–100. https://doi.org/10.1016/j.tox.2007.12.022.

(156) Nel, A. E.; Mädler, L.; Velegol, D.; Xia, T.; Hoek, E. M. V.; Somasundaran, P.; Klaessig,

F.; Castranova, V.; Thompson, M. Understanding Biophysicochemical Interactions at the Nano-Bio Interface. *Nat. Mater.* **2009**, *8* (7), 543–557. https://doi.org/10.1038/nmat2442.

(157) Xia, T.; Kovochich, M.; Liong, M.; Mädler, L.; Gilbert, B.; Shi, H.; Yeh, J. I.; Zink, J. I.; Nel, A. E. Comparison of the Mechanism of Toxicity of Zinc Oxide and Cerium Oxide Nanoparticles Based on Dissolution and Oxidative Stress Properties. *ACS Nano* **2008**, *2* (10), 2121–2134. https://doi.org/10.1021/nn800511k.

(158) Demokritou, P.; Gass, S.; Pyrgiotakis, G.; Cohen, J. M.; Goldsmith, W.; McKinney, W.; Frazer, D.; Ma, J.; Schwegler-Berry, D.; Brain, J.; Castranova, V. An in Vivo and in Vitro Toxicological Characterisation of Realistic Nanoscale CeO2 Inhalation Exposures. *Nanotoxicology* **2013**, *7* (8), 1338–1350. https://doi.org/10.3109/17435390.2012.739665.

(159) Wiemann, M.; Vennemann, A.; Sauer, U. G.; Wiench, K.; Ma-Hock, L.; Landsiedel, R. An in Vitro Alveolar Macrophage Assay for Predicting the Short-Term Inhalation Toxicity of Nanomaterials. *J. Nanobiotechnology* **2016**, *14* (1), 16. https://doi.org/10.1186/s12951-016-0164-2.

(160) Rosenkranz, P.; Fernández-Cruz, M. L.; Conde, E.; Ramírez-Fernández, M. B.; Flores, J. C.; Fernández, M.; Navas, J. M. Effects of Cerium Oxide Nanoparticles to Fish and Mammalian Cell Lines: An Assessment of Cytotoxicity and Methodology. *Toxicol. Vitr.* **2012**, *26* (6), 888–896. https://doi.org/10.1016/j.tiv.2012.04.019.

(161) Cappellini, F.; Di Bucchianico, S.; Karri, V.; Latvala, S.; Malmlöf, M.; Kippler, M.; Elihn, K.; Hedberg, J.; Odnevall Wallinder, I.; Gerde, P.; Karlsson, H. L. Dry Generation of CeO2 Nanoparticles and Deposition onto a Co-Culture of A549 and THP-1 Cells in Air-Liquid Interface—Dosimetry Considerations and Comparison to Submerged Exposure. *Nanomaterials* **2020**, *10* (4), 618. https://doi.org/10.3390/nano10040618.

(162) Lehner, R.; Zanoni, I.; Banuscher, A.; Costa, A. L.; Rothen-Rutishauser, B. Fate of Engineered Nanomaterials at the Human Epithelial Lung Tissue Barrier in Vitro

after Single and Repeated Exposures. *Front. Toxicol.* **2022**, *4* (September), 1–13. https://doi.org/10.3389/ftox.2022.918633.

(163) Precupas, A.; Gheorghe, D.; Botea-Petcu, A.; Leonties, A. R.; Sandu, R.; Popa, V. T.; Mariussen, E.; Naouale, E. Y.; Rundén-Pran, E.; Dumit, V.; Xue, Y.; Cimpan, M. R.; Dusinska, M.; Haase, A.; Tanasescu, S. Thermodynamic Parameters at Bio-Nano Interface and Nanomaterial Toxicity: A Case Study on BSA Interaction with ZnO, SiO2, and TiO2. *Chem. Res. Toxicol.* **2020**, *33* (8), 2054–2071. https://doi.org/10.1021/acs.chemrestox.9b00468.

(164) Yamani, N. El; Collins, A. R.; Rundén-Pran, E.; Fjellsbø, L. M.; Shaposhnikov, S.; Zienolddiny, S.; Dusinska, M. In Vitro Genotoxicity Testing of Four Reference Metal Nanomaterials, Titanium Dioxide, Zinc Oxide, Cerium Oxide and Silver: Towards Reliable Hazard Assessment. *Mutagenesis* **2017**, *32* (1), 117–126. https://doi.org/10.1093/mutage/gew060.

(165) Cao, Y.; Roursgaard, M.; Kermanizadeh, A.; Loft, S.; Møller, P. Synergistic Effects of Zinc Oxide Nanoparticles and Fatty Acids on Toxicity to Caco-2 Cells. *Int. J. Toxicol.* **2015**, *34* (1), 67–76. https://doi.org/10.1177/1091581814560032.

(166) Brzicova, T.; Javorkova, E.; Vrbova, K.; Zajicova, A.; Holan, V.; Pinkas, D.; Philimonenko, V.; Sikorova, J.; Klema, J.; Topinka, J.; Rossner, P. Molecular Responses in THP-1 Macrophage-like Cells Exposed to Diverse Nanoparticles. *Nanomaterials* **2019**, *9* (5), 1–19. https://doi.org/10.3390/nano9050687.

(167) Sauer, U. G.; Vogel, S.; Aumann, A.; Hess, A.; Kolle, S. N.; Ma-Hock, L.; Wohlleben, W.; Dammann, M.; Strauss, V.; Treumann, S.; Gröters, S.; Wiench, K.; van Ravenzwaay, B.; Landsiedel, R. Applicability of Rat Precision-Cut Lung Slices in Evaluating Nanomaterial Cytotoxicity, Apoptosis, Oxidative Stress, and Inflammation. *Toxicol. Appl. Pharmacol.* **2014**, *276* (1), 1–20. https://doi.org/10.1016/j.taap.2013.12.017.

(168) Fruijtier-Pölloth, C. The Safety of Nanostructured Synthetic Amorphous Silica (SAS) as a Food Additive (E 551). *Arch. Toxicol.* **2016**, *90* (12), 2885–2916.

https://doi.org/10.1007/s00204-016-1850-4.

(169) Di Cristo, L.; Ude, V. C.; Tsiliki, G.; Tatulli, G.; Romaldini, A.; Murphy, F.; Wohlleben, W.; Oomen, A. G.; Pompa, P. P.; Arts, J.; Stone, V.; Sabella, S. Grouping of Orally Ingested Silica Nanomaterials via Use of an Integrated Approach to Testing and Assessment to Streamline Risk Assessment. *Part. Fibre Toxicol.* **2022**, *19* (1), 68. https://doi.org/10.1186/s12989-022-00508-4.

(170) Lai, X.; Wei, Y.; Zhao, H.; Chen, S.; Bu, X.; Lu, F.; Qu, D.; Yao, L.; Zheng, J.; Zhang, J. The Effect of Fe 2 O 3 and ZnO Nanoparticles on Cytotoxicity and Glucose Metabolism in Lung Epithelial Cells. *J. Appl. Toxicol.* **2015**, *35* (6), 651–664. https://doi.org/10.1002/jat.3128.

(171) HERZOG, E.; CASEY, A.; LYNG, F.; CHAMBERS, G.; BYRNE, H.; DAVOREN, M. A New Approach to the Toxicity Testing of Carbon-Based Nanomaterials—The Clonogenic Assay. *Toxicol. Lett.* **2007**, *174* (1–3), 49–60. https://doi.org/10.1016/j.toxlet.2007.08.009.

(172) Moschini, E.; Gualtieri, M.; Colombo, M.; Fascio, U.; Camatini, M.; Mantecca, P. The Modality of Cell-Particle Interactions Drives the Toxicity of Nanosized CuO and TiO2 in Human Alveolar Epithelial Cells. *Toxicol. Lett.* **2013**, *222* (2), 102–116. https://doi.org/10.1016/j.toxlet.2013.07.019.

(173) Kwon, J.-T.; Kim, Y.; Choi, S.; Yoon, B.; Kim, H.-S.; Shim, I.; Sul, D. Pulmonary Toxicity and Proteomic Analysis in Bronchoalveolar Lavage Fluids and Lungs of Rats Exposed to Copper Oxide Nanoparticles. *Int. J. Mol. Sci.* **2022**, *23* (21), 13265. https://doi.org/10.3390/ijms232113265.

(174) Safar, R.; Doumandji, Z.; Saidou, T.; Ferrari, L.; Nahle, S.; Rihn, B. H.; Joubert, O. Cytotoxicity and Global Transcriptional Responses Induced by Zinc Oxide Nanoparticles NM 110 in PMA-Differentiated THP-1 Cells. *Toxicol. Lett.* **2019**, *308* (July 2018), 65–73. https://doi.org/10.1016/j.toxlet.2018.11.003.

(175) El Yamani, N.; Mariussen, E.; Gromelski, M.; Wyrzykowska, E.; Grabarek, D.; Puzyn, T.; Tanasescu, S.; Dusinska, M.; Rundén-Pran, E. Hazard Identification of

Nanomaterials: In Silico Unraveling of Descriptors for Cytotoxicity and Genotoxicity. *Nano Today* **2022**, *46*, 101581. https://doi.org/10.1016/j.nantod.2022.101581.

(176) NanoGenoTox partnership. NANOGENOTOX Final Report. Facilitating the Safety Evaluation of Manufactured Nanomaterials by Characterising Their Potential Genotoxic Hazard. *Nanogenotox* **2013**, 60.

(177) Di Ianni, E.; Erdem, J. S.; Møller, P.; Sahlgren, N. M.; Poulsen, S. S.; Knudsen, K. B.; Zienolddiny, S.; Saber, A. T.; Wallin, H.; Vogel, U.; Jacobsen, N. R. In Vitro-in Vivo Correlations of Pulmonary Inflammogenicity and Genotoxicity of MWCNT. *Part. Fibre Toxicol.* **2021**, *18* (1), 1–16. https://doi.org/10.1186/s12989-021-00413-2.

(178) Lindner, K.; Ströbele, M.; Schlick, S.; Webering, S.; Jenckel, A.; Kopf, J.; Danov, O.; Sewald, K.; Buj, C.; Creutzenberg, O.; Tillmann, T.; Pohlmann, G.; Ernst, H.; Ziemann, C.; Hüttmann, G.; Heine, H.; Bockhorn, H.; Hansen, T.; König, P.; Fehrenbach, H. Biological Effects of Carbon Black Nanoparticles Are Changed by Surface Coating with Polycyclic Aromatic Hydrocarbons. *Part. Fibre Toxicol.* **2017**, *14* (1), 1–17. https://doi.org/10.1186/s12989-017-0189-1.

(179) Loret, T.; Rogerieux, F.; Trouiller, B.; Braun, A.; Egles, C.; Lacroix, G. Predicting the in Vivo Pulmonary Toxicity Induced by Acute Exposure to Poorly Soluble Nanomaterials by Using Advanced in Vitro Methods. *Part. Fibre Toxicol.* **2018**, *15* (1), 25. https://doi.org/10.1186/s12989-018-0260-6.

(180) Srinivas, A.; Rao, P. J.; Selvam, G.; Murthy, P. B.; Reddy, P. N. Acute Inhalation Toxicity of Cerium Oxide Nanoparticles in Rats. *Toxicol. Lett.* **2011**, *205* (2), 105–115. https://doi.org/10.1016/j.toxlet.2011.05.1027.

(181) Tarantini, A.; Huet, S.; Jarry, G.; Lanceleur, R.; Poul, M.; Tavares, A.; Vital, N.; Louro, H.; João Silva, M.; Fessard, V. Genotoxicity of Synthetic Amorphous Silica Nanoparticles in Rats Following Short-Term Exposure. Part 1: Oral Route. *Environ. Mol. Mutagen.* **2015**, *56* (2), 218–227. https://doi.org/10.1002/em.21935.

(182) Klein, C. L.; Wiench, K.; Wiemann, M.; Ma-Hock, L.; Van Ravenzwaay, B.; Landsiedel,

R. Hazard Identification of Inhaled Nanomaterials: Making Use of Short-Term Inhalation Studies. *Arch. Toxicol.* **2012**, *86* (7), 1137–1151. https://doi.org/10.1007/s00204-012-0834-2.

(183) Bannuscher, A.; Hellack, B.; Bahl, A.; Laloy, J.; Herman, H.; Stan, M. S.; Dinischiotu, A.; Giusti, A.; Krause, B.-C.; Tentschert, J.; Roșu, M.; Balta, C.; Hermenean, A.; Wiemann, M.; Luch, A.; Haase, A. Metabolomics Profiling to Investigate Nanomaterial Toxicity in Vitro and in Vivo. *Nanotoxicology* **2020**, *14* (6), 807–826. https://doi.org/10.1080/17435390.2020.1764123.

(184) Landsiedel, R.; Ma-Hock, L.; Hofmann, T.; Wiemann, M.; Strauss, V.; Treumann, S.; Wohlleben, W.; Gröters, S.; Wiench, K.; van Ravenzwaay, B. Application of Short-Term Inhalation Studies to Assess the Inhalation Toxicity of Nanomaterials. *Part. Fibre Toxicol.* **2014**, *11* (1), 16. https://doi.org/10.1186/1743-8977-11-16.

(185) Jehng, J.-M.; Wachs, I. E.; Ford, M. Temperature-Programmed (TP) Techniques. In *Springer Handbook of Advanced Catalyst Characterization. Springer Handb. Chapter 45*; 2023; Vol. 4, pp 1005–1029. https://doi.org/10.1007/978-3-031-07125-6_45.

(186) Davydov, A. *Molecular Spectroscopy of Oxide Catalyst Surfaces*; Wiley, 2003. https://doi.org/10.1002/0470867981.

(187) Collins, S. E.; Briand, L. E.; Gambaro, L. A.; Baltanás, M. A.; Bonivardi, A. L. Adsorption and Decomposition of Methanol on Gallium Oxide Polymorphs. *J. Phys. Chem. C* **2008**, *112* (38), 14988–15000. https://doi.org/10.1021/jp801252d.

(188) Bazin, P.; Thomas, S.; Marie, O.; Daturi, M. New Insights into the Methanol Oxidation Mechanism over Au/CeO2 Catalyst through Complementary Kinetic and FTIR Operando SSITKA Approaches. *Catal. Today* **2012**, *182* (1), 3–11. https://doi.org/10.1016/j.cattod.2011.10.001.

(189) Darne, C.; Desforges, A.; Berrada, N.; Fontana, C.; Guichard, Y.; Gaté, L.; Bégin, D.; Le Normand, F.; Valsaque, F.; Ghanbaja, J.; Gleize, J.; Vigolo, B. A Non-Damaging Purification Method: Decoupling the Toxicity of Multi-Walled Carbon Nanotubes

and Their Associated Metal Impurities. *Environ. Sci. Nano* **2019**, *6* (6), 1852–1865. https://doi.org/10.1039/C8EN01276H.

(190) Janssen, N. A. H.; Yang, A.; Strak, M.; Steenhof, M.; Hellack, B.; Gerlofs-Nijland, M. E.; Kuhlbusch, T.; Kelly, F.; Harrison, R.; Brunekreef, B.; Hoek, G.; Cassee, F. Oxidative Potential of Particulate Matter Collected at Sites with Different Source Characteristics. *Sci. Total Environ.* **2014**, *472*, 572–581. https://doi.org/10.1016/j.scitotenv.2013.11.099.

(191) Breznan, D.; Nazemof, N.; Kunc, F.; Hill, M.; Vladisavljevic, D.; Gomes, J.; Johnston, L. J.; Vincent, R.; Kumarathasan, P. Acellular Oxidative Potential Assay for Screening of Amorphous Silica Nanoparticles. *Analyst* **2020**, *145* (14), 4867–4879. https://doi.org/10.1039/d0an00380h.

(192) Kramer, A. L.; Dorn, S.; Perez, A.; Roper, C.; Titaley, I. A.; Cayton, K.; Cook, R. P.; Cheong, P. H. Y.; Massey Simonich, S. L. Assessing the Oxidative Potential of PAHs in Ambient PM2.5 Using the DTT Consumption Assay. *Environ. Pollut.* **2021**, *285* (May), 117411. https://doi.org/10.1016/j.envpol.2021.117411.

(193) *Haase, A. & Klaessig, F., (2018). EU US Roadmap Nanoinformatics 2030. EU Nanosafety Cluster. Https://Doi.Org/10.5281/Zenodo.1486012*. https://doi.org/10.5281/zenodo.1486012.

(194) Jeevanandam, J.; Barhoum, A.; Chan, Y. S.; Dufresne, A.; Danquah, M. K. Review on Nanoparticles and Nanostructured Materials: History, Sources, Toxicity and Regulations. *Beilstein J. Nanotechnol.* **2018**, *9* (1), 1050–1074. https://doi.org/10.3762/bjnano.9.98.

(195) Yang, H.; Liu, C.; Yang, D.; Zhang, H.; Xi, Z. Comparative Study of Cytotoxicity, Oxidative Stress and Genotoxicity Induced by Four Typical Nanomaterials: The Role of Particle Size, Shape and Composition. *J. Appl. Toxicol.* **2009**, *29* (1), 69–78. https://doi.org/10.1002/jat.1385.

(196) Setyawati, M. I.; Tay, C. Y.; Leong, D. T. Effect of Zinc Oxide Nanomaterials-Induced Oxidative Stress on the P53 Pathway. *Biomaterials* **2013**, *34* (38), 10133–10142.

https://doi.org/10.1016/j.biomaterials.2013.09.024.

(197) Čapek, J.; Roušar, T. Detection of Oxidative Stress Induced by Nanomaterials in Cells—the Roles of Reactive Oxygen Species and Glutathione. *Molecules* **2021**, *26* (16). https://doi.org/10.3390/molecules26164710.

(198) Crobeddu, B.; Aragao-Santiago, L.; Bui, L. C.; Boland, S.; Baeza Squiban, A. Oxidative Potential of Particulate Matter 2.5 as Predictive Indicator of Cellular Stress. *Environ. Pollut.* **2017**, *230*, 125–133. https://doi.org/10.1016/j.envpol.2017.06.051.

(199) Øvrevik, J. Oxidative Potential Versus Biological Effects: A Review on the Relevance of Cell-Free/Abiotic Assays as Predictors of Toxicity from Airborne Particulate Matter. *Int. J. Mol. Sci.* **2019**, *20* (19), 4772. https://doi.org/10.3390/ijms20194772.

(200) Crobeddu, B.; Baudrimont, I.; Deweirdt, J.; Sciare, J.; Badel, A.; Camproux, A. C.; Bui, L. C.; Baeza-Squiban, A. Lung Antioxidant Depletion: A Predictive Indicator of Cellular Stress Induced by Ambient Fine Particles. *Environ. Sci. Technol.* **2020**, *54* (4), 2360–2369. https://doi.org/10.1021/acs.est.9b05990.

(201) Çetin, Y. A.; Martorell, B.; Serratosa, F.; Aguilera-Porta, N.; Calatayud, M. Analyzing the TiO 2 Surface Reactivity Based on Oxygen Vacancies Computed by DFT and DFTB Methods. *J. Phys. Condens. Matter* **2022**, *34* (31), 314004. https://doi.org/10.1088/1361-648X/ac7025.

(202) Chou, H.-H.; Ya-Hsuan Liou, S.; Calatayud, M. Modelling Rutile TiO2nanorod Growth Preferences: A Density Functional Theory Study. *Catal. Today* **2020**, *356* (February), 49–55. https://doi.org/10.1016/j.cattod.2020.02.007.

(203) Dumit, V. I.; Ammar, A.; Bakker, M. I.; Bañares, M. A.; Bossa, C.; Costa, A.; Cowie, H.; Drobne, D.; Exner, T. E.; Farcal, L.; Friedrichs, S.; Furxhi, I.; Grafström, R.; Haase, A.; Himly, M.; Jeliazkova, N.; Lynch, I.; Maier, D.; Noorlander, C. W.; Shin, H. K.; Soler-Illia, G. J. A. A.; Suarez-Merino, B.; Willighagen, E.; Nymark, P. From Principles to Reality. FAIR Implementation in the Nanosafety Community. *Nano Today* **2023**, *51*, 101923. https://doi.org/10.1016/j.nantod.2023.101923.

(204) Reinosa, J. J.; Rojo, M. M.; del Campo, A.; Martín-González, M.; Fernández, J. F. Highly Efficient Antimicrobial Ceramics Based on Electrically Charged Interfaces. *ACS Appl. Mater. Interfaces* **2019**, *11* (42), 39254–39262. https://doi.org/10.1021/acsami.9b10690.

(205) Diabaté, S.; Armand, L.; Murugadoss, S.; Dilger, M.; Fritsch-Decker, S.; Schlager, C.; Béal, D.; Arnal, M. E.; Biola-Clier, M.; Ambrose, S.; Mülhopt, S.; Paur, H. R.; Lynch, I.; Valsami-Jones, E.; Carriere, M.; Weiss, C. Air–Liquid Interface Exposure of Lung Epithelial Cells to Low Doses of Nanoparticles to Assess Pulmonary Adverse Effects. *Nanomaterials* **2021**, *11* (1), 1–23. https://doi.org/10.3390/nano11010065.

(206) Meng, H.; Xia, T.; George, S.; Nel, A. E. A Predictive Toxicological Paradigm for the Safety Assessment of Nanomaterials. *ACS Nano* **2009**, *3* (7), 1620–1627. https://doi.org/10.1021/nn9005973.

(207) Han, X.; Gelein, R.; Corson, N.; Wade-Mercer, P.; Jiang, J.; Biswas, P.; Finkelstein, J. N.; Elder, A.; Oberdörster, G. Validation of an LDH Assay for Assessing Nanoparticle Toxicity. *Toxicology* **2011**, *287* (1–3), 99–104. https://doi.org/10.1016/j.tox.2011.06.011.

(208) Korzeniewski, C.; Callewaert, D. M. An Enzyme-Release Assay for Natural Cytotoxicity. *J. Immunol. Methods* **1983**, *64* (3), 313–320. https://doi.org/10.1016/0022-1759(83)90438-6.

(209) Decker, T.; Lohmann-Matthes, M.-L. A Quick and Simple Method for the Quantitation of Lactate Dehydrogenase Release in Measurements of Cellular Cytotoxicity and Tumor Necrosis Factor (TNF) Activity. *J. Immunol. Methods* **1988**, *115* (1), 61–69. https://doi.org/10.1016/0022-1759(88)90310-9.

(210) Ishiyama, M. A Highly Water-Soluble Disulfonated Tetrazolium Salt as a Chromogenic Indicator for NADH as Well as Cell Viability. *Talanta* **1997**, *44* (7), 1299–1305. https://doi.org/10.1016/S0039-9140(97)00017-9.

(211) Berridge, M. V.; Herst, P. M.; Tan, A. S. Tetrazolium Dyes as Tools in Cell Biology: New Insights into Their Cellular Reduction. In *Biotechnology Annual Review*; 2005;

Vol. 11, pp 127–152. https://doi.org/10.1016/S1387-2656(05)11004-7.

(212) Kermanizadeh, A.; Jantzen, K.; Ward, M. B.; Durhuus, J. A.; Juel Rasmussen, L.; Loft, S.; Møller, P. Nanomaterial-Induced Cell Death in Pulmonary and Hepatic Cells Following Exposure to Three Different Metallic Materials: The Role of Autophagy and Apoptosis. *Nanotoxicology* **2017**, *11* (2), 184–200. https://doi.org/10.1080/17435390.2017.1279359.

(213) Fulda, S.; Gorman, A. M.; Hori, O.; Samali, A. Cellular Stress Responses: Cell Survival and Cell Death. *Int. J. Cell Biol.* **2010**, *2010*, 1–23. https://doi.org/10.1155/2010/214074.

(214) Gozuacik, D.; Kimchi, A. Autophagy as a Cell Death and Tumor Suppressor Mechanism. *Oncogene* **2004**, *23* (16), 2891–2906. https://doi.org/10.1038/sj.onc.1207521.

(215) Seong, Y.-A.; Shin, P.-G.; Yoon, J.-S.; Yadunandam, A. K.; Kim, G.-D. Induction of the Endoplasmic Reticulum Stress and Autophagy in Human Lung Carcinoma A549 Cells by Anacardic Acid. *Cell Biochem. Biophys.* **2014**, *68* (2), 369–377. https://doi.org/10.1007/s12013-013-9717-2.

(216) Stern, S. T.; Adiseshaiah, P. P.; Crist, R. M. Autophagy and Lysosomal Dysfunction as Emerging Mechanisms of Nanomaterial Toxicity. *Part. Fibre Toxicol.* **2012**, *9* (1), 20. https://doi.org/10.1186/1743-8977-9-20.

(217) He, C.; Klionsky, D. J. Regulation Mechanisms and Signaling Pathways of Autophagy. *Annu. Rev. Genet.* **2009**, *43* (1), 67–93. https://doi.org/10.1146/annurev-genet-102808-114910.

(218) Meldrum, K.; Evans, S. J.; Vogel, U.; Tran, L.; Doak, S. H.; Clift, M. J. D. The Influence of Exposure Approaches to in Vitro Lung Epithelial Barrier Models to Assess Engineered Nanomaterial Hazard. *Nanotoxicology* **2022**, *16* (1), 114–134. https://doi.org/10.1080/17435390.2022.2051627.

(219) Yokel, R. A.; MacPhail, R. C. Engineered Nanomaterials: Exposures, Hazards, and

Risk Prevention. *J. Occup. Med. Toxicol.* **2011**, *6* (1), 7. https://doi.org/10.1186/1745-6673-6-7.

(220) Oberdörster, G.; Oberdörster, E.; Oberdörster, J. Nanotoxicology: An Emerging Discipline Evolving from Studies of Ultrafine Particles. *Environ. Health Perspect.* **2005**, *113* (7), 823–839. https://doi.org/10.1289/ehp.7339.

(221) Wang, B.; Zhang, Y.; Mao, Z.; Yu, D.; Gao, C. Toxicity of ZnO Nanoparticles to Macrophages Due to Cell Uptake and Intracellular Release of Zinc Ions. *J. Nanosci. Nanotechnol.* **2014**, *14* (8), 5688–5696. https://doi.org/10.1166/jnn.2014.8876.

(222) Wohlleben, W.; Hellack, B.; Nickel, C.; Herrchen, M.; Hund-Rinke, K.; Kettler, K.; Riebeling, C.; Haase, A.; Funk, B.; Kühnel, D.; Göhler, D.; Stintz, M.; Schumacher, C.; Wiemann, M.; Keller, J.; Landsiedel, R.; Broßell, D.; Pitzko, S.; Kuhlbusch, T. A. J. The NanoGRAVUR Framework to Group (Nano)Materials for Their Occupational, Consumer, Environmental Risks Based on a Harmonized Set of Material Properties, Applied to 34 Case Studies. *Nanoscale* **2019**, *11* (38), 17637–17654. https://doi.org/10.1039/c9nr03306h.

(223) Mortensen, N. P.; Moreno Caffaro, M.; Patel, P. R.; Uddin, M. J.; Aravamudhan, S.; Sumner, S. J.; Fennell, T. R. Investigation of Twenty Metal, Metal Oxide, and Metal Sulfide Nanoparticles' Impact on Differentiated Caco-2 Monolayer Integrity. *NanoImpact* **2020**, *17* (February), 100212. https://doi.org/10.1016/j.impact.2020.100212.

(224) Ong, K. J.; MacCormack, T. J.; Clark, R. J.; Ede, J. D.; Ortega, V. A.; Felix, L. C.; Dang, M. K. M.; Ma, G.; Fenniri, H.; Veinot, J. G. C.; Goss, G. G. Widespread Nanoparticle-Assay Interference: Implications for Nanotoxicity Testing. *PLoS One* **2014**, *9* (3), e90650. https://doi.org/10.1371/journal.pone.0090650.

(225) He, T.; Long, J.; Li, J.; Liu, L.; Cao, Y. Toxicity of ZnO Nanoparticles (NPs) to A549 Cells and A549 Epithelium in Vitro: Interactions with Dipalmitoyl Phosphatidylcholine (DPPC). *Environ. Toxicol. Pharmacol.* **2017**, *56* (October), 233–240. https://doi.org/10.1016/j.etap.2017.10.002.

(226) Saptarshi, S. R.; Feltis, B. N.; Wright, P. F. A.; Lopata, A. L. Investigating the Immunomodulatory Nature of Zinc Oxide Nanoparticles at Sub-Cytotoxic Levels in Vitro and after Intranasal Instillation in Vivo. *J. Nanobiotechnology* **2015**, *13* (1), 6. https://doi.org/10.1186/s12951-015-0067-7.

(227) Hufnagel, M.; Neuberger, R.; Wall, J.; Link, M.; Friesen, A.; Hartwig, A. Impact of Differentiated Macrophage-Like Cells on the Transcriptional Toxicity Profile of CuO Nanoparticles in Co-Cultured Lung Epithelial Cells. *Int. J. Mol. Sci.* **2021**, *22* (9), 5044. https://doi.org/10.3390/ijms22095044.

(228) Zhao, H.; Li, L.; Zhan, H.; Chu, Y.; Sun, B. Mechanistic Understanding of the Engineered Nanomaterial-Induced Toxicity on Kidney. *J. Nanomater.* **2019**, *2019*, 1–12. https://doi.org/10.1155/2019/2954853.

(229) Cohen, J.; Ji, Z.; Xia, T.; Demokritou, P. An Integrated Approach for the in Vitro Dosimetry of Engineered Nanomaterials : Relevant in Vitro Dose ( RID ) Functions Background ( 1 of 2 ). *Part. Fibre Toxicol.* **2014**, *11* (20), 1–12.

(230) Pei, B.; Wang, W.; Dunne, N.; Li, X. *Applications of Carbon Nanotubes in Bone Tissue Regeneration and Engineering: Superiority, Concerns, Current Advancements, and Prospects*; 2019; Vol. 9. https://doi.org/10.3390/nano9101501.

(231) Rahman, G.; Najaf, Z.; Mehmood, A.; Bilal, S.; Shah, A.; Mian, S.; Ali, G. An Overview of the Recent Progress in the Synthesis and Applications of Carbon Nanotubes. *C* **2019**, *5* (1), 3. https://doi.org/10.3390/c5010003.

(232) Saliev, T. The Advances in Biomedical Applications of Carbon Nanotubes. *C* **2019**, *5* (2), 29. https://doi.org/10.3390/c5020029.

(233) Schnorr, J. M.; Swager, T. M. Emerging Applications of Carbon Nanotubes. *Chem. Mater.* **2011**, *23* (3), 646–657. https://doi.org/10.1021/cm102406h.

(234) Poulsen, S. S.; Jackson, P.; Kling, K.; Knudsen, K. B.; Skaug, V.; Kyjovska, Z. O.; Thomsen, B. L.; Clausen, P. A.; Atluri, R.; Berthing, T.; Bengtson, S.; Wolff, H.; Jensen, K. A.; Wallin, H.; Vogel, U. Multi-Walled Carbon Nanotube Physicochemical

Properties Predict Pulmonary Inflammation and Genotoxicity. *Nanotoxicology* **2016**, *10* (9), 1263–1275. https://doi.org/10.1080/17435390.2016.1202351.

(235) Alig, I.; Pötschke, P.; Lellinger, D.; Skipa, T.; Pegel, S.; Kasaliwal, G. R.; Villmow, T. Establishment, Morphology and Properties of Carbon Nanotube Networks in Polymer Melts. *Polymer (Guildf).* **2012**, *53* (1), 4–28. https://doi.org/10.1016/j.polymer.2011.10.063.

(236) Hiura, H.; Ebbesen, T. W.; Tanigaki, K.; Takahashi, H. Raman Studies of Carbon Nanotubes. *Chem. Phys. Lett.* **1993**, *202* (6), 509–512. https://doi.org/10.1016/0009-2614(93)90040-8.

(237) Costa, S.; Borowiak-Palen, E.; Kruszyñska, M.; Bachmatiuk, A.; Kaleńczuk, R. J. Characterization of Carbon Nanotubes by Raman Spectroscopy. *Mater. Sci. Pol.* **2008**, *26* (2), 433–441.

(238) Dresselhaus, M. S.; Dresselhaus, G.; Jorio, A.; Souza Filho, A. G.; Saito, R. Raman Spectroscopy on Isolated Single Wall Carbon Nanotubes. *Carbon N. Y.* **2002**, *40* (12), 2043–2061. https://doi.org/10.1016/S0008-6223(02)00066-0.

(239) Poulsen, S. S.; Saber, A. T.; Williams, A.; Andersen, O.; Købler, C.; Atluri, R.; Pozzebon, M. E.; Mucelli, S. P.; Simion, M.; Rickerby, D.; Mortensen, A.; Jackson, P.; Kyjovska, Z. O.; Mølhave, K.; Jacobsen, N. R.; Jensen, K. A.; Yauk, C. L.; Wallin, H.; Halappanavar, S.; Vogel, U. MWCNTs of Different Physicochemical Properties Cause Similar Inflammatory Responses, but Differences in Transcriptional and Histological Markers of Fibrosis in Mouse Lungs. *Toxicol. Appl. Pharmacol.* **2015**, *284* (1), 16–32. https://doi.org/10.1016/j.taap.2014.12.011.

(240) Rasmussen, K.; Mast, J.; Temmerman, P.-J.; Verleysen, E.; Waegeneers, N.; Steen, F. *Multi-Walled Carbon Nanotubes, NM-400, NM-401, NM-402, NM-403: Characterisation and Physico-Chemical Properties In: NM-Series of Representative Manufactured Nanomaterials*; 2014. https://doi.org/10.2788/10753.

(241) Guimarães, B.; Gomes, S.; Campodoni, E.; Sandri, M.; Sprio, S.; Blosi, M.; Costa, A.; Amorim, M.; Scott-Fordsmand, J. Environmental Hazards of Nanobiomaterials

(Hydroxyapatite-Based NMs)—A Case Study with Folsomia Candida—Effects from Long Term Exposure. *Toxics* **2022**, *10* (11), 704. https://doi.org/10.3390/toxics10110704.

(242) Hernández-Moreno, D.; Navas, J. M.; Fernández-Cruz, M. L. Short and Long-Term Effects of Nanobiomaterials in Fish Cell Lines. Applicability of RTgill-W1. *Chemosphere* **2022**, *309* (April), 136636. https://doi.org/10.1016/j.chemosphere.2022.136636.

(243) Tampieri, A.; Sprio, S.; Sandri, M.; Valentini, F. Mimicking Natural Bio-Mineralization Processes: A New Tool for Osteochondral Scaffold Development. *Trends Biotechnol.* **2011**, *29* (10), 526–535. https://doi.org/10.1016/j.tibtech.2011.04.011.

(244) Fontaine, M.; Bartolami, E.; Prono, M.; Béal, D.; Blosi, M.; Costa, A. L.; Ravagli, C.; Baldi, G.; Sprio, S.; Tampieri, A.; Fenoglio, I.; Tran, L.; Fadeel, B.; Carriere, M. Nanomaterial Genotoxicity Evaluation Using the High-Throughput P53-Binding Protein 1 (53BP1) Assay. *PLoS One* **2023**, *18* (9 SEPTEMBER), 1–29. https://doi.org/10.1371/journal.pone.0288737.

(245) Gomes, S. I. L.; Guimarães, B.; Campodoni, E.; Sandri, M.; Sprio, S.; Blosi, M.; Costa, A. L.; Scott-Fordsmand, J. J.; Amorim, M. J. B. Safer and Sustainable-by-Design Hydroxyapatite Nanobiomaterials for Biomedical Applications: Assessment of Environmental Hazards. *Nanomaterials* **2022**, *12* (22). https://doi.org/10.3390/nano12224060.

(246) Saleh, T.; Rasheed, A. N.; Muthalif, A. G. A. Experimental Study on Improving µ-WEDM and µ-EDM of Doped Silicon by Temporary Metallic Coating. *Int. J. Adv. Manuf. Technol.* **2015**, *78* (9–12), 1651–1663. https://doi.org/10.1007/s00170-014-6732-4.

(247) Wallyn; Anton; Vandamme. Synthesis, Principles, and Properties of Magnetite Nanoparticles for In Vivo Imaging Applications—A Review. *Pharmaceutics* **2019**, *11* (11), 601. https://doi.org/10.3390/pharmaceutics11110601.

(248) Alamelu, K.; Jaffar Ali, B. M. Sunlight Driven Photocatalytic Performance of a Pt

Nanoparticle Decorated Sulfonated Graphene–TiO 2 Nanocomposite. *New J. Chem.* **2020**, *44* (18), 7501–7516. https://doi.org/10.1039/D0NJ00394H.

(249) He, H.; Pham-Huy, L. A.; Dramou, P.; Xiao, D.; Zuo, P.; Pham-Huy, C. Carbon Nanotubes: Applications in Pharmacy and Medicine. *Biomed Res. Int.* **2013**, *2013*, 1–12. https://doi.org/10.1155/2013/578290.

(250) Mahanta, U.; Khandelwal, M.; Deshpande, A. S. TiO2@SiO2 Nanoparticles for Methylene Blue Removal and Photocatalytic Degradation under Natural Sunlight and Low-Power UV Light. *Appl. Surf. Sci.* **2022**, *576* (PA), 151745. https://doi.org/10.1016/j.apsusc.2021.151745.

(251) Kitsou, I.; Panagopoulos, P.; Maggos, T.; Arkas, M.; Tsetsekou, A. Development of SiO2@TiO2 Core-Shell Nanospheres for Catalytic Applications. *Appl. Surf. Sci.* **2018**, *441*, 223–231. https://doi.org/10.1016/j.apsusc.2018.02.008.

(252) Mudunkotuwa, I. A.; Grassian, V. H. Biological and Environmental Media Control Oxide Nanoparticle Surface Composition: The Roles of Biological Components (Proteins and Amino Acids), Inorganic Oxyanions and Humic Acid. *Environ. Sci. Nano* **2015**, *2* (5), 429–439. https://doi.org/10.1039/C4EN00215F.

(253) Lee, E. L.; Wachs, I. E. In Situ Raman Spectroscopy of SiO 2 -Supported Transition Metal Oxide Catalysts: An Isotopic 18 O− 16 O Exchange Study. *J. Phys. Chem. C* **2008**, *112* (16), 6487–6498. https://doi.org/10.1021/jp076485w.

(254) Montenegro, D. N.; Hortelano, V.; Martínez, O.; Martínez-Tomas, M. C.; Sallet, V.; Muñoz-Sanjosé, V.; Jiménez, J. Non-Radiative Recombination Centres in Catalyst-Free ZnO Nanorods Grown by Atmospheric-Metal Organic Chemical Vapour Deposition. *J. Phys. D. Appl. Phys.* **2013**, *46* (23), 235302. https://doi.org/10.1088/0022-3727/46/23/235302.

(255) Calleja, J. M.; Cardona, M. Resonant Raman Scattering in ZnO. *Phys. Rev. B* **1977**, *16* (8), 3753–3761. https://doi.org/10.1103/PhysRevB.16.3753.

(256) Lin, Y.-C.; Chen, C.-H.; Chen, L.-Y.; Hsu, S.-C.; Qian, S. Enhancing the Insulation of

Wide-Range Spectrum in the PVA/N Thin Film by Doping ZnO Nanowires. *RSC Adv.* **2014**, *4* (85), 45419–45424. https://doi.org/10.1039/C4RA05667A.

(257) Zhuo, R. F.; Feng, H. T.; Liang, Q.; Liu, J. Z.; Chen, J. T.; Yan, D.; Feng, J. J.; Li, H. J.; Cheng, S.; Geng, B. S.; Xu, X. Y.; Wang, J.; Wu, Z. G.; Yan, P. X.; Yue, G. H. Morphology-Controlled Synthesis, Growth Mechanism, Optical and Microwave Absorption Properties of ZnO Nanocombs. *J. Phys. D. Appl. Phys.* **2008**, *41* (18), 185405. https://doi.org/10.1088/0022-3727/41/18/185405.

(258) Cox, K. D.; Covernton, G. A.; Davies, H. L.; Dower, J. F.; Juanes, F.; Dudas, S. E. Human Consumption of Microplastics. *Environ. Sci. Technol.* **2019**, *53* (12), 7068–7074. https://doi.org/10.1021/acs.est.9b01517.

(259) Paul, M. B.; Stock, V.; Cara-Carmona, J.; Lisicki, E.; Shopova, S.; Fessard, V.; Braeuning, A.; Sieg, H.; Böhmert, L. Micro- And Nanoplastics-Current State of Knowledge with the Focus on Oral Uptake and Toxicity. *Nanoscale Advances*. Royal Society of Chemistry October 2020, pp 4350–4367. https://doi.org/10.1039/d0na00539h.

(260) Senathirajah, K.; Attwood, S.; Bhagwat, G.; Carbery, M.; Wilson, S.; Palanisami, T. Estimation of the Mass of Microplastics Ingested – A Pivotal First Step towards Human Health Risk Assessment. *J. Hazard. Mater.* **2021**, *404*, 124004. https://doi.org/10.1016/j.jhazmat.2020.124004.

(261) Tamargo, A., Jiménez-Gómez, M. B., Bartolomé, B., Cueva, C., & Moreno-Arribas, M. V. Micro and Nanoplastics: From Food Occurrence to Impact on Human Gastrointestinal Health. *Trends Food Sci. Technol.* **2021**, *under revi*.

(262) EFSA. Initial Statement by the Group of Chief Scientific Advisors: A Scientific Perspective on Microplastic Pollution and Its Impacts. *Eu Publ.* **2018**, No. June, 1–4.

(263) Presence of Microplastics and Nanoplastics in Food, with Particular Focus on Seafood. *EFSA J.* **2016**, *14* (6), e04501. https://doi.org/10.2903/j.efsa.2016.4501.

(264) Koelmans, A. A.; Mohamed Nor, N. H.; Hermsen, E.; Kooi, M.; Mintenig, S. M.; De France, J. Microplastics in Freshwaters and Drinking Water: Critical Review and Assessment of Data Quality. *Water Research*. Elsevier Ltd May 2019, pp 410–422. https://doi.org/10.1016/j.watres.2019.02.054.

(265) Europe., P. *Plastics - the Facts 2020*. Plastics - the Facts 2020.

(266) Shruti, V. C., Pérez-Guevara, F., Elizalde-Martínez, I., & Kutralam-Muniasamy, G. First Study of Its Kind on the Microplastic Contamination of Soft Drinks, Cold Tea and Energy Drinks - Future Research and Environmental Considerations. *Sci. Total Environ.* **2020**, *726*.

(267) Schwabl, P.; Koppel, S.; Konigshofer, P.; Bucsics, T.; Trauner, M.; Reiberger, T.; Liebmann, B. Detection of Various Microplastics in Human Stool: A Prospective Case Series. *Ann. Intern. Med.* **2019**, *171* (7), 453–457. https://doi.org/10.7326/M19-0618.

(268) Stock, V.; Fahrenson, C.; Thuenemann, A.; Dönmez, M. H.; Voss, L.; Böhmert, L.; Braeuning, A.; Lampen, A.; Sieg, H. Impact of Artificial Digestion on the Sizes and Shapes of Microplastic Particles. *Food Chem. Toxicol.* **2020**, *135* (November 2019). https://doi.org/10.1016/j.fct.2019.111010.

(269) Fackelmann, G.; Sommer, S. Microplastics and the Gut Microbiome: How Chronically Exposed Species May Suffer from Gut Dysbiosis. *Marine Pollution Bulletin*. Elsevier Ltd June 2019, pp 193–203. https://doi.org/10.1016/j.marpolbul.2019.04.030.

(270) Jin, Y.; Lu, L.; Tu, W.; Luo, T.; Fu, Z. Impacts of Polystyrene Microplastic on the Gut Barrier, Microbiota and Metabolism of Mice. *Sci. Total Environ.* **2019**, *649*, 308–317. https://doi.org/10.1016/j.scitotenv.2018.08.353.

(271) Lu, L.; Wan, Z.; Luo, T.; Fu, Z.; Jin, Y. Polystyrene Microplastics Induce Gut Microbiota Dysbiosis and Hepatic Lipid Metabolism Disorder in Mice. *Sci. Total Environ.* **2018**, *631–632*, 449–458. https://doi.org/10.1016/j.scitotenv.2018.03.051.

(272) Li, B.; Ding, Y.; Cheng, X.; Sheng, D.; Xu, Z.; Rong, Q.; Wu, Y.; Zhao, H.; Ji, X.; Zhang, Y. Polyethylene Microplastics Affect the Distribution of Gut Microbiota and Inflammation Development in Mice. *Chemosphere* **2020**, *244*, 125492. https://doi.org/10.1016/j.chemosphere.2019.125492.

(273) Bahl, S. K.; Cornell, D. D.; Boerio, F. J.; McGraw, G. E. Interpretation of the Vibrational Spectra of Poly(Ethylene Terephtalate). *J Polym Sci Part B Polym Lett* **1974**, *12* (1), 13–19. https://doi.org/10.1002/pol.1974.130120103.

(274) Melveger, A. J. Laser-Raman Study of Crystallinity Changes in Poly(Ethylene Terephthalate). *J. Polym. Sci. Part A-2 Polym. Phys.* **1972**, *10* (2), 317–322. https://doi.org/10.1002/pol.1972.160100211.

(275) Štokr, J.; Schneider, B.; Doskočilová, D.; Lövy, J.; Sedláček, P. Conformational Structure of Poly(Ethylene Terephthalate). Infra-Red, Raman and n.m.r. Spectra. *Polymer (Guildf).* **1982**, *23* (5), 714–721. https://doi.org/10.1016/0032-3861(82)90057-X.

(276) Tamargo, A.; Molinero, N.; Reinosa, J. J.; Alcolea-Rodriguez, V.; Portela, R.; Bañares, M. A.; Fernández, J. F.; Moreno-Arribas, M. V. PET Microplastics Affect Human Gut Microbiota Communities during Simulated Gastrointestinal Digestion, First Evidence of Plausible Polymer Biodegradation during Human Digestion. *Sci. Rep.* **2022**, *12* (1), 528. https://doi.org/10.1038/s41598-021-04489-w.

(277) Bistričić, L.; Borjanović, V.; Leskovac, M.; Mikac, L.; McGuire, G. E.; Shenderova, O.; Nunn, N. Raman Spectra, Thermal and Mechanical Properties of Poly(Ethylene Terephthalate) Carbon-Based Nanocomposite Films. *J. Polym. Res.* **2015**, *22* (3). https://doi.org/10.1007/s10965-015-0680-z.

(278) Lin, C. C.; Krommenhoek, P. J.; Watson, S. S.; Gu, X. Depth Profiling of Degradation of Multilayer Photovoltaic Backsheets after Accelerated Laboratory Weathering: Cross-Sectional Raman Imaging. *Sol. Energy Mater. Sol. Cells* **2016**, *144*, 289–299. https://doi.org/10.1016/j.solmat.2015.09.021.

(279) Adar, F.; Noether, H. Raman Microprobe Spectra of Spin-Oriented and Drawn

Filaments of Poly(Ethylene Terephthalate). *Polymer (Guildf)*. **1985**, *26* (13), 1935–1943. https://doi.org/10.1016/0032-3861(85)90171-5.

(280) Bistričić, L.; Borjanović, V.; Leskovac, M.; Mikac, L.; McGuire, G. E.; Shenderova, O.; Nunn, N. Raman Spectra, Thermal and Mechanical Properties of Poly(Ethylene Terephthalate) Carbon-Based Nanocomposite Films. *J. Polym. Res.* **2015**, *22* (3). https://doi.org/10.1007/s10965-015-0680-z.

(281) Tamargo, A.; Molinero, N.; Reinosa, J. J.; Alcolea-Rodríguez, V.; Portela, R.; Bañares, M. A.; Fernández, J. F. PET Microplastics Affect Human Gut Microbiota Communities During Simulated Gastrointestinal Digestion. First Evidence of Plausible Polymer Biodegradation During Human Digestion. *Sci. Rep.* **2022**, No. 0123456789, 1–17. https://doi.org/10.1038/s41598-021-04489-w.

(282) Ainali, N. M.; Kalaronis, D.; Evgenidou, E.; Kyzas, G. Z.; Bobori, D. C.; Kaloyianni, M.; Yang, X.; Bikiaris, D. N.; Lambropoulou, D. A. Do Poly(Lactic Acid) Microplastics Instigate a Threat? A Perception for Their Dynamic towards Environmental Pollution and Toxicity. *Sci. Total Environ.* **2022**, *832* (April), 155014. https://doi.org/10.1016/j.scitotenv.2022.155014.

(283) Jiménez-Arroyo, C.; Tamargo, A.; Molinero, N.; Reinosa, J. J.; Alcolea-Rodriguez, V.; Portela, R.; Bañares, M. A.; Fernández, J. F.; Moreno-Arribas, M. V. Simulated Gastrointestinal Digestion of Polylactic Acid (PLA) Biodegradable Microplastics and Their Interaction with the Gut Microbiota. *Sci. Total Environ.* **2023**, *902* (May), 166003. https://doi.org/10.1016/j.scitotenv.2023.166003.

(284) Kister, G.; Cassanas, G.; Vert, M. Effects of Morphology, Conformation and Configuration on the IR and Raman Spectra of Various Poly(Lactic Acid)S. *Polymer (Guildf)*. **1998**, *39* (2), 267–273. https://doi.org/10.1016/S0032-3861(97)00229-2.

(285) Qin, D.; Kean, R. T. Crystallinity Determination of Polylactide by FT-Raman Spectrometry. *Appl. Spectrosc.* **1998**, *52* (4), 488–495. https://doi.org/10.1366/0003702981943950.

(286) Smith, P. B.; Leugers, A.; Kang, S.; Yang, X.; Hsu, S. L. Raman Characterization of

Orientation in Poly(Lactic Acid) Films. *Macromol. Symp.* **2001**, *175*, 81–94. https://doi.org/10.1002/1521-3900(200110)175:1<81::AID-MASY81>3.0.CO;2-1.

(287) Vano-Herrera, K.; Vogt, C. Degradation of Poly(L-Lactic Acid) Coating on Permanent Coronary Metal Stent Investigated Ex Vivo by Micro Raman Spectroscopy. *J. Raman Spectrosc.* **2017**, *48* (5), 711–719. https://doi.org/10.1002/jrs.5111.

(288) Cialla-May, D.; Rösch, P.; Popp, J. Raman-Spektroskopie in Der Infektionsforschung. *BIOspektrum* **2022**, *28* (6), 597–599. https://doi.org/10.1007/s12268-022-1845-z.

(289) Horiue, H.; Sasaki, M.; Yoshikawa, Y.; Toyofuku, M.; Shigeto, S. Raman Spectroscopic Signatures of Carotenoids and Polyenes Enable Label-Free Visualization of Microbial Distributions within Pink Biofilms. *Sci. Rep.* **2020**, *10* (1), 7704. https://doi.org/10.1038/s41598-020-64737-3.

(290) Pezzotti, G. Raman Spectroscopy in Cell Biology and Microbiology. *J. Raman Spectrosc.* **2021**, *52* (12), 2348–2443. https://doi.org/10.1002/jrs.6204.

# Figure index

# Scientific contributions

## Publications

*Published (4)*

· Tamargo, A., Molinero, N., Reinosa, J. J., **Alcolea-Rodriguez, V**., Portela, R., Bañares, M. A., ... & Moreno-Arribas, M. (2022). PET microplastics affect human gut microbiota communities during simulated gastrointestinal digestion, first evidence of plausible polymer biodegradation during human digestion**. Scientific Reports**, 12(1), 1-15. DOI: https://doi.org/10.1038/s41598-021-04489-w

· Serrano-Lotina, A., Portela, R., Baeza, P., **Alcolea-Rodriguez, V**., Villarroel, M., & Ávila, P. (2022). Zeta potential as a tool for functional materials development. **Catalysis Today**. DOI: https://doi.org/10.1016/j.cattod.2022.08.004

· Jiménez-Arroyo, C., Tamargo, A., Molinero, N., Reinosa, J. J., **Alcolea-Rodriguez, V**., Portela, R., ... & Moreno-Arribas, M. V. (2023). Simulated gastrointestinal digestion of polylactic acid (PLA) biodegradable microplastics and their interaction with the gut microbiota. **Science of The Total Environment**, 166003. DOI: https://doi.org/10.1016/j.scitotenv.2023.166003

· Robles-Martín, A., Amigot-Sánchez, R., Fernandez-Lopez, L., Gonzalez-Alfonso, J. L., Roda, S., **Alcolea-Rodriguez, V**., ... & Guallar, V. (2023). Sub-micro-and nano-sized polyethylene terephthalate deconstruction with engineered protein nanopores. **Nature Catalysis**, 1-12. DOI: https://doi.org/10.1038/s41929-023-01048-6

*In preparation (8)*

· **Alcolea-Rodriguez. V**.... & Portela, R, Bañares, M. A. (2024). In chemico methodology to rank nanomaterials according to number, nature and oxidative capacity of surface sites. Status: u*nder review in* ***Environmental Science: nano***

· Stobernack, T., Dommershausen N., **Alcolea-Rodríguez, V**.,... & Dumit, V. Advancing Nanomaterial Toxicology Screening through Efficient and Cost-Effective Quantitative Proteomics. (2023). *Status: under review in* ***SMALL.***

· **Alcolea-Rodriguez. V**…. & Portela, R, Bañares, M. A. (2024). Reactive sites-based dose metrics for nanotoxicity: an in chemico approach to categorize the reactive surface oxidative potential of engineered nanomaterials. *Status: Under review by international collaborators*

· **Alcolea-Rodriguez. V**…. & Portela, R, Bañares, M. A. (2024). Differentially induced autophagy by engineered nanomaterial treatment has an impact at cellular homeostasis and cytotoxicity. *Status: Under review by international collaborators*

· **Alcolea-Rodriguez. V**…. & Portela, R, Bañares, M. A. (2024). Surface reactive and dissolution rates implications in hydroxyapatite and iron-based nanobiomaterials. *Status: Under review by international collaborators*

· Burgum, M., **Alcolea-Rodriguez. V**…. & Portela, R, Bañares, M. A. (2024). The dispersion approach alters the surface of carbon nanotubes but it does not involve their *in vitro* mutagenicity to human cells. *Status: writing discussion and conclusions*

· **Alcolea-Rodriguez. V**…. & Portela, R, Bañares, M. A. (2024). Raman monitoring of nanoPET depolymerization. *Status: writing results and discussion*

· Altmann, K., Portela, R., Waniek, T., Wachtendorf, V., **Alcolea-Rodriguez, V.,** … & Lea Ann Dailey. (2024). Current good practices for the production of test and reference materials for micro- and nanoplastic research. *Status: Under review by international collaborators*

## Poster and talks

1) 2022. I Congreso de la Sociedad Iberoamericana de Microbiota, Probióticos y Prebióticos. Oral communication "Impacto de la ingesta de microplásticos en el tracto gastrointestinal y en la microbiota colónica humana"
2) 2022. Annual meeting NanoInformaTiX. Oral communication "MODELS' VALIDATION AND INTEGRATION, FEEDING TO DATABASES. Surface reactivity descriptors"
3) 2022. Nanoweek Cyprus 2022. Oral communication "New descriptor to quantify the number, nature and specific reactivity (Oxidative Turnover Frequency) of surface reactive sites for nanomaterials evaluation, grouping and dose metrics"
4) 2022. Nanoweek Cyprus 2022. Poster The Cytotoxic and Genotoxic Effects of Carbon Nanotubes on Human Cells *In vitro*"
5) 2022. ICT2022. Poster "Investigating the cytotoxic and genotoxic potential of carbon nanotubes in

6) human cells *In vitro*"
7) 2023. EuropaCat23. Oral communication "Biological air quality: catalytic inactivation of airborne viruses"
8) 2023. SECAT23. Oral communication "Correlación de la capacidad oxidativa con la capacidad biocida"
9) 2023. NAM28. Oral communication "Efficient Technology for Catalytic Virus Inactivation"

## University teaching

- Co-supervision of Bachelor's Thesis. Student: Miguel Armas. Degree: Chemical Engineering (UAM)
- Co-supervision of Bachelor's Thesis. Student: Belen Leon. Degree: Chemistry (UAM)
- Complutense university of Madrid. Pharmacy faculty.
    - 2019-2020: 30 h. Subject: Analytical chemistry II
    - 2020-2021: 45 h. Subject: Analytical chemistry II
    - 2021-2022: 45 h. Subject: Analytical chemistry II
    - 2022-2023: 30 h. Subject: Analytical chemistry I

## Trainings

- Nanosafety Training School (Online). From basic science to risk governance. 15 hours
- Nanosafety Training School (Venice 2022). From basic science to risk governance. 15 hours
- Nanosafety Training School (Venice 2023). From basic science to risk governance. 15 hours
- Spanish National Research Council (CSIC). Course in material characterization and instrumental techniques. Module II. 31 hours
- Spanish National Research Council (CSIC). Course in material characterization and instrumental techniques. Module III. 30 hours
- Spanish National Research Council (CSIC). Advanced Applied Statistics. Design of experiments, modeling and multivariate analysis with IBM SPSS statistics. 20 hours
- Spanish National Research Council Foundation. Courses in Good Scientific Practices. 25 hours

## Participation in EU projects

- BIORIMA. Risk management of biomaterials. Tasks performed: preparation of acellular assays that help predict the toxicity of nanoparticulate biomaterials. *2019, Spanish National Research Council (CSIC)*.
- SUNSHINE. Development of safety assessment strategies for new advanced multicomponent nanomaterials for commercial use in the industry. *2021-2022, Spanish National Research Council (CSIC)*.
- NANOINFORMATIX. Development and implementation of a sustainable modeling platform for NanoInformatics. Tasks performed: development of probe reactions for physicochemical characterization of nanoparticles, and toxicity assays. *2019 – 2023, Spanish National Research Council (CSIC) and BfR (Berlin, Germany)*
- PlasticFate. Risk assessment of plastics on human health and synthesis of micro and nanoplastics that serve as reference materials. *2023, Spanish National Research Council (CSIC)*.
- Harmless. Risk assessment of next-generation multicomponent nanomaterials relevant to human health and the environment. *2022-2023, BfR (Berlin, Germany)*.